Titre: Title:	Principes fondamentaux de la RTD en phase gazeuse dans les réacteurs à lit fluidisé
Auteur: Author:	Ariane Bérard
Date:	2020
Type:	Mémoire ou thèse / Dissertation or Thesis
Référence: Citation:	Bérard, A. (2020). Principes fondamentaux de la RTD en phase gazeuse dans les réacteurs à lit fluidisé [Thèse de doctorat, Polytechnique Montréal]. PolyPublie. https://publications.polymtl.ca/5484/

POLYTECHNIQUE MONTRÉAL
affiliée à l'Université de Montréal

Principes fondamentaux de la RTD en phase gazeuse dans les réacteurs à lit fluidisé

ARIANE BÉRARD
Département de génie chimique

Thèse présentée en vue de l'obtention du diplôme de *Philosophiæ Doctor*
Génie chimique

Octobre 2020

POLYTECHNIQUE MONTRÉAL
affiliée à l'Université de Montréal

Cette thèse intitulée :

Principes fondamentaux de la RTD en phase gazeuse dans les réacteurs à lit fluidisé

présentée par **Ariane BÉRARD**
en vue de l'obtention du diplôme de *Philosophiæ Doctor*
a été dûment acceptée par le jury d'examen constitué de :

Paul STUART, président
Gregory PATIENCE, membre et directeur de recherche
Bruno BLAIS, membre et codirecteur de recherche
Michel PERRIER, membre
Benjamin AMBLARD, membre externe

DÉDICACE

À mes parents et mes amies,
qui m'ont soutenu tout au long de mes études...

REMERCIEMENTS

Tout au long de mon doctorat, plusieurs personnes m'ont accompagné dans ce projet d'envergure. Tout d'abord, j'aimerais remercier mon directeur de recherche, Prof. Gregory Patience, qui, sans lui, je n'aurais pas accompli tout cela en peu de temps. Il m'a toujours appuyé dans mes projets, même les plus farfelus. Puis, j'aimerais remercier Prof. Bruno Blais, mon co-directeur, pour son temps, sa patience et son écoute dans les moments les plus difficiles. Ces deux personnes ont toujours cru en mes capacités et je vous en remercie.

Puis, ce projet de doctorat n'aurait pas été possible sans les nombreux stagiaires qui m'ont accompagné tout au long de ce projet. Tout d'abord, Meaghan Kilmartin qui a été la première à m'accompagner au début de mon doctorat quand tout n'était pas très clair. Merci pour ta patience et ta compréhension. Puis, Roberto Valquèz, qui est resté près d'un an avec nous dans l'équipe. Cela a été un vrai plaisir de travailler avec toi. Puis, Valentin Hours qui m'a sauvé la vie mainte et mainte fois quand j'étais à l'université de Cambridge. Merci pour ton temps et ta compréhension. Ce n'était pas toujours évident de travailler à distance. Finalement, merci à Juliane Rastoueix qui m'a aidé à débuter la simulation de mon réacteur à lit fluidisé par CFD-DEM.

Par la suite, un gros merci à Yannick Landry-Ducharme qui a toujours été là pour moi quand j'avais de la difficulté au laboratoire. J'ai vraiment aimé travailler avec toi, dommage que tu sois parti avant la fin. Puis, merci à Alejandro le nouveau technicien de notre groupe. Malgré le peu de temps que nous avons travaillé ensemble, tu as toujours été efficace et très bon ! J'espère encore travailler avec toi dans un futur rapproché. Ensuite, un gros merci à Martine Lamarche et Gino Robin, qui s'en eux, le département serait très ennuyeux. C'était toujours agréable de prendre de vos nouvelles à 7h le matin. Un merci aussi à Sébastien Chénard, toujours présent pour m'aider avec les bouteilles de gaz et à faire des commandes très très spéciales.

Puis, un gros merci à mes parents qui sont toujours là pour me supporter dans mes idées folles. Je vous aime fort, c'est grâce à vous si je me suis rendue aussi loin dans mes études. Aussi, un merci tout particulier à mes amies du baccalauréat RAMAK : Amel Sarah Nouas, Malika Abdul Mohamed et Raïssa Manzo. Vous m'appuyez toujours dans mes décisions et ça me fait chaud au cœur !

Ensuite, un gros merci à tous ceux que j'ai croisés durant mes 10 années à Polytechnique Montréal. Ce fut un réel plaisir de vous côtoyer. Particulièrement, un gros merci à Patrice Farand qui a été le premier à croire en mes capacités !

Finalement, un grand merci à tous les membres de mon jury soit Prof. Paul Stuart, Prof. Michel Perrier et mon membre externe, M. Benjamin Amblard pour leur temps consacré à la lecture et la révision de ma thèse.

RÉSUMÉ

La distribution du temps de résidence (RTD) est une technique de diagnostic appliquée par les chercheurs pour évaluer l'hydrodynamique dans les réservoirs, les tuyaux, les réacteurs et les systèmes à composants multiples. Il détecte les écarts par rapport aux modèles d'écoulement idéaux tels que les zones mortes, les canaux et la dispersion. Les expériences RTD consistent à introduire un traceur détectable soit un gaz inerte, un solide ou un liquide, puis à détecter sa concentration à un certain point du système, généralement à la sortie.

Nous avons développé une méthodologie RTD précise et reproductible pour mesurer l'hydrodynamique en phase gazeuse et l'avons appliquée à un micro-réacteur à lit fluidisé (8 mm de diamètre). Nous avons comparé une injection en continu (*heaviside step*) à une injection d'un volume précis (*bolus*). Dans le premier cas, nous substituons instantanément la composition du débit de gaz et examinons l'évolution de la concentration avec le temps à l'aide d'un spectromètre de masse à une fréquence de 2 Hz. Dans le second cas, nous pivotons une vanne multiport qui pousse un volume du traceur gazeux à travers une bobine vers le réacteur. Pour comprendre l'effet de la diffusivité, de la dispersion et de l'adsorption, nous avons comparé 7 gaz avec des coefficients de diffusivité distincts - Kr, O_2, CO_2, CO, CH_4, He et H_2. Nous avons étudié l'hydrodynamique de ces gaz dans le réacteur à lit fluidisé avec des catalyseurs du groupe Geldart A - l'hémihydrate d'hydrogénophosphate de vanadyle (VPOP), le pyrophosphate de vanadyle calciné (VPPC) et équilibré (VPPE), le catalyseur pour le craquage catalytique en lit fluidisé (FCC) ainsi qu'avec une poudre du groupe Geldart B — le sable. H_2 et He, avec leurs coefficients de diffusivité élevés, sortent toujours du réacteur à l'avance autant avec un catalyseur poreux et que non poreux ainsi qu'à température ambiante ou à 300 °C. Nous avons ajusté toutes les courbes de réponse RTD avec un modèle de dispersion axiale avec des conditions frontière fermées ouvertes. Lorsqu'un gaz de synthèse simulé — CO_2, CO, CH_4 et H_2 — est injecté sous forme de pulse dans le micro-réacteur chargé de catalyseur FCC, le CO_2 est adsorbé à température ambiante. Ceci est représenté sur la courbe de réponse par une queue étendue et un grand écart par rapport au modèle de dispersion axiale. De plus, le CO_2 prend deux fois plus de temps pour sortir du réacteur que H_2. Ce phénomène chromatographique était inattendu et pourrait être appliqué pour éliminer le CO_2 de l'air ou des courants industriels.

Cet écart important par rapport à un comportement idéal nous a conduits à développer un nouveau modèle de réservoirs en série (*tanks-in-series*) basé sur la phase apparente (*bulk*), le volume des pores et l'équilibre molaire des espèces adsorbées. Nous avons résolu simulta-

nément les équations pour le CO, le CO_2 et le CH_4 en considérant 40 CSTR en série. Avec ce modèle, nous avons quantifié les taux de transfert de masse entre la phase apparente et solide, le taux d'adsorption / désorption et le taux de circulation interne solide.

Enfin, nous avons débuté une étude de simulation numérique appliquant la mécanique des fluides numériques couplée à des méthodes par éléments discrets (CFD-DEM) pour le réacteur à lit fluidisé de 8 mm. L'objectif est de comparer la RTD par simulations numériques avec des données expérimentales.

ABSTRACT

Residence time distribution (RTD) is a diagnostic technique researcher apply to evaluate hydrodynamics in vessels, pipes, reservoirs, and multi-component systems. It detects deviations from ideal flow patterns non-homogeneity like dead zones, channelling, and dispersion. RTD experiments consist of introducing an identifiable, inert gas, solid or liquid tracer and then detecting it at some point in the system, usually the exit.

We developed a precise, reproducible RTD methodology to measure gas phase hydrodynamics and applied it to a micro-fluidized bed reactor (8 mm diameter). We compared a Heaviside step function injection against a bolus injection. In the former, we instantaneously switch the composition of the gas flow and monitor the change in concentration with time with a mass spectrometer at a frequency of 2 Hz. In the second case, we switch a multiport valve that pushes a volume of tracer gas from a coil into the reactor. To understand the diffusivity, dispersion, and adsorption effect, we compared 7 gases with distinct diffusivity coefficients – Kr, O_2, CO_2, CO, CH_4, He and H_2. We examined the hydrodynamics of these gases in the fluidized bed reactor for Geldart group A catalyst – vanadyl hydrogen phosphate hemihydrate (VPOP), vanadyl pyrophosphate calcined (VPPC) and equilibrated (VPPE), fluid catalytic cracking (FCC), and Geldart group B powder – sand. H_2 and He, with high diffusivity coefficients, always egress from the reactor in advance with porous and non-porous catalyst as well as ambient temperature and 300 °C. We fitted all the response curves with an axial dispersion model with closed-open boundary conditions. When a simulated syngas – CO_2, CO, CH_4, and H_2 – is injected as a pulse in the micro reactor loaded with FCC catalyst, CO_2 adsorbed at ambient temperature. This is represented on the response curve by an extended tail and a large deviation to the axial dispersion model. Also, CO_2 takes double the time to egress the reactor compared to H_2. This chromatographic phenomenon was unexpected and might be applied to remove CO_2 from the air or industrial streams.

This important deviation from an ideal behaviour led us to develop a new tanks-in-series model based on bulk phase, pore volume, and adsorbed species mole balance. We resolved simultaneously the equations for CO, CO_2, and CH_4 considering 40 CSTRs in series. With this model, we quantified the mass transfer rates between the bulk and solid phase, the adsorption/desorption rate, and the solid internal circulation rate.

Finally, we initiated a numerical simulation study applying computational fluid dynamics coupled with discrete element methods (CFD-DEM) for the 8 mm fluidized bed reactor. The objective is to compare RTD by numerical simulations with experimental data.

TABLE DES MATIÈRES

LISTE DES TABLEAUX

LISTE DES FIGURES

LISTE DES SIGLES ET ABRÉVIATIONS

BET	Brunauer–Emmett–Teller
CFB	réacteur à lit fluidisé circulant
CFD	Computational Fluid Dynamics
CSTR	Continuous Stirred-Tank Reactor
DEAE	diéthyl-aminoéthyl
DEM	Discrete Element Method
FCC	Fluid catalytic cracking catalyst ou catalyseur pour le craquage catalytique en lit fluidisé
FFT	transformé de Fourrier rapide
FFT^{-1}	inverse du transformé de Fourrier
KTGF	théorie cinétique de l'écoulement granulaire
MA	anhydride maléique (MA)
MS	Spectromètre de masse
PFR	réacteur à écoulement piston ou Plug Flow Reactor
RTD	Distribution du temps de résidence ou Residence Time Distribution
SSE	Erreur de la somme des carrés ou error sum of squares
VPOP	vanadyl hydrogen phosphate hemihydrate ou hydrogénophosphate de vanadyle hémihydraté
VPPC	vanadyl pyrophosphate calcined ou pyrophosphate de vanadyle calciné
VPPE	vanadyl pyrophosphate equilibrated ou pyrophosphate de vanadyle équilibré

LISTE DES VARIABLES

a	rayon d'une particule (m)
A_i	amplitude de la fonction blob, adimensionnel
A_p	aire projetée de la particule (m^2)
C	concentration ($\mathrm{mol\,L^{-1}}$)
C^*	concentration de la phase gazeuse à l'intérieur d'un pore ($\mathrm{mol\,L^{-1}}$)
C_A	concentration de la molécule A dans le gaz ($\mathrm{mol\,L^{-1}}$)
$C_\mathrm{A,b}$	concentration de la molécule A dans la bulle ($\mathrm{mol\,L^{-1}}$)
C_A^i	concentration de la molécule A à la surface de la particule ($\mathrm{mol\,L^{-1}}$)
C_{AB}	constante de Sutherland (°C)
$C_\mathrm{A,c}$	concentration dans le nuage ($\mathrm{mol\,L^{-1}}$)
C^ads	concentration de la molécule adsorbée ($\mathrm{mol\,L^{-1}}$)
$C_\mathrm{A,e}$	concentration dans la phase émulsion ($\mathrm{mol\,L^{-1}}$)
C_Aire	Aire sous la courbe (compte s)
C_D	coefficient de traînée, adimensionnel
C_LR	coefficient de portance dû à la rotation, adimensionnel
$C_\mathrm{modèle}$	Concentration calculée à l'aide du modèle de dispersion axiale (compte)
C_MS	concentration enregistrée par le spectromètre de masse (compte)
C_p	capacité thermique à pression constante ($\mathrm{kJ\,kg^{-1}\,K^{-1}}$)
C_v	capacité thermique à volume constant ($\mathrm{kJ\,kg^{-1}\,K^{-1}}$)
C_v	coefficient de variation, adimensionnel
c_{pg}	chaleur spécifique du gaz ($\mathrm{J\,K^{-1}\,kg^{-1}}$
c_{pp}	chaleur spécifique des particules solide ($\mathrm{J\,K^{-1}\,kg^{-1}}$
$\mathscr{D}$	coefficient de diffusion ($\mathrm{cm^2\,s^{-1}}$)
$\mathscr{D}_\mathrm{AB}$	coefficient de diffusion moléculaire pour un mélange binaire gazeux A et B ($\mathrm{cm^2\,s^{-1}}$)
$\mathscr{D}_\mathrm{eff}$	diffusivité intraparticule effective ($\mathrm{cm^2\,s^{-1}}$)
$\mathscr{D}_\mathrm{K}$	coefficient de diffusion de Knudsen ou intraparticule ($\mathrm{cm^2\,s^{-1}}$)
$\mathcal{D}$	coefficient de dispersion axiale ($\mathrm{m^2\,s^{-1}}$)
$\mathcal{D}_\mathrm{S}$	coefficient de dispersion de la phase solide ($\mathrm{m^2\,s^{-1}}$)
$\mathcal{D}_\mathrm{sa}$	coefficient de dispersion axiale pour la phase solide ($\mathrm{m^2\,s^{-1}}$
$\mathcal{D}_\mathrm{sr}$	coefficient de dispersion radiale pour la phase solide ($\mathrm{m^2\,s^{-1}}$
D_reactor	diamètre du réacteur (m)

D_t	diamètre du tube (m)
d	diamètre moyen d'une particule (m)
d_{AB}	diamètre moléculaire (m)
d_b	diamètre des bulles (m)
d_c	diamètre du nuage (m)
d_p	diamètre des particles (m)
d_pore	diamètre des pores (m)
d_sph	diamètre d'une sphère ayant le même volume que les particules (m)
E_k	énergie cinétique (J)
F	flux de diffusion ($\mathrm{kg\,m^{-2}\,s^{-1}}$)
$\boldsymbol{F}_\mathrm{Basset}$	force de Basset (N)
$\boldsymbol{F}_\mathrm{D}$	force de traînée (N)
$\boldsymbol{F}_\mathrm{drag,ss}$	force de traînée en régime permanent (N)
$\boldsymbol{F}_\mathrm{L}$	force de portance (N)
$\boldsymbol{F}_\mathrm{Mag}$	force de portance de Magnus (N)
$\boldsymbol{F}_\mathrm{p}$	force de pression (N)
$\boldsymbol{F}_\mathrm{pf}$	terme de transfert d'élan entre le fluide et la phase solide ($\mathrm{N\,m^{-3}}$)
$\boldsymbol{F}_\mathrm{Saff}$	force de portance de Saffman (N)
$\boldsymbol{F}_\tau$	force de cisaillement visqueuse (N)
$\boldsymbol{F}_\mathrm{ud}$	force d'écoulement non perturbée (N)
$\boldsymbol{F}_\mathrm{Vm}$	force de masse virtuelle (N)
f	fonction de poids, adimensionnel
$\boldsymbol{f}_{c,ij}$	force exercée au point de contact entre deux particules i et j (N)
$\boldsymbol{f}_{c,iw}$	force exercée au point de contact entre une particule i et une section du mur w appartenant à la géométrie (N)
$\boldsymbol{f}_{g,i}$	force corporelle agissant sur les particules (par exemple, la gravité ou un champ magnétique) (N)
f_i	donnée prédite
$\boldsymbol{f}_{nc,ik}$	force sans contact sur la particule i dû à la particule k (N)
$\boldsymbol{f}_{pf,i}$	force d'interaction particule-fluide (N)
G	débit massique du gaz ($\mathrm{kg\,s^{-1}}$
G_k	production d'énergie cinétique en turbulence causée par le gradient de vitesse moyenne (J)
G_p	débit massique des particules ($\mathrm{kg\,s^{-1}}$)
g	gravité ($\mathrm{m\,s^{-2}}$)
H	hauteur du lit du réacteur (m)

H_e	hauteur du lit en expension (m)
H_mf	hauteur du lit du réacteur à la vitesse minimale de fluidisation (m)
H_r	ratio d'Hausner, adimensionnel
h_c	coefficient de convection ($\mathrm{W\,m^{-2}\,K^{-1}}$)
h_d	coefficient de transfert de masse pour un contact avec la phase dense (particule) ($\mathrm{W\,m^{-2}\,K^{-1}}$)
h_l	coefficient de transfert de masse avec la phase gazeuse ($\mathrm{W\,m^{-2}\,K^{-1}}$)
I_i	moment d'inertie d'une particule i ($\mathrm{kg\,m^2}$)
K_a	constante pour une adsorption isotherme, adimensionnel
K_bc	coefficient d'échange du gaz entre la phase bulle et le nuage ($\mathrm{m^3\,s^{-1}}$)
K_GB	coefficient d'échange entre la phase bulle et la phase émulsion ($\mathrm{s^{-1}}$)
K_GC	coefficient d'échange entre le gaz et la bulle-nuage ($\mathrm{s^{-1}}$)
k	énergie cinétique par unité de masse ($\mathrm{J\,kg^{-1}}$)
k_1 et k_2	constantes cinétiques
k_ads	coefficient d'adsorption ($\mathrm{s^{-1}}$)
k_des	coefficient de désorption ($\mathrm{s^{-1}}$)
k_f	coefficient de transfert de masse dans le film ($\mathrm{m\,s^{-1}}$)
k_g	conductivité thermique du gaz ($\mathrm{W\,m^{-1}\,K^{-1}}$)
k_gb	coefficient de transfert de masse basé sur la surface de la bulle ($\mathrm{m\,s^{-1}}$)
k_gc	coefficient de transfert de masse entre le nuage et la phase émulsion ($\mathrm{m\,s^{-1}}$)
$k_\mathrm{g,lit}$	moyenne des coefficients de transfert de masse de l'ensemble des particules ($\mathrm{m\,s^{-1}}$
$k_\mathrm{g,particule}$	coefficient de transfert de masse de la particule ($\mathrm{m\,s^{-1}}$
k_m	coefficient de transfert de masse ($\mathrm{m\,s^{-1}}$)
$k_{n,ij}$	coefficients de rigidité normaux ($\mathrm{N\,m^{-1}}$)
$k_{t,ij}$	coefficients de rigidité tangentielle ($\mathrm{N\,m^{-1}}$)
L	longueur (m)
L_s	échelle du procedé (m)
l	moitié de l'épaisseur de la plaque (m)
M	masse molaire (mol)
M_A	masse molaire de A ($\mathrm{g\,mol^{-1}}$
$\boldsymbol{M}_{c,ij}$	moment de la force de contact appliqué sur la particule i en raison de sa collision avec la particule j ($\mathrm{N\,m}$)
$\boldsymbol{M}_{c,iw}$	moment de la force de contact appliqué sur la particule i en raison de la collision entre la particule i et la section du mur ($\mathrm{N\,m}$)

M_{F}	masse de fluide déplacée par la particule (kg)
M_{m}	coefficient de mélange axial ($\mathrm{m^2\,s^{-1}}$)
M_{s}	terme d'écoulement de la circulation des solides (convection) ($\mathrm{kg\,s^{-1}}$)
$\boldsymbol{M}_{r,ij}$	couple de friction de roulement appliqué sur la particule i en raison de sa collision avec la particule j (N m)
$\boldsymbol{M}_{r,iw}$	couple de friction de roulement appliqué sur la particule i en raison de la collision entre la particule i et une section du mur (N m)
m_i	masse d'une particule i (kg)
m	masse (kg)
N_0	moles de traceur injecté (mol)
N_{A}	mole de A (mol)
N_{Ar}	nombre d'Archimède, adimensionnel
N_{Bi}	nombre de Biot, adimensionnel
N_{Da}	nombre de Damkohler, adimensionnel
N_{Ma}	nombre de Mach, adimensionnel
N_{Nu}	nombre de Nussel, ratio du transfert de chaleur par convection sur celui par conduction, adimensionnel
N_{Pe}	nombre de Péclet, adimensionnel
$N_{\mathrm{Pe_{sa}}}$	nombre de Péclet axial pour la phase solide, adimensionnel
$N_{\mathrm{Pe_{sr}}}$	nombre de Péclet radial pour la phase solide, adimensionnel
N_{Pr}	nombre de Prandtl, adimensionnel
N_{Re}	nombre de Reynolds, adimensionnel
$N_{\mathrm{Re_c}}$	nombre de Reynolds critique, débit lorsque le régime change de la loi de Stokes à la loi de Newton, adimensionnel
$N_{\mathrm{Re_G}}$	nombre de Reynolds de cisaillement, ratio entre la granulométrie sur l'épaisseur de la couche limite laminaire. $N_{Re_G} = d/(v/u_s)$ où u_s est la vitesse de cisaillement ($\mathrm{m\,s^{-3}}$) et v est la viscosité cinématique du fluide ($\mathrm{m^2\,s^{-1}}$), adimensionel
$N_{\mathrm{Re_m}}$	nombre de Reynolds lorsque le coefficient de traînée est un minimum. Cette valeur dépend de la forme de la particule. Un graphique du coefficient de traînée en fonction du nombre de Reynolds peut être trouvé dans la littérature, adimensionnel
$N_{\mathrm{Re_p}}$	nombre de Reynolds de particules, adimensionnel
N_{Sc}	nombre de Schmidt, adimensionnel
N_{Sh}	nombre de Sherwood, adimensionnel
n_0	quantité de gaz sur le solide/particules initialement (mol)

n_{CSTR}	nombre de CSTRs en série
n_{p}	nombre de particules (particules)
P	pression (Pa)
P_o	Pression atmosphérique (Pa)
Q	débit volumique ($\mathrm{m^3\,s^{-1}}$)
$\tilde{Q}_{\mathrm{rxn}}$	débit molaire ($\mathrm{mol\,s^{-1}}$)
R	constante des gaz parfaits, $8.314\,\mathrm{J\,mol^{-1}\,K^{-1}}$
R^2	coefficient de détermination, adimensionnel
R_{p}	rayon externe de la particule (m)
R_{reacteur}	rayon interne d'un réacteur (m)
$R_{w,i}$	rayon d'un blob (m)
r	taux de réaction ($\mathrm{mol\,L^{-1}\,s^{-1}}$)
r_{p}	rayon des pores (m)
r_{s}	rayon (m)
S	propagation du temps de résidence, adimensionnel
S_{A}	aire de surface spécifique ($\mathrm{m^2\,g^{-1}}$)
$S_{\mathrm{ext,lit}}$	valeur totale de la surface extérieure des particules ($\mathrm{m^2}$)
$S_{\mathrm{ext,nuage}}$	surface extérieure du nuage ($\mathrm{m^2}$)
$S_{\mathrm{ext,particule}}$	surface extérieure de la particule ($\mathrm{m^2}$)
s	déviation standard d'un échantillon
s^3	asymétrie ($\mathrm{s^3}$)
T	température (K)
t	temps (s)
$\bar{t}$	temps de résidence moyen (s)
t_0	moment de commencement d'une expérience RTD
$t_{0,\mathrm{MS}}$	temps de début de l'enregistrement par le spectromètre de masse
t_{d}	fraction de temps où il y a un contact avec la phase dense (particule), adimensionnel
t_{MS}	temps enregistré par le spectromètre de masse (ms)
t_{n}	temps de mélange dans chaque réservoir (s)
t_{p}	temps du piston (s)
t_{peak}	instant où le maximum de la courbe RTD est atteint (s)
t_{rel}	temps réel (s)
$\bar{t}_{\mathrm{res}}$	temps moyen de résidence résolue à l'aide du modèle de dispersion axiale (s)
U_{b}	vitesse des bulles ($\mathrm{m\,s^{-1}}$)

U_c	vitesse critique ($\mathrm{m\,s^{-1}}$)
U_g	vitesse du gaz ($\mathrm{m\,s^{-1}}$)
U_l	vitesse superficielle de la phase liquide ($\mathrm{m\,s^{-1}}$)
U_mb	vitesse de bullage minimale ($\mathrm{m\,s^{-1}}$)
U_mf	vitesse de fludisation minimale ($\mathrm{m\,s^{-1}}$)
U_sl	vitesse de glissement ($\mathrm{m\,s^{-1}}$)
u	vitesse ($\mathrm{m\,s^{-1}}$)
$\bar{u}$	vitesse moléculaire moyenne ($\mathrm{m\,s^{-1}}$)
$\boldsymbol{u}$	vecteur de vitesse du fluide ($\mathrm{m\,s^{-1}}$)
$\dot{u}$	accélération des particules ($\mathrm{m\,s^{-2}}$)
u_b	vitesse de montée des bulles ($\mathrm{m\,s^{-1}}$)
$u_{\mathrm{s}\infty}$	vitesse interstitielle du gaz dans un lit intact ($\mathrm{m\,s^{-1}}$)
V	volume total du système ($\mathrm{m^3}$)
V_bulle	volume occupé par la phase bulle ($\mathrm{m^3}$)
V_g	volume de la phase gazeuse ($\mathrm{m^3}$)
V_loop	volume de la boucle d'échantillonnage ($\mathrm{m^3}$)
V_m	volume sans les internes ($\mathrm{m^3}$)
V_nuage	volume du gaz dans la bulle et le nuage ($\mathrm{m^3}$)
V_p	volume des particules ($\mathrm{m^3}$)
$V_\mathrm{réacteur}$	volume du réacteur ($\mathrm{m^3}$)
V_seq	volume du lit de catalyseur ($\mathrm{m^3}$)
V_T	nombre de sites vacants
V_t	vitesse terminale d'une particule ($\mathrm{m\,s^{-1}}$)
v	volume molaire à la température d'ébullition ($\mathrm{m^3}$)
$\boldsymbol{v}$	vecteur de vitesse des particles ($\mathrm{m\,s^{-1}}$)
$\dot{v}$	accélération du fluide ($\mathrm{m\,s^{-2}}$)
$\vec{\boldsymbol{v}}$	vitesse de la phase Eulérien en simulation CFD ($\mathrm{m\,s^{-1}}$)
v_A	volume atomique de diffusion ($\mathrm{m^3}$)
$\boldsymbol{v_i}$	mouvement de translation de la particule i ($\mathrm{m\,s^{-1}}$)
v_pore	volume spécifique des pores ($\mathrm{mL\,g^{-1}}$)
W	masse de particules/catalyseurs (kg)
w	flux ($\mathrm{kg\,m^{-2}\,s^{-1}}$)
w_s	flux de solide ($\mathrm{kg\,m^{-2}\,s^{-1}}$)
X_A	section transversale ($\mathrm{m^2}$)
$\boldsymbol{x}$	coordonné dans l'espace, adimensionel
$\boldsymbol{x}_i$	position du centre de la gravité de la particule, adimensionnel

y	fraction logarithmique du gaz inerte, adimensionnel
$\bar{y}$	moyenne des données expérimentales
y_{i}	fraction massique ou donnée expérimentale
Z	longueur caractéristique du système (m)
z	longueur (m)

Lettres grecques

α	angle entre l'axe principal de la particule et la direction de l'écoulement (°)
α_{c}	épaisseur du nuage (m)
α_{g}	fraction volumique de la phase gazeuse
α_{p}	porosité de la particule, adimensionnel
Δ_{t}	pas de temps (s)
Δ_f	incertitude d'une fonction f
ΔP	perte de charge (Pa)
Δt_{CFD}	pas de temps de la simulation (s)
Δ_x	incertitude (-)
Δx	taille caractéristique d'une cellule/grille, adimensionnel
ΔZ	hauteur du lit (m)
δ_{b}	fraction de bulle dans le réacteur à lit fluidisé, adimensionnel
$\boldsymbol{\delta}_{n,ij}$	chevauchements normaux (m)
$\dot{\boldsymbol{\delta}}_{n,ij}$	dérivées des chevauchements normaux ($\mathrm{m\,s^{-1}}$)
$\boldsymbol{\delta}_{t,ij}$	chevauchements tangentiel (m)
$\dot{\boldsymbol{\delta}}_{t,ij}$	dérivées des chevauchements tangentiel ($\mathrm{m\,s^{-1}}$)
ϵ_{gs}	porosité du lit de catalyseur
ϵ_s	fraction du volume de solide, adimensionnel
ϵ_v	fraction de vide, adimensionnel
$\epsilon_{\mathrm{v,lit}}$	fraction de vide du lit, adimensionnel
$\epsilon_{\mathrm{v,mf}}$	fraction de vide à la vitesse minimale de fluidisation, adimensionnel
$\epsilon_{\mathrm{v,rx}}$	fraction de vide dans le réacteur, adimensionnel
ε	dissipation ($\mathrm{m^2\,s^{-3}}$)
γ	tension de surface ($\mathrm{J\,m^{-2}}$)
$\gamma_{n,ij}$	coefficient d'amortissement normal ($\mathrm{kg\,s^{-1}}$)
$\gamma_{t,ij}$	coefficient d'amortissement tangentiel ($\mathrm{kg\,s^{-1}}$)
λ	échelle de longueur (m)
$\bar{\mu}$	ratio de la viscosité, adimensionnel

μ	viscosité dynamique du fluide (Pa s)
μ_f	viscosité du fluide, valeur moyenne ($\mathrm{N\,s\,m^{-2}}$)
μ_s	coefficient de friction statique, adimensionnel
ν	nombre adimensionnel de Nusselt modifié, adimensionnel
Ω	paramètre de rotation (rad/s)
Ω_D	intégrale de collision pour la diffusion, adimensionnel
$\boldsymbol{\omega}$	vecteur du taux de rotation (rad/s)
$\boldsymbol{\omega}_{p,i}$	mouvement de rotation de la particule i (rad/s)
ω_i^2	racine de l'équation transcendantale, adimensionnel
ϕ	sphéricité, adimensionnel
ϕ_p	sphéricité d'une particule, adimensionnel
ρ_b	masse volumique apparente ($\mathrm{kg\,m^{-3}}$)
ρ_bed	masse volumique du lit du réacteur ($\mathrm{kg\,m^{-3}}$)
ρ_f	masse volumique du fluide ($\mathrm{kg\,m^{-3}}$)
ρ_g	masse volumique du gaz ($\mathrm{kg\,m^{-3}}$)
ρ_p	masse volumique des particules ($\mathrm{kg\,m^{-3}}$)
ρ_sk	masse volumique squelettique ($\mathrm{kg\,m^{-3}}$)
σ	écart-type
σ^2	variance ($\mathrm{s^2}$)
σ_{AB}^2	« diamètre de collision » paramètre de l'équation de Lennard-Jones (Å)
σ_e	nombre de Prandtl pour le taux de dissipation en turbulence, adimensionnel
σ_k	nombre de Prandtl pour l'énergie cinétique en turbulence, adimensionnel
τ	temps de résidence théorique (s)
$\boldsymbol{\tau}$	contrainte de cissaillement (Pa)
τ_bolus	temps d'injection (s)
τ_c contact time (s) τ_D	constante de temps pour la diffusion intraparticule (s)
τ_f	constante de temps pour la diffusion du film (s)
θ	temps adimensionnel $[tu/Z]$
θ_ang	angle de repos (°)
θ_c	angle de contact (°)
ξ	distance adimensionnel $[z/Z]$
$\boldsymbol{\xi}$	champ à lisser, adimensionnel

Indice

B	phase bulle
c	phase du nuage
e	phase d'émulsion
i	grille
j	espèce moléculaire
k	time
S	phase solide

LISTE DES ANNEXES

CHAPITRE 1 INTRODUCTION

L'analyse de la distribution du temps de résidence (RTD) est une technique qui a vu le jour en 1935[6]. L'objectif était d'analyser l'hydrodynamique dans les réacteurs chimiques. C'est seulement 20 ans plus tard que la technique a pris de l'expansion dans plusieurs domaines : mélange, réacteurs, distillation et tout récemment en pharmaceutique et dans les bioprocédés[7,8,9,10]. C'est aussi à cette époque que les chercheurs ont commencé à étudier en profondeur les modèles mathématiques reliés à cette méthode[11]. Le modèle le plus appliqué pour la RTD est le modèle de dispersion axiale[12]. Il permet de comparer les résultats avec un comportement idéal, soit le *plug-flow*. Aujourd'hui, c'est plus de 1600 articles par année qui inclut la RTD[13,14].

1.1 Concepts de base

La RTD est une méthode pour déterminer l'hydrodynamique d'un système en continue. Elle permet de détecter les anomalies telles que les zones mortes, la présence de canal, la dispersion, et l'adsorption. L'expérience consiste à injecter un traceur dans le réservoir et à détecter sa concentration à la sortie. Ainsi, le temps de résidence dans le réservoir est mesuré. L'injection est soit de type échelon où le traceur est injecté en continu, ou soit de type *pulse* où un volume prédéfini s'introduit dans le réservoir.

L'étude RTD se fait sur une phase en particulier (solide, liquide, gaz). Donc, par exemple, dans un réacteur à lit fluidisé à trois phases, trois analyses RTD peuvent être faites indépendamment. Le traceur choisi est dans la même phase que l'étude et est détecté par une technique adéquate (Tableau 1.1). Celui-ci est non-réactif, facilement détectable, et a des propriétés physiques similaires au système à l'étude[15].

Ce projet se concentre sur l'analyse de la RTD de la phase gazeuse dans un réacteur à lit fluidisé de 8 mm de diamètre. Ce type de réacteurs est reconnu pour sa température uniforme tout au long du lit catalytique ce qui autorise les réactions fortement exothermiques et même explosives. En contre parti, la mise à l'échelle industrielle résulte souvent à des défaillances. C'est pour cette raison, qu'une étude approfondit de l'hydrodynamique est nécessaire.

La concentration des traceurs gazeux (Kr, CO_2, O_2, CO, CH_4, H_2, He) est détectée par un spectromètre de masse (MS). Ce dernier ionise les molécules d'intérêt en cations radicaux. Par la suite, ceux-ci traversent un filtre de masse où un champ électrique ou magnétique fera dévier leurs trajectoires. Finalement, une coupe de Faraday et/ou un multiplicateur d'électron

Tableau 1.1 Exemple de techniques pour détecter les traceurs en fonction de la phase de la RTD

Phase	Technique	Référence
Solide	— Spectroscopie infrarouge — Caméra haute vitesse — Peser le poids par intervalle de temps — Localisation des particules d'émission de positrons (radioactives)	[9,16,17,18]
Liquide	— Spectroscopie UV/VIS — Analyseur électrochimique (conductivité) — Capteurs conductimétries	[7,8,19,20]
Gazeuse	— Spectromètre de masse — Détecteur de la conductivité thermique	[12,21,22]

détecte(nt) l'abondance relative des molécules sélectionnées. Le MS permet de mesurer la concentration en continu. Cependant, puisque la technique se base sur la masse molaire des molécules et de ses fragments, plusieurs molécules ont la même valeur — par exemple, le CO_2 et le CO. Donc, une correction est nécessaire pour connaitre la concentration réelle [23].

Le réacteur à lit fluidisé est rempli d'un catalyseur. Dans ce projet, ceux-ci sont poreux : l'hydrogénophosphate de vanadyle hémihydraté (VPOP), le pyrophosphate de vanadyle calciné (VPPC), le pyrophosphate de vanadyle équilibré (VPPE) et le catalyseur pour le craquage catalytique fluide (FCC). De plus, ces catalyseurs ont été comparés avec le sable, une poudre non poreuse.

Le modèle de dispersion axiale est analogique à la loi de Fick. Des conditions frontières doivent être établies préalablement pour obtenir une solution analytique. Ces conditions sont soit ouvert-ouvert, fermé-fermé (Danckwerts) [24] ou fermé-ouvert (ce projet). La résolution du modèle permet d'obtenir le nombre de Péclet (N_{Pe}) qui est relié au coefficient de dispersion ($\mathcal{D}$). Puis, nombre de Péclet est relié au nombre de CSTR (n_{CSTR}) en série tel que [25] :

$$N_{\mathrm{Pe}} = 2(n_{\mathrm{CSTR}} - 1) \tag{1.1}$$

Cette valeur est appliquée lors du développement de la cinétique d'une ou de plusieurs ré-

actions. Il précise le nombre de CSTR en série qu'équivaut le système. Une erreur dans le nombre de CSTR se propage tout au long du développement du modèle cinétique. Donc, une valeur précise est primordiale.

1.2 Problématique et objectifs de recherche

Aucune norme n'a été développée pour les études RTD. Dans la littérature, elles sont toutes disparates. Par exemple, aucune règle n'est précisée au niveau du choix du traceur, des volumes autour du lit catalytique (volume mort), les interactions possibles entre le catalyseur et le gaz, ainsi que l'impact de la porosité sur la RTD.

Puis, lorsque le phénomène d'adsorption est présent, le modèle de dispersion axiale ne concorde pas avec les données. Donc, le premier objectif de ce projet de doctorat est d'augmenter la précision des études RTD expérimentales.

Pour se faire, les sous-objectifs reliés à l'étude RTD expérimentale sont :

- Développer une méthodologie précise pour l'analyse du temps de résidence dans un réacteur à lit fluidisé ;
- Analyser l'effet des traceurs sur la RTD ;
- Analyser l'effet de la porosité des catalyseurs sur la RTD ;
- Développer un modèle mathématique pour la RTD qui permettra de résoudre simultanément plusieurs traceurs gazeux. Ce modèle devra inclure le phénomène d'adsorption.

Les expériences RTD en laboratoire demandent beaucoup de temps et d'énergie particulièrement lorsque plusieurs conditions d'opérations doivent être expérimentées. De plus, lors de la mise à l'échelle, toutes les expériences doivent être refaites, car l'hydrodynamique change. Par contre, le développement d'une simulation par mécanique des fluides numériques par méthodes des éléments discrets (CFD-DEM) permettrait de contrer ce désavantage en fournissant un modèle de la réalité. Ainsi, la seconde partie de ce projet est de simuler des expériences RTD dans un réacteur à lit fluidisé par CFD-DEM.

Les sous-objectifs reliés à l'étude RTD par simulation CFD-DEM sont :

- Simuler un réacteur à lit fluidisé qui est identique à celui utilisé en laboratoire ;
- Simuler l'hydrodynamique du réacteur à lit fluidisé (perte de charge) ;
- Injecter un traceur gazeux par *pulse* et mesurer la concentration à la sortie par CFD-DEM ;
- Comparer les résultats expérimentaux aux résultats de CFD-DEM.

1.3 Plan du mémoire

Cette thèse est séparée en deux grands sujets soit l'étude du temps de résidence (RTD) et la simulation par CFD-DEM. Tout d'abord, une revue de littérature est présentée. Celle-ci est complémentaire aux articles de mini-revue sur les réacteurs à lit fluidisé, la RTD et la CFD-DEM. La revue de littérature proposée dans ce document approfondit les phénomènes affectant la RTD soit la dispersion, la diffusion, la convection, et l'adsorption. Puis, les modèles basés sur les bilans de transfert de masse dans les réacteurs à lit fluidisé et ceux spécifiques à la RTD sont précisés. La caractérisation des traceurs gazeux et des catalyseurs utilisés pour cette thèse est étudiée en plus de leur effet sur la RTD. Finalement, la revue de littérature se conclut par une section sur la simulation numérique et ces applications pour les analyses RTD.

Le chapitre suivant décrit la démarche de l'ensemble de la thèse. Il débute par un rappel des objectifs, puis décrit les articles présentés en ordre chronologique.

Le cœur de la thèse est les 4 articles suivants :

1. *Experimental methods in Chemical Engineering : Residence Time Distribution — RTD*
2. *Residence Time Distribution in Fluidized Beds : Diffusion, Dispersion, Adsorption*
3. *Fluidized Bed Hydrodynamic Modelling of CO2 in Syngas : Distorted RTD Curves due to Adsorption on FCC*
4. *Experimental Methods in Chemical Engineering : Unresolved CFD-DEM*

Puis, l'article *Experimental methods in Chemical Engineering : Reactors — Fluidized Beds* est présenté en annexe. Il s'agit d'une revue de littérature complémentaire à ce projet.

À la suite des articles, une discussion générale sur le développement de la méthodologie RTD et du nouveau modèle est mise de l'avant. De plus, nous expliquons les difficultés rencontrées lors de ce projet. Finalement, la conclusion fait une synthèse des travaux, présente les limitations ainsi que les améliorations et les travaux futurs.

CHAPITRE 2 REVUE DE LITTÉRATURE

L'article, *Experimental methods in chemical engineering : Residence time distribution – RTD* (Chapitre 4), présente une revue de littérature sur la technique RTD. Celle-ci inclut : la théorie, le modèle de dispersion axiale et ses conditions frontières, les applications en génie chimique, les incertitudes, les limitations du modèle, les types d'injection, le volume mort, la répétabilité des expériences et la fréquence d'échantillonnage. Pour comprendre le comportement de la phase gazeuse dans un réacteur à lit fluidisé, plus de 500 expériences RTD ont été réalisées dans cet article. Ainsi, une méthodologie générale a été développée pour les essais RTD.

Par la suite, l'article, *Experimental methods in chemical engineering : Reactors – Fluidized Beds* (Annexe A), présente une revue de littérature sur les réacteurs à lit fluidisé qui sont ceux impliqués dans les études RTDs. Cette revue englobe les régimes de fluidisation, la caractérisation des poudres, les techniques annexes, les applications en génie chimique, les incertitudes, les limitations, les sources d'erreurs ainsi qu'une section sur l'hydrodynamique en phase gazeuse.

Ce chapitre de revue de littérature est donc complémentaire à ces deux revues. Il comprend une section sur les quatre phénomènes affectant la RTD dans les réacteurs à lit fluidisé soit la dispersion, la diffusion, la convection et l'adsorption. Puis, les différents modèles basés sur le transfert de masse sont étudiés. Une section sur les gaz servant de traceurs ainsi qu'une section sur les catalyseurs impliqués dans le projet sont également discutées.

La dernière partie porte sur la simulation par mécanique des fluides numériques par méthode des éléments discret (CFD-DEM). L'article, *Experimental methods in chemical engineering – Unresolved CFD-DEM* (Chapitre 7), présente une revue de littérature générale sur le sujet incluant les équations gouvernant la DEM, les équations gouvernant la CFD, le couplage CFD-DEM, les applications en génie chimique ainsi que les incertitudes et limitations. Pour complémenter cet article, la dernière section de cette revue de littérature s'oriente sur les simulations par CFD ou par DEM dans le cas précis d'analyse RTD.

2.1 Définition des phénomènes affectant la RTD

Dans un réacteur à lit fluidisé, quatre phénomènes sont présents : la dispersion, la diffusion, la convection et l'adsorption (Figure 2.1). Le mécanisme d'adsorption a lieu seulement en présence de catalyseur poreux ayant une interaction avec le gaz ou le liquide. Approfondir

ces phénomènes permettra de comprendre d'avantages le comportement hydrodynamique dans un réacteur.

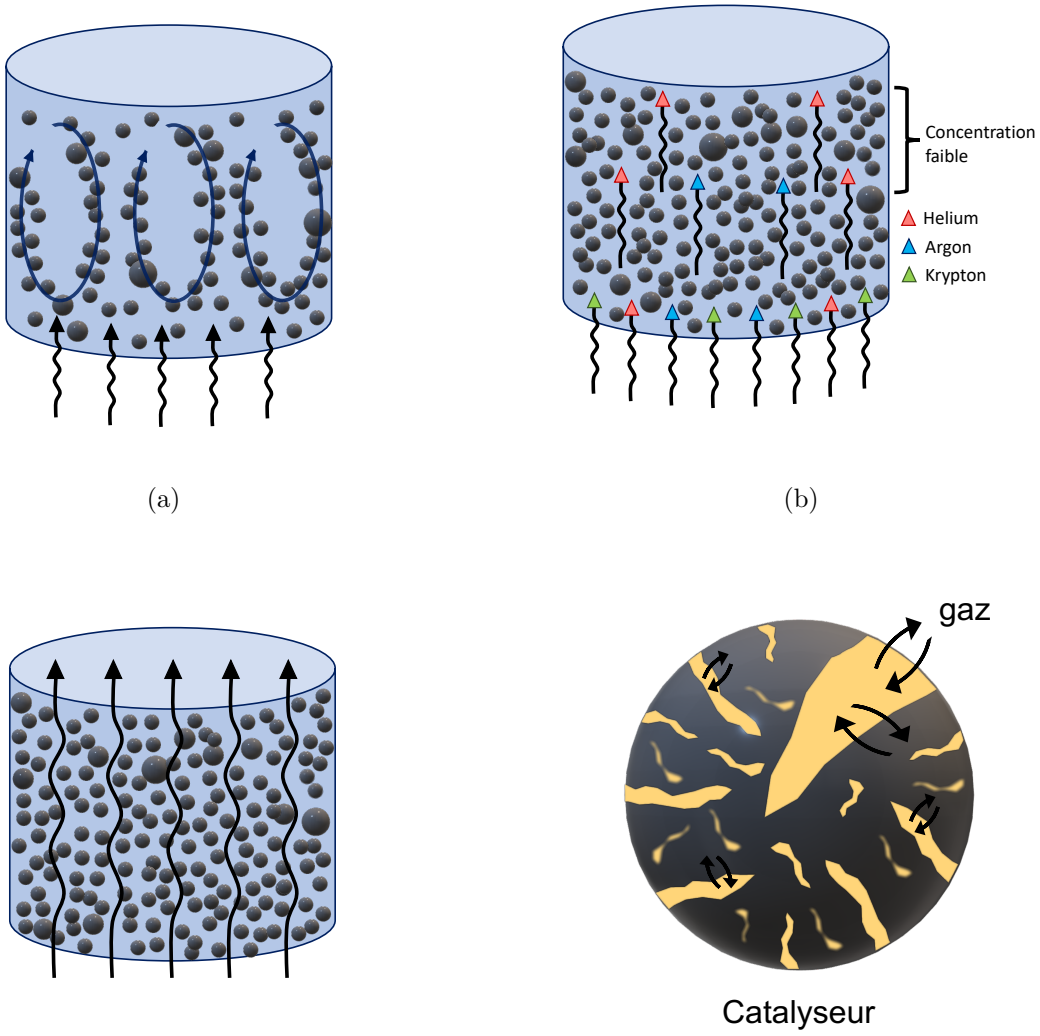

(a) (b)

(c) (d)

Figure 2.1 Quatre phénomènes présents dans un réacteur à lit fluidisé. (a) Dispersion (b) Diffusion (c) Convection (d) Adsorption.

2.1.1 Dispersion

La dispersion représente le degré de mélange entre les différentes phases[26,27]. Chaque phase possède sa propre dispersion. Elle peut avoir lieu dans l'axe radial ou axial du réacteur[26],

mais à quelques exceptions près, l'axe radial est négligé. La dispersion axiale est représentée par le coefficient de dispersion ($\mathcal{D}$) ou le nombre de Péclet (N_{Pe}). Ces variables sont reliées au nombre de Reynolds (N_{Re}), au nombre d'Archimède (N_{Ar}), au nombre de Schmidt (N_{Sc}) et/ou au pourcentage de vide dans le lit de catalyseurs[27]. L'analyse du temps de résidence (RTD) permet de déterminer la dispersion[26,27]. Celle-ci augmentera en présence d'agglomération ou de micro-canal dans le lit de catalyseur[28]. C'est pour cette raison que la connaissance de ce phénomène est cruciale lors de la conception, l'optimisation et la mise à l'échelle de réacteurs[27].

Dispersion dans un réacteur à lit fluidisé

Un réacteur à lit fluidisé contient deux phases (gaz-solide ou liquide-solide) ou trois phases qui auront chacune un coefficient de dispersion distinct[29]. Le transfert de masse dans le réacteur est affecté par les phases présentes, particulièrement la phase liquide[27].

La dispersion axiale de la phase liquide est fonction de la vitesse du liquide, la vitesse du gaz (si présent), la viscosité du liquide, la tension de surface et la taille des particules[29].

Pour la phase gazeuse, la dispersion axiale dépend de la taille des bulles et la taille du réacteur[26]. Dans un lit fluidisé en circulation (CFB), le coefficient de dispersion augmente avec la vitesse du gaz, le taux de circulation des solides et la masse volumique de la suspension[30].

La dispersion de la phase solide est fonction de la porosité et la sphéricité des particules, de la masse volumique, de la vitesse de circulation du solide et du diamètre des particules[31]. Par contre, certains chercheurs proposent une valeur constante du coefficient de dispersion de la phase solide :

— Pour l'axe radial : $\mathcal{D}_{\mathrm{sr}} = 0.1\,\mathrm{m^2\,s^{-1}}$ [31]
— Pour l'axe axial : $\mathcal{D}_{\mathrm{sa}} = 1\,\mathrm{m^2\,s^{-1}}$ [32]

Corrélation du coefficient de dispersion avec le nombre de Péclet

Le nombre de Péclet est directement lié au coefficient de dispersion tel que[33] :

$$N_{\mathrm{Pe}} = \frac{uZ}{\mathcal{D}} \tag{2.1}$$

Où u est vitesse et Z représente la longueur du réacteur pour la dispersion axiale et le diamètre du réacteur pour la dispersion radiale.

Il s'agit d'un nombre adimensionnel représentant le ratio du flux de convection sur le flux de

dispersion. Les corrélations impliquant le N_{Pe} sont nombreuses. Certaines corrélations ont été développées pour une phase particulière tandis que d'autres sont plus générales (Tableau 2.1). Dans la littérature, il existe une grande discordance entre les différentes valeurs des coefficients de dispersion selon la phase et l'axe étudiés[31].

La dispersion et le temps de résidence

L'analyse du temps de résidence (RTD) est une technique permettant de déterminer le nombre de Péclet. Les grandes étapes de cette méthode dans un réacteur à lit fluidisé (système gaz-solide) sont :

1. Injecter en continu un gaz inerte dans le réacteur
2. Au moment, $t = 0$, injecter un traceur par *pulse* (volume précis) ou par pas de temps (injection continue)
3. Analyser la sortie du gaz à l'aide d'un détecteur
4. Appliquer le modèle de dispersion axiale sur les données obtenues
   (a) Choisir les conditions limites
   (b) Résoudre pour connaître la solution analytique
   (c) Minimiser la somme des erreurs au carré entre le modèle et les données
5. Trouver la valeur du nombre de Péclet

Les détails approfondis de la méthode RTD se retrouvent dans la revue de littérature : *Experimental Methods in Chemical Engineering : Residence Time Distribution – RTD* (Chapitre 4).

Lors d'une analyse RTD, il est possible de détecter la dispersion dans un système. En effet, la courbe obtenue lors d'une injection par *pulse* sera plus large et plus base comparer à un système où la dispersion est faible (Figure 2.2)[33].

Tableau 2.1 Corrélation du nombre de Péclet (N_{Pe}) en fonction de la phase, variance ou des nombres adimensionnels.

Spécification		Corrélation	Caractéristique	Reference
Phase solide	(1)	$N_{\mathrm{Pe_{sa}}} = 71.86(1-\epsilon_v)^{-0.67} N_{\mathrm{Re}}^{0.23}$	axiale	[34]
	(2)	$N_{\mathrm{Pe_{sr}}} = 225.7(1-\epsilon_v)^{-0.29} N_{\mathrm{Re}}^{0.43}$	radiale	[34]
Phase liquide	(3)	$\mathcal{D} = \dfrac{U_{\mathrm{l}} H_{\mathrm{e}}}{N_{\mathrm{Pe}}}$	axiale	[27,29]
	(4)	$N_{\mathrm{Pe_l}} = \dfrac{d_{\mathrm{p}} U_{\mathrm{l}}}{\mathcal{D}} \propto \dfrac{d_{\mathrm{p}} U_{\mathrm{l}}}{D_{\mathrm{reactor}}[g(U_{\mathrm{l}}+U_{\mathrm{g}}]} \propto d\left(\dfrac{d_{\mathrm{p}}}{D_{\mathrm{reactor}}}\right)^{e}\left(\dfrac{U_{\mathrm{l}}}{U_{\mathrm{l}}+U_{\mathrm{g}}}\right)^{f}$	axiale	[27,29]
Phase gazeuse	(5)	$\mathcal{D}_{\mathrm{gr}} = \dfrac{ZU_{\mathrm{g}}}{N_{\mathrm{Pe}}} = \dfrac{ZU_{\mathrm{g}}}{3.23 N_{\mathrm{Re_m}}^{0.297}}$ $N_{\mathrm{Re_m}} = \dfrac{2Z(w_{\mathrm{s}} + \rho_{\mathrm{g}} U_{\mathrm{g}})}{\mu}$	radiale $40 < N_{\mathrm{Re_m}} < 300$ $150 < N_{\mathrm{Pe}} < 300$	[35]
Fonction de la variance	(6)	$\sigma^2 = \dfrac{1}{N_{\mathrm{Pe}}^2}(2N_{\mathrm{Pe}} + 3)$	toutes les phases	[29]
	(7)	$\sigma_\theta^2 = \dfrac{2}{N_{\mathrm{Pe}}}\left[-\dfrac{1}{N_{\mathrm{Pe}}}(1-e^{-N_{\mathrm{Pe}}})\right]$ $N_{\mathrm{Pe}} = \dfrac{2}{\sigma_\theta^2}$	adimensionnel	[27,36]
	(8)	$\dfrac{\bar{t}}{\sigma} = \sqrt{\dfrac{2}{N_{\mathrm{Pe}}} - \dfrac{8}{N_{\mathrm{Pe}}^2}}$	toutes les phases	[37]
Fonction nombre adimensionnelle	(9)	$N_{\mathrm{Pe}} = N_{\mathrm{Re}} \cdot N_{\mathrm{Sc}} = \left(\dfrac{\rho u Z}{\mu}\right)\left(\dfrac{\mu}{\rho \mathcal{D}}\right) = \dfrac{uZ}{\mathcal{D}}$	axiale ou radiale toutes les phases	[31]

Légende : (3) U_{l} est la vitesse superficielle de la phase liquide et H_{e} est la hauteur du lit en expension.
(4) d_{p} est le diamètre des particules, D_{reactor} est le diamètre du réacteur, g est la gravité, U_{g} est la vitesse superficielle du gaz, et d, e et f sont les constantes de corrélation ($d = 20.19$, $e = 1.66$ et $f = 1.03$).
(5) w_{s} est le flux de solide, ρ_{g} est la masse volumique du gaz, et μ la viscosité.
(6) σ^2 est la variance.
(7) $\bar{t}$ est le temps de résidence moyen.
(8) Z est la longueur du réacteur si la dispersion est axiale et le diamètre du réacteur si la dispersion est radiale.

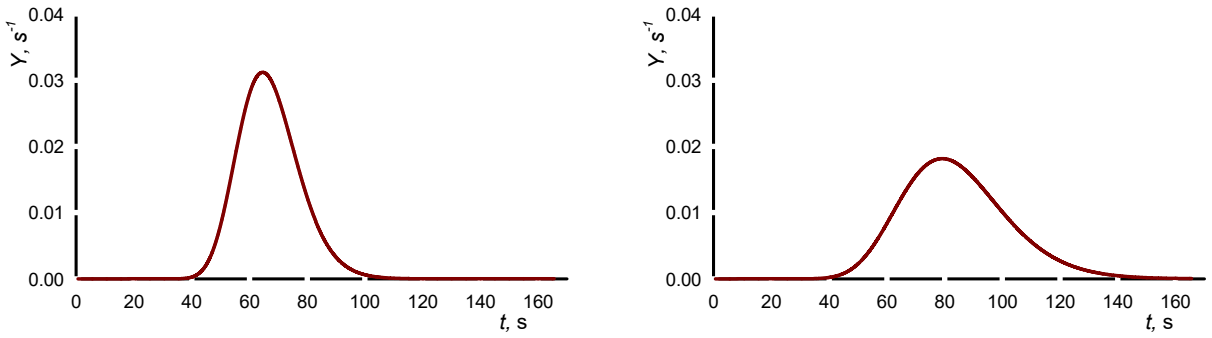

(a) (b)

Figure 2.2 Détection de la dispersion dans une analyse RTD. (a) Système où la dispersion est faible. (b) Système où la dispersion est élevée

2.1.2 Diffusion

La diffusion est décrite par l'action des molécules ou des atomes de se répandre dans toutes les directions pour atteindre un état d'équilibre. Ce mouvement est dépendant de la température ou de la concentration. Une molécule aura tendance à se déplacer du milieu le plus concentré vers le milieu le moins concentré. Dans le cas d'un réacteur à lit fluidisé, deux types de diffusion est possible : (1) la diffusion dans la phase gazeuse ou diffusion moléculaire et (2) la diffusion de Knudsen. Cette dernière se produit à l'intérieur des particules de catalyseurs — dans les pores[15].

Loi de Fick

Le flux de diffusion (F) qui est le taux de transfert de masse causé par la diffusion par unité de surface ($\mathrm{kg\,m^{-2}\,s^{-1}}$) est défini par la première loi de Fick[38] :

$$F = -\mathscr{D}\frac{\partial C}{\partial x} \tag{2.2}$$

Où C est la concentration et $\mathscr{D}$ le coefficient de diffusion.

De plus, la seconde loi de Fick pour un gradient de concentration dans la direction de l'axe des x est décrit par[38] :

$$\frac{\partial C}{\partial t} = \mathscr{D}\frac{\partial^2 C}{\partial x^2} \tag{2.3}$$

Cette équation est valide seulement si le milieu est isotrope.

Puis, en considérant des particules sphériques, la seconde loi de Fick devient, en coordonnées polaires sphérique[38] :

$$\frac{\partial C}{\partial t} = \frac{\mathscr{D}}{r^2}\left\{\frac{\partial}{\partial r}r^2\frac{\partial C}{\partial r} + \frac{1}{\sin\phi}\frac{\partial}{\partial\theta}\sin\theta\frac{\partial C}{\partial\theta} + \frac{1}{\sin^2\theta}\frac{\partial^2 C}{\partial\phi^2}\right\} \tag{2.4}$$

Corrélation du coefficient de diffusion moléculaire

Dans la littérature, plusieurs corrélations empiriques sont proposées pour décrire le coefficient de diffusion moléculaire ($\mathscr{D}_{\mathrm{AB}}$) entre deux espèces A et B (Tableau 2.2). Ceux-ci sont fonction de la température (T) et de la pression (P) ambiante telles que[15] :

$$\mathscr{D}_{\mathrm{AB}}(T_2, P_2) = \mathscr{D}_{\mathrm{AB}}(T_1, P_1)\left(\frac{P_1}{P_2}\right)\left(\frac{T_2}{T_1}\right)^{1/2} \tag{2.5}$$

Diffusion de Knudsen ou intraparticule

La diffusion de Knudsen est la diffusivité du gaz à l'intérieur des pores du catalyseur lors d'une réaction en phase gazeuse. Celle-ci dépend de la pression du gaz ainsi que de la texture des pores[39]. Il est important de connaitre la diffusion de Knudsen, car celle-ci pourrait limiter le taux de réaction. En effet, si une réaction est rapide et que le réactant se diffuse lentement, alors, le gaz n'atteindra pas l'intérieur du catalyseur. Une mauvaise conversion sera obtenue. Cette limitation est bien maitrisée dans le milieu industriel et est observée particulièrement lors de l'utilisation de catalyseur de 5 à 15 mm de diamètre. C'est pour cette raison qu'il est recommandé d'utiliser des catalyseurs ayant un diamètre de moins de 3 mm pour obtenir une efficacité optimale lors de réaction en phase gazeuse[39].

De plus, la diffusivité de Knudsen joue sur la sélectivité d'une réaction. Par exemple, la réaction $A \rightarrow B \rightarrow C$, si le produit d'intérêt est le B et que la diffusivité intraparticule est trop faible, le gaz restera à l'intérieur du catalyseur et produira C. À l'inverse, si le produit d'intérêt est C, cela aura un effet positif[39].

La corrélation de la diffusion de Knudsen ($\mathscr{D}_{\mathrm{K}}$) est[40] :

$$\mathscr{D}_{\mathrm{K}} = \frac{2}{3}r_p\bar{u} = \frac{2}{3}r_p\left(\frac{8RT}{\pi M}\right)^{1/2} \tag{2.6}$$

Où, r_p est le rayon des pores, $\bar{u}$ est la vitesse moléculaire moyenne, et M est la masse molaire.

Tableau 2.2 Corrélation pour calculer le coefficient de diffusion moléculaire entre l'espèce A et B ($\mathscr{D}_{\mathrm{AB}}$)

Nom	Corrélation	Caractéristique	Réference
(1) Fuller-Schettler et Gidding	$\mathscr{D}_{\mathrm{AB}} = \dfrac{0.00143T^{1.75}}{PM_{AB}^{0.5}\left[(\sum_v)_A^{1/3} + (\sum_v)_B^{1/3}\right]}$ $M_{\mathrm{AB}} = 2\left[\dfrac{1}{M_{\mathrm{A}}} + \dfrac{1}{M_{\mathrm{B}}}\right]^{-1}$	molécule non-polaire	[41]
(2) Théorie de Chapman-Enskog	$\mathscr{D}_{\mathrm{AB}} = \dfrac{(1.858\times10^{-7})T^{3/2}\left(\left(\frac{1}{M_A}\right)+\left(\frac{1}{M_B}\right)\right)^{1/2}}{P\sigma_{AB}^2\Omega_D}$ $\Omega_D = \dfrac{a}{(T^*)^b} + \dfrac{c}{\exp(dT^*)} + \dfrac{e}{\exp(fT^*)} + \dfrac{g}{\exp(hT^*)}$ $T^* = \dfrac{kT}{\varepsilon_{AB}},\ \sigma_{AB} = 0.5(\sigma_A+\sigma_B),\ \varepsilon_{AB} = (\varepsilon_A+\varepsilon_B)^{1/2}$	a = 1.0636 b = 0.15610 c = 0.19300 d = 0.47635 e = 1.3587 f = 1.52996 g = 1.76474 h = 3.89411	[42,43]
(3) Wilke et Lee	$\mathscr{D}_{\mathrm{AB}} = \dfrac{\left[3.03 - \left(\frac{0.98}{M_{AB}^{0.5}}\right)\right](10^{-3})T^{3/2}}{PM_{AB}^{0.5}\sigma_{AB}^2\Omega_D}$		[43,44]
(4) Méthode d'Arnold	$\mathscr{D}_{\mathrm{AB}} = \dfrac{0.00837T^{3/2}\left(\frac{M_A+M_B}{M_AM_B}\right)^{1/2}}{P\left(v_A^{1/3}+v_B^{1/3}\right)^2\left(1+\frac{C_{AB}}{T}\right)}$ $C_{AB} = \left[\dfrac{2\sqrt{v_A^{1/3}v_B^{1/3}}}{v_A^{1/3}+v_B^{1/3}}\right]^3 \sqrt{C_AC_B} = F\sqrt{C_AC_B} = 1.47F(T_{Ba}T_{Bb})^{1/2}$		[45]
(5) Méthode de Hirschfelder, Bird et Spotz	$\mathscr{D}_{\mathrm{AB}} = \dfrac{(9.2916\times T^{3/2}\left(\frac{M_A+M_B}{M_AM_B}\right)^{1/2}}{Pd_{AB}^2\Omega_D(1-\Delta)}$	molécule non-polaire	[46]

Légende : (1) M_{A} et M_{B} sont la masse molaire de A et B, v_A,v_B sont les volumes atomiques de diffusion[47]. (2) et (3) σ_{AB}^2 est le « diamètre de collision » paramètre de l'équation de Lennard-Jones, Ω_D est l'intégrale de collision pour la diffusion (4) C_{AB} est la constante de Sutherland, C_A et C_B sont calculés grâce à la température d'ébullition : $C_A = 1.47T_{Ba}$, v est le volume molaire à la température d'ébullition. (5) $d_{AB} = (d_A + d_B)/2$ est le diamètre moléculaires et Δ est un facteur de correction entre 0 et 0.04.

Cette valeur est dépendante uniquement de la température. Ainsi[15] :

$$\mathscr{D}_{\mathrm{K}}(T_2) = \mathscr{D}_{\mathrm{K}}(T_1)\left(\frac{T_2}{T_1}\right)^{1/2} \tag{2.7}$$

La diffusion et le temps de résidence (RTD)

Le coefficient de diffusivité des traceurs injectés dans un réacteur affecte la réponse de la courbe RTD. En effet, les molécules ayant un coefficient élevé (H_2, He) quitteront avant ceux dont le coefficient est plus faible (O_2, CO, CO_2) (Chapitre 5) (Figure 2.3).

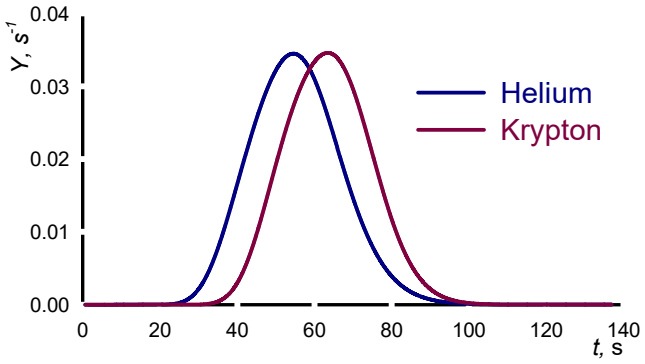

Figure 2.3 Effet du coefficient de diffusion sur les courbes RTD. Pour l'hélium — $\mathscr{D} = 0.716\,\mathrm{cm\,s^{-1}}$ et pour le Kr — $\mathscr{D} = 0.136\,\mathrm{cm\,s^{-1}}$ à 25 °C

2.1.3 Convection

La convection décrit le transport de chaleur ou d'un courant causé par le déplacement d'un fluide. Dans un réacteur à lit fluidisé, le transport de la chaleur se fait par convection de la phase gazeuse ainsi que par conduction lors du contact avec les particules[48,49]. De cette façon, le coefficient de transfert de chaleur par convection (h_c) englobe deux termes[49] :

$$h_c = t_d h_d + (1 - t_d) h_l \tag{2.8}$$

Où h_d est le coefficient de transfert de masse pour un contact avec la phase dense (particule), h_l est le coefficient de transfert de masse avec la phase gazeuse et t_d est la fraction de temps où il y a un contact avec la phase dense (particule).

Corrélation empirique du coefficient de convection

Plusieurs corrélations empiriques du coefficient de convection (h_c) ont été développées (Tableau 2.3). Ceux-ci sont prennent en considération les propriétés physico-chimiques du gaz ainsi que le diamètre des particules. Les équations empiriques relient la convection au nombre de Nussel en fonction du diamètre du tube ($N_{\mathrm{Nu_t}}$) ou du diamètre des particules ($N_{\mathrm{Nu_p}}$) tel que[49] :

$$N_{\mathrm{Nu_t}} \equiv \frac{h_{\mathrm{c}} D_{\mathrm{t}}}{k_{\mathrm{g}}} \text{ et } N_{\mathrm{Nu_p}} \equiv \frac{h_{\mathrm{c}} d_{\mathrm{p}}}{k_{\mathrm{g}}} \tag{2.9}$$

Où N_{Nu} est le ratio du transfert de chaleur par convection sur celui par conduction, D_{t} est le diamètre du tube et k_{g} est la conductivité thermique du gaz.

Transfert gazeux entre les bulles et la phase dense

Dans un réacteur à lit fluidisé, le transfert de masse entre les bulles et la phase dense se fait par convection et diffusion[50]. Le gaz entre dans une des bulles et ressort à son extrémité. Puis, celui-ci est emporté par les particules de la phase dense vers le dessous de la bulle et entre à nouveau dans celle-ci. C'est ainsi que se forme une coquille de phase dense autour de la bulle qui est appelée « nuage » (Figure 2.4). Ce nuage est un échange convectif continuel entre le gaz et l'intérieur de la bulle qui est dépendant du gradient de pression. Il s'agit aussi du lieu où interagissent le gaz et le solide. Ainsi, les réactions et l'adsorption sont possibles. L'épaisseur du nuage (α_{c}) se calcul tel que[50] :

$$\alpha_{\mathrm{c}} = \frac{U_{\mathrm{b}}}{u_{\mathrm{s}\infty}} \tag{2.10}$$

Où U_{b} est la vitesse des bulles et $u_{\mathrm{s}\infty}$ est vitesse interstitielle du gaz dans un lit intact.

Tableau 2.3 Corrélation empirique du coefficient de convection (h_c)

Nom	Corrélation	Caractéristique	Réference
Tubes horizontaux			
(1) Vreedenberg	$\frac{h_c D_t}{k_g} = 420 \left(\frac{\rho_p}{\rho_g} N_{\mathrm{Re_t}}\right)^{0.3} \left(\frac{\mu_g^2}{g\rho_p^2 d_p^3}\right)^{0.3} \left(N_{\mathrm{Pr_g}}\right)^{0.3}$	$\left(\frac{\rho_p}{\rho_g} N_{\mathrm{Re_p}}\right) > 2550$	[51]
	$\frac{h_c D_t}{k_g} = 0.66 N_{\mathrm{Pr_g}}^{0.3} \left(\frac{\rho_p(1-\epsilon_v)}{\rho_g \epsilon_v}\right)^{0.44} N_{\mathrm{Re_t}}^{0.44}$	$\left(\frac{\rho_p}{\rho_g} N_{\mathrm{Re_p}}\right) \leqslant 2550$	
(2) Andeen & Glicksman	$\frac{h_c D_t}{k_g} = 900(1-\epsilon_v) \left(\frac{\rho_p}{\rho_g} N_{\mathrm{Pr_g}} \left(\frac{\mu_g^2}{g\rho_p^2 d_p^3}\right)\right)^{0.3} N_{\mathrm{Re_t}}^{0.3}$	$\left(\frac{\rho_p}{\rho_g} N_{\mathrm{Re_p}}\right) > 2550$	[52]
Tubes verticaux			
(3) Leva	$\frac{h_c d_p}{k_g} = 0.525 (N_{\mathrm{Re_p}})^{0.75}$	Grosses particules	[53]
(4) Borodulya	$\frac{h_c d_p}{k_g} = 0.74 (N_{\mathrm{Ar}})^{0.1} \left(\frac{\rho_p}{\rho_g}\right)^{0.14} \left(\frac{c_{pp}}{c_{pg}}\right)^{0.24} (1-\epsilon_v)^{0.67} + 0.46 (N_{\mathrm{Re_p}} N_{\mathrm{Pr_g}}) \frac{(1-\epsilon_v)^{0.67}}{\epsilon_v}$		[54]
(5) Wender & Cooper	$\frac{h_c d_p}{k_g} = 0.033(1-\epsilon_v) \left(\frac{c_{pp}}{c_{pg}}\right)^{0.8} \left(\frac{\rho_p}{\rho_g}\right)^{0.66} \left(\frac{d_p G}{\mu_g}\right)^{0.23} \left(\frac{c_{pg}\rho_g}{k_g}\right)^{0.43}$		[55]

Légende : N_{Re} est le nombre de Reynolds, μ est la viscosité, d est le diamètre moyen, N_{Pr} est le nombre de Prandtl, N_{Ar} est le nombre d'Archimède, c_{pp} est la chaleur spécifique des particules solide, c_{pg} est la chaleur spécifique du gaz, ϵ_v est la fraction de vide globale et G est le débit massique du gaz. **Indice** : g est pour le gaz, p pour les particules et t pour le tube ou le réacteur

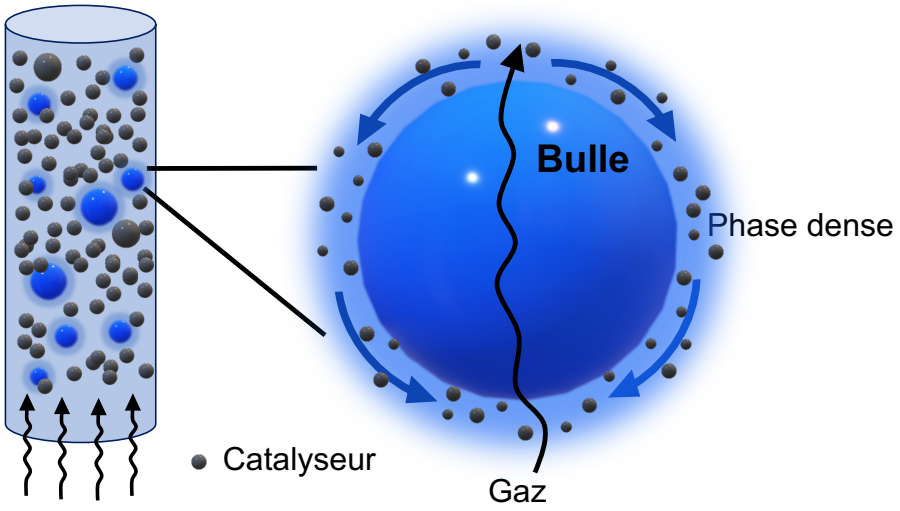

Figure 2.4 Nuage autour d'une bulle causée par la convection dans un réacteur à lit fluidisé. À noter que la forme sphérique de la bulle est une simplification de la réalité.

Effet de la température et de la convection sur la RTD

La température influence la RTD à deux niveaux. Tout d'abord, la convection du système est modifiée. En effet, à haute température, le transfert de masse entre la phase d'émulsion et la phase bulle augmente avec la vitesse. De plus, le transfert de masse entre le solide et la phase émulsion sera plus faible[56].

De plus, à une température donnée, un traceur aura plus tendance à être adsorbé. Par exemple, le butène à 150 °C est adsorbé plus facilement, ce qui augmente son temps de résidence dans le réacteur[57]. Pour le CO_2, plus la température augmente, moins le temps de contact entre le catalyseur et le CO_2 est important (adsorption faible). Donc, la RTD est plus rapide[56].

2.1.4 Adsorption

L'adsorption est un phénomène de surface dépendant de la température où les molécules de gaz ou de liquide (adsorbat) se fixent à la surface d'un solide (adsorbant). Dans le cas d'un réacteur à lit fluidisé, ceci se produit lorsque le gaz ou le liquide pénètre dans les pores des catalyseurs et est adsorbé sur sa surface interne[58]. L'adsorption est exothermique tandis que

l'action inverse, la désorption, est endothermique[59]. L'adsorption se produit principalement dans les catalyseurs poreux hétérogènes[58].

Adsorption dans les réacteurs à lit fluidisé

La réaction d'adsorption est utilisée dans plusieurs procédés impliquant les réacteurs à lit fluidisé (Tableau 2.4), particulièrement dans la purification des gaz. Le choix de l'adsorbant (catalyseur) est basé sur sa capacité de transport de matière dans le réacteur ainsi que sa résistance à l'environnement gazeux ou liquide[28]. La performance de l'adsorption sera fonction de[28] :

1. La hauteur du lit d'adsorbant (catalyseur) - une hauteur minimale est requise.
2. Le débit du liquide ou du gaz
3. Le diamètre des pores des particules de catalyseur. Ceci influence la diffusion dans les pores et la dispersion.
4. Dans le cas où l'adsorbat est liquide, la viscosité du fluide. En effet, si la viscosité augmente, la dispersion augmentera et par conséquent la résistance au transfert de masse sera plus élevée.

Modèle pour l'adsorption

Un des premiers modèles théoriques de l'adsorption a été développé par Kasten & Amundson en 1950. Ceux-ci ont divisé l'adsorption en 2 possibilités : (1) l'adsorption est rapide et donc suit la théorie de l'équilibre ou (2) l'adsorption est lente et suit une relation cinétique. Dans les deux cas, les hypothèses posées sont[58] :

— Le système est isotherme ;
— La concentration est uniforme ;
— Les catalyseurs sont des sphères solides et poreuses ;
— Le régime permanent est établi ;
— Les catalyseurs sont tellement petits qu'ils agissent tel un fluide.

Tableau 2.4 Exemple d'adsorption dans les procédés impliquant les réacteurs à lit fluidisé

Objectif	Intrant	Adsorbant	Adsorbat	Conditions	Référence
(1) Adsorption et désorption d'un gaz pollué dans 2 réacteurs à lit fluidisé	Gaz pollué (adsorption), Air chauffé ou vapeur (désorption)	Charbon actif, tamis moléculaire et résine échangeuse d'ions, quantité : 11.5 kg	CO_2	Température = 55 °C Mode en continu	[59]
(2) Capture des protéines à partir de cellule contenant le liquide de fermentation	Solution tampon 10 mM de phosphate de potassium (liquide)	Matrice échangeuse d'ions (DEAE) sur Agarose	Protéine : Albumine de sérum bovin	Réacteur : — Diamètre : 2 cm — Hauteur : 2 m Vitesse : 3 à 9 cm min^{-1}	[59]
(3) Désulfurisation de l'essence	Essence (2 mélanges)	NiO/ZnO–SiO_2–Al_2O_3 Quantité : 20 g	Soufre	Température : 250 à 400 °C Pression : 1 à 3 MPa Vitesse : 0 2 à 1.0 m s^{-1}	[60]
(4) Adsorption de quantité minime de métaux lourds dans les eaux polluées	Solution d'eau déminéralisée où des ions de zinc, cobalt, cuivre ou nickel ont été ajoutés	Résine : Chelamine Standard © traité à l'acide sulfurique	Sels métalliques hydratés	Réacteur : — Diamètre : 5.2 cm — Hauteur : 102 cm Température : 20 °C Durée : 30 h	[61]
(5) Adsorption du CO_2 des gaz de combustion	Un mélange d'azote et de CO_2	Charbon actif, DARCO FGD (Norit)	CO_2	Lit fluidisé acoustique : — Diamètre : 4 cm — Hauteur : 150 cm — 140 dB et 80 Hz (optimal) Température : 18 à 130 °C	[62]

Légende : DEAE : diéthyl-aminoéthyl

Cas no. 1 - Réaction à l'équilibre

La concentration en gaz (C) est reliée à la constante pour une adsorption isotherme (K_a). Plus cette dernière valeur est élevée, plus le catalyseur est adsorbant. La relation est [58] :

$$\frac{C_1 - C_2}{C_0 - C_1} = \frac{G_\mathrm{p}(K_\mathrm{a} + \alpha_\mathrm{p})}{\rho_\mathrm{b} Q} \sum_{i=1}^{\infty} \frac{6\nu^2}{[\omega_\mathrm{i}^2 + \nu(\nu - 1)](\omega_\mathrm{i}^2 + \delta)} \tag{2.11}$$

Où C_0 est la concentration initiale en gaz dans la particule (souvent 0), C_1 est la concentration en gaz dans le réacteur, C_2 est concentration du gaz à l'entrée, G_p est le débit massique des particules, α_p est la porosité de la particule, ρ_p est la masse volumique apparente de la particule, Q est débit volumique du gaz, et ω_i^2 est la racine de l'équation transcendantale ($\omega \cot \omega = 1 - \nu$).

De plus, ν est le nombre adimensionnel de Nusselt modifié et est décrit par :

$$\nu = \frac{k_\mathrm{f} R}{\mathscr{D}} \tag{2.12}$$

Où, k_f est le coefficient de transfert de masse dans le film, R est le rayon externe de la particule, et $\mathscr{D}$ est le coefficient de diffusion du gaz.

Puis, un second terme adimensionnel, δ, est résolu par :

$$\delta = \frac{G_\mathrm{p} R^2}{\gamma W} \text{ et } \gamma = \frac{\mathscr{D}\alpha_\mathrm{p}}{(K_\mathrm{a} + \alpha_\mathrm{p})} \tag{2.13}$$

Où W est la masse de particules/catalyseurs.

Cas no. 2 - Réaction cinétique (l'équilibre n'est pas atteint)

Le second cas est quand le taux d'adsorption est lent comparé à la diffusion dans les pores. L'équation lorsque la cinétique est réversible est [58] :

$$\frac{C_2 - C_1}{C_0 - C_1} = \frac{\mathscr{D} W \alpha_\mathrm{p} J}{R^2 \rho_\mathrm{b} Q} \sum_{n=1}^{\infty} \frac{6\nu^2 L_\mathrm{n}}{\omega_\mathrm{n}^2 + \nu(\nu - 1)} \tag{2.14}$$

$$J = 1 + \left[\frac{k_2(\alpha_\mathrm{p} C_0 + n_0) - C_1(k_2 \alpha_\mathrm{p} + k_1)}{C_0 - C_1} \right] \frac{W}{G_\mathrm{p}} \tag{2.15}$$

$$L_\mathrm{n} = \left[1 + \frac{W}{G_\mathrm{p}}(k_1 + k_2 \alpha_\mathrm{p} + b_\mathrm{n}) + \left(\frac{W}{G_\mathrm{p}} \right)^2 k_2 \alpha_\mathrm{p} b_\mathrm{n} \right]^{-1} \tag{2.16}$$

$$b_{\mathrm{n}} = \frac{\mathscr{D}\omega_{\mathrm{n}}^2}{R^2} \tag{2.17}$$

Où, k_1 et k_2 sont les constantes cinétiques et n_0 est la quantité de gaz sur le solide/particules initialement.

Les modèles de Kasten & Amundson sont utilisés lors de la conception de réacteur pour optimiser et mesurer l'impact économique en jouant sur la quantité (W) et le débit massique (G_{p}) d'adsorbant[58].

Adsorption et le temps de résidence (RTD)

L'adsorption d'un gaz par un catalyseur peut facilement être observée par l'étude du temps de résidence. En effet, la courbe RTD résultante aura une queue caractéristique dans la section descendante[28] (Figure 2.5).

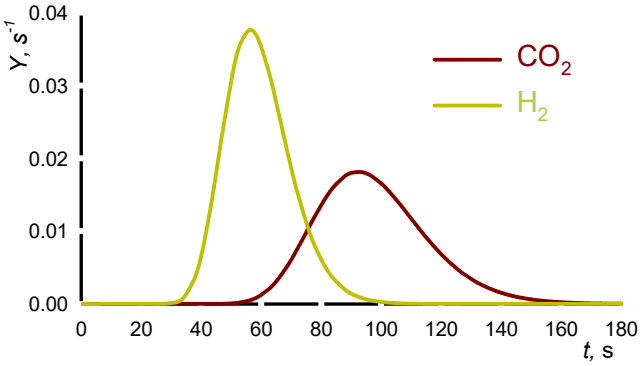

Figure 2.5 Effet de l'adsorption sur le temps de résidence. L'hydrogène n'est pas adsorbé sur le catalyseur de FCC. La courbe RTD pour le CO_2 présente une queue caractéristique qui est causé par le phénomène d'adsorption.

2.2 Les modèles

Pour comprendre le transfert de masse entre les différentes phases d'un réacteur à lit fluidisé, plusieurs modèles à 1, 2 ou 3 phases ont été développés. La première phase, la phase d'émulsion, inclut le gaz et les particules. La seconde phase, la phase bulle, est exempte de particules et finalement la phase solide inclut les pores et la surface solide des catalyseurs.

Dans le cas particulier de l'étude du temps de résidence (RTD), les modèles les plus communs dans la littérature sont le modèle à une phase de dispersion axiale et le modèle de réservoirs en

série (*tanks-in-series*). Par contre, certains chercheurs ont développé et appliqué des modèles à 2 ou 3 phases pour la RTD[56].

2.2.1 Modèle basé sur le transfert de masse

Les modèles de transfert de masse dans un réacteur à lit fluidisé sont basés soit sur l'hypothèse que le lit est homogène (1 phase), soit que le réacteur contient la phase bulle et la phase émulsion (2 phases) ou soit qu'une troisième phase solide est présente (3 phases).

Modèle à 1 phase ou lit homogène

Dans les modèles à une phase, le bilan de masse est analogue au modèle *plug-flow* pour un lit fixe. Trois niveaux de complexité sont présentés (Figure 2.6). Tout d'abord, le transfert de masse entre une seule sphère et une seule molécule de gaz est analysé. Puis, le lit est considéré comme fixe. Finalement, le transfert de masse est étudié entre les particules et le gaz fluidisé[26].

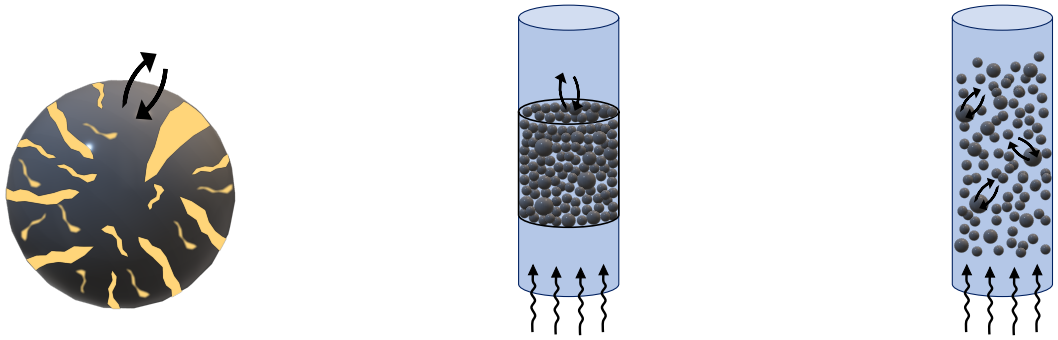

(a) (b) (c)

Figure 2.6 Développement des modèles à lit homogène – 1 phase. (a) Transfert de masse entre une sphère et un fluide. (b) Transfert de masse considérant un lit fixe. (c) Transfert de masse considérant un lit fluidisé.

Modèle A : Transfert de masse entre une sphère et une molécule de gaz

Tout d'abord, l'équation du transfert de masse entre une seule particule et une molécule A est donnée par[63] :

$$\frac{dN_{\mathrm{A}}}{dt} = k_{\mathrm{g,particule}} S_{\mathrm{ext,particule}} (C_{\mathrm{A}}^{i} - C\mathrm{A}) \tag{2.18}$$

Où $\frac{dN_A}{dt}$ est le taux de transfert de la molécule A entre la surface de la particule et le gaz, $k_{g,particule}$ est le coefficient de transfert de masse de la particule, $S_{ext,particule}$ est la surface extérieure de la particule, C_A^i est la concentration de la molécule A à la surface de la particule et C_A est la concentration de la molécule A dans le gaz.

La valeur de $k_{g,particule}$ est calculé empiriquement tel que[64] :

$$N_{Sh_{particule}} = \frac{k_{g,particule} d_p y}{\mathscr{D}} = 2 + 0.6 \left(N_{Re_{sph}}\right)^{0.5} (N_{Sc})^{0.333} \tag{2.19}$$

Où $N_{Sh_{particule}}$ est le nombre de Sherwood, d_p est le diamètre de la particule, y est la fraction logarithmique du gaz inerte (lorsque le transfert de masse est nul), $\mathscr{D}$ est le coefficient de diffusion du gaz, $N_{Re_{sph}}$ est le nombre de Reynolds de la particule et N_{Sc} est le nombre de Schmidt.

Cette équation est valide seulement pour une seule particule. Dans le cas d'un réacteur à lit fluidisé, le coefficient de transfert de masse ($k_{g,particule}$) sera sous ou sur estimé, selon le nombre de Reynolds, si cette équation est utilisée[26].

Modèle B : Transfert de masse entre un lit fixe de particules et le débit gazeux

Au second niveau, le modèle de transfert de masse dans un lit fixe a été développé basé sur le bilan pour une seule particule. Celui-ci est très similaire à l'équation 2.18 précédente :

$$\frac{dN_A}{dt} = k_{g,lit} S_{ext,lit} (C_A^i - CA) \tag{2.20}$$

Par contre, $\frac{dN_A}{dt}$ représente le transfert de masse de toutes les particules dans le lit, $k_{g,lit}$ est la moyenne des coefficients de transfert de masse de l'ensemble des particules et $S_{ext,lit}$ est la valeur totale de la surface extérieure des particules.

Le $k_{g,lit}$ est défini par une corrélation empirique[65] :

$$N_{Sh_{lit}} = \frac{k_{g,lit} d_p y}{\mathscr{D}} = 2 + 1.8 \left(N_{Re_p}\right)^{0.5} (N_{Sc})^{0.333} \tag{2.21}$$

Par la suite, pour estimer la surface totale des particules, la méthode de Kunii & Levenspiel est appliquée[63] :

$$S_{ext,lit} = V_{seq} \frac{6(1 - \epsilon_{v,lit})}{\phi d_{sph}} \tag{2.22}$$

Où V_{seq} est le volume du lit de catalyseur, $\epsilon_{\text{v,lit}}$ est la fraction de vide du lit, ϕ est la sphéricité des particules et d_{sph} est le diamètre d'une sphère ayant le même volume que les particules.

Modèle C : Transfert de masse dans un lit fluidisé entre les particules et le gaz

Dans le cas d'un réacteur à lit fluidisé du modèle homogène, l'équation de transfert de masse entre les molécules et la phase gazeuse est identique à celle pour un réacteur à lit fixe (équation 2.20). Par contre, $k_{\text{g,lit}}$ sera toujours plus élevée pour des conditions à lit fluidisé que pour un lit fixe.

Pour un lit fluidisé, le nombre de Sherwood, qui est relié directement au coefficient de transfert ($k_{\text{g,lit}}$), est fonction du nombre de Reynolds ainsi que la taille des particules (Tableau 2.5). Puis, la surface extérieure ($S_{\text{ext,lit}}$) est calculé similairement à un lit fixe[26].

Tableau 2.5 Corrélation du nombre de Sherwood selon la taille des particules dans un réacteur à lit fluidisé[1]

Maillage du tamis	Diamètre moyen des particules (d_{p})	Corrélation du $N_{\text{Sh}_{\text{lit}}}$	Validité selon le $N_{\text{Re}_{\text{p}}}$
14 à 20	1000 µm	$0.2N_{\text{Re}_{\text{p}}}^{0.937}$	$30 < N_{\text{Re}_{\text{p}}} < 90$
20 à 28	711 µm	$0.274N_{\text{Re}_{\text{p}}}^{0.709}$	$15 < N_{\text{Re}_{\text{p}}} < 80$
28 à 35	570 µm	$0.773N_{\text{Re}_{\text{p}}}^{1.107}$	$8 < N_{\text{Re}_{\text{p}}} < 60$
35 à 48	410 µm	$0.071N_{\text{Re}_{\text{p}}}^{0.926}$	$6 < N_{\text{Re}_{\text{p}}} < 40$
48 à 65	275 µm	$0.041N_{\text{Re}_{\text{p}}}^{1.036}$	$4 < N_{\text{Re}_{\text{p}}} < 15$

Il est difficile de modéliser parfaitement l'hydrodynamique d'un réacteur à lit fluidisé avec le modèle homogène. En effet, le comportement complexe des bulles n'est pas représenté dans ce modèle, c'est pourquoi le modèle à 2 phases a été développé[26].

Modèle à 2 phases ou lit avec bulles

Dans ces modèles, le réacteur à lit fluidisé est considéré hétérogène. Il contient la phase d'émulsion et la phase bulle. Deux modèles basés sur le transfert de masse entre ces deux phases sont étudiés (Figure 2.7). Un modèle incluant plusieurs particules est également présenté. Dans tous les cas, les bulles sont sphériques et entourées d'un nuage[26].

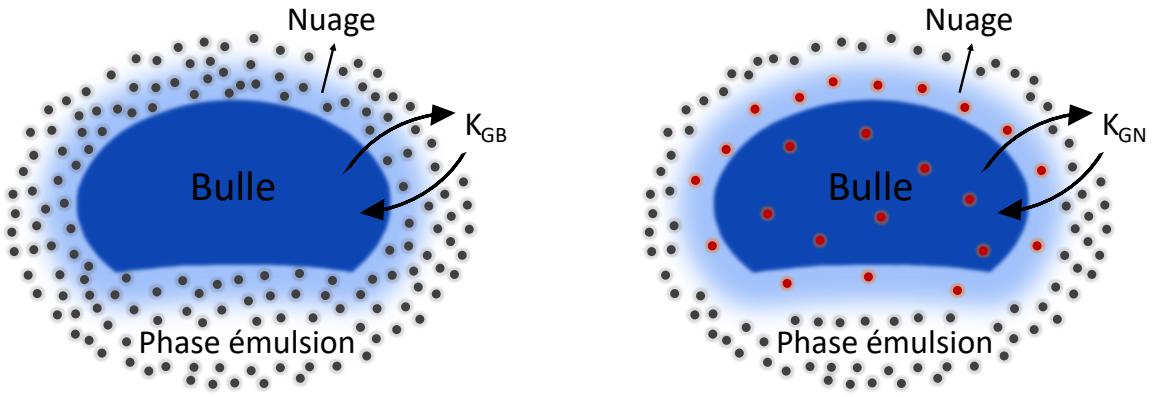

(a) (b)

Figure 2.7 Différence entre les modèles avec bulle – 2 phases. (a) Modèle de Kunii & Levensipiel. Dans ce modèle, la phase émulsion et le nuage sont considéré comme une seule région (catalyseur gris). (b) Modèle de Partridge & Rowe. Dans ce cas, le transfert de masse se fait entre la phase bulle qui inclue le nuage (catalyseur rouge) et la phase émulsion (catalyseur gris).

Modèle A : Modèle de Kunii & Levenspiel[63]

Ce modèle est basé sur le transfert de masse entre la phase bulle et la phase émulsion. Dans ce cas, le nuage et la phase émulsion sont considéré comme une seule région[26]. L'équation de transfert de masse est[63] :

$$\frac{dN_{\mathrm{A}}}{dt} = u_{\mathrm{b}} V_{\mathrm{bulle}} \left(\frac{dC_{\mathrm{A,b}}}{dz} \right) = K_{\mathrm{GB}} V_{\mathrm{bulle}} (C_A^i - C_{\mathrm{A,b}}) \tag{2.23}$$

Où u_{b} est la vitesse de montée des bulles, V_{bulle} est le volume occupé par la phase bulle, K_{GB} est le coefficient de transfert de masse entre la phase bulle et la phase émulsion et $C_{\mathrm{A,b}}$ est la concentration de la molécule A dans la bulle.

En fusionnant l'équation 2.20 avec l'équation précédente et en posant l'hypothèse que l'équilibre est atteint rapidement, que la concentration est identique à la surface de la particule, dans la phase d'émulsion et dans le nuage, le transfert de masse devient[63] :

$$\frac{dN_{\mathrm{A}}}{dt} = u_{\mathrm{b}} V_{\mathrm{bulle}} \left(\frac{dC_{\mathrm{A,b}}}{dz} \right) = \frac{k_{\mathrm{g,lit}} (1 - \epsilon_{\mathrm{v,rx}}) a'}{\delta_{\mathrm{b}}} V_{\mathrm{bulle}} (C_{\mathrm{A,c}} - C_{\mathrm{A,b}}) \tag{2.24}$$

Ainsi,

$$k_{\mathrm{g,lit}} = \frac{\delta_{\mathrm{b}}}{(1-\epsilon_{\mathrm{v,rx}})a'} K_{\mathrm{GB}} \tag{2.25}$$

Où δ_{b} est la fraction de bulle dans le réacteur à lit fluidisé ($\delta_{\mathrm{b}} = (U - U_{\mathrm{mf}})/u_{\mathrm{b}}$), $\epsilon_{\mathrm{v,rx}}$ est la fraction de vide dans le réacteur et $a' = \frac{6}{d_{\mathrm{p}}\phi}$.

Dans le cas où les particules sont non-poreuses et n'adsorbent pas[66] :

$$K_{\mathrm{GB}} = K_{\mathrm{bc}} = 4.5\frac{U_{\mathrm{mf}}}{d_{\mathrm{b}}} + 5.85\frac{\mathscr{D}^{0.5} g^{0.25}}{d_{\mathrm{b}}^{1.25}} \tag{2.26}$$

Inversement, dans le cas où les particules adsorbent :

$$K_{\mathrm{GB}} = \gamma_{\mathrm{b}} \frac{6 N_{\mathrm{Sh_{sph}}} \mathscr{D}}{d_{\mathrm{p}}^2 \phi y} + K_{\mathrm{bc}} \tag{2.27}$$

Où K_{bc} est le coefficient d'interchange du gaz entre la phase bulle et le nuage, d_{b} est le diamètre des bulles et $N_{\mathrm{Sh_{sph}}}$ est le nombre de Sherwood pour une seule particule sphérique.

Modèle B : Modèle de Partridge & Rowe[67]

Ce second modèle est basé sur le transfert de masse entre le nuage et la phase émulsion. Dans ce cas-ci, la phase bulle et le nuage sont considérés comme une seule région. Ainsi, l'équation est[67] :

$$\frac{dN_{\mathrm{A}}}{dt} = V_{\mathrm{nuage}} \left(\frac{dC_{\mathrm{A,c}}}{dt}\right) = k_{\mathrm{gc}} S_{\mathrm{ext,nuage}} (C_{\mathrm{A,e}} - C_{\mathrm{A,c}}) = K_{\mathrm{GC}} V_{\mathrm{nuage}} (C_{\mathrm{A,e}} - C_{\mathrm{A,c}}) \tag{2.28}$$

Où V_{nuage} est le volume du gaz dans la bulle et le nuage, k_{gc} est le coefficient de transfert de masse entre le nuage et la phase émulsion, K_{GC} est le coefficient d'échange entre le gaz et la bulle-nuage, $S_{\mathrm{ext,nuage}}$ est la surface extérieure du nuage, $C_{\mathrm{A,e}}$ est la concentration dans la phase émulsion et $C_{\mathrm{A,c}}$ est la concentration dans le nuage.

Les coefficients de transfert de masse sont déterminés à l'aide des équations[67] :

$$N_{\mathrm{Sh_c}} = \frac{k_{\mathrm{gc}} d_{\mathrm{c}}}{\mathscr{D}} = 2 + 0.69 N_{\mathrm{Sc}}^{0.33} N_{\mathrm{Re_c}} \tag{2.29}$$

$$K_{\mathrm{GC}} = \frac{3.9 \epsilon_{\mathrm{v,mf}} \mathscr{D} N_{\mathrm{Sh_c}}}{(V_{\mathrm{nuage}})^{0.67}} \tag{2.30}$$

Où d_c est le diamètre du nuage et $\epsilon_{v,mf}$ est la fraction de vide à la vitesse minimale de fluidisation.

Modèle C : Modèle pour un lit de bulles

Les équations empiriques pour déterminer le K_{GC} et le K_{GB} sont basées sur des expériences où une seule bulle est impliquée. Or, le mécanisme de transfert de masse entre les bulles et la phase d'émulsion est beaucoup plus complexe[26]. Ainsi, une corrélation pour un ensemble de bulles a été développée pour déterminer le coefficient de transfert de masse[68] :

$$K_{GB,m} = \left(\frac{6}{d_{b,m}}\right) k_{gb,m} = \frac{2U_{mf}}{d_{b,m}} + \frac{12}{d_{b,m}^{1.5}} \left(\frac{\mathscr{D}\epsilon_{v,mf} u_{b,m}}{\pi d_{b,m}}\right)^{0.5} \tag{2.31}$$

Où l'indice m représente la moyenne de l'ensemble des bulles et k_{gb} est le coefficient de transfert de masse basé sur la surface de la bulle. Cette équation est valable dans les systèmes où le phénomène d'adsorption est absent. Elle correspond aussi à K_{GB} dans l'équation 2.23.

Modèle à 3 phases

Le modèle à 3 phases est basé sur l'équation de flux pour chaque phase p[56] :

$$w_p = U_{g,p} C_p - M_{m,p} \frac{\partial C_p}{\partial x} \tag{2.32}$$

Où w est le flux, U_g est la vitesse du gaz, C est la concentration et M_m est le coefficient de mélange axial. L'indice p représente la phase d'émulsion (E), bulle (B) ou solide (S).

À cela, il faut rajouter l'équation de continuité pour chaque phase E, B et S[56] :

$$\frac{\partial w_p}{\partial x} + \frac{\partial C_p}{\partial t} = r_p \tag{2.33}$$

Où r est le taux de réaction.

Ces deux équations peuvent être calculées pour un système à 2 phases ou 3 phases. Les conditions initiales sont :

$$C_p = 0 \text{ pour } t = 0 \tag{2.34}$$

Et les conditions limites sont :

$$w_E = \delta, w_B = 0, w_S = 0 \text{ pour } x = 0 \tag{2.35}$$

$$C_{\mathrm{p}} = \text{ finit pour } x < \infty \tag{2.36}$$

Où δ est l'injection par *pulse* (dirac-δ)

Pour résoudre ces équations, il est supposé que la vitesse de la phase solide ainsi que son coefficient de mélange soient proches de 0 ($u_{\mathrm{S}} = M_{\mathrm{S}} \approx 0$). Le transformé de Laplace bivariable résultant est [56] :

$$\begin{vmatrix} M_{\mathrm{E}}v^2 - u_{\mathrm{E}}v - S - K_{\mathrm{EB}} - K_{\mathrm{ES}} & K_{\mathrm{EB}} & K_{\mathrm{ES}} \\ K_{\mathrm{EB}} & M_{\mathrm{B}}v^2 - u_{\mathrm{B}}v - S - K_{\mathrm{EB}} & 0 \\ K_{\mathrm{ES}} & 0 & -S - K_{\mathrm{ES}} \end{vmatrix} \begin{vmatrix} C_{\mathrm{E}} \\ C_{\mathrm{B}} \\ C_{\mathrm{S}} \end{vmatrix} = \begin{vmatrix} M_{\mathrm{E}}\psi_{\mathrm{E}} - 1 \\ M_{\mathrm{B}}\psi_{\mathrm{B}}v \\ 0 \end{vmatrix} \tag{2.37}$$

Où S et v sont les constantes de Laplace, $\psi = C_{\mathrm{p}}(v, S)|_{x=0}$ et $K_{\mathrm{p,q}}$ est le coefficient entre les phases p et q.

Donc, six paramètres devront être résolus pour modéliser le réacteur à lit fluidisé avec trois phases : u_{E}, u_{B}, M_{E}, M_{B}, K_{EB} et K_{ES}. Pour un système à deux phases (émulsion et bulle), cinq paramètres sont à résoudre : u_{E}, u_{B}, M_{E}, M_{B} et $k_{\mathrm{EB}} = k_{\mathrm{BE}}$.

2.2.2 Modèle spécifique à la RTD

Les modèles à deux et trois phases sont complexes et demandent la résolution de plusieurs paramètres. Pour cette raison, la distribution du temps de résidence est principalement modélisée grâce au modèle de dispersion axial à une phase ou le modèle de réservoirs en série (*tanks-in-series*). Ces deux modèles permettent de représenter la non-idéalité du profil RTD pour la phase analysée (liquide, gazeuse ou solide). L'article *Experimental Methods in Chemical Engineering : Residence Time Distribution* (Chapitre 4) présente en détail ces deux modèles. De plus, les trois moments caractéristiques à la RTD sont présentés (moyenne du temps de résidence ($\bar{t}$), variance (σ^2) et l'asymétrie (s^3) ainsi que la fonction RTD ($E(t)$) et la distribution cumulative – F-courbe ($F(t)$).

Modèle de dispersion axial

Ce modèle est analogue à la loi de Fick et est le plus utilisé dans la littérature[37]. Il permet de décrire la non-idéalité d'un système en assumant un débit idéal (*plug flow*) dans un réacteur à écoulement piston (PFR). Sa forme adimensionnelle est[69,70,71] :

$$\frac{\partial C}{\partial \theta} + \frac{\partial C}{\partial \xi} = \frac{1}{N_{\mathrm{Pe}}} \frac{\partial^2 C}{\partial \xi^2} \tag{2.38}$$

Où C est la concentration adimensionnelle (C/C_0), θ est le temps adimensionnel, ξ est la longueur adimensionnelle et N_{Pe} est le nombre de Péclet. Ce dernier est le seul paramètre à résoudre.

Lorsque la valeur du nombre de Péclet est entre 10 et 50, la dispersion est faible et donc le système est considéré comme *plug flow*. Si la valeur de Péclet est inférieure à 10, alors le coefficient de dispersion est élevé ce qui indique un grand degré de mélange[72].

Lorsqu'une réaction est impliquée, le modèle de dispersion axial devient[73] :

$$\frac{\partial C}{\partial \xi} = \frac{1}{N_{Pe}} \frac{\partial^2 C}{\partial \xi^2} + \frac{\tau}{c_0} r \tag{2.39}$$

Où, τ est le temps de résidence théorique (le ratio de la longueur du réacteur sur la vitesse superficielle du gaz) et r est le taux de réaction.

Lors de la résolution, différentes possibilités de conditions limites peuvent être appliquées au modèle de dispersion axiale (Tableau 2.6). Le plus simple est les conditions de Danckwerts pour les systèmes fermés-fermés. Par contre, ceux-ci sont valables uniquement pour de faibles valeurs du nombre de Péclet (dispersion est grande), donc pour un système parfaitement mélangé.

Lorsqu'une réaction est impliquée, les conditions limites de Salmi & Romanainen sont à prioriser[73]. La solution analytique représente la forme générale de résolution du modèle de dispersion axiale avec réaction. En effet, lorsque $n = 1$, l'équation est identique à ce qui a été développé par Wehner & Wilhelm[74]. Puis, lorsque $n = 2$, il s'agit de la solution proposée par Vortmeyer[73]. Finalement, lorsque la réaction est de 1$^{\mathrm{er}}$ ordre ($r = -kC$), la solution est similaire aux conditions de Danckwerts[73].

Tableau 2.6 Conditions initiales et limites pour résoudre le modèle de dispersion

Type	Conditions initiales et limites	Restrictions	Solution analytique
Fermé-Fermé [24]	$C_{0,\xi} = 0$	$0 \leq \xi \leq 1, t \geq 0$	-
	$C_{\tau,0} = C\|_{\xi=0} - \frac{1}{Pe}\frac{\partial C}{\partial \xi}\Big\|_{\xi=0}$	$\xi = 0$	
	$\frac{\mathrm{d}C}{\mathrm{d}\xi} = 0$	$\xi = 1$	
Fermé-Ouvert [11,71]	$C_{0,\xi} = 0$	$0 \leq \xi \leq 1$	
	$C_{\tau,0} = \rho_0$	$\tau > 0$	$G(\theta) = \frac{1}{2}\left[\mathrm{erfc}\sqrt{\frac{N_{\mathrm{Pe}}}{4\theta}(1-\theta)} + \mathrm{e}^{N_{\mathrm{Pe}}}\mathrm{erfc}\sqrt{\frac{N_{\mathrm{Pe}}}{4\theta}(1+\theta)}\right]$
	$\frac{\mathrm{d}C_{\tau,1}}{\mathrm{d}\xi} = 0$	$\tau > 0$	
Ouvert-Ouvert [70,75]	-	-	$E_{\grave{},\mathrm{OO}} = \frac{1}{\sqrt{4\pi\theta}/N_{\mathrm{Pe}}}\exp\left[\frac{N_{\mathrm{Pe}}(1-\theta)^2}{4\theta}\right]$
Fermé-Ouvert (Réaction) [73]	$C_{\tau,0} = C\|_{\xi=0} - \frac{1}{Pe}\frac{\partial C}{\partial \xi}\Big\|_{\xi=0}$	$\xi = 0$	
	$\frac{\partial C}{\partial \xi} = f(N_{\mathrm{Pe}})\frac{\tau}{C_0}r$	$\xi = 1$	$C(\xi) = \frac{2\left[(1+\beta)^n e^{-\frac{N_{\mathrm{Pe}}(1-\beta)(1-\xi)}{2}} - (1-\beta)^n e^{-\frac{N_{\mathrm{Pe}}(1+\beta)(1-\xi)}{2}}\right]}{(1+\beta)^{n+1}e^{-N_{\mathrm{Pe}}(1-\beta)/2} - (1-\beta)^{n+1}e^{-N_{\mathrm{Pe}}(1+\beta)/2}}$
	$f(N_{\mathrm{Pe}}) = e^{-\frac{\alpha}{N_{\mathrm{Pe}}}}$		

Légende : $\alpha = 10$ est une bonne approximation de la réalité, $\beta = \sqrt{1 + \frac{4k\tau}{N_{\mathrm{Pe}}}}$, k est la constante cinétique

Modèle réservoir en série (*tanks-in-series*)

Ce modèle consiste à considérer le mélange parfait de réacteurs CSTRs en séries. Lorsque le nombre de CSTRs est infini, cela signifie que l'injection du tracer est parfaite (*pulse* δ-Dirac) et que le modèle suit le comportement d'un réacteur à écoulement piston (*plug flow*)[37]. L'équation de la fonction RTD ($E(\theta)$) sous la forme adimensionnelle est[33] :

$$E(\theta) = \frac{n_{\mathrm{CSTR}}(n_{\mathrm{CSTR}}\theta)^{n_{\mathrm{CSTR}}-1}}{(n_{\mathrm{CSTR}}-1)!}\exp(-n_{\mathrm{CSTR}}\theta) \tag{2.40}$$

Où n_{CSTR} est le nombre de CSTRs en série et est décrit tel que :

$$n_{\mathrm{CSTR}} = \frac{1}{\sigma_\theta^2} \tag{2.41}$$

Modèle par régression

Les modèles par régression sont peu nombreux dans la littérature pour modéliser le temps de résidence. Néanmoins, Khaled et *al.* ont développé un modèle de prédiction du coefficient de dispersion pour analyser un réacteur à lit fluidisé en phase liquide. Le catalyseur est le charbon actif ($d_{\mathrm{p}} = 0.18\,\mathrm{cm}$), la phase liquide est l'eau et le tracer est une solution de NaCl. Deux facteurs sont significatifs : x_1 qui est le débit volumique du courant liquide et x_2 qui est la température. Chaque facteur a été analysé à 5 niveaux chacun. L'équation du coefficient de dispersion axiale ($\mathcal{D}$) qui en découle est[27] :

$$\mathcal{D} = 2.4137 + 2.5447x_1 + 0.9844x_2 + 1.4729x_1x_2 - 0.9994x_1^2 - 0.1240x_2^2 \tag{2.42}$$

Par la suite, il est possible de relier le coefficient de dispersion au nombre de Péclet et ainsi en déduire la distribution du temps de résidence. Les modèles par régression sont très avantageux, car ils sont simples et permettent une mise à l'échelle efficace. Par contre, les résultats sont valides seulement pour les mêmes conditions d'opération et ne peuvent être aucunement extrapolé. Dans ce cas-ci, les résultats sont valides pour le même intervalle de débit [210 et $1000\,\mathrm{L\,h^{-1}}$] et de température [20 et $40\,^{\circ}\mathrm{C}$] ainsi que le même catalyseur et la même phase liquide.

Convolution

La convolution est une technique de correction dans le cas où l'injection du traceur n'est pas parfaite (*pulse* imparfait). En d'autres mots, cette méthode est nécessaire lorsque le temps

de résidence est court en comparaison avec le temps d'injection[37]. La correction est définie tel que[24] :

$$E_{\text{out}}(t) = E_{\text{in}}(t) \otimes E(t) \tag{2.43}$$

Où $E_{\text{out}}(t)$ est la courbe RTD avant la correction et $E_{\text{in}}(t)$ est la courbe RTD de l'injection imparfaite mesurée à l'entrée du réacteur. Ainsi, pour résoudre, il est nécessaire d'utiliser les transformés de Fourrier[37] :

$$E(t) = FFT^{-1}\left\{\frac{FFT\left\{E_{\text{out}}(t)\right\}}{FFT\left\{E_{\text{in}}(t)\right\}}\right\} \tag{2.44}$$

Où FFT est la transformée de Fourier rapide et FFT^{-1} est l'inverse de cette transformée.

2.2.3 Limitation des modèles pour décrire la RTD

Il existe beaucoup de modèles pour décrire le temps de résidence dans les réacteurs à lit fluidisé. La plupart d'entre eux sont basés sur des corrélations empiriques qui sont valident seulement pour des conditions précises[31].

Le modèle de dispersion axial est simple et efficace pour la majorité des réacteurs non idéaux[37]. Par contre, il fait intervenir seulement la dispersion d'une seule phase et l'adsorption dans les catalyseurs poreux n'est pas prise en considération. De plus, dans le cas où plusieurs traceurs sont injectés en même temps, ceux-ci sont analysés indépendamment les uns des autres. Or, la réalité est plus complexe et la dépendance des traceurs a été démontrée[12] (Chapitre 5). Ainsi, le modèle de dispersion est limité à des systèmes simples.

C'est pour ces raisons qu'il serait primordial de développer un nouveau modèle incluant les phénomènes de dispersion, diffusion, d'adsorption en plus de la convection pour modéliser le temps de résidence dans les systèmes avec des traceurs multiples.

2.3 Les traceurs gazeux

Le choix du traceur est primordial lors d'essai RTD, puisqu'il influencera les résultats obtenus[12] (Chapitre 5). Pour démontrer leur effet, les expériences RTD ont été produites avec plusieurs traceurs gazeux.

2.3.1 Propriétés des traceurs gazeux

Sept traceurs gazeux ont été choisis pour leur caractéristique physiques (coefficient de diffusivité, masse volumique), leur implication dans de nombreuses réactions (CO, CO_2 et O_2) ainsi que l'absence d'interaction entre eux lors de la détection par spectromètre de masse (bouteille 3). Ces gaz, en ordre décroissant selon leur masse molaire sont : Kr, CO_2, O_2, CO, CH_4, He et H_2. Leurs valeurs de coefficient de diffusivité sont inversement proportionnelles à leurs masses molaires, c'est-à-dire plus la masse molaire est élevée, moins la molécule diffusera. Il en est de même pour le volume spécifique, la conductivité thermique et les capacités calorifiques (C_p et C_v) (Tableau 2.7). La viscosité dynamique est plus faible pour l'hydrogène que pour le krypton, mais aucune tendance n'est observée en fonction de la masse molaire. Par contre, le nombre de liaisons diminue la valeur de la viscosité dynamique.

2.3.2 Effet des traceurs sur la RTD

Le choix du traceur influencera la RTD. Les caractéristiques de base d'un traceur sont [15] :

1. Inerte, ne réagit pas avec les autres molécules et n'est pas adsorbé par les parois du réacteur ;
2. Facilement détectable ;
3. Soluble dans le mélange liquide ou gazeux ;
4. Ses propriétés physiques sont similaires à ceux du système à l'étude.

Plusieurs articles ont expérimenté plusieurs traceurs. Par exemple, Yates *et al.* ont choisi le butène-1, un gaz adsorbable et l'ont comparé au méthane, un gaz non-adsorbable. Ils ont, par la suite, exécuté des analyses RTD dans un réacteur à lit fluidisé avec un catalyseur poreux – la silice-alumine. Les résultats démontrent que le traceur qui est adsorbé dans les pores du catalyseur se déplace avec les particules dans le réacteur. Un traceur peut alors être adsorbé juste avant la sortie du réacteur, se promener, et être sortir des pores à l'entrée. Il devra parcourir à nouveau le réacteur avant de quitter celui-ci [57]. Cela a un impact direct sur les résultats RTD. Donc, si le système de départ contient un gaz adsorbable, et que l'étude hydrodynamique est faite avec un gaz inerte, les résultats sont faussés.

Tableau 2.7 Propriétés physiques des traceurs gazeux

	Kr	CO_2	O_2	CO	CH_4	He	H_2
Molécule[3]	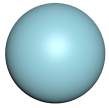	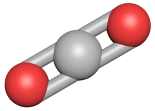	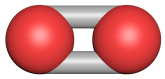	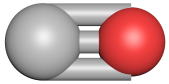	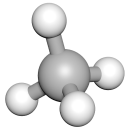		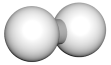
Masse molaire ($g\,mol^{-1}$)	84	44	32	28	16	4	2
Masse volumique ($kg\,m^{-3}$)[1,5]	3.4314	1.8075	1.3085	1.145	0.6567	0.1635	0.0823
Coefficient de diffusivité ($T = 25\,°C$)[6]	0.136	0.150	0.194	0.195	0.208	0.716	0.796
Coefficient de diffusivité ($T = 300\,°C$)[6]	0.436	0.479	0.619	0.622	0.664	2.90	2.54
Diamètre cinétique (Å)[2]	3.61	3.30	3.46	3.76	3.80	2.60	2.89
Viscosité dynamique ($Pa\,s$)[1,5,4]	2.5132E-4	1.4932E-4	2.055-4	1.7649E-4	1.1067E-4	1.9846E-4	8.915E-5
Volume spécifique ($m^3\,kg^{-1}$)[1,5]	0.2914	0.5532	0.7643	0.8734	1.5227	6.117	11.983
Conductivité thermique ($mW\,mK^{-1}$)[1,5]	9.363	16.643	26.340	26.478	33.931	155.31	184.88
Capacité thermique à pression constante ($kJ\,kg^{-1}\,K^{-1}$)[1,5]	0.2492	0.85085	0.9196	1.0421	2.2316	5.1929	14.306
Capacité thermique à volume constant ($kJ\,kg^{-1}\,K^{-1}$)[1,5]	0.1490	0.6575	0.6585	0.7437	1.709	3.116	10.180
Température critique (°C)[1]	-63.8	31.06	-118.57	-140.23	-82.59	-267.95	-239.96
Pression critique (atm)[1]	54.3	72.86	49.77	34.53	45.39	2.245	12.96

Légende : [1] AirLiquide©, [2] [76] [3] ChemDoodle3D©, [4] $v = \mu \times \rho$ où μ est la viscosité cinématique [5] phase gazeuse à 25 °C et 1.013 bar [6] Calculé à l'aide de la corrélation de Fuller-Schettler-Gidding (Table 5.2).

2.3.3 Éléments manquants sur les traceurs et la RTD

Dans la littérature, aucun auteur ne prend en considération une injection de plusieurs traceurs simultanément. Cela est particulièrement important quand les phases étudiées sont gazeuses ou liquides. Prenons un exemple simple – un réacteur où la réaction est l'oxydation du CO :

$$CO + O_2 \longrightarrow CO_2 \tag{2.45}$$

Le système comporte trois gaz qui pourraient agir ensemble. Ils pourraient être dépendants les uns des autres. Or, si l'analyse RTD est faite seulement avec un traceur non réactif, les résultats seront faussés, car la réalité pourrait ne pas être représentée. Donc, une étude plus approfondie sur les interactions dans les systèmes comprenant plusieurs gaz ou liquides est nécessaire.

De plus, plusieurs articles présentent des traceurs ayant des coefficients de diffusion nettement différents du système à l'étude. Par exemple, l'hélium ($\mathscr{D} = 0.716\,\mathrm{cm\,s^{-1}}$ à 25 °C) a été choisi pour des études RTD dans un microréacteur à lit fluidisé[77]. Le modèle de dispersion axiale concorde avec les résultats, mais il faudrait approfondir pour confirmer que cette exactitude n'est pas causée par la valeur élevée du coefficient de diffusion de l'hélium.

2.4 Les catalyseurs

Les réacteurs à lit fluidisé impliquent, dans la majorité des cas, l'utilisation d'un catalyseur solide qui acte comme un fluide. L'avantage de ce type de réacteur est que le mélange est amélioré ce qui permet une distribution homogène de la chaleur tout au long du réacteur ainsi qu'un meilleur contact gaz-solide. Ainsi, les réacteurs à lit fluidisé offrent un excellent transfert de masse et de chaleur.

Les catalyseurs sont divisés en 4 groupes Geldart en fonction de leur diamètre et de leur masse volumique : A – aéré, B – similaire au sable, C – cohésif et D – jaillissant (Figure A.1). Le groupe Geldart A est le plus commun pour la fluidisation, car les particules sont faciles à fluidiser et à produire à l'aide du séchoir-atomiseur[22]. Les groupes Geldart, en ordre croissant de diamètre de particules, sont : C, A, B et D.

2.4.1 Caractérisation des catalyseurs employés pour la RTD

Le temps de résidence dans un réacteur à lit fluidisé est dépendant du type de catalyseur employé. Ce projet de recherche fait intervenir quatre catalyseurs du groupe Geldart A :

1. Catalyseur pour le craquage catalytique en lit fluidisé, FCC ;
2. Hydrogénophosphate de vanadyle hémihydraté, VPOP
3. Pyrophosphate de vanadyle calciné, VPPC
4. Pyrophosphate de vanadyle équilibré, VPPE

De plus, pour comparer l'effet de la porosité sur la RTD, le sable a aussi été expérimenté. Ce dernier est du groupe Geldart B. Plusieurs caractéristiques physiques se retrouvent dans les articles (Tableau 5.1) ainsi que les images par microscopie électronique à balayage (SEM) (Figure 5.3).

FCC

Le FCC est un catalyseur impliqué principalement dans le procédé de craquage catalytique qui est au cœur des raffineries de pétrole. Cette étape a pour objectif de diminuer le poids moléculaire de produits lourds, tels l'huile sous-vide et les résidus, en produits plus légers[78]. Ainsi, des alcènes légers, de l'essence à haut niveau d'octane, du diésel, du kérosène et du gaz de pétrole liquéfié (GPL) son produits[79,80]. L'essence est constituée d'un mélange de C_5 à C_{11} d'alcanes, d'alcènes et d'aromatiques[80].

La composition générale du FCC est[79] :

1. Une matrice : qui permet d'augmenter l'activité totale du catalyseur. Celle-ci est constituée : 1 – D'un composé actif, une alumine, qui a de larges pores aidant ainsi le précraquage des molécules lourdes. 2 – D'un composé inerte, l'argile, qui donne les propriétés physiques du catalyseur. 3 – D'un liant permettant de maintenir les liaisons du catalyseur.
2. Un composant actif : qui est responsable de l'activité catalytique. Il s'agit de Y-Zéolite ou ZSM-5 dont la structure est de forme *faujasite*.
3. Des ingrédients fonctionnels pour accomplir une fonction spécifique (optionnel).

Le procédé de production du FCC est en continuel évolution pour permettre une diminution de la formation de coke, pour mieux résister aux métaux (vanadium, nickel et fer) ainsi que pour obtenir une meilleure conversion[79].

Les catalyseurs de FCC sont produits par séchoir-atomiseur (Figure 2.8). Ainsi, la distribution de la taille des particules est étroite et cette méthode procure une bonne résistance à l'attrition qui est une problématique récurrente dans les procédés de craquage catalytique[79].

Au niveau commercial, les catalyseurs de FCC subissent le phénomène de cokage et doivent être régénérés fréquemment. Pour pouvoir être efficace dans le craquage catalytique, le FCC

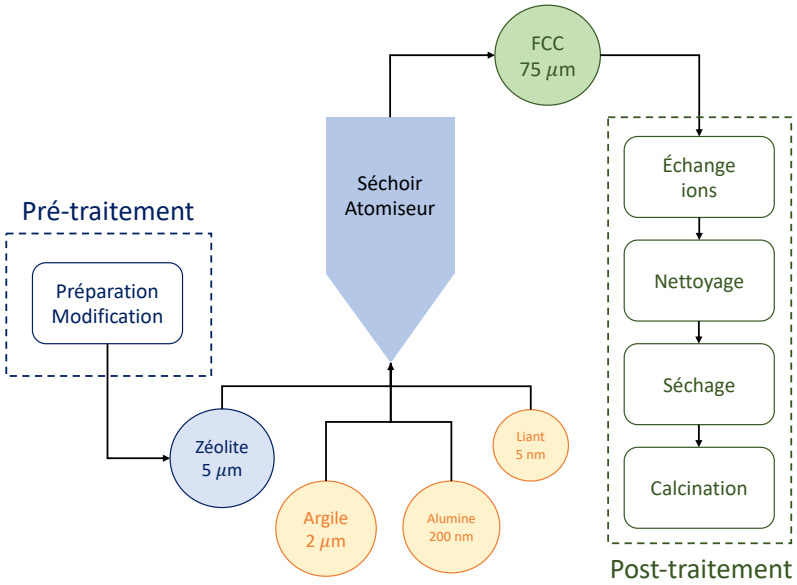

Figure 2.8 Étape de production du catalyseur FCC. La production débute avec les prétraitements de la zéolite : la préparation et la modification. La formation du catalyseur FCC se fait dans le séchoir-atomiseur en injectant simultanément la zéolite, l'alumine, le liant et l'argile. Finalement, le catalyseur, d'environ 75 µm, subit un post-traitement incluant un échange d'ions, un nettoyage, un séchage et une calcination. Cette dernière étape doit être faite avec précaution en raison de la faible tolérance à la calcination de la zéolite[79].

doit être hautement stable à température élevée ($T > 870\,°C$), doit avoir une structure 3D, doit avoir une activité élevée et donc doit être acide et avoir des pores d'au moins 7.5 Å[78].

Oxyde de phosphore de vanadium

L'oxyde de phosphore de vanadium (VPO) est un catalyseur impliqué principalement dans l'oxydation partielle du *n*-butane pour produire l'anhydride maléique et l'acide maléique[81]. Ensuite, par hydrogénation, cet acide est transformé en tétrahydrofurane – le monomère du Lycra® [82]. La production commerciale dans les réacteurs à lit fluidisé a débuté vers la fin des années 80[81]. Puis, au milieu des années 90, les lits fluidisés circulants (CFB) ont fait leur apparition. Par conséquent, il était possible d'obtenir des courants plus concentrés (diminution de la taille du réacteur) ainsi qu'une production à grande échelle[83].

Les équations principales de la conversion du *n*-butane (C_4H_{10}) en anhydride maléique (MA) à l'aide du VPO sont[81] :

$$C_4H_{10} \longrightarrow MA + CO_x + H_2O \tag{2.46}$$

$$MA \longrightarrow CO_x + H_2O \tag{2.47}$$

DuPont a développé un catalyseur qui est résistant à l'attrition ce qui est particulièrement important pour les réacteurs CFB. Celui-ci est constitué d'un noyau de VPO et est enrobé d'une coquille de silice poreuse[84]. Son précurseur (VPOP) est l'hydrogénophosphate de vanadyle hémihydraté ($VOHPO_4 \cdot 0.5H_2O$). La production de ce catalyseur se fait en plusieurs étapes (Figure 2.9). Tout d'abord, le VPOP subit une micronisation pour diminuer sa taille entre 1 et 2 µm. Puis, il est injecté, avec l'acide polysilicique, dans un séchoir atomiseur pour former un catalyseur sphérique. La forme active (VPPC) est appelée pyrophosphate de vanadyle ($(VO)_2P_2O_7$) calciné puisqu'il a subi une calcination à 390 °C. Il est ensuite envoyé dans le CFB où la réaction d'oxydation du *n*-butane a lieu. Finalement, après 2 années d'activité, celui-ci est retiré et est classé comme état d'équilibre (VPPE)[82].

Sable

Le sable est une roche sédimentaire qui s'est dégradée en fines particules variant de 0 02 à 2 mm. Sa composition principale est le dioxyde de silicium (SiO_2) (Figure 2.10). En fonction de sa provenant, celui-ci contient un pourcentage différent d'argile, de charbon et d'autres minéraux. Plusieurs structures du SiO_2 sont présentes dans la nature en fonction de leur processus de cristallisation : quartz, trydimite, cristobalite, opale ($SiO_2 + H_2O$) et léchatelierite. Ces structures se différencient par leur masse volumique qui est fonction de la température[85].

Le sable est une poudre fréquemment employée en fluidisation. Il fait partie du groupe Geldart B, amorphe, et est non-poreux. Il permet une fluidisation plus uniforme[86].

Par exemple, le sable est utilisé dans la fluidisation :

- Lorsqu'un catalyseur du groupe cohésif (Geldart groupe C) est nécessaire, le sable acte comme média pour permettre la fluidisation[87]
- Lors de la combustion du charbon dans une fournaise, l'air fluidise le lit de sable[88]
- Lors d'étude hydrodynamique du réacteur (essai de pression, température, vitesse minimale de fluidisation)[89]
- Lors d'étude des types de régimes de fluidisation, particulièrement pour le régime de *slugging*[90]

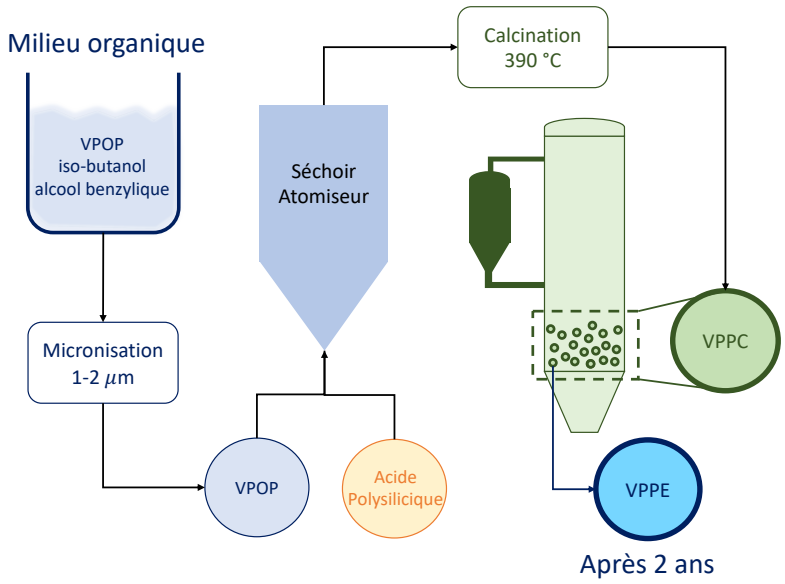

Figure 2.9 Cycle de vie du pyrophosphate de vanadyle du précurseur (VPOP), à l'état actif ou calciné (VPPC) et à l'état d'équilibre (VPPE). Le VPOP est dans un milieu organique constitué d'*iso*-butanol et d'alcool benzylique. Puis, ce précurseur subit une micronisation pour diminuer la taille des particules entre 1 à 2 µm. Le VPOP et l'acide polysilicique (10 % silice) sont injectés dans le séchoir atomiseur pour former le catalyseur contenant un noyau de VPO enrobé de silice. Pour l'activer, le catalyseur est calciné à 390 °C (VPPC). Ainsi, le VPPC passe 2 années dans le CFB pour produire l'anhydride maléique. Finalement, il atteint l'état d'équilibre (VPPE) [82].

(a) (b)

Figure 2.10 Structure du sable. (a) Dioxyde de silicium. (b) Structure de Quartz ©ChemDoodle3D

2.4.2 Effet des catalyseurs sur la RTD

La porosité des catalyseurs influence la RTD. En effet, lorsque le catalyseur a de larges pores et que la vitesse est basse, le traceur aura plus accès à l'intérieur des pores et donc le temps de contact sera plus élevé. Par conséquent, le temps de résidence augmentera [91].

Un second aspect particulier pour les réacteurs à lit fluidisé remplit de catalyseurs (aire de surface élevée et traceur adsorbable) est que la courbe de réponse peut être différente pour des conditions d'opérations identiques. En effet, puisque le lit est en mouvement circulaire continu, le traceur entrera dans les pores et pourrait ressortir n'importe où dans le réacteur [57]. Cela influence grandement la RTD.

Des catalyseurs avec de larges pores influenceront la RTD, car le transfert de masse intraparticule est causé non seulement par la diffusion, mais aussi la convection à l'intérieur des pores. Ceci est le même principe que les colonnes HPLC en séparation : plus la porosité est élevée (Giga pores), plus la colonne est efficace. La convection intraparticule influence la RTD dans le cas où [92] :

— Le nombre de Péclet (N_{Pe}) est faible et donc la dispersion axiale ($\mathcal{D}$) n'est pas négligeable.
— Le nombre de Biot (N_{Bi}) est faible :

$$N_{\mathrm{Bi}} = \frac{\tau_{\mathrm{D}}}{\tau_{\mathrm{f}}} = \frac{k_{\mathrm{f}} l}{\mathscr{D}_{\mathrm{eff}}} \tag{2.48}$$

Où τ_{D} est la constante de temps pour la diffusion intraparticule, τ_{f} est la constante de temps pour la diffusion du film, k_{f} est le coefficient de transfert de masse du film, l est la moitié de l'épaisseur de la plaque, et $\mathscr{D}_{\mathrm{eff}}$ est la diffusivité intraparticule effective.

— Le ratio α est faible, donc la diffusivité est élevée :

$$\alpha = \frac{\tau_{\mathrm{D}}}{\tau} \tag{2.49}$$

Où τ est le temps théorique (longueur du lit divisé par la vitesse du gaz). Quand α est infini, le lit de catalyseur acte comme un catalyseur non-poreux.

2.4.3 Éléments manquants sur les catalyseurs et la RTD

La porosité joue un rôle important dans l'exactitude et la répétabilité des résultats, principalement dans les réacteurs à lit fluidisé. Une méthodologie pourrait être développée pour augmenter le niveau de précision dans ce type de réacteur.

De plus, il est difficile de voir la ligne qui sépare l'influence de la RTD en fonction de la porosité. Les chercheurs comparent un catalyseur poreux et non poreux[77], mais aucune étude ne met en parallèle plusieurs catalyseurs de même dimension avec des porosités différentes. Il serait intéressant d'approfondir cette suggestion.

2.5 Simulation par CFD-DEM

L'article *Experimental methods in chemical engineering : Unresolved CFD-DEM* (Chapitre 7) présente une revue de littérature sur cette technique de simulation. Les équations mathématiques qui sont au cœur de la CFD-DEM sont présentées. Tout d'abord, la phase solide (DEM) est gouvernée par la seconde loi de mouvement de Newton. Le fluide (CFD) est guidé par les équations de Navier-Stokes moyenné en volume (VANS). Le couplage CFD-DEM se fait à l'aide des forces hydrodynamiques. Celles-ci sont : la force de traînée, les forces causées par la pression et le cisaillement, la force de Basset, la force de masse virtuelle et la portance. De plus, cette revue de littérature propose 2 exemples d'applications en génie chimique soit la simulation d'un réacteur à lit fluidisé et d'un mélange solide liquide. Finalement, les limitations et les incertitudes sur la CFD-DEM sont décrites[93].

2.5.1 La RTD et la simulation numérique

L'étude du temps de résidence à l'aide de la simulation numérique est de plus en plus présente dans la littérature. Les applications sont nombreuses telles que les mélangeurs/réacteurs à micro-canaux[19], les réacteurs à lit fluidisé[94,95], et les séchoirs[96]. L'avantage principal de la simulation numérique est qu'il est possible d'expérimenter plusieurs conditions d'opérations rapidement. Par contre, pour s'assurer de la robustesse des simulations, celles-ci doivent être comparer à des données expérimentales en provenance soit d'un laboratoire ou soit de la littérature. Lors de la simulation d'un réacteur à lit fluidisé, il existe deux grandes méthodes de résolutions : Eulérien-Eulérien ou Eulérien- Lagrangien.

Fluide Eulérien-Eulérien

La simulation Eulérien-Eulérien considère les deux phases gaz-solide ou liquide-solide comme des fluides en continu[97,98]. La mécanique des fluides numérique (CFD) est la méthode la plus fréquemment proposée pour la simulation de la RTD dans un réacteur à lit fluidisé[99]. En effet, l'avantage est que le nombre de particules pouvant être modélisé est dans l'intervalle de 10^9 à 10^{12} particules, ce qui est idéal pour des simulations à l'échelle d'ingénierie[100]. Par contre, il est primordial d'ajouter les équations de la théorie cinétique de l'écoulement

granulaire (modèle KTGF) pour simuler les interactions de la phase solide[97,101]. Il s'agit d'équations de fermeture pour modéliser les collisions particules-particules non idéales ainsi que la force de traînée gaz-particule. Cette série d'équations à résoudre comprise dans le modèle KTGF inclus[98,100] :

— La pression de la phase solide ;
— Le tenseur des contraintes visqueuses de la phase solide ;
— Le flux pseudo-Fourier d'énergie de fluctuation cinétique ;
— Le taux de dissipation dû à des collisions mutuelles inélastiques des particules ;
— La fonction de distribution radiale ;

De plus, en général, le modèle k-ϵ pour la turbulence est ajouté à la CFD[98]. Les équations de transport pour un système gaz-solide sont[97] :

$$\frac{\partial}{\partial t}(\alpha_{\mathrm{g}}\rho_{\mathrm{g}}k_{\mathrm{g}}) + (\vec{\boldsymbol{v}}_{\mathrm{g}} \cdot \nabla)(\alpha_{\mathrm{g}}\rho_{\mathrm{g}}k_{\mathrm{g}}) = \nabla \cdot \left[\alpha_{\mathrm{g}}\left(\mu_{\mathrm{g}} + \frac{\mu_{\mathrm{tu,g}}}{\sigma_{\mathrm{k,g}}}\right)\nabla k_{\mathrm{g}}\right] + \alpha_{\mathrm{g}}G_{\mathrm{k,g}} - \alpha_{\mathrm{g}}\rho_{\mathrm{g}}\varepsilon_{\mathrm{g}} \qquad (2.50)$$

$$\frac{\partial}{\partial t}(\alpha_{\mathrm{g}}\rho_{\mathrm{g}}\varepsilon_{\mathrm{g}}) + (\vec{\boldsymbol{v}}_{\mathrm{g}} \cdot \nabla)(\alpha_{\mathrm{g}}\rho_{\mathrm{g}}\varepsilon_{\mathrm{g}}) = \nabla \cdot \left[\alpha_{\mathrm{g}}\left(\mu_{\mathrm{g}} + \frac{\mu_{\mathrm{tu,g}}}{\sigma_{\text{”,g}}}\right)\nabla \varepsilon_{\mathrm{g}}\right] + \alpha_{\mathrm{g}}\frac{\varepsilon_{\mathrm{g}}}{k_{\mathrm{g}}}(y_1 G_{\mathrm{k,g}} - y_2\rho_{\mathrm{g}}\varepsilon_{\mathrm{g}}) \quad (2.51)$$

Où α_{g} est la fraction volumique de la phase gazeuse, ρ est la masse volumique, k est l'énergie cinétique par unité de masse, $\vec{\boldsymbol{v}}$ est la vitesse de la phase Eulérien en simulation CFD, μ est la viscosité, μ_{tu} est la viscosité turbulente, σ_{k} est le nombre de Prandtl pour l'énergie cinétique en turbulence, G_{k} est la production d'énergie cinétique en turbulence causée par le gradient de vitesse moyenne, ε est le taux de dissipation turbulent, σ_{e} est nombre de Prandtl pour le taux de dissipation en turbulence, y_1 et y_2 sont les fractions massiques. L'indice g représente la phase gazeuse.

Plusieurs recherches récentes appliquent la CFD pour simuler le temps de résidence dans les réacteurs à lit fluidisé (Tableau 2.8 et 2.9). Les systèmes à l'étude sont soit gaz-solide ou liquide-solide. Les traceurs choisis pour analyser la RTD sont soit dans la phase gazeuse, liquide ou solide. La différence majeure entre les simulations est le choix des équations pour modéliser la force de traînée (voir Chapitre 7 pour plus de détails) ainsi que la condition frontière au niveau du glissement des particules sur le mur. Le glissement peut être total, partiel ou non existant. La CFD est résolue principalement avec le logiciel ANSYS FLUENT.

Tableau 2.8 Exemple de simulation de la RTD dans des réacteurs à lit fluidisé par CFD – modèle 2 fluides eulérien-eulérien (partie 1)

Étude[ref]	Phase RTD / traceur	Réacteur	Modèle de traînée	Condition frontière[1]	Dimension	Logiciel
(1) Réacteur à lit fludisé gaz-solide[102]	Gazeuse He	Diamètre : 76 mm Hauteur : 1830 mm Catalyseur : FCC et bille de verre (155 µm	-	Aucun, partiel ou total	2D et 3D	FLUENT 6.3
(2) Réacteur à lit fluidisé gaz-solide injection par jet et étude des bulles[103]	Gazeuse CO_2	Diamètre : 0.3 m Hauteur : 1.0 m Hauteur lit : 0.4 m Catalyseur : bille de verre (460 à 700 µm)	Ergun Wen & Yu Koch & Hill	Gaz : aucun Solide : partiel	2D	CFX4.4 AEA Technology
(3) Réacteur à lit fluidisé gaz-solide en régime bulle[104]	Gazeuse	Diamètre : 0.1 m Hauteur : 0.65 m Hauteur lit : 0.4 m Solide : 150 µm	Gidaspow	Gaz : aucun Solide : partiel	3D	MFIX[2]
(4) Réacteur à lit fluidisé horizontal échelle industrielle[97]	solide	Solide : γ-Al_2O_3 (1.8 mm)	Gidaspow	Gaz et solide : aucun	3D	ANSYS FLUENT 6.1

[1] Conditions frontière du glissement sur le mur du réacteur

[2] MFIX : Multiphase Flow with Interphase Exchanges – code CFD du département américain de l'énergie (https ://www.mfix.org)

Tableau 2.9 Exemple de simulation de la RTD dans des réacteurs à lit fluidisé par CFD – modèle 2 fluides eulérien-eulérien (partie 2)

Étude[ref]	Phase RTD / traceur	Réacteur	Modèle de traînée	Condition frontière[1]	Dimension	Logiciel
(5) Réacteur à lit fluidisé inversé[98]	Gazeuse (CO2) Solide	Diamètre : 0.14 m Hauteur : 7 m Solide : 25 à 100 µm	Wen & Yu	-	2D	ANSYS FLUENT
(6) Lit fluidisé circulant (CFB)[70]	Solide FCC	Diamètre : 0.11 m Hauteur : 9 m Solide : 70 µm	EMMS[3]	total	2D	ANSYS FLUENT
(7) Réacteur à lit fluidisé solide-liquide[99]	Liquide	Diamètre : 100 mm Hauteur : 1400 mm Liquide : eau Solide : résine échangeur d'ions (0 36 à 0.72 mm) ou bille de verre (0 1 à 0.7 mm	Prandit & Joshi[4]	aucun	3D	ANSYS FLUENT Géométrie : Gambit 2.0.4

[1] Conditions frontière du glissement sur le mur du réacteur
[3] Modèle de traînée : energy minimization multi scale[105]
[4] Modèle basé sur les bilans d'énergie[106,107]

Fluide Eulérien-Lagrangien

Le second type de simulation est Eulérien-Lagrangien. Dans ce cas-ci, comme la CFD, la phase gazeuse est en continu. La différence est au niveau de la phase solide. En effet, chaque particule est modélisée individuellement et suit la seconde loi de mouvement de Newton [98,108]. Ainsi, il est possible d'étudier en profondeur la phase solide et la phase gazeuse ou liquide et toutes les interactions qui en découlent [101]. De plus, aucune équation supplémentaire tel que le modèle KTGF n'est nécessaire [100]. Effectivement, les collisions particules-particules et particules–mur sont déjà intégrées lors de la résolution [109]. La CFD-DEM est la méthode la plus présente dans la littérature pour les simulations Eulérien-Lagrangien. La partie CFD se résous habituellement sur FLUENT, tandis que l'aspect DEM est codé en langage C et est incorporé à la CFD [110].

Par contre, la CFD-DEM demande beaucoup de temps de calcul pour simuler des systèmes complexes. C'est particulièrement le cas pour les réacteurs à lit fluidisé où le nombre de particules est très élevé [98]. Dans la littérature, seulement de petits systèmes sont à l'étude (échelle micro) [99]. En effet, la limite est dans l'ordre de 10^6 particules. Donc, pour des simulations à l'échelle industrielle, cette méthode est inappropriée [100].

L'étude du temps de résidence dans les réacteurs à lit fluidisé simulé par la CFD-DEM est très peu présente dans la littérature. Zhao *et al.* ont simulé, en 2D, un réacteur à lit fluidisé de type *riser/downer* de 2 à 6 m de hauteur et 10 cm de largeur. Le modèle de DiFelice a été choisi pour la force de traînée. La RTD a été faite sur les particules ayant un diamètre de 500 à 520 µm [110].

Un second exemple d'application de la simulation CFD-DEM pour la RTD est l'étude de Luo *et al.* sur un réacteur à lit fluidisé circulant (CFB). Il a simulé un réacteur de 1.2 m de hauteur et 0.065 m de diamètre comprenant 300 000 particules de 1.6 mm de diamètre – Geldart groupe D. L'analyse RTD a été faite sur la phase solide [108].

2.5.2 Éléments manquants dans la littérature

La simulation par CFD-DEM de la RTD dans les réacteurs à lit fluidisé est très peu étudiée dans la littérature en raison du temps gigantesque nécessaire pour la résolution. Plusieurs simplifications sont faites pour diminuer le temps de calcul. Par exemple, l'étude est faite sur un plan 2D au lieu de 3D [70,100]. Or, il est connu que le 3D est plus précis, car moins d'hypothèses simplificatrices sont faites [108]. De plus, pour simplifier la RTD par CFD-DEM, l'étude est faite avec des particules ayant une grande taille, un faible nombre de particules ou un temps réel de la simulation très petite [70]. Toutes ces simplifications font dévier le modèle

de la réalité.

Malgré le fait que plusieurs réacteurs à lit fluidisé ont été simulés par CFD-DEM[111,112,113], peu de recherche a intégré la RTD. Certains ont étudié le temps de résidence de la phase solide[94,108,110], mais aucune recherche n'a été faite au niveau de l'hydrodynamique de la phase gazeuse.

CHAPITRE 3 DÉMARCHE DE L'ENSEMBLE DU TRAVAIL DE RECHERCHE ET ORGANISATION GÉNÉRALE DU DOCUMENT

Cette thèse comporte 5 articles, dont 3 revues de littérature sur les thèmes importants impliqués dans cette recherche – les réacteurs à lit fluidisé, la distribution du temps de résidence et la CFD-DEM. Le 4^{e} article est basé uniquement sur des essais expérimentaux et porte sur l'étude des traceurs gazeux lors de la RTD. Le 5^{e} article est un mélange entre l'expérimentation et la modélisation de la RTD en présence d'adsorption. Finalement, le dernier chapitre est consacré aux résultats préliminaires de la CFD-DEM (Figure 3.1).

3.1 Rappel des objectifs

Le premier objectif de ce projet de doctorat est de standardiser la méthodologie pour les études RTD. Puis, de développer un modèle RTD qui inclue l'adsorption. Finalement, le dernier objectif est d'explorer une nouvelle approche pour l'étude du temps de résidence dans les réacteurs à lit fluidisé — la simulation par CFD-DEM. Les sous-objectifs ainsi que les articles qui y sont reliés sont présentés dans le tableau 3.1.

3.2 Revue de littérature sur la fluidisation

L'étude de la distribution du temps de résidence (RTD) a été analysée dans un réacteur à lit fluidisé de 8 mm de diamètre et 36 cm d'hauteur. Ainsi, la première étape de cette recherche a été de comprendre les subtilités de ce type de réacteur. L'article, *Experimental Methods for Chemical Engineering : Reactors – Fluidized Beds* (Annexe A) a permis d'approfondir sur les régimes de fluidisation. Leur influence sur la RTD a été analysée dans le second article.

Puis, nous avons établi les normes sur les caractéristiques essentielles qui doivent être présentées lors d'études impliquant les poudres. Tous les articles subséquents présentent cette liste de caractérisation : la vitesse minimale de fluidisation (U_{mf}), les masses volumiques : apparente ou bulk (ρ_{b}), particule (ρ_{p}) et squelettique (ρ_{sk}), la fraction de vide (ϵ_{v}), le ratio de Hausner (H_{r}), l'angle de repos (θ_{ang}), le diamètre des particules (d_{10}, d_{50} et d_{90}), la sphéricité (ϕ) et les résultats du BET (aire de surface, volume des pores et diamètre des pores).

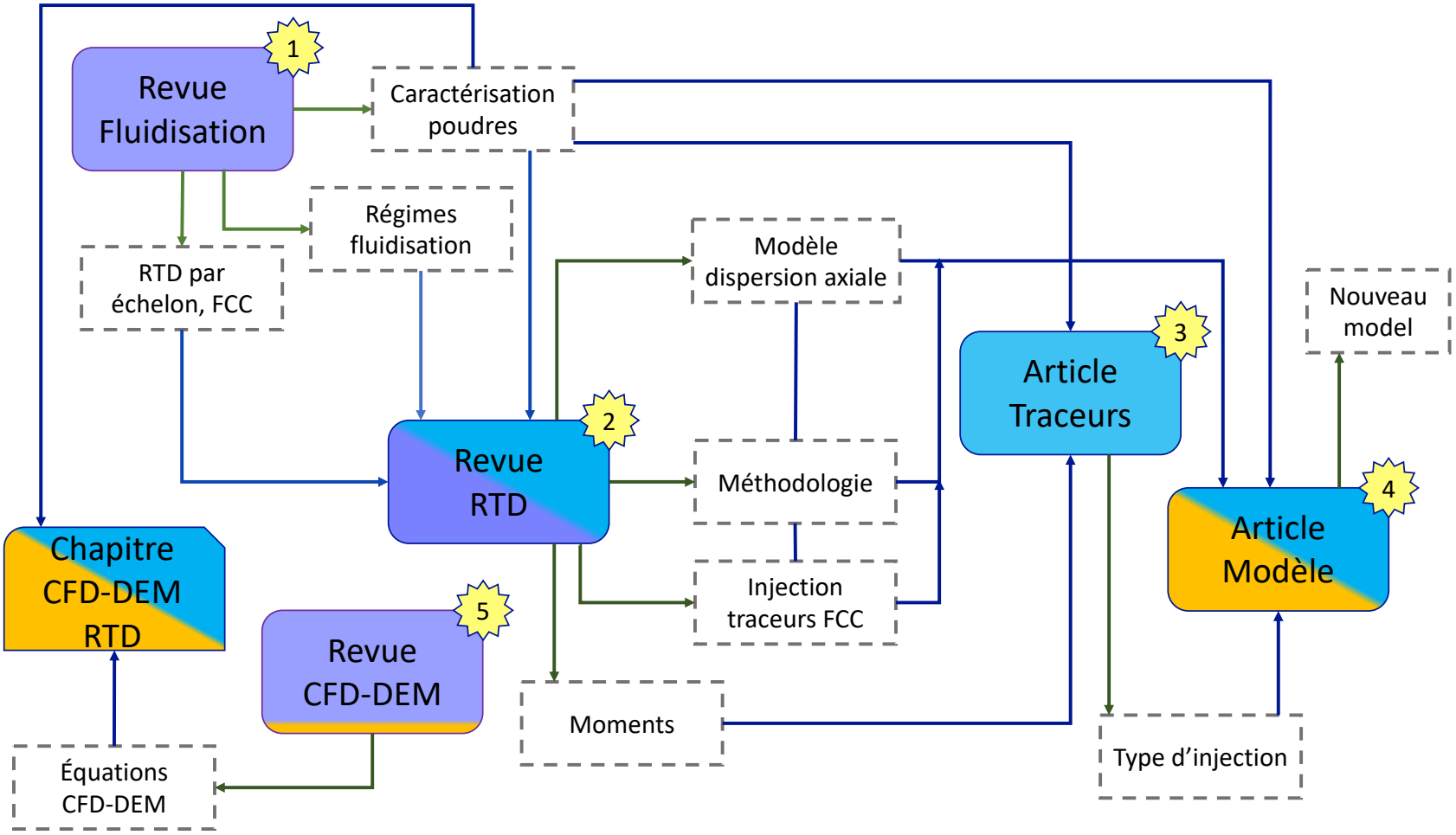

Figure 3.1 Démarche de la thèse. Chaque boîte de couleurs représente un article qui est numéroté en ordre chronologique. Le mauve représente un article de revue de littérature, le bleu représente des articles où des données expérimentales ont été recueillies et l'orange représente les modèles ou simulations. Les flèches vertes sont des résultats obtenus dans l'article et les flèches bleues sont des résultats précédents qui ont été appliqués dans l'article.

Tableau 3.1 Accomplissement des sous-objectifs par article

Objectifs / sous-objectifs	Article relié[1]
1 Développer une méthodologie précise pour la RTD dans un réacteur à lit fluidisé	1-2-3
1.1 Analyser l'effet du spectromètre de masse sur la RTD	2
1.2 Analyser la répétabilité des études RTD	2
1.3 Analyser la résolution par le modèle de dispersion axiale	2-4
1.4 Analyser la configuration des valves et les types d'injection	2-3
1.5 Analyser l'effet des traceurs sur la RTD	2-3-4
1.6 Analyser l'effet de la porosité sur la RTD	2-3-4
2 Développer un modèle mathématique pour la RTD qui inclut l'adsorption	4
2.1 Développer un modèle basé sur les bilans molaires	4
2.2 Résoudre simultanément plusieurs traceurs gazeux	4
3 Explorer la CFD-DEM	5 - Chapitre 8
3.1 Faire une revue de littérature	5
3.2 Construire un micro-réacteur de 8 mm de diamètre 36 cm cm de hauteur	Chapitre 8
3.3 Insérer des particules dans le micro-réacteur	Chapitre 8

[1]Article 1 : *Experimental Methods for Chemical Engineering : Reactors – Fluidized Beds*,
Article 2 : *Experimental Methods for Chemical Engineering : Residence Time Distribution — RTD*,
Article 3 : *Residence time distribution in fludized beds : diffusion, dispersion, adsorption*,
Article 4 :*Fluidized bed hydrodynamic modelling of CO_2 in syngas : Distorted RTD curves due to adsorption on FCC*,
Article 5 : *Experimental Methods for Chemical Engineering : Unresolved CFD-DEM*

Certaines techniques de caractérisation annexe au réacteur à lit fluidisé ont été expliquées telles que les mesures de pression et la CFD. Celles-ci ont été par la suite appliquées à ce projet.

Finalement, l'embryon de l'entièreté de ce projet réside dans cet article, plus précisément, dans la section de l'étude hydrodynamique de la phase gazeuse d'un réacteur à lit fluidisé. Nous avons comparé la RTD d'une injection par échelon entre 2 types d'entrées de gaz (grille ou pulvérisation). Les difficultés encourues (choix de la fréquence du MS, traceur, type d'injection, volume mort) pour accomplir les expériences RTD, nous ont motivés à approfondir et à développer une méthodologie pour cette technique (2^{e} article).

3.3 Revue de littérature et standardisation de la méthodologie de la RTD

Lors des essais RTD pour l'article de revue de littérature sur la fluidisation, plusieurs questionnements ont émergé :

1. Comment choisir le traceur ? Sa quantité ? Et sa concentration ?
2. Quand faut-il tourner la valve ?
3. Le type d'injection : échelon ou *pulse* ? Et le type de valve ?
4. Quel est le temps total de l'essai ?
5. Quelle est la fréquence du spectromètre de masse ?
6. Quelles sont les distances avant et après le lit de catalyseur ?
7. Quel catalyseur choisir ? La quantité ?
8. Quelle température choisir ?
9. Quels débits choisir ? (fonction de U_{mf})
10. Un ou deux MS ? À l'entrée et à la sortie ?
11. Quel modèle pour l'analyse des données ? Modèle de dispersion axiale ? Condition frontière ?

Toutes ces questions nous ont étonnés, car ces essais sont, au premier regard, d'une simplicité : un traceur est injecté dans le réacteur et la concentration de celui-ci est mesurée dans le temps. C'est alors qu'une standardisation de la méthode RTD a été développé dans l'article : *Experimental Methods in Chemical Engineering : Residence time distribution – RTD* (Chapitre 4).

Tout d'abord, le modèle de dispersion axiale avec des conditions frontière fermé-ouvert a été choisi. Celui-ci est appliqué dans tous les articles subséquents et est défini comme le modèle de référence d'un comportement idéal *plug flow*. À cela s'ajoute la définition des trois moments : le temps de résidence moyen ($\bar{t}$), la variance (σ^2), et l'asymétrie (s^3). Ces variables sont toujours omniprésentes dans les expériences RTD. La démarche de résolution avec le modèle de dispersion axiale se retrouve en annexe (Annexe B).

Malgré plusieurs recherches sur la méthodologie, plusieurs questionnements étaient sans réponse. Ainsi, plus de 500 expériences ont été réalisées pour définir une méthodologie précise. L'étude a porté sur la configuration de la valve, la minimisation des volumes morts, la répétabilité des résultats, la fréquence d'échantillonnage, et sur les paramètres du modèle. Nous avons présenté une liste des contributions aux erreurs lors d'expériences RTD, ainsi qu'une procédure détaillée étape par étape pour une injection *pulse* et par échelon. Cette méthodologie a été la base pour la suite.

La dernière section de cette revue porte sur l'injection simultanée de plusieurs traceurs : CO_2, H_2, CH_4 et CO. L'expérience a lieu dans un tube vide et rempli de FCC poreux. À notre étonnement, plusieurs déviations du modèle idéal ont été observées portant à croire la présence de diffusion et d'adsorption du CO_2. À la vue des résultats, encore plus d'interrogations sur le choix du traceur se sont posées. C'est ainsi que l'article sur les traceurs et l'article du modèle RTD ont été développés.

3.4 Article sur les traceurs simultanés

L'article *Residence time distribution in fludized beds : diffusion, dispersion, adsorption* (Chapitre 5) contient les résultats de plus de 300 expériences RTD analysées avec le modèle de dispersion axiale pour détecter les anomalies. Tout d'abord, certains aspects de la méthodologie ont été mis de l'avant. Il s'agit d'une analyse du réacteur vide et une analyse sur le type d'injection. Il a été conclu que seule l'injection de type *pulse* était adéquate pour détecter les anomalies dans la RTD (Chapitre 4). À partir de cette découverte, seulement ce type d'injection a été employé.

Cet article approfondit l'effet de la porosité, donc le choix du catalyseur, et l'effet des traceurs gazeux sur la RTD. Cinq poudres (VPOP, VPPC, VPPE, FCC et sable) ainsi que sept gaz (Kr, CO_2, O_2, CO, CH_4, He et H_2) ont été comparés.

La dernière section démontre l'effet d'adsorption du CO_2 par le FCC lorsqu'un mélange de gaz (CO_2, CO, H_2 et CH_4) est injecté. De plus, l'hydrogène, ayant un coefficient de diffusion nettement plus élevée, quitte le réacteur 15 s en avance. Le modèle de dispersion axiale ne s'adapte pas à cette situation. Ainsi, le modèle ne concorde pas avec les données ($R^2 = 0.92$ pour le CO_2). C'est pour cette raison qu'un modèle, basé sur les bilans de matière, a été développé. L'article suivant présente ce nouveau modèle pour les RTDs complexes.

3.5 Article sur le modèle RTD

L'article *Fluidized bed hydrodynamic modelling of CO_2 in syngas : Distorted RTD curves due to adsorption on FCC* (Chapitre 6) a pour objectif de développer un modèle qui s'adaptera lorsque plusieurs traceurs gazeux sont injectés simultanément et qu'il y a présence d'adsorption. Tout d'abord, les résultats expérimentaux sont présentés et le modèle de dispersion axiale est appliqué. Ainsi, la problématique est visible.

Le nouveau modèle est basé sur : (1) un bilan molaire de la phase gazeuse, (2) un bilan molaire sur le volume des pores, et (3) un bilan molaire des espèces adsorbées. Les 4 traceurs

sont dépendants les uns des autres par leur débit. Ce modèle reflète cette dépendance en résolvant simultanément trois des quatre courbes RTDs. Le code Fortran du nouveau modèle se retrouve en Annexe (Annexe C).

3.6 Revue de littérature CFD-DEM

Jusqu'à présent, les expériences RTDs ont été faites en laboratoire. Un point de vue différent serait intéressé pour pouvoir comparer nos résultats. C'est pour cette raison que l'approche par la simulation CFD-DEM a été choisi.

La troisième revue de littérature est : *Experimental Methods in Chemical Engineering : Unresolved CFD-DEM* (Chapitre 7). Cet article a pour objectif de comprendre les équations qui sont impliquées dans ce type de simulation. Il inclut les équations qui gouvernent la phase solide (DEM), les équations qui gouvernent le fluide (CFD), le couplage CFD-DEM (les forces hydrodynamiques), les applications en génie chimique, les incertitudes et les limitations de la technique. Il s'agit d'une introduction pour tous ceux qui débutent en simulation par CFD-DEM.

3.7 Simulation d'expérience RTD par CFD-DEM

Ce dernier chapitre (Chapitre 8) débute la simulation par CFD-DEM d'un réacteur à lit fluidisé ayant les mêmes dimensions que celui des essais RTDs fait en laboratoire. Ainsi, l'objectif final est de simuler les RTDs avec différents débits et poudres. L'avantage de la simulation comparé à l'expérimentation est qu'une fois le montage simulé, il est facile de changer les conditions d'opérations et de voir les résultats. Aussi, la mise à l'échelle est grandement simplifiée.

Les résultats préliminaires sur la simulation du réacteur à lit fluidisé sont présentés. L'objectif ultime étant la publication des résultats en comparant la simulation CFD-DEM avec l'expérimentation pour le FCC et le sable.

CHAPITRE 4 ARTICLE 1 : EXPERIMENTAL METHODS IN CHEMICAL ENGINEERING : RESIDENCE TIME DISTRIBUTION - RTD

Ariane Bérard, Bruno Blais, Gregory S. Patience

Journal : The Canadian Journal of Chemical Engineering

reçu : 24 septembre 2019 **revisé :** 26 novembre 2019 **accepté :** 29 novembre 2019

4.1 Abstract

Reactor performance, solids-(gas)-mixing, flow through porous media, distillation columns or through granulators improve as the fluid dynamics of the system approaches ideal plug flow. The residence time distribution is a diagnostic measure of how close fluid flow approaches ideal conditions. The technique introduces a step change to the inlet concentration—a Dirac-δ function, Heaviside step function, or a rectangular pulse (bolus)—while a high frequency detector monitors the concentration along the vessel and/or at the exit. The effluent concentration profile spreads due to the variance introduced by the form of the input pulse, the lines leading to the vessel and at the exit, the detector response, and the system. We quantify how much each of these contribute to the overall variance in a fluidized bed with 9 g of fluid cracking catalyst in 8 mm diameter quartz tubes. The injection variance is lowest for a GC sample loop configuration, compared to a 3-way valve or 4-way valve geometry.

RTD measurements detect bypassing due to dead zones in vessels and the axial-dispersion model and continuous stirred-tank model to characterize deviation from plug flow. However, when the contribution to variance from the ancillary lines and detector is large compared to the system, the uncertainty in the model parameters is high. Research on RTD fundamentals concentrate on boundary conditions while, here, we focus on experimental errors : mechanical, physicochemical mathematical, and instrumental.

keywords : residence time distribution, axial-dispersion model, boundary conditions, tracer, backmixing

4.2 Introduction

The residence time distribution (RTD) of a tracer injected into a flowing stream identifies non-homogeneities like channeling, dispersion, and dead volumes. Inert, reactive, and absorbing tracers follow the path of the fluid through the system and as they leave the environment,

detectors monitor their concentration. Mass spectrometry, infrared, and thermal conductivity detectors (TCD) are common techniques to follow gas concentration.[21,23,77,114]. For liquid phase applications, NaCl and KCl solutions are good tracers particularly with conductivity detectors.[8,20,69,115,116,117,118] A second option is a colorful dye like blue indigo carmine that UV-Vis spectrophotometers and high speed cameras detect.[16,19,119] Irradiating solids and detecting the gamma ray emission or bremsstrahlung radiation with scintillating NaI detectors is the most effective method for the solids phase[120,121,122] Other techniques for solids include injecting salt or other sorbents[123,124,125] and followed by sampling at different points in the reactor and fluorescent[126] and ferromagnetic particles[127,128]

We first evaluate the deviation of the fluid dynamics from ideal plug flow—a system for which all elements of the fluid remain in the vessel for the same amount time and travel in parallel paths with constraining walls.[15] Chemical engineers develop hydrodynamic models based on the tracer profile and then apply them in reactor models to characterize the reaction rates[115] identify characteristic mixing phenomena for design, optimization.[16,70,129] Industrial researchers will be able to control and predict particle mixing as well as compare different options to maximize the profitability of the process and minimize waste. Moreover, combined with chemical kinetics, RTD analysis predicts chemical reaction conversion.[16] Researchers apply RTD analysis to fixed and fluidized bed reactors, two phases stirred tanks, heat exchangers, distillation and absorption columns, chromatography columns, and trickle bed reactors.[9]

MacMullin and Weber (1935) pioneered RTD analysis[6] and it became more prevalent in the literature after seminal work by Lapidus and Amundson (1952)[11] who derived the one-dimensional axial dispersion model with an open-closed boundary condition, Danckwerts (1953)[24] who proposed a modified inlet boundary condition including dispersion at the interface, and a Taylor series (1954).[130] Danckwerts[24] specifically concentrated on describing the impact of non-ideal mixing in chemical reactors and examined continuous, sinusoidal, instantaneous and step pulses, and other or other cycling inputs. He developed the F-curve for step injection and C-curve for a pulse. Levenspiel and Smith (1957) continued this work and developed models for open-open boundary conditions.[75] In the same year, Levenspiel associated $\mathcal{D}/uZ$ (Pe^{-1}, the inverse of the Peclet number) with the variance and the C-curve.[75] In 1958, Van der Laan was the first to apply numerical methods to calculate the mean residence time and the variance for closed-closed boundary conditions.[131] Voncken et al. (1964) studied non-ideal reactors with recirculation and included axial dispersion.[132] Many years later, in 1996, Levenspiel focused on open-closed and closed-open boundary conditions proposed equations and curves for these systems.[33]

This mini-review is among a series of articles that *Can. J. Chem. Eng.* has published to des-

cribe experimental methods to students, practicing chemical engineers and researchers not specialized in the field.[133] Here, we introduce the RTD theory, describe the applications, and concentrate on the details of conducting the tests quantitatively. Rather than the mathematics of the boundary conditions, we demonstrate experimentally how the RTD changes with injection configuration, and recommend precise procedures to conduct the experiments.

4.3 Theory

Gas chromatographs (GC) rely on the principles of residence time distribution and inject mixtures of compounds that separate based on their affinity to polar and/or non-polar compounds in packed beds and capillary tubes (stationary phase) with diameters as little as 0.1 µm and over 100 m long. Detectors at the exit of the columns record a signal with respect to time and we compare the peak position with respect to the residence time of a compound that has little or no affinity to the column. The shape of these peaks depend on eddy diffusion, longitudinal diffusion, and mass transfer between the mobile phase and stationary phase.[134] Residence time distribution measurements to study hydrodynamics of vessels generally rely on non-adsorbing tracers with a pulse input that injects a known amount of tracer for a time shorter time than the vessel residence time, like GCs.[7,15] This technique is fast, direct, and the small quantity of tracer identifies non-standard behavior that becomes clear in a graph. An instantaneous injection pulse is ideal and it is best to minimize residence time between the injector and the entrance of the reactor and the reactor effluent and detector.[9,15] If the pulse injection is narrow compared to the residence time distribution, we approximate it as a Dirac $\delta-$pulse.[116] A step injection pulse introduces a tracer instantaneously and continuously at $t = 0$. The dirac $\delta-$pulse is more challenging to achieve but the mathematics are easier to manipulate.[15]

4.3.1 Curves

Three curves characterize the behaviour of the vessel fluid dynamics and we identify stagnancy, channeling, or plug flow tendencies based on their shape.[19] The C-curve plots the concentration of the tracer versus time. The residence time distribution function $E(t)$ represents the time that the tracer fluid stays in the vessel.[15] A narrow $E(t)$ distribution indicates that all tracer remain in the vessel approximately the same time :[15,20,119]

$$E(t) = \frac{QC(t)}{N_0} = \frac{C(t)}{\int_0^\infty C(t)\,\mathrm{d}t} = \frac{2}{\sigma\sqrt{\pi}} \exp - \left[\frac{(t+\bar{t})^2}{\sigma^2}\right] \tag{4.1}$$

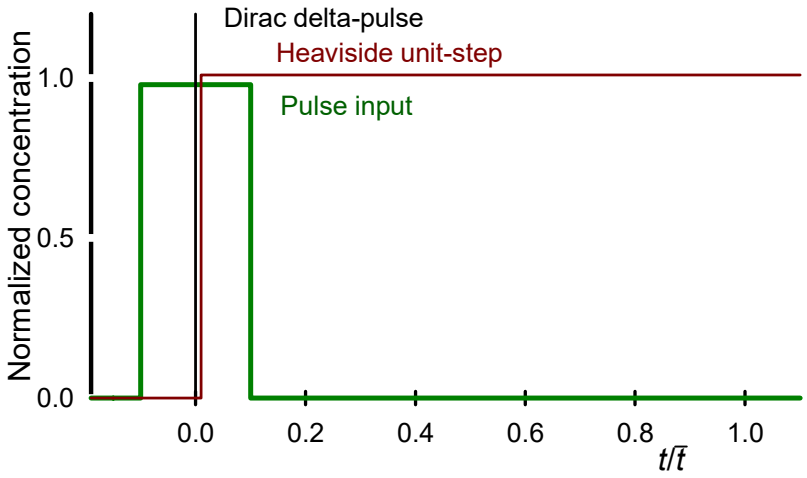

Figure 4.1 Input injection functions : The dirac *delta*−pulse is infinite at time equals zero, while the heaviside (unit) step function takes a value of 1 at $t = 0$, and the ideal pulse injection takes a value of 1 between $-\Delta t < 0 < +\Delta t$. In ideal plug flow, the peaks will emerge with the identical input at the mean residence time $t = \bar{t}$ $(t/\bar{t} = 1)$.

Where Q is the volumetric flow rate, $C(t)$ is the concentration of the tracer, N_0 is the moles of tracer injected in the reactor, $\bar{t}$ is the mean residence time, and σ^2 is the variance. The denominator represents the area under the C-curve. $E(t)$ is the probability that a fluid element (tracer) that enters the reactor at $t = 0$ leaves the reactor at the time t and :[20]

$$\int_0^\infty E(t)\,\mathrm{d}t = 1 \tag{4.2}$$

The RTD curve is analogous to the E-curve and the area under the curve at any time represents the fraction of tracer that has left the vessel up to that point.

The integral of the E-curve gives the cumulative distribution function, $F(t)$—F-curve. It represents the fraction of the tracer is left in the vessel less than t :[15]

$$F(t) = \int_0^t E(t)\,\mathrm{d}t \tag{4.3}$$

We apply this curve mainly to the Heaviside unit-step function. The first derivative with respect to time of the Heaviside unit step function equals the Dirac δ−pulse.

Plotting the curves helps find anomalies in the system such as double peaks, unsymmetrical distributions, or long tails.[33] The first, second, and third moments quantify the extent of these anomalies and mixing performance. The first moment is the mean of the residence

time :

$$\bar{t} = \sum_{t=0}^{\infty} tE(t)\Delta t \tag{4.4}$$

$$= \frac{\int_0^\infty tE(t)\,\mathrm{d}t}{\int_0^\infty E(t)\,\mathrm{d}t} = \frac{\int_0^\infty tC\,\mathrm{d}t}{\int_0^\infty C\,\mathrm{d}t} \tag{4.5}$$

$$= \frac{\sum t_i C_i \Delta t_i}{\sum C_i \Delta t_i} \tag{4.6}$$

The spread of the residence time, S, is a function of the time to recover 10 % ($t_{0.1}$), 50 % ($t_{0.5}$), and 90 % ($t_{0.9}$) of the injected tracer :[118]

$$S = \frac{t_{0.9} - t_{0.1}}{t_{0.5}} \tag{4.7}$$

The second moment, variance (σ^2), represents the spread of the curve and how far the fluid elements deviate from plug flow.[69] Larger value corresponds to a higher amplitude of the distribution and thereby an elevated deviation from plug flow,[7] while lower values signify less intermixing effect between fluid elements :[119]

$$\sigma^2 = \frac{\int_0^\infty t^2 E(t)\,\mathrm{d}t}{\int_0^\infty E(t)\,\mathrm{d}t} - \bar{t}^2 \tag{4.8}$$

$$= \int_0^\infty (t-\bar{t})^2 E(t)\,\mathrm{d}t = \frac{\int_0^\infty (t-\bar{t})^2 C\,\mathrm{d}t}{\int_0^\infty C\,\mathrm{d}t} \tag{4.9}$$

$$\cong \frac{\sum t_i^2 C_i \Delta t_i}{\sum C_i \Delta t_i} - \bar{t}^2 \tag{4.10}$$

The third moment, skewness (s^3), measures the degree of asymmetry of the probability distribution function :[9,135]

$$s^3 = \int_0^\infty (t-\bar{t})^3 E(t)\,\mathrm{d}t = \frac{\int_0^\infty (t-\tau)^3 E(t)\,\mathrm{d}t}{\sigma^{3/2}} \tag{4.11}$$

It represents the non-ideality of the mixing system and depends on the degree of positivity or negativity. It detects bypassing and a high degree of back-mixing. A positive value means that the tracer is by-passing the mixing zone thus traveling faster than the bulk flow. The distribution curve for a pulse injection will have a long tail. A negative value indicates that the tracer is held back in the system, sticking to the wall and segregation, are examples. When most of the tracer moves slower than the average the distribution will show a tail on the left side.[9]

Another variable applied to compare several RTD experiments together is the coefficient of variation, C_{v}, that measures the relative spreading of the distribution $E(t)$:[69,135]

$$C_{\mathrm{v}} = \frac{\sigma}{\bar{t}} \tag{4.12}$$

Low values of C_{v} means that the residence time distribution is narrower thus a better mixing quality :[19,117]

1. $C_v = 0$, complete distributive mixing[69], thus near 0 flow state tends to a perfectly mixed flow.[70]
2. $C_v = 1$, total segregation[69], thus near 1 the flow state is close to plug flow.[70]

We compare the mean residence time with the theoretical residence time (τ) to identify dead volumes and short-circuiting :[7,69]

$$\tau = \frac{V_m}{Q} \tag{4.13}$$

where, $V_m = V_{\mathrm{empty}} - V_{\mathrm{internals}}$ (m^3) and Q is the volumetric flow rate ($\mathrm{m}^3\,\mathrm{s}^{-1}$). Thus, when $\bar{t} > \tau$, the fluid is possibly bypassing or channelling.[7]

4.3.2 Axial Dispersion model

The one-dimensional axial dispersion model and the n tanks-in-series model (n_{CSTR}) are two approaches to better quantify how the prevailing hydrodynamic regime. The dispersion model is analogous Fick's law. When the flow regime is turbulent, the radial variation of the concentration and the velocity are negligible. The model considers the flow inside the vessel to be plug flow and it superimposes a certain degree of back-mixing—axial diffusion/dispersion—that is independent of the position inside the vessel :[69,70,71]

$$\frac{\partial C}{\partial t} + u\frac{\partial C}{\partial z} = \mathcal{D}\frac{\partial^2 C}{\partial z^2} \tag{4.14}$$

where, C is the tracer concentration, u is the tracer convective velocity (uniform radially) and $\mathcal{D}$ is the axial dispersion coefficient. In non-dimensional form, we divide through by u/Z, where Z is a characteristic system length :

$$\frac{\partial C}{\partial \theta} + \frac{\partial C}{\partial \xi} = \frac{1}{N_{\mathrm{Pe}}}\frac{\partial^2 C}{\partial \xi^2} \tag{4.15}$$

where $\theta = tu/Z$ (non-dimensional time), $\xi = z/Z$, (non-dimensional length), and $N_{\mathrm{Pe}} = uZ/\mathcal{D}$, the dimensionless Peclet number, which is the ratio of the flow convection to the flow dispersion. The Peclet number is linked to the moments by :[75]

$$N_{\mathrm{Pe}} = \frac{8}{\sqrt{8\sigma^2/\bar{t}^2 + 1} - 1} \tag{4.16}$$

For large deviation from plug flow :[33]

$$\frac{\sigma^2}{\bar{t}^2} \approx \frac{N_{\mathrm{Pe}}}{2} \tag{4.17}$$

For moderate and low degrees of dispersion, we solve the analytical equation to calculate the Peclet number.[70] The system is close to plug flow when $N_{\mathrm{Pe}} > 50$[136] but even values in the vicinity of 20 are good approximations to most reactor systems, particularly when conversion is less than 90 %.[22] For small deviations from plug flow, $N_{\mathrm{Pe}} > 100$, the analytical solution is :[33]

$$E(t) = \sqrt{\frac{u^3}{4\pi\mathcal{D}Z}} \exp\left[-\frac{(Z-ut)^2}{4\mathcal{D}Z/u}\right] \tag{4.18}$$

and in dimensionless form :

$$E_\theta = \frac{1}{\sqrt{4\pi/N_{\mathrm{Pe}}}} \exp\left[-\frac{N_{\mathrm{Pe}}(1-\theta)^2}{4}\right] \tag{4.19}$$

The analytic solution for the mean residence and the variance are :

$$\bar{t} = \frac{V}{Q} = \frac{Z}{u} \tag{4.20}$$

$$\sigma^2 = 2\left(\frac{\mathcal{D}Z}{u^3}\right) \tag{4.21}$$

4.3.3 Boundary conditions

When the deviation from plug flow is large ($N_{\mathrm{Pe}} < 100$), we must consider the boundary conditions to solve the axial dispersion model : (1) closed-closed, (2) open-open, (3) closed-open, (4) open-closed, (5) the Danckwerts boundary condition (mass continuity).[24] An open boundary condition considers the flow undisturbed as it passes the boundary of the system. In opposite, a closed boundary condition assumes plug flow at the outside limit of the vessel (Figure 4.2).[33]

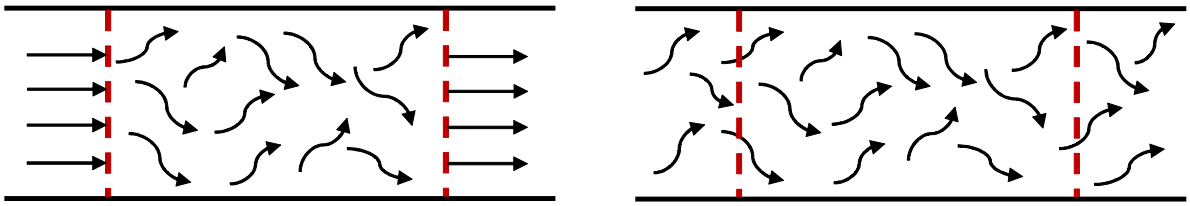

(a) (b)

Figure 4.2 Type of boundary conditions. (a) Closed-closed. Outside the boundaries it is plug-flow while inside the system the flow is disturbed. (b) Open-open. The flow is undisturbed as it passes the entrance and exit of the system.[33]

Closed-closed boundary conditions

The Danckwerts initial and boundary conditions for a closed-closed system are :[24]

$$C_{0,\xi} = 0, 0 \leq \xi \leq 1, t \geq 0 \tag{4.22}$$

$$C_{\tau,0} = C|_{\xi=0} - \frac{1}{Pe}\frac{\partial C}{\partial \xi}\bigg|_{\xi=0}, \xi = 0 \tag{4.23}$$

$$\frac{\mathrm{d}C}{\mathrm{d}\xi} = 0, \xi = 1 \tag{4.24}$$

The analytic expression for the E-curve of a closed vessel yet to bed derived.[33] However, the solution for the mean residence time ($\bar{t}_{\mathrm{CC}}$) and the variance ($\sigma^2_{\zeta,\mathrm{CC}}$) are :[20,33]

$$\bar{t}_{\mathrm{CC}} = t_{\mathrm{m,CC}} = \frac{V}{Q} \tag{4.25}$$

$$\sigma^2_{\zeta,\mathrm{CC}} = \frac{2}{N_{\mathrm{Pe}}} - \frac{2}{N^2_{\mathrm{Pe}}}\left[1 - e^{-N_{\mathrm{Pe}}}\right] \tag{4.26}$$

Closed-open boundary conditions

The initial and boundary conditions for a closed-open system are :[11,71]

$$C_{0,\xi} = 0, 0 \leq \xi \leq 1 \tag{4.27}$$

$$C_{\tau,0} = \rho_0, \tau > 0 \tag{4.28}$$

$$\frac{\mathrm{d}C_{\tau,1}}{\mathrm{d}\xi} = 0, \tau > 0 \tag{4.29}$$

The exact dimensionless solution for the concentration, $G(\theta) = C_{\theta,\xi}/C_0$, with respect to dimensionless time, θ, and at the exit, $\xi = 1$, is :[71]

$$G(\theta) = \frac{1}{2}\left[\mathrm{erfc}\sqrt{\frac{N_{\mathrm{Pe}}}{4\theta}(1-\theta)} + \mathrm{e}^{N_{\mathrm{Pe}}}\mathrm{erfc}\sqrt{\frac{N_{\mathrm{Pe}}}{4\theta}(1+\theta)}\right] \tag{4.30}$$

In the case of a bolus injection, introducing a defined volume of tracer gas such as through a sample loop in a GC,

$$\frac{C_{t,\xi}}{C_0} = G(\theta) - H(\theta - \tau_{\mathrm{bolus}})G(\theta - \tau_{\mathrm{bolus}}) \tag{4.31}$$

where $H(\tau_{\mathrm{bolus}}) = 1$, $\tau_{\mathrm{bolus}} > \frac{V_{\mathrm{loop}}}{Q}$ (Heaviside step function), V_{loop} is the volume of the sample, and Q is the volumetric flow rate.[71]

Open-open boundary conditions

The expression for the E-curve for an open-open system is valid for a long pipes :[70,75]

$$E_{\mathrm{OO}}(t) = \frac{u}{\sqrt{4\pi\mathcal{D}t}}\exp\left[-\frac{(Z-ut)^2}{4\mathcal{D}t}\right] \tag{4.32}$$

$$= \frac{1}{\bar{t}}\sqrt{\frac{N_{\mathrm{Pe}}\cdot\bar{t}}{4\pi t}}\exp\left[-N_{\mathrm{Pe}}\frac{(t-\bar{t})^2}{4t}\right] \tag{4.33}$$

The dimensionless form is ;

$$E_{\theta,\mathrm{OO}} = \frac{1}{\sqrt{4\pi\theta}/N_{\mathrm{Pe}}}\exp\left[\frac{N_{\mathrm{Pe}}(1-\theta)^2}{4\theta}\right] \tag{4.34}$$

In this case, $\bar{t}$ is not equivalent to t_m, thus :[70]

$$\bar{t} = \frac{Z}{u} = \frac{t_m}{1+\left(\frac{2}{N_{\mathrm{Pe}}}\right)} = \frac{V}{Q}\left(1+\frac{2}{N_{\mathrm{Pe}}}\right) \tag{4.35}$$

The analytic solution for the variance ($\sigma^2_{\theta,OO}$) is :[70,75]

$$\sigma^2_{\theta,OO} = \frac{\sigma^2}{t_m^2} = \frac{8 + 2N_{\mathrm{Pe}}}{4 + 4N_{\mathrm{Pe}} + N_{\mathrm{Pe}}^2} \tag{4.36}$$

4.3.4 Tanks-in-series model

Continuously stirred tank reactors (n_{CSTRs}) assume perfect mixing for each successive tank in series. The composition in each tank is the same everywhere including the exit.[20] The tanks-in-series model and the dispersion model are roughly equivalent. Indeed, the results are the same for small deviation from plug flow[33] and they are linked by :[25]

$$N_{\mathrm{Pe}} = 2(n_{\mathrm{CSTR}} - 1) \tag{4.37}$$

The main conditions for n tanks in series models are :[137]

$$E_{\mathrm{ts}}(t) = 0; t < t_{\mathrm{p}} \tag{4.38}$$

$$E_{\mathrm{ts}}(t) = \frac{(t - t_p)^{N-1}}{t_n^n} \frac{e^{(t-t_{\mathrm{p}})/t_{\mathrm{n}}}}{(n-1)!}; t \geq t_{\mathrm{p}} \tag{4.39}$$

where t_{p} is the piston time and t_{n} is the time of mixing in each one of the tanks in the RTD model.

RTD equation for the 4th tank is represented by the Laplace transforms (Levinspiel/MacMullin and Weber 1935)

$$\bar{t}_{ts} E_{ts} = \left(\frac{t}{\bar{t}_{ts}}\right)^{N-1} \frac{N^N}{(N-1)!} e^{-tN/\bar{t}_{ts}} \tag{4.40}$$

where,

$$\bar{t}_{ts} = N\bar{t}_{ts,i} \tag{4.41}$$

The dimensionless form is :

$$E_{\theta,ts} = (N\bar{t}_{ts,i}) = N\frac{(N\theta)^{N-1}}{(N-1)!} e^{-N\theta} \tag{4.42}$$

The variance in function of time (σ^2_{ts}) and dimensionless ($\sigma^2_{\theta,ts}$) are :[129]

$$\sigma^2_{ts} = \frac{\bar{t}^2_{ts}}{N} \text{ and } \sigma^2_{\theta,ts} = \frac{1}{N} \tag{4.43}$$

4.4 Applications

In 2016 and 2017, residence time distribution appeared in over 1600 articles indexed by Web of Science Core Collection (WoS).[13] VOSViewer generated a bibliometric map from the keywords of these articles (Figure 4.3) and identified five major clusters of related research : model, simulation, CFD and flow, mass transfer and, systems and pharmacokinetics. Over 20 % of the articles are in the WoS category chemical engineering (344), followed by 152 in environmental sciences, and 124 in water resources.

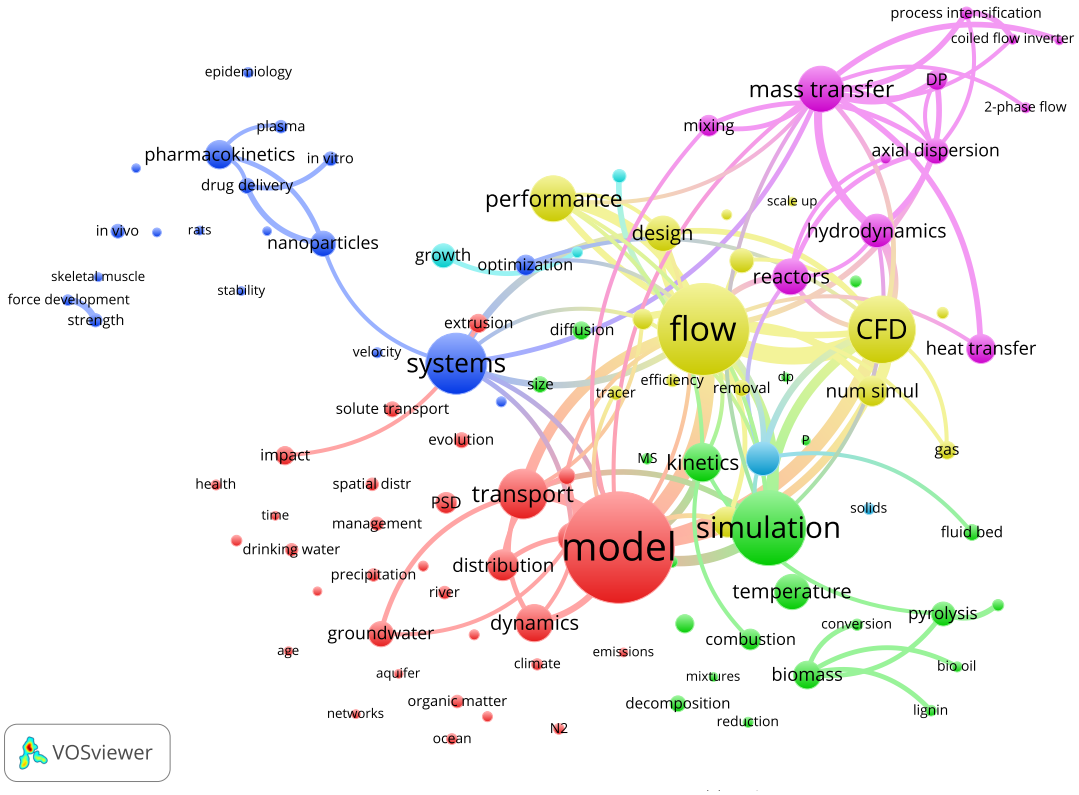

Figure 4.3 Residence time distribution bibliometric map :[13,14] in 2016 and 2017 WoS indexed 1600 articles that mention RTD. The plot includes the 100 most frequent keywords in the top 10 000 cited articles. The text font size and diameter of the circles are proportional to the number of occurrences of the keywords. After PSD with 185 occurrences (not shown), the most frequent keywords are model (98 articles) and then flow (97). The smallest circles (scale up networks) appear 11 times. VOSViewer groups the keywords into five clusters (represented by colours) and demonstrates links between the keywords with lines.

Residence time distribution is cited in over 170 of the 250 WoS scientific categories. We selected twenty articles published between 2008 and 2018 from several categories to demonstrate the extent of how researchers apply the technique (Table 4.1, 4.2). Mixing and reactor

modelling are two of the major themes that apply RTD analysis. These two areas appear in the bibliometric map of the mass transfer cluster. The mixing studies are mostly micro, static, screw and T-junction mixers. For reactors, the most common type studied are tubular loop, fluidized beds (bubbling and circulating), and liquid reactors. Bio-processes and pharmaceutical applications have emerged over the last few years. Bio-process studies, including hydrolysis and fermentation, evaluate how long bacteria are in contact with biomass and the presence of dead zones. These processes operate with heterogeneous mixtures and so achieving adequate contact between the fluid an biomass determines how well the substrate reacts.[117,138] Biomass appears in the same cluster as simulation in the bibliometric map. Pharmaceutical applications belong mostly to the blue cluster including drug delivery, cancer, in vivo, in vitro, tissue distribution, and skeletal muscle. Continuous flow chemistry has been applying RTD to monitor and optimize the contact time and design micro-mixers.[9,10]

The axial dispersion model is the most widespread. It is the only one present on the bibliometric map (magenta cluster). Other models such as semi-empirical model, particle dispersion model, dispersive plug flow and tanks-in-series are also mentioned (Table 4.1,4.2).

The yellow cluster of the bibliometric map includes numerical simulation and Computational Fluid Dynamics (CFD). With the ever increasing computational power, CFD simulations of reactors (e.g. stirred-tanks) have has become more common in the literature. Uisng CFD, the velocity field (and other variables like pressure) can be obtained at all points of the mesh discretizing the geometry. This large quantity of information, often million of velocity vectors at different moments in time, does not readily give insight on global mixing occuring in the process and does not allow for an easy comparison between geometries. Consequently, RTD is often used a post-processing tool to characterize the hydrodynamics of a *virtual* reactor, a reactor simulated by CFD. There are two major CFD strategies to calculate the RTD. The Euler-Euler approach solves the transient advection-diffusion of a passive scalar field using the fluid velocity profile. This can be achieve while the CFD simulations are running or during post-processing since the scalar used to calculate the RTD does not affect the flow patterns.[98] However, since the advection-diffusion equation is hyperbolic at high Peclet number, proper upwinding must be used to ensure that no oscillations occur in the passive scalar field. Furthermore, if the mesh is unsufficiently fine, numerical diffusion can dominate over physical diffusion and artificially flatten the RTD.

The Euler-Lagrange approach tracks the position of particles. The particles can either be tracer particles which follow the streamlines of the fluid or solid particles which are part of a CFD-DEM simulation.[110] The particle trajectory from inlet to outlet or from insertion to homogeneization is used to calculate the RTD. The Euler-Lagrange approach is accurate

since it does not induce numerical diffusion, however it is computationnaly expensive since the trajectory of a large number of particles (>10k) must be tracked over a potentially long time.

For both approaches, simulation procedures for the residence time distribution are always validated with experimental data to confirm their accuracy.[70]

4.5 Uncertainty

An RTD measures the average residence and variance from which we postulate a hydrodynamic regime—plug flow, degree of backmixing, dispersion, and bypassing. The contributions to the variance of the signal include all piping upstream and downstream of the system as well as the detectors, and the valve configuration. Minimizing the contributions from ancillary piping by reducing their volume, maximizes the signal contribution from the system. Ideally, the system residence time represents at least 50 % of the total.

Model limitation

Several assumptions limit the validity of the axial dispersion model :[9,33,77,118]

- The process is continuous or semi-continuous ;
- The steady state is reached ;
- The inlet and outlet of the system have unidirectional flows (closed-closed boundary conditions) ;
- Perfect horizontal mixing ;
- Long pipe/tube ;
- Non-viscous materials ;
- The tracer does not affect the system and is distributed evenly in all all the system ;
- The radial diffusion is negligible.

The axial dispersion model is applicable for small deviation from ideal plug flow.[33,69] Moreover, to neglect the radial diffusion, the ratio height to the inner diameter (H/D) must be high.[139] For a short tube or if a viscous material is present and the flow regime is laminar, the dispersion model is inapplicable. In these two scenarios, it is recommended to apply the pure convection model. This model considers each element of fluid slides in front of its neighbour without interaction by molecular diffusion. Thereby, only velocity variations dictate the spread of residence time distribution.[33]

Table 4.1 Application of the residence time distribution in literature between 2008 to 2018 (part 1)

Application[ref]	E/C	Tracer	Input	Tracer detection	Regime	Model	Phase
Koflo and kenics static mixers[7]	E/C	eriochrome black T	pulse (5 mL)	spectroscopy UV/VIS	L	-	water
Model to predict RTD in tubular loop reactors[8]	E	NaCl	pulse (3 mL)	conductivity, electrochemical analyzer	L/Tu	ADM	tap water
Modular catalytic structured packing for distillation[115]	E	NaCl	pulse	conductivity meter	L	ADM	water, air
Simulation of quasi plug-flow for enzymatic hydrolysis[138]	C	enzymolysis liquid	pulse	simulation	L	TS	slurry
Purging system in a silo of storage wood pellets[21]	E	helium	positive step	thermal conductivity detectors (TCD)	L	LD	air
Multilaminated/elongational flow and a T-junction[19]	E/C	uranine solution	pulse (1 µL)	UV-vis absorption spectroscopy	L	SEM	water
Best tracer in continuous powder blending (pharmaceutical)[9]	E	7 tracers[1]	pulse	On-line near infrared (NIR) spectroscopy	-	ADM	solid
Multi-compartment fluidized bed simulation[129]	C	gas tracers	pulse	simulation	-	species transport	glass, gas
Fluid distribution in a millimetric multichannel device[16]	E	carbon ink	pulse (15 µL)	fast camera	L	DPF, PF-CSTR	water
Control in retention reactor and coaxial heat exchanger[20]	E	NaCl solution	positif step	conductimetric sensors	L	ADM	water

Table 4.2 Application of the residence time distribution in literature between 2008 to 2018 (part 2)

Application	E/C	Tracer	Input	Tracer detection	Regime	Model	Phase
Three-chamber feed frame system with powder blends[119]	E	dye	pulse	spectroscopy UV/VIS	-	-	micro-crystalline
Tubular contactor with woven mesh, screen-type static mixers[69]	E	KCl solution	pulse 5.8 mL	conductivity sensors	Tr/Tu	ADM	RO water
Rapid spinning fluids reactor[116]	E	NaCl	pulse 5 mL	conductivity sensors	Tu	-	liquid, gas
Horizontal screw hydrolysis reactors[117]	E	NaCl	pulse	electrical conductivity	-	-	slurry
Circulating fluidized bed risers (CFB)[70]	C	solid particles	pulse	simulation	Tu	EMMS	gas-solids
Micro fluidized bed reactors[77]	E	helium	pulse	mass spectrometer	Tu	ADM	FCC, sand, glass, air
Scale up of bubbling fluidized beds (BFBs)[17]	E	coal particles	pulse 2 %	weight solids at the outlet each 30 s	-	PDM	silicia sand, air
Effect of regimes in the riser of a CFB[18]	E	radioactive ^{18}F	step	Positron Emission Particle Tracking	Tr/Tu	-	sand
Riser of a small scale cold CFB[118]	E/C	NaCl crystals	pulse 50 g	electrical conductivity	Tu	ADM	FCC, air
Fluidized bed coating of microparticles[137]	E	acetone	pulse 1 mL	UV on-line analyzer	-	TS	glass beads, CO_2

[1]Acetaminophen, anhydrous calcium di-phosphate, croscarmellose sodium, crospovidone, maize startch, API3, API4.
Legend: E: experimental, C: CFD simulation. **Regime:** L: Laminar, Tr: transient and Tu: turbulent. **Model:** ADM: Axial Dispersion Model, TS: Semi-Empirical Model, PDM: Particle Dispersion Model, DPF: Dispersive Plug Flow, TS: Tanks-in-Series, ZD: Longitudinal Dispersion

Together with experimental configuration, two other challenges are choosing appropriate tracers and an analyser to detect them.[16] Here we assess contributions to the variance introduced by the valves, the dead volumes in tubes, dwell time of the analyser, the valve switch time, the contribution of the tail to the model best fit parameters, repeatability, and tracer.

The total variance for the entire system (σ_T^2) is :

$$\sigma_T^2 = \sigma_{\text{system}}^2 + \sigma_{\text{injection}}^2 + \sigma_{\text{detection}}^2 + \sigma_{\text{inlet}}^2 + \sigma_{\text{outlet}}^2 \tag{4.44}$$

where, $\sigma_{\text{injection}}^2 = \tau^2/12$

The objective is to minimize the contribution to the variance from all ancillary lines, valves fittings, and analytical instruments. When the system represents only 5 % of the total residence time, the uncertainty (θ_i) in the variance in all other components of the experimental set-up may be too great to derive meaningful results.

$$\theta_T = \theta_{\text{system}} + \theta_{\text{injection}} + \theta_{\text{detection}} + \theta_{\text{inlet}} + \theta_{\text{outlet}} \tag{4.45}$$

where, $\theta_{\text{injection}} = \tau^2/2$

We completed well over 500 RTD experiments in an 8 mm inner-diameter quartz tube, 360 mm long (Figure 4.4) with oxygen as the tracer. Two Brooks mass flow controllers metered the the argon and air flow rates continuously. Before each series of tests, we calibrated the MFC with a bubble meter and measured both barometric pressure and ambient temperature. Within the span of a week, barometric pressure varies up to 5 %.[134]

A Hiden quadrupole MS monitored the effluent composition and it had a pulse ion counting (SCEM) detector with an oxide coated iridium. The operating pressure was 6.2×10^{-5} mPa. The capillary 0.9 m long from the head of the MS was and 0.20 mm in diameter and operated at 160 °C. We repeated each experiment and measured both the effluent and the entrance composition.

Each test was performed with Fluid Catalytic Catalyst (FCC) belonging to Geldart group A classification with a sphericity close to one ($\phi \approx 1$) (Figure 4.5) and its minimum fluidization velocity (U_{mf}) about 2.2 mm s^{-1} (Table 4.3).[22,140] The reactor operated at 10 , 20 and 60 mm s^{-1}, which represents 4.5 , 9 or 27 times U_{mf}. The Reynolds numbers at 21°C associated with these velocities are 230 , 460 and 1390 respectively. Thus, all RTD tests conducted are in the laminar regime.

The minimum bubbling velocity (U_{mb}) is 5.8 mm s^{-1} which is less than all the experimental

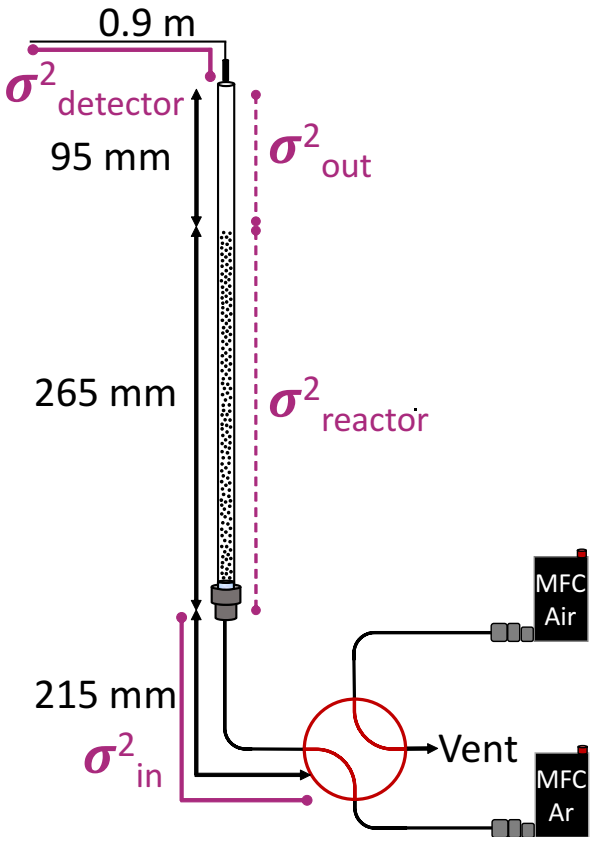

Figure 4.4 Fluidized bed reactor configuration. The quartz tube was 8 mm in diameter and 360 mm long. The high vacuum in the tubes aspirates gas at 8 mL min^{-1}, so its nominal residence time in the capillary is close to 5 s. We tested a second capillary operating at 20 mm min^{-1} and a nominal residence time less than 2 s. At a low aspiration rate, the ingress of oxygen to the MS was 40 times lower than with the higher flow rate capillary. The slumped bed height with FCC catalyst was 188 mm and it expanded to 265 mm during the fluidization.

velocities tested so the bed operated in the bubbling regime is reached. However slugs form at H/D_{reactor} ratios greater than 2 Since $H/D_{\text{reactor}} = 33$, slugs form at gas velocities several times greater than U_{mf} according to:[26,141]

$$U - U_{\text{mf}} > 0.07\sqrt{gD_{\text{reactor}}} + 1.6 \times 10^{-3}\left(60D_{\text{reactor}}^{0.175} - H_{\text{mf}}\right)^2 \tag{4.46}$$

where, H_{mf} is the bed height at the minimum fluidization. According to this criterion, only the highest velocity ($U = 60\,\text{mm}\,\text{s}^{-1}$) is in the slugging flow regime. The bed surface follows a regular frequency corresponding to large pressure fluctuations. Gas-solid mixing is poorer in this regime.[26]

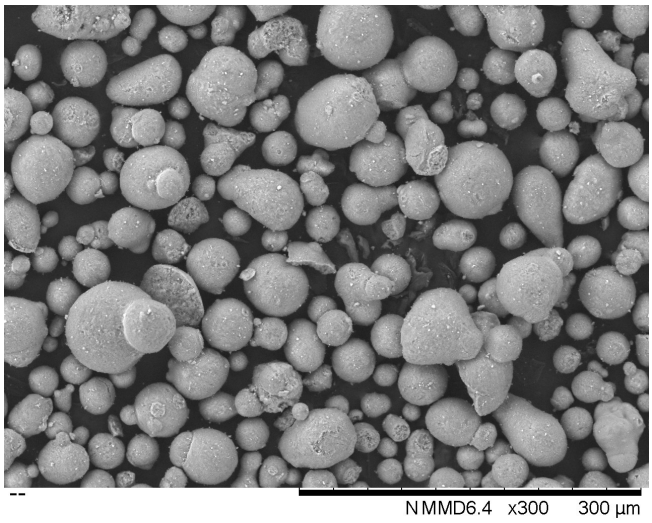

Figure 4.5 Scanning Electron Microscopy (SEM) image of FCC. Most of the particle are spheroids but some are fractured, and others form agglomerates. [22]

4.5.1 Valve configuration

A sharp injection pulse minimizes the uncertainty in the parameter estimates when deconvoluting the RTD curves. Piping upstream must be minimized together with flow perturbations due valve switching, and flow metering. With radioactive tracers, collimating NaI Scintillator detectors with lead restricts $\gamma-$ rays to a small window (even slit), which sharpens the RTD peak. The boundary conditions are considered open-open when the detectors are positioned along the column of the vessel. When injecting and detecting in the lines leading to the reactor and at the exit, we might consider the inlet boundary condition as closed-closed if we consider that backmixing (reverse flow) is negligible and their volume is orders of magnitude smaller than the vessel, which is best to confirm experimentally. [7]

We consider introducing a tracer through a valve switch as a closed boundary condition (Figure 4.4). We tested a 3-way, 4-way, and an 8-way valve configuration. At time, $t = 0$, the valve switched from argon to air. The 3-way valve configuration is simplest (Figure 4.6): in position (a), argon goes to the reactor and when the valve is switched to position (b) air flushes out the Ar. In position (a) the air flow rate is zero and it takes 5 s for the MFC to reach the set point of $30\,\mathrm{mL\,min^{-1}}$. During this transient the air flow rate peaks to a value $5\times$ greater than the set point (Figure 4.7). When switching back to Ar, the flow rate drops to below $5\,\mathrm{mL\,min^{-1}}$ before reaching the set point of $27\,\mathrm{mL\,min^{-1}}$ after 10 s.

The flow perturbation introduced when switching the 3-way valve introduces a substantial error in the RTD measurement. For this reason, we developed a 4-way valve configuration in

Table 4.3 FCC properties. Fifteen graduate students and interns generated the data base. They conducted the tests with no prior instruction and repeated U_{mf} and density measurements at least 3 times. FCC catalysts include a variety of compositions and particle properties.[22]

Property	value	s	n	Comment
U_{mf}, mm s^{-1}	2.2	0.7	3	$D_t = 8$ mm
U_{mb}, mm s^{-1}	5.8	0.7	3	Geldart 1978[140]
ρ_b, kg m^{-3}	905	10	70	Scott density
	911	15	48	poured density
	1003	32	48	tapped density
	945		1	Hg porosimetry
ρ_p, kg m^{-3}	1610		1	Hg porosimetry
ρ_{sk}, kg m^{-3}	2360	2	9	gas pycnometer
ϵ_v	0.44		1	
H_r	1.10	0.04	48	Hausner ratio
θ_{ang}, °	25	7	45	angle of repose
d_{10}, µm	34.5	0.1	3	laser diffraction
d_{50}, µm	55.7	0.6	3	laser diffraction
d_{90}, µm	89	1	3	laser diffraction
ϕ	0.99		1	Ergun equation
s_A, m^2 g^{-1}	237		1	BET
	27		1	BJH
v_{pore}, mL g^{-1}	0.22	1	1	BET
d_{pore}, nm	3.1	1	1	BET, BJH

which the MFC actively controls the flow rate of the gas going to vent (Figure 4.9). However, even with this configuration, the MFC took 3 s to reach the set-point (Figure 4.9).

We assumed that the time delay was due to the difference in pressure between the vent line and the reactor effluent. So, for the third valve configuration we installed a precision needle-valve to create a pressure drop equal to the ΔP across the reactor (Figure 4.10). This configuration still introduces an error with respect to volumetric flow rate: our intention was to feed both the Ar and air at 30 mL min^{-1} but the Ar flow meter was controlling at 27 mL min^{-1}—10 % lower than what we had targeted.

To minimize this type of error, we developed a modified GC injection configuration (Figure 4.11). In position (a) Ar enters through port 1 and passes through port 3 that leads to a sample loop and finally goes to the reactor. Air enters through port 7 and fills the sample look then goes to port 5 and exits at port 6 to the vent. In position (b), the argon exits

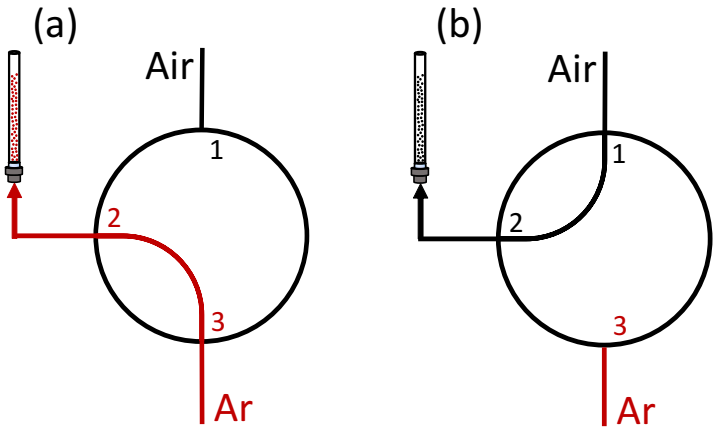

Figure 4.6 3-way valve configuration.

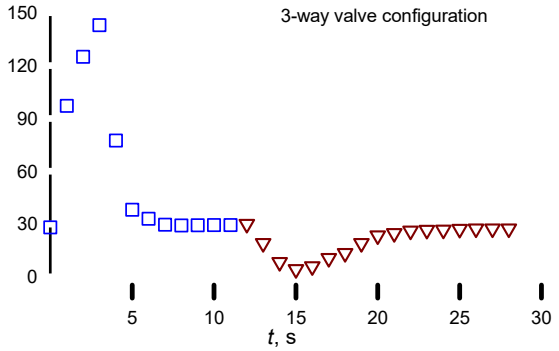

Figure 4.7 3-way valve flow perturbation: While switching from Ar to air, the volumetric flow rate overshoots to 150 mL min (squares). The flow rate undershoots to close to 0 mL min switching from air to Ar (triangles).

port 5 that leads to the sample loop and flushes out the air through port 8 leading to the reactor. In this configuration, only one MFC feeds to the reactor, which minimizes uncertainty trying to match flow rates. Furthermore, the flow path is identical as we introduce a dummy sample loop that serves only to match the geometry of the flushing stage. While the 3-way and 4-way valve configurations approximate a Heaviside-side unit pulse, the 8-way valve produces a bolus injection pulse. The MS detects a pulse response of the tracers and the experiment is complete when the concentration of oxygen reaches the original base line (Appendix 4.7.1).

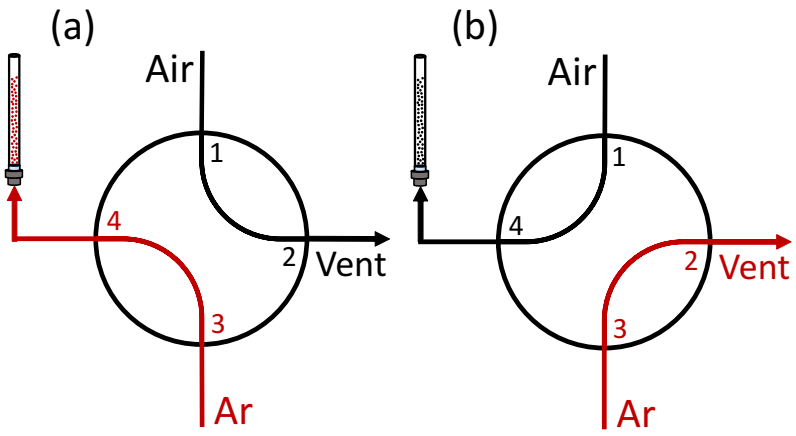

Figure 4.8 4-way valve configuration

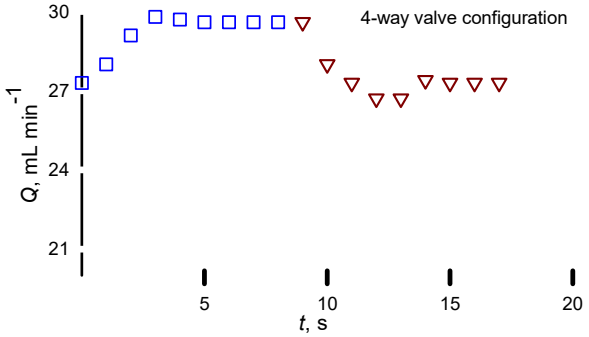

Figure 4.9 4-way valve flow perturbation: The MFC took 3 s to reach the set-point volumetric flow rate while switching from Ar to air (squares) and air to Ar (triangles). The Ar MFC was set-point was 27 mL min^{-1} while the air MFC was 30 mL min^{-1}.

We compared three valve configurations (4-way, 4-way correcting for ΔP, and 8-way) at a gas velocity of 20 mm s^{-1} (Figure 4.12). The best fit Peclet numbers in the axial-dispersion model with closed-open boundary conditions (Eq. 6.10) were 29 , 33 , and 44 for the 4-way valve, 4-way valve correcting for ΔP, and 8-way valve, respectively. The RTD response with a pressure restriction shows a delay of 1 s ($\Delta P = 1990$ Pa) compared to a simple injection. Thus, all restrictions added before the inlet of the micro reactor influence the RTD. The break-through time for the 4-way valve and 8-way valve was much less than 1 s.

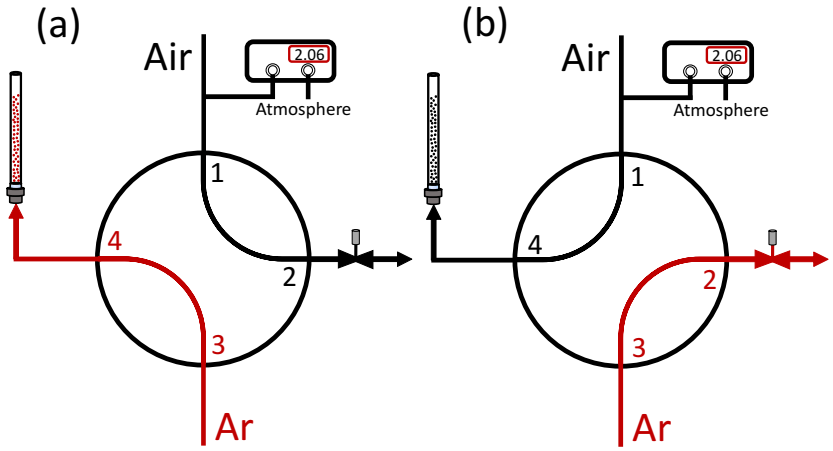

Figure 4.10 4-way valve configuration with pressure drop compensation: A needle valve restricts the flow at the vent to match the ΔP across the reactor side.

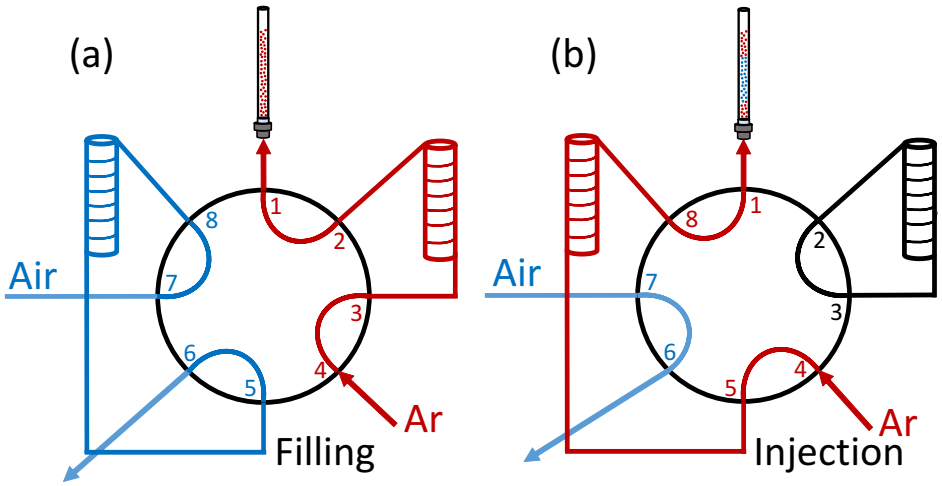

Figure 4.11 Modified GC valve configuration. In valve position (a), air passes the reactor through a sample loop while argon fills the second sample loop. In valve position (b), after the valve switch, air flushes the Ar in the sample loop to the reactor. The same MFC feeds the reactor in positions (a) and (b).

With increasing gas velocity, the breakthrough curve becomes sharper: At $10\,\mathrm{mm\,s^{-1}}$ the MS records 15 concentrations between $0.1 < C/C_\mathrm{o} < 0.9$ while at $60\,\mathrm{mm\,s^{-1}}$, it barely records 5 measurements (Figure 4.13). The best fit *npe* for a step response are: 64(3) , 28(5) and

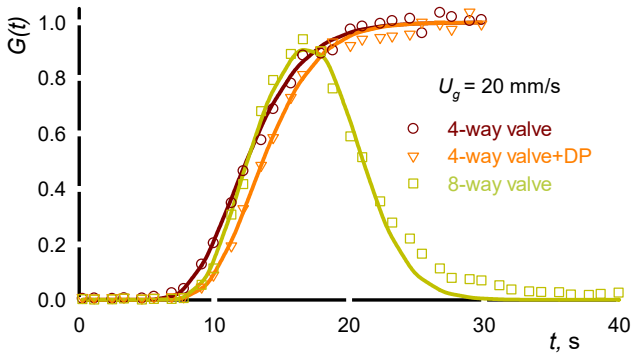

Figure 4.12 $G(t)$ vs time for FCC. Oxygen response for three different valve configurations. The 4-way valve gives a step response while the 8-way valve is a bolus-pulse. The fluidized bed operated at a gas velocity of 20 mm s^{-1}. The symbols represent experimental data while the continuous line is the axial dispersion.

10(2) at U_g = 10 mm s^{-1}, 20 mm s^{-1} and 60 mm s^{-1}, and an R^2 =0.998, 0.998, and 0.982, respectively. For a pulse response, the $N_{Pe}$is: 81(3) , 44(4) , and 23(2) for the corresponding velocities. The difference between a step and a pulse response for the three velocities is constant at 14(2) In an ideal system the N_{Pe} is identical for both injection configuration except that the step function adds $\tau^2/12$ to the overall variance. For the sample loop with a constant volume, the contribution due to the bolus injection decreases with increasing gas velocity and represents 10 % of the system variance at U_g =10 mm s^{-1} but less than 0.1 % at U_g =60 mm s^{-1}.

4.5.2 Dead volume

Dead volume refers to space in vessels and lines that are extraneous to the system of interest. Fluidized beds have a freeboard above the powder to reduce solids carry over to the cyclones and a windbox below the grid to distribute gas across the reactor at the grid. Both of these zones contribute to the overall residence time and variance but not to reactor performance. Indeed, most vessels like mixers, distillation columns, tanks, reservoirs, and analyzers (gas chromatographs) also have empty space at the entrance and exit. This dead volume is inevitable in commercial facilities but when evaluating hydrodynamics for research, we minimize this space to more easily identify system hydrodynamics (but is difficult in cases like micro-reactors).

To quantify the impact of dead volume, we compared reactor lengths of 360 mm and 460 mm both in an 8 mm ID tube. We filled both with 9.15 g of FCC and applied a step pulse following

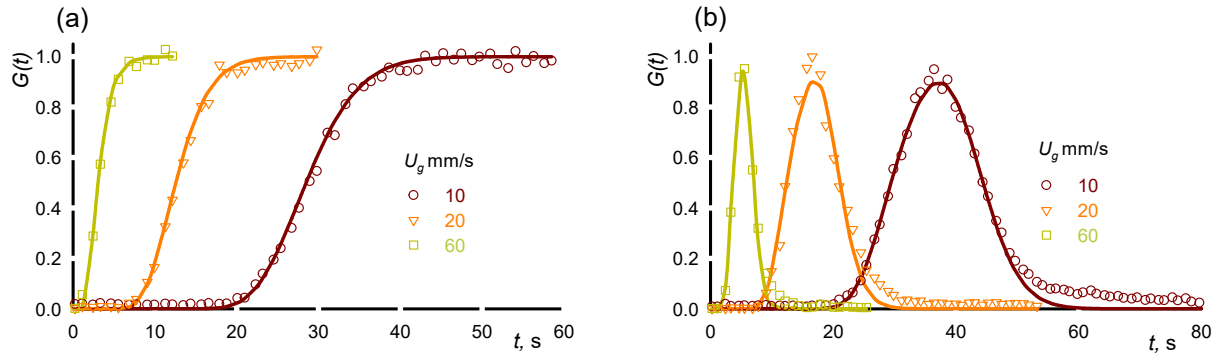

(a) (b)

Figure 4.13 $G(t)$ vs time with 9.15 g FCC at 10 , 20 and 60 mm s^{-1}. (a) Oxygen response measures with a mass spectrometer of a step function with the 4-way valve. (b) Oxygen response of a pulse function with the 8-way valve. The dots represent experimental data while the continuous line is the axial dispersion model after fitting each parameter.

the protocol in Appendix 4.7.1 at 10 mm s^{-1}, 20 mm s^{-1}, and 60 mm s^{-1} (Figure 4.14). The mean residence time in the 460 mm reactor is always higher compared to the short tube and increases with decreasing gas velocity (Table 4.4). N_{Pe}follows the same behavior as the residence time. For an increase of 30 % of the total length of the microreactor the mean residence time rises 58 % from its initial value and N_{Pe}decreases up to 39 %.

Table 4.4 N_{Pe} and $\bar{t}$ for the 360 mm and 460 mm quartz tubes.

U_{g} mm s^{-1}	Length mm	N_{Pe}	ΔN_{Pe}	$\bar{t}$ s	$\Delta\bar{t}$ s
10	360 460	47 33	-14	36 57	21
20	360 460	31 24	-7	16 27	11
60	360 460	15 14	-1	4.5 7.6	3.1

To determine the impact of the mass of catalyst, we measured the RTD of the tube empty, and with 2 g and 9.15 g of FCC (Figure 4.15). The velocity for air and argon was 20 mm s^{-1}. In this case, the mean residence time is approximately the same ($\bar{t} = 27$ s) regardless of the mass of catalyst (Table 4.5). The height of the dead volume over the catalyst bed does not affect the mean residence time. On the other hand, N_{Pe} decreases with an increase in the

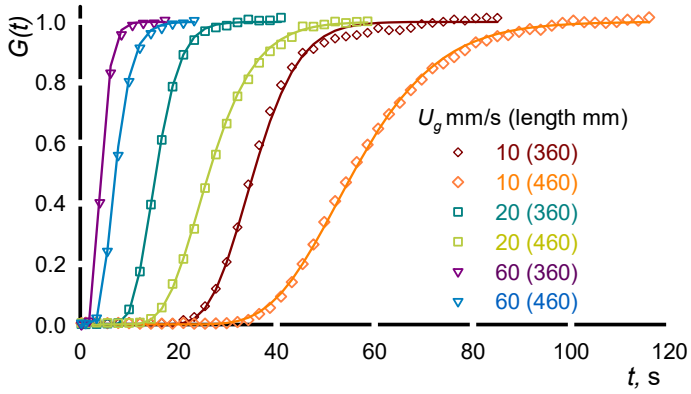

Figure 4.14 $G(t)$ vs time for a 360 mm and 460 mm length 8 mm ID microfluidized bed. The 4-way valve switched argon to oxygen with the fluidized bed operating at $U_g = 10\,\mathrm{mm\,s^{-1}}$, $20\,\mathrm{mm\,s^{-1}}$, and $60\,\mathrm{mm\,s^{-1}}$ with 9.15 g of FCC. Symbols represent data and continuous lines the axial dispersion model with the best fit estimates of $\bar{t}$ and N_{Pe}.

amount of catalyst. The difference between the empty and fill tube with 9.15 g is 52 %. The system is close to plug flow when $N_{\mathrm{Pe}} > 50$.[136] For the empty tube, $N_{\mathrm{Pe}} = 48$ but decreases to 24 with 9.15 g of FCC. Overall, more catalyst reduces N_{Pe}, which corresponds to a rise in backmixing and bypassing or channelling.

Table 4.5 Comparison of the Peclet number (N_{Pe}) and the mean residence time ($\bar{t}$) for different amounts of FCC

mass FCC g	N_{Pe}	$\bar{t}$ s
0	48	27
2	36	28
9.15	24	27

Considering that the volume of the 9.15 g occupied by the solids of the catalyst is

$$V = \frac{m}{\rho_{\mathrm{sk}}} = \frac{9.15\,\mathrm{g}}{2360\,\mathrm{g\,mL^{-1}}} = 3.7\,\mathrm{mL} \tag{4.47}$$

we expected that the average residence time with FCC would be shorter by $V/Q = 3.7\,\mathrm{mL\,min^{-1}}$ / $1\,\mathrm{mL\,s^{-1}} = 3.7\,\mathrm{s}$ (14 %). The contributions to this large deviation in $\bar{t}$ include

Injection: Switching valves perturbs the MFC and it takes as much as 3 s to recover its set point - a contribution of > 1 % (Figure 4.9) but this could increase at higher gas

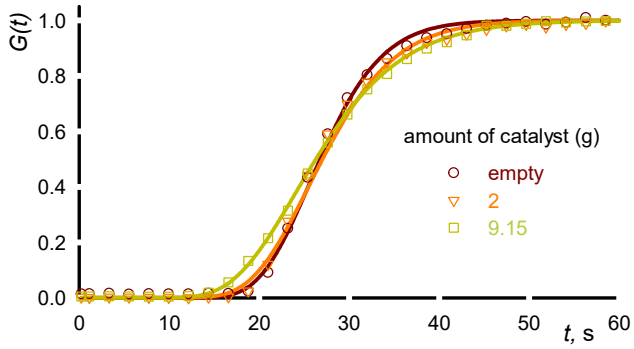

Figure 4.15 $G(t)$ vs time for the empty tubed and filled with 2 g and 9.15 g of FCC. At steady state, the mass flow controller injects argon at $U_g = 20\,\mathrm{mm\,s^{-1}}$ in a 460 mm length, 8 mm ID fluidized bed. At $t = 0$, we switched the 4-way valve to air at the same velocity while the mass spectrometer detects oxygen on-line. Symbols represent data and continuous lines the axial dispersion model with the best fit N_{Pe} and $\bar{t}$.

velocities.

ΔP: The gas density at the bottom of the reactor, the windbox, and lines are higher due to the pressure drop across the bed of solids ($\Delta P = \rho_{\mathrm{bed}} g z$) and consequently the residence time is higher versus an empty tube. The residence time in the bed accounting for pressure drop is

$$t = \frac{z}{U_{\mathrm{g}}}\left(1 + \frac{\rho_{\mathrm{bed}} g z}{P}\right) \tag{4.48}$$

$$t = \frac{z}{U_{\mathrm{g}}}\left(1 + \frac{g m_{\mathrm{bed}}}{P \cdot X_{\mathrm{A}}}\right) \tag{4.49}$$

where the second term is the additional time due to the solids and equals 0.5 s

P, T: The temperature in the laboratory varied little and we monitored the pressure in the laboratory, but this contributes as much as 5 %.

Variability: To minimize the variance in the tests, we must repeat it several times. In our case, the RTD curve variability was highest at the highest gas velocity (shortest residence time). Instrument measuring frequency also contributes to the variance.

Tail: Defining when the curve reaches a steady value or a long tail contribute to the first and second moments. Tailing is prevalent in systems with pores and solids recirculation as gas.

Adsorption: Gases that adsorb to the surface of the catalyst will increase the residence time—chromatographic affect. Non-adsorbing tracers like noble gases are ideal but

then may not track the process gas.

4.5.3 Repeatability

We repeated experiments 10 times each for the step and bolus injection experiments (Appendix 4.7.1) at 10 , 20 , and 60 mm s^{-1} (Figure 4.16) then calculated the average and the standard deviation at each time step for the entire duration of the experiment. The MS recorded concentration at 4 Hz. The uncertainty increases with increasing velocity particularly in the vicinity of the inflection point in the curve. The maximum deviation in the data for a step change curve varies as low as 5 % for the lowest velocity and reaches 25 % for the highest velocity. For the pulse, the variation is higher and ranges from 8 % to 44 %. The variability in the residence time at high velocity maybe attributable to the fluctuations in the gas velocity attributable to the slugging or the low sampling frequency at the inflection point. At 60 mm s^{-1} the pressure fluctuates by as much as 25 Pa while the total pressure drop is 1700 Pa.

4.5.4 Sample frequency

The uncertainty in the counts recorded by a NaI scintillator detector is proportional to the square root of the total number of counts. So, the lower dwell time is bound by how many counts accumulate in that time, which ideally should be greater than 10. The MS also accumulates counts so a longer dwell time (lower sample frequency) improves it the concentration estimate but at the expense of precision.[23] When the sample frequency is too high, the MS signal to noise ratio decreases, which affects the RTD curve around the inflection point most(Figure 4.17). The 95 % confidence interval ($\Delta_G, n = 7$) of the RTD curve after it achieves 99 % of the steady value was 0.13 at sample frequency of 44 Hz and dropped by a factor of 3 to 0.044 at 22 Hz, and then dropped to 0.017 at 4 Hz. The best fit N_{Pe}increases from 20, 25, to 30 for a frequency of 44 , 24 and 4 Hz, respectively. The resolution in the graph is lowest with the low frequency sampling but the eight points in the region $0.1 < G(t) < 0.9$ is sufficient to resolve the curve. An optimal value between accuracy and data per second is specific to each instrument. We recommend that the RTD curve have at least 5 sample points in the range $0.1 < G(t) < 0.9$ as long as the $\Delta_G <\approx 2$ %.

To determine the relationship between sample frequency and model fit, we averaged the 44 Hz data to create an RTD curve with a sample frequency at 4 Hz (Figure 4.18). The 95 % confidence interval improved from 0.13 to 0.09 at $U_{\mathrm{g}} = 20$ mm s^{-1}, which is a marginal improvement, but the fit in the region $0.1 < G(t) < 0.9$ was essentially identical between the original 4 Hz experiment and the averaged data. The fit was equally good at the low gas

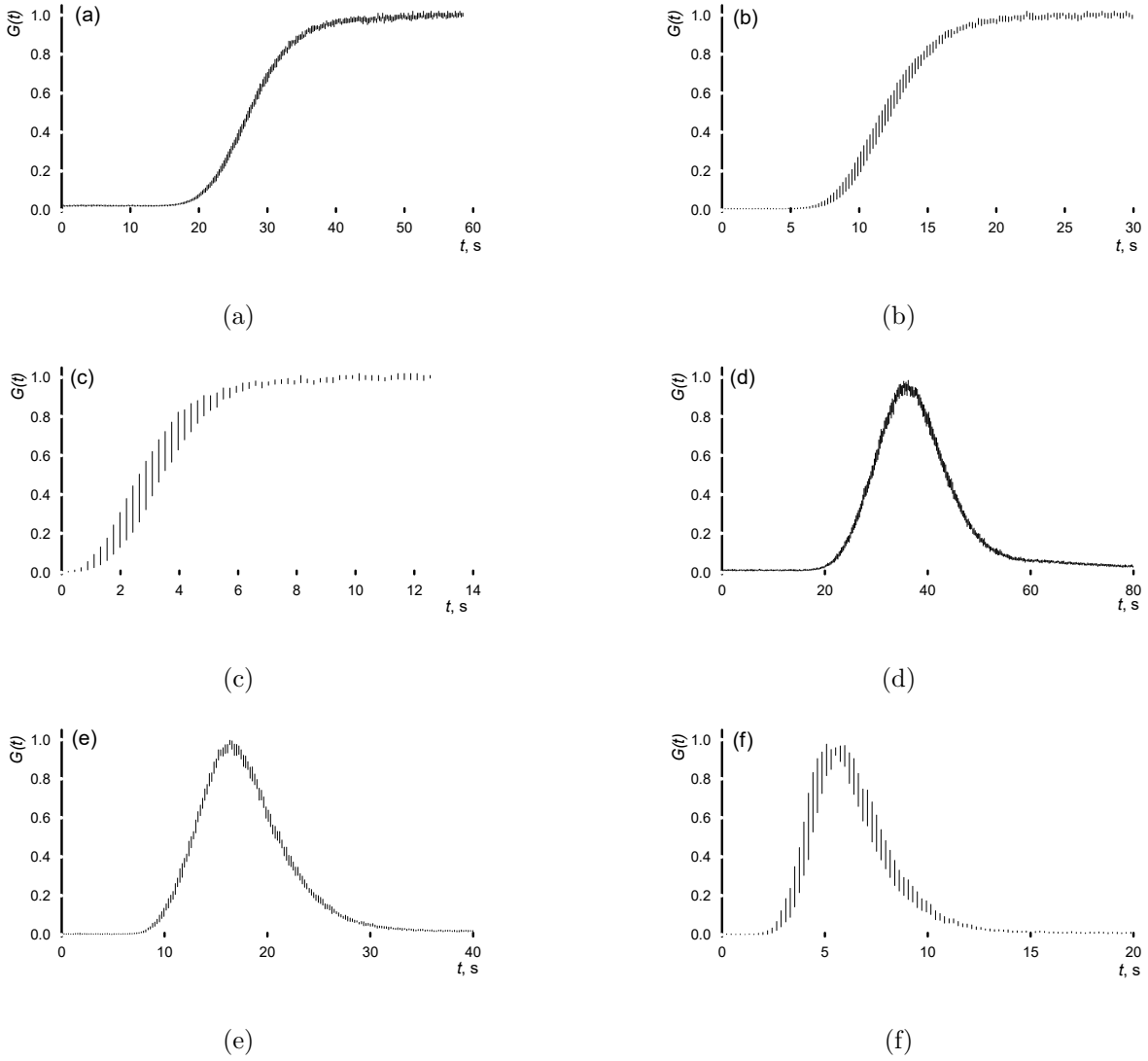

(a) (b)

(c) (d)

(e) (f)

Figure 4.16 Repetition of $G(t)$ vs time with FCC as a catalyst. Confidence intervals of the experimental data of 10 repetitions taken continuously. We switched from argon to air with a 4-way valve for the step response and with an 8-way valve for the pulse. The velocities are $10\,\mathrm{mm\,s^{-1}}$ for the figure (a) and (d), $20\,\mathrm{mm\,s^{-1}}$ for (b) and (e) and $60\,\mathrm{mm\,s^{-1}}$ for (c) and (f). The mass spectrometer acquires the concentration on-line.

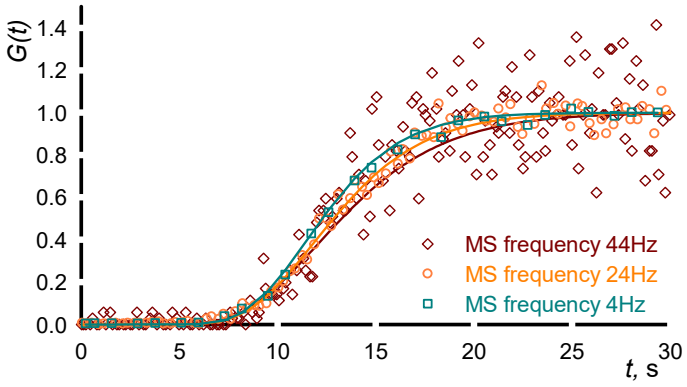

Figure 4.17 MS sample frequency. Comparison of mass spectrometer frequency. The 4-way valve switched from Ar to air while the reactor operated at 20 mm s^{-1}. The MS samples at 44 Hz, 22 Hz, and 4 Hz. The symbols represent experimental data while the continuous line is the axial dispersion model.

velocity, but at the high gas velocity the breakthrough time of the averaged data was shorter, consequently the $N_{\mathrm{Pe}}$is higher.

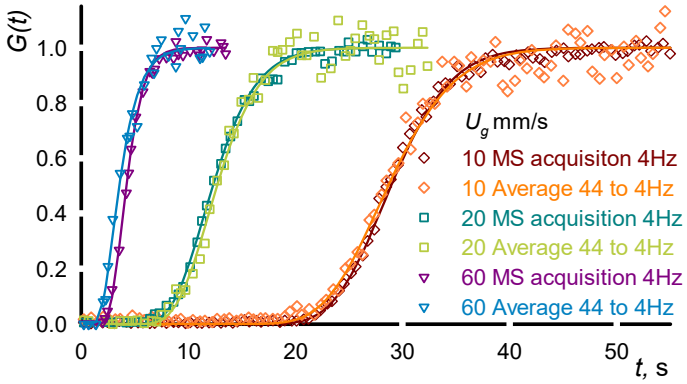

Figure 4.18 Synthetic data vs mass spectrometer acquisition data. The synthetic data are averages of 10 samples recorded at 44 Hz so that the frequency matches the second experiment run at the same conditions and a sample frequency of 4 Hz. The symbols represent synthetic and experimental data while the lines are best fit to the axial dispersion model.

4.5.5 Model fitting

The fitted model parameters of the axial dispersion model are sensitive to the physical configuration like the volume of the lines, the detector sampling, the assumed boundary conditions, the start time (t_0), and the time at which the curve reaches a plateau.

t_0

When the dispersion in the lines is very small compared to the system dispersion, we ignore the signal during that time and assume that $t_0 = t_{0,\mathrm{MS}} - t_{\mathrm{lines}}$, where $t_{0,\mathrm{MS}}$ is the original time as recorded by the MS. The 0.9 m MS capillary line also introduces a time delay to the RTD curve. By measuring the residence time just below the reactor after the valve, we quantify both the detector delay and the delay due to the lines (but not below the grid): $t_0 = t_{0,\mathrm{MS}} - t_{\mathrm{lines}} - t_{\mathrm{detector}}$. Ideally, the valve switches at the same time as when the MS begins collecting data. Triggering a solenoid valve and the analysis electronically minimizes random error compared to turning the valve manually. In our 4-way valve configuration, $t_{\mathrm{lines}} - t_{\mathrm{detector}}$ was 7.3 s, 6.6 s, and 5.7 s at U_{g} =10 , 20 , and 60 mm s^{-1}, respectively. For the bolus injection, $t_{\mathrm{lines}} - t_{\mathrm{detector}}$ was 6.9 s, 5.5 s, and 4.6 s. An error assigning this time affects the best fit approximation of the vessel mean residence time and consequently N_{Pe}. The importance of the impact increases as the residence time decreases (increasing gas velocity (Figure 4.19). However, the change in $N_{\mathrm{Pe}}$is proportional to the relative change in time. In our case, the best fit N_{Pe}drops from 42 with assuming $t_0 = 4$ s to 25 assuming $t_0 = 5$ s for the 8-way valve configuration at 60 mm s^{-1} and the n_{CSTR} decreases from 22 to 14.

Plateau

A second contribution to error in interpreting the RTD is related to the plateaus or the tail. A long tail indicates dead volume or adsorption, neither of which are accounted for in the one-dimensional axial dispersion model. A tail increases the mean residence time and variance disproportionately. The challenge is to decide at which point the curve has reached a steady value. When the dead volumes and adsorption phenomena are negligible $N_{\mathrm{Pe}}$and $\bar{t}$ are insensitive to the contribution from a long tail or the cut-off time fitting the RTD curve. In Figure 4.20, when the MS sampled the effluent at 4 Hz, we assumed that the signal reached a steady value, $G(t) = 1$ at $t = 25$ s. Regardless if we had assumed the curve plateaued at $t = 30$ s or $t = 55$ s, the best fit value of $N_{\mathrm{Pe}}$is the same. For the bolus input function, we assumed that the time the peak reached a maximum, $C_{\max}$ was $G(t) = 1$. This assumption is invalid when the dispersion is high and the pulse volume is insufficient to reach the same

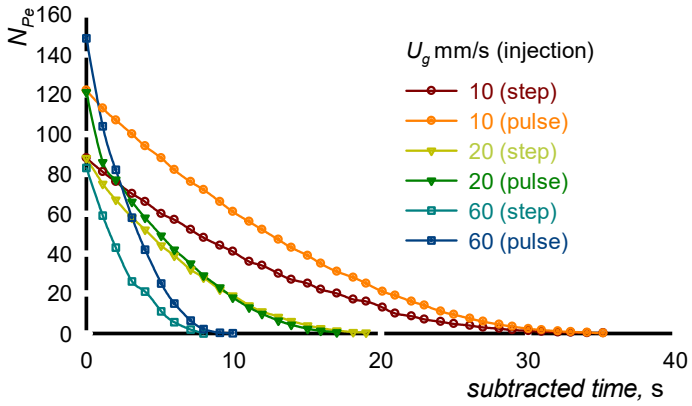

Figure 4.19 N_{Pe}vs subtracted time from a step and pulse response for $U_{\mathrm{g}} = 10\,,\ 20\,$and $60\,\mathrm{mm\,s^{-1}}$. We applied the axial dispersion model to fit the data to calculate N_{Pe} assuming $t_0 = t_{0,\mathrm{MS}} - t_{\mathrm{lines}} - t_{\mathrm{detector}}$. We then subtracted 1 s from t_0 in increments and recalculated N_{Pe}.

value as for the step pulse input. With the bolus injection, N_{Pe}decreased by more than a factor of two in some cases when increasing the time beyond $G(t) = 1$. This variation in N_{Pe}suggests that additional phenomena like diffusion, gas recirculation, or dead volume must be considered. This injection mode is much more sensitive to these phenomena compared to an input pulse where tailing was imperceptible.

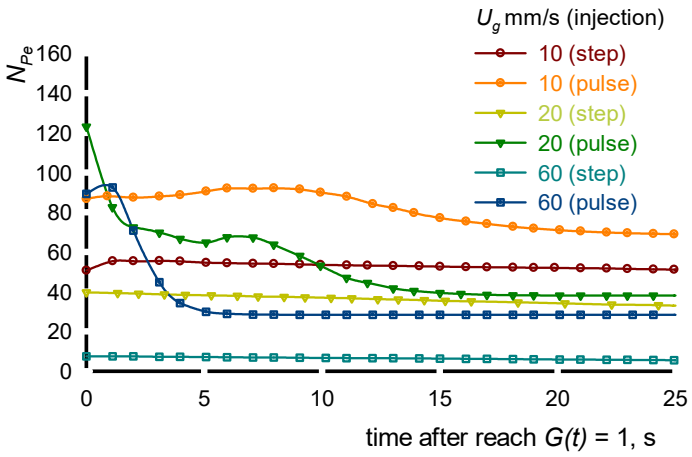

Figure 4.20 Best fit N_{Pe}vs time after reaching $C_{\max}$ $---$ $G(t) = 1$. To assess the effect of the tail, we fit the parameters $\bar{t}$ and N_{Pe}at times beyond what was necessary to reach $C_{\max}$ (x-axis) $N_{\mathrm{Pe}}$is independent of the additional time in the 4-way valve configuration (dark red curve, lime, and dark cyan) the . For the 8-way valve configuration (orange, green, and navy blue), N_{Pe}decreases with increasing time

4.5.6 Tracers

We choose a tracer that follows the path of the substrates identically and so match the physico-chemical properties—ρ, μ, and diffusivity of the species of interest.[137] A good tracer is easy to detect, inert, and absent of interactions with walls or other species (absorption/adsorption, or chemisorption).[21] However, often we must compromise between a good tracer and one that we can detect but the consequences are that the path the tracer is not identical or that it introduces diffusional affects. Any type of interaction with the system is undesirable. Moreover, its introduction must not perturb the vessel hydrodynamics, like an instantaneous pulse.[137]

To analyze the effect of the nature of the tracers on RTD response, we first injected argon in the micro reactor. At time zero, we switched the 4-way valve or the 8-way valve to a mixture of carbon dioxide (CO_2), carbon monoxide (CO), hydrogen (H_2) and methane (CH_4). The mass spectrometer detected each gas at a frequency of 2 Hz. We analyzed the residence time distribution in an empty tube (Figure 4.21 (a) and (c)) and with 9.15 g of FCC (Figure 4.21 (b) and (d)). Hydrogen, the lightest gas, exits the reactor 10.0(19) s before the other gases. CO and CH_4 have the same hydrodynamic behavior with and without the catalyst. However,CO_2 is delayed by 16(4) s in presence of FCC compared with CO and CH_4. We observed the same tendency at a velocity of 20 mm s^{-1} and 60 mm s^{-1} with less important delay for CO_2 and H_2 (data not shown). Absorption of CO_2 by FCC may cause the delay while future tests will elaborate.

4.6 Conclusion

The residence time distribution identifies mal-distribution and bypassing in flow systems and stirred tanks but the experimental set-up requires care to minimize errors due to the mechanical configuration, environmental conditions and tracer physico-chemical properties, mathematical treatment, and analytical instrumentation (Appendix 4.7.2). Fitting the RTD curve to an axial dispersion model will identify diffusion and backmixing phenomena—high $N_{\mathrm{Pe}}(> 20 - 50)$ represents plug flow while $N_{\mathrm{Pe}} < 10$ is backmixed. Multi-zone models are required to characterize systems with bypassing and dead zones in the system.

Boundary conditions which define the analytical solution of the axial dispersion model—open-open, closed-closed, open-closed, and closed-open—are only one of many contributions to the uncertainty of assessing the RTD. In our 8 mm diameter, 360 mm height microreactor, an 8-way valve that introduces a bolus pulse best identifies tailing. For a heaviside step pulse, controlling the pressure on the vent side to match the reactor side, minimizes flow pertur-

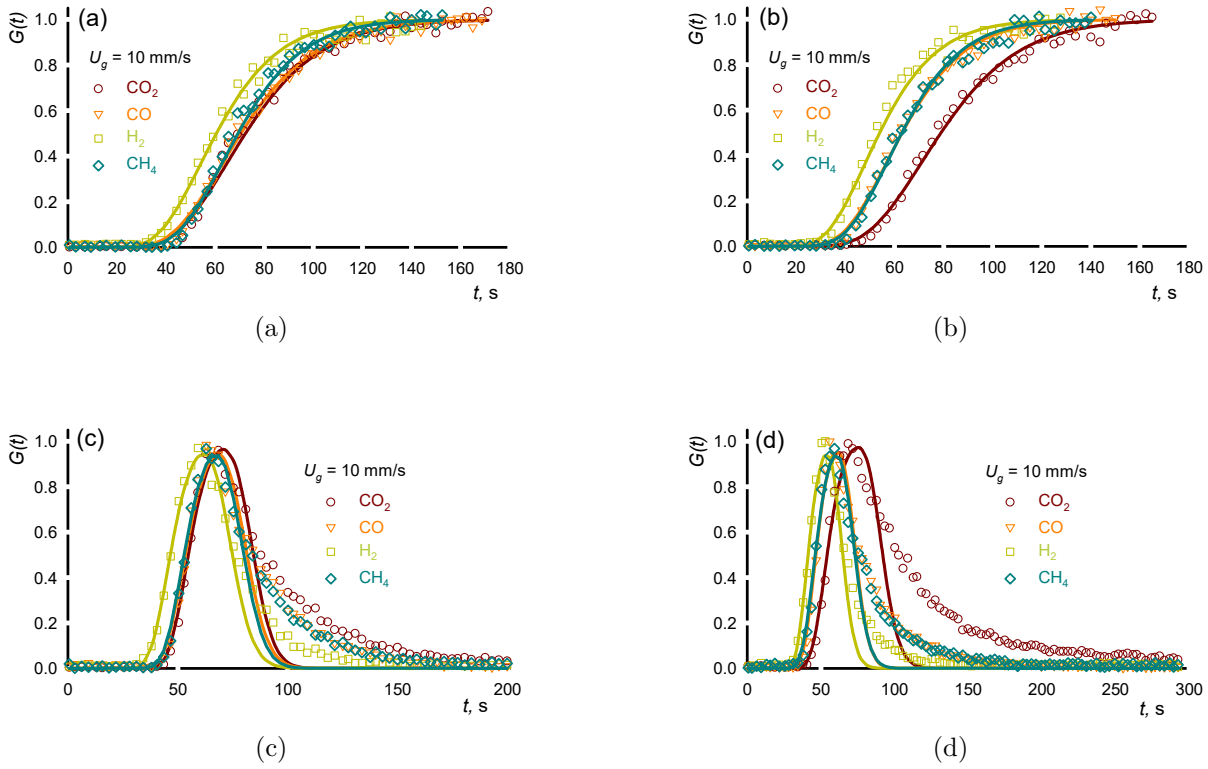

Figure 4.21 Effect of the tracers on: $G(t)$ vs time. Argon was initially injected in the reactor with a velocity of $10\,\mathrm{mm\,s^{-1}}$. At the time equals 0 , (a) and (b) we switched the 4-way valve for a gas mixture of 15 % CO_2, 15 % CO, 20 % H_2, 15 % CH_4 and the balance Ar. (c) and (d) we switched the 8-way valve for the same gas mixture. (a) and (c) empty tube, (b) and (d) reactor are filled with 9.15 g of FCC. The dots represent experimental data while the continuous line is the axial dispersion model after fitting each parameter.

bations when switching the valve between two mass flow controllers. The model parameter estimates, τ and N_{Pe} or n_{CSTR} are less sensitive to experimental errors when $N_{\mathrm{Pe}} < 10$ (high dispersion) compared to plug flow and short residence times ($t < 20\,\mathrm{s}$). Indeed, at a gas velocity of $60\,\mathrm{mm\,s^{-1}}$ and a mean residence time of 5 s, the uncertainty in the oxygen concentration was greater than 10 % ($\Delta_{\mathrm{o_2}} \approx 15\,\%$) in the region $0.1 < G(\tau) < 0.9$.

The detector response and sensitivity contribute to the uncertainty in the measure of concentration and thus first and second moments (residence time and variance). For the mass spectrometer, when the sample frequency was greater than 20 Hz, the uncertainty in the measured concentration increased to $\Delta_{95\,\%,n=7} = 0.15$. We choose a tracer that best follows the flow pattern of the fluid phase but must be easily detected. However, tracers adsorb to surfaces, which produces a long tail and which will increase the residence time and variance.

Researchers apply RTD broadly to flow systems but when the time in the system is less than 20 % of the total time, deriving accurate model parameters requires a tremendous attention to detail. The main applications in chemical engineering are fluidized and fixed bed, stirring tanks, heat exchangers, and distillation or absorption columns. In the mixing field, micro devices and microchannel by CFD and experiments are new applications where RTD is an essential approach to understand the global fluid dynamics.[16] Coupling reactive gases with an inert tracer is an area of future research that could better evaluate system dynamics. Another application is to identify the effect of pore size distribution on RTD as a compliment to turnover number in catalysis.

4.7 Appendix

4.7.1 Experimental procedure to conduct an RTD test

To perform accurate RTD tests, we established a precise procedure. We repeated twice each experiment except for the ten repetitions tests.

Procedure for the 4-way valve

1. Apply the same velocity for argon and air stream;
2. Insure the 4-way valve is on the argon stream line and there is only argon inside the reactor;
3. Start the mass spectrometer (MS) software;
4. Wait 1 minute;
5. Switch the 4-way valve from argon to air;
6. Wait 3 minutes (for $U_g = 10\,mm\,s^{-1}$), 2 minutes (for $U_g = 20\,mm\,s^{-1}$) or 1.5 minutes (for $U_g = 60\,mm\,s^{-1}$);
7. Stop the MS software;
8. Switch back the 4-way valve to argon;
9. Before a new experiment: wait 3 minutes (for $U_g = 10\,mm\,s^{-1}$), 2 minutes (for $U_g = 20\,mm\,s^{-1}$) or 1.5 minutes (for $U_g = 60\,mm\,s^{-1}$).

Procedure for the 8-way valve

1. Apply the same velocity for argon and air stream;
2. Insure position A on the 8-way valve (Figure 4.11 (a));

3. Start the mass spectrometer (MS) software;
4. Wait 3 minutes (for $U_g = 10\,mm\,s^{-1}$), 2 minutes (for $U_g = 20\,mm\,s^{-1}$) or 1 minute (for $U_g = 60\,mm\,s^{-1}$);
5. Switch to position B with the 8-way valve (Figure 4.11 (b));
6. Wait 2 minutes (for $U_g = 10\,mm\,s^{-1}$) or 1 minute (for $U_g = 20$ and $60\,mm\,s^{-1}$);
7. Stop the MS software;
8. Switch back to the 8-way valve position 1;
9. Before a new experiment: wait 1 minute.

4.7.2 Contributions to errors while measuring RTD

Mechanical

1. Valve configuration—3-way, 4-way, bolus
2. Valve leakage
3. Slow valve switch
4. Exit configuration: Possible ingress of air at the exit
5. System ΔP that changes gas velocity along the column
6. Hold up in tees for sample line and ΔP taps
7. Grid distribution: high ΔP improves distribution but increases residence time in downstream lines
8. Volume of chamber/windbox below grid
9. Precision of the flowmeter (rotameter versus MFC)
10. Large dead volume

Physicochemical

1. Gas properties—diffusivity
2. Adsorption
3. Temperature of the reactor/gas/room
4. Ambient pressure (remember to measure it)

Mathematical

1. Assumed boundary conditions
2. Plateau—maximum concentration to normalize data
3. Valve switch defining time zero
4. Time to reach the plateau, or length of tail

Instrumental

1. Sample frequency
2. Instrument resolution
3. Dispersion in sample line and analytical instrument
4. Detector blockage (particles, water)

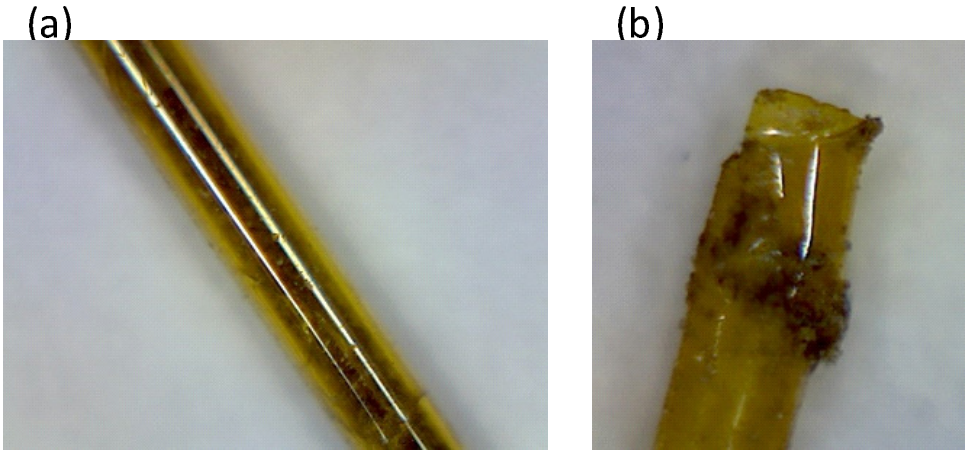

Figure 4.22 Mass spectrometer capillary blocked by particles (blacks spots on the capillary wall). (a) Capillary (b) Zoom on the capillary extremity.

CHAPITRE 5 ARTICLE 2: RESIDENCE TIME DISTRIBUTION IN FLUIDIZED BEDS: DIFFUSION, DISPERSION, ADSORPTION

Ariane Bérard, Bruno Blais, Gregory S. Patience

Journal: Advanced Powder Technology

reçu: 15 juillet 2020 **révisé:** - **accepté:** -

5.1 Abstract

Residence time distribution (RTD) is a diagnostic tool to evaluate non-homogeneity—channeling, dispersion, dead volume, and back-mixing—in flow systems. Understanding the flow patterns in experimental reactors is imperative to derive the reaction kinetics. However, characterizing the hydrodynamics is compromised when the ancillary volumes are several times larger than the reactor volume. Here, we measured the RTD in an 8 mm diameter quartz micro fluidized bed reactor to examine relationship between gas physico-chemical properties and porous and non-porous powder. We tested syngas species and noble gases with a pulse injection and a Heaviside step input function. Deviation from plug flow model was undetectable with the step input. For all catalysts tested, He and H_2 egress the reactor faster compared to Kr and syngas species. Tracer egressed 7 % sooner with equilibrated vanadium pyrophosphate (VPP) with a lower porosity versus calcined (virgin) VPP: which suggests this method is sensitive enough to detect changes in catalyst morphology and could be applied to probe *in situ* coking, for example. Both RTD curves for CO or CH_4 had an extended tail while the curve for CO_2 had additionally a delay, due to adsorption (a chromatographic effect). RTD experiments with krypton, which has a lower diffusion coefficient, has a longer residence time compared to CO or CH_4 but shorter than CO_2, which confirms the reactive nature of the FCC surface with CO_2. These data demonstrate that the choice of tracer contributes to the RTD and must be taken into account when building reactor models.

keywords: residence time distribution, tracers, adsorption, diffusion, porosity

5.2 Introduction

Residence time distribution is a diagnostic tool to evaluate the deviation from ideal flow behaviour—plug flow and backmixed—in vessels. The technique consists of introducing an inert tracer as a pulse or step function and monitoring its concentration with time at the

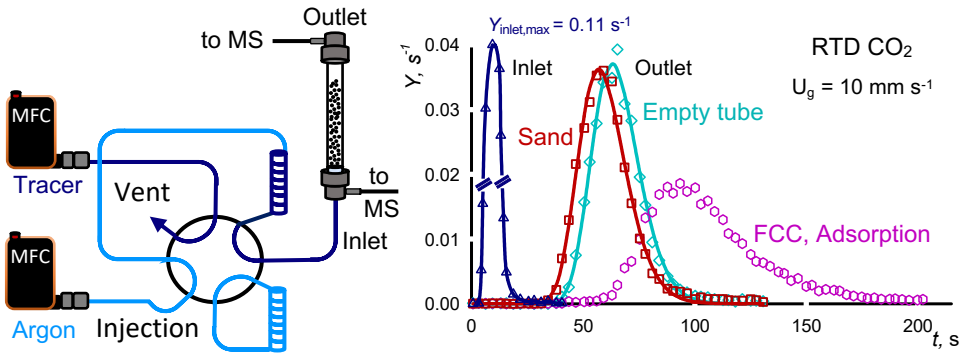

Figure 5.1 Graphical abstract

exit or anywhere along the system. We then develop hydrodynamic models that characterize the tracer profile. Applications in chemical engineering include assessing bypassing in distillation columns[9] and the extent of mixing of pharmaceutical active ingredients[9,10], for example. Reaction engineers characterize experimental and industrial fixed beds, fluidized beds, trickle beds and other types to then derive reaction kinetics that account for the hydrodynamics.[12,16,25,129,142]

Traditionally, we select tracers that are convenient and easy to detect—oxygen, nitrogen (with thermal conductivity detectors), radioactive argon and krypton (NaI scintillator detectors), CO_2 (UV on-line analyzers). High frequency mass spectrometers have the capability to detect multiple gases simultaneously to identify the contribution of gas physicochemical properties to the RTD curves. Good tracers are easily detected at low concentration (that minimize any perturbation that arises when introduced to the system), and are inert with respect to any materials and compounds in the system[21,77,143]. Furthermore, we must report the volumes of all ancillary lines to evaluate their contribution on the RTD curve[144]. However, in the case when the inlet and exit boundary condition concentrations are measured in line, the contribution of entrance and exit to the variance is obviated. This is also the case when measuring the electrical conductivity of a fluid in a pipe[145].

The interphase transport between gas and solids depend on the tracers and their absorption/desorption kinetics[25,146,147]. For step mode, similar physicochemical properties—μ, ρ and diffusivity with respect to the fluid—are favoured. Otherwise, researchers apply the pulse mode[137]. In this regard, other phenomena affect the RTD of systems charged with porous and large catalyst[57]. The solid motion within the bed influences the gas mixing characteristics of the bulk gas, but also of the gas within pores[57]. If the pores are large, intraparticle diffusion occurs as well as convection[92]. Species that enter the pores may adsorb to the

surface and then desorb as the concentration changes. Additionally, at low velocity, the accessibility of species to the pores is larger, which increases the contact time and consequently the RTD [91]. Analogically, in the analytical field and separations, the most efficient HPLC columns are highly porous (giga-porosity) [92].

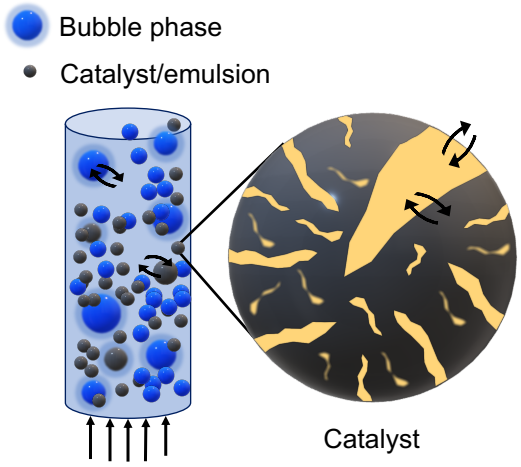

Figure 5.2 Mass transfer in fluidized bed reactor. The bubble phase is free of particles. The dense or emulsion phase includes the interstitial gas and particles while the solid phase consider catalyst with or without pores. In a porous catalyst the phenomena are intraparticle diffusivity and convection. Moreover, with some tracers adsorb than desorb from the outer catalyst surface and the surface in the pores. The arrows represent mass transfer between the different phases.

Gas mass transfer between bubbles and emulsion (and bubbles and the cloud-wake phase) dictates conversion and product selectivity (Figure 5.2). The solids phase is perfectly backmixed from the minimum fluidization velocity to beyond the turbulent velocity. Near U_{mf}, we assume the gas phase is essentially in plug flow. Bubble gas diameters and velocities are low and most of the gas passes through the emulsion. Deviation from plug flow increases with increasing gas velocity but a 6 CSTR model approximates the gas phase hydrodynamics of an 8 m diameter commercial acrylonitrile reactor operating in the turbulent regime at $0.7\,\mathrm{m\,s^{-1}}$. This test was completed with a non-adsorbing Kr tracer but for adsorbing gases, a perfectly backmixed model may characterize the gas phase hydrodynamics than multiple tanks-in-series. Here we characterize fluidized bed hydrodynamics with a single-phase axial

dispersion model that lumps bubbles and emulsion as a unique phase[56].

Here we quantify how the RTD varies as a function of the injection mode, velocity, porosity, Geldart group A and B powders, and tracers. We fit the effluent tracer concentration with the axial dispersion model as, in general, the data correlate with this flow pattern.

5.3 Experimental

5.3.1 Catalysts

We studied the residence time distribution of 4 Geldart group A powders:

1. **Fluid Catalytic Cracking catalyst (FCC)**: porous catalyst from Total.
2. **vanadyl hydrogen phosphate hemihydrate (VPOP precursor)**: $VOHPO_4 \cdot 0.5\,H_2O$ prepared in an organic medium with iso-butanol and benzyl alcohol. The process comprises precursor micronization to 2.6 µm following by spray drying with polysilicic acid, which produces a precursor with a porous silica shell[148].
3. **vanadyl pyrophosphate calcined (VPPC)**: $VOHPO_4 \cdot 0.5\,H_2O$ calcined at 390 °C. The silica shell is porous, and surface is rough[82,149].
4. **vanadyl pyrophosphate equilibrated (VPPE)**: This sample operated in an industrial circulating reactor for over 2 years. X-ray photoelectron spectroscopy analysis detected the presence of iron (3.5 % atom) on the surface due to erosion and corrosion of the reactor walls with time and subsequently accumulated on the catalyst. The silica shell is uniform, dense and smooth[82].

To quantify how porosity affects the RTD, we also tested sand—a nonporous Geldart group B particle. The sand particles are angular while the catalyst powders were more spherical. The precursor has small (satellite) particles attached to the mother particle while the equilibrated VPP has very few of these satellite particles but it does have some angular particles that are produced when the shell breaks (Figure 5.3). The U_{mf}, particle diameter, and density of the sand is highest at $13\,mm\,s^{-1}$, 87 µm, and $2280\,kg\,m^{-3}$ but the d_{50} of the precursor is not much smaller at 80 µm (Table 5.1). The Hausner ratio of all the powders varies little (from 1.09 for the precursor to 1.13 for all others), while the angle of repose of the sand is almost double that of all the catalysts. The BJH surface area correlates reasonably well with the pore volume (but not very well with the BET surface area, and not at all with the pore diameter)[150].

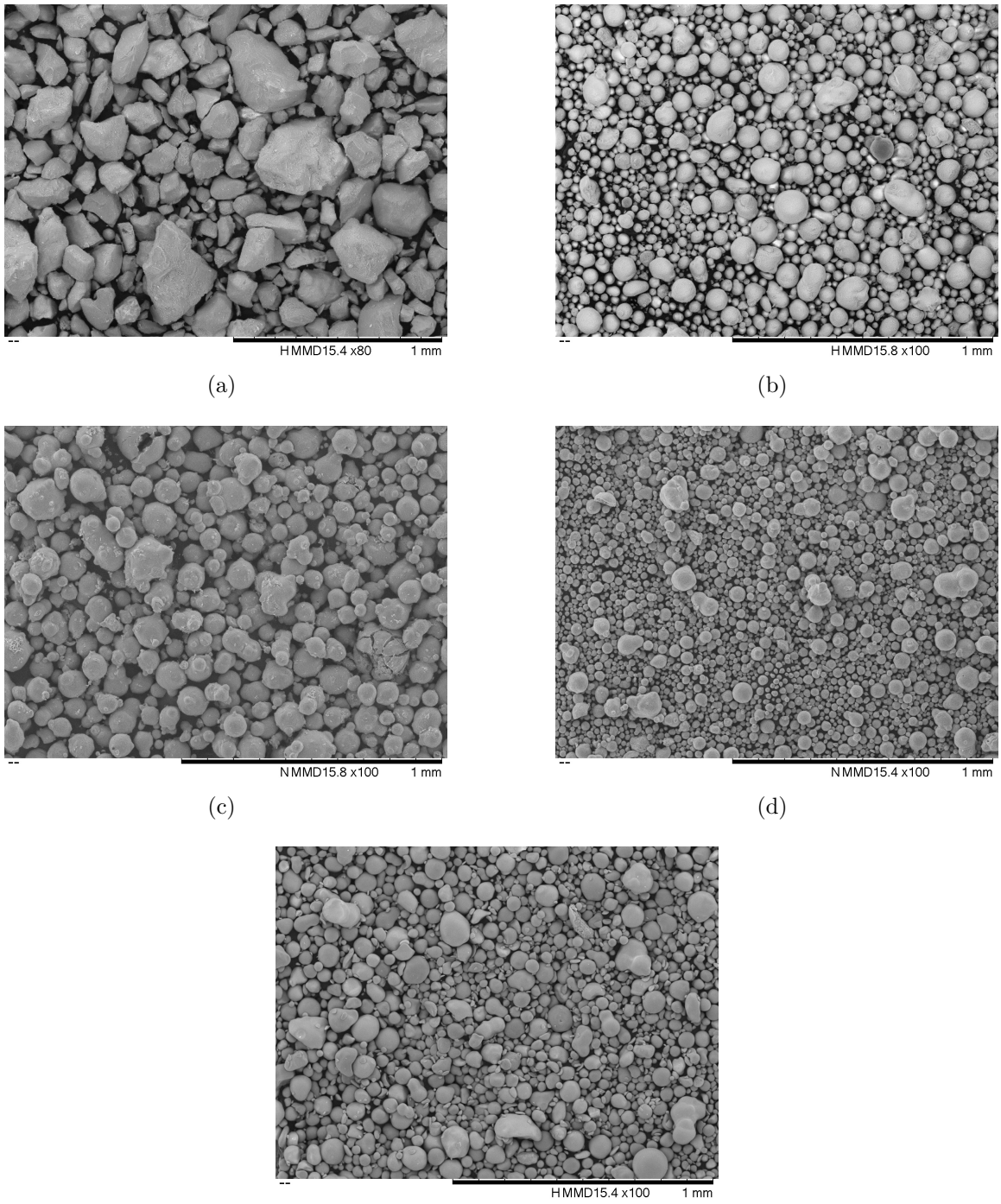

Figure 5.3 SEM images of the powders: (a) Sand—large cuboid or polygonal particles; (b) FCC—most particles are spheroids; (c) precusor—spheroid particles most of which have satellite particles (but not asperities); (d) VPPC—the VPP particles have less satellite particles and so the average d_{50} is smaller; and (e) VPPE—after two years of continual operation at 400 °C the particles become shiny and some fracture to form elongated angular shapes.

Table 5.1 Catalyst properties. The uncertainties represent standard deviation.

Property	FCC	VPOP	VPPC	VPPE	Sand	n	Comments
Composition	mixed[1]	$VOHPO_4 \cdot 0.5\,H_2O$	$(VO)_2P_2O_7$	$(VO)_2P_2O_7$ + β-$VOPO_4$	Silica (SiO_2)	-	-
Geldart Group	A	A	A	A	B	-	-
U_{mf}, $mm\,s^{-1}$	2.2	4.7	5.0	3.9	13	1	-
ρ_b, $kg\,m^{-3}$	874(4)	905(9)	899(33)	1098(3)	1328(10)	5	Scott density
	853(19)	913(8)	913(17)	1114(9)	1366(27)	5	Poured density
	965(10)	997(16)	1033(18)	1259(18)	1529(47)	5	Tapped density
	945	-	-	-	1426	1	Hg porosimetry
ρ_p, $kg\,m^{-3}$	1610	-	-	-	2279	1	Hg porosimetry
	-	1551(53)	2032(57)	2018(104)	-	5	Water
ρ_{sk}, $kg\,m^{-3}$	2360(2)	2496(3)	2739(1)	2774(6)	2777(5)	10	Gas
ϵ_v	0.44	0.42	0.56	0.46	0.37	1	-
H_r	1.13(3)	1.09(2)	1.13(3)	1.13(3)	1.12(4)	5	Hausner ratio
θ_{angle}, °	24(1)	26(2)	24(2)	23(1)	44(2)	6	Angle of repose
d_{10}, µm	39.4(4)	50(1)	28(1)	32.3(2)	58(2)	3	Laser diffraction
d_{50}, µm	64.0(6)	80(2)	59(3)	55.7(1)	87(2)	3	Laser diffraction
d_{90}, µm	104(1)	137(5)	116(3)	91.3(3)	120(2)	3	Laser diffraction
ϕ	0.99	0.45	0.30	0.43	0.68	1	Ergun equation
S_A, $m^2\,g^{-1}$	93.3	22.2	23.3	11.6	0.56	1	BET
	34.5	33.8	28.0	15.3	0.41	1	BJH[2]
v_{pore}, $mL\,g^{-1}$	0.145	0.114	0.139	0.090	0.003	1	BJH[2]
d_{pore}, nm	38	14 [82]	-	15 [82]	21	1	BJH[2]

[1] FCC catalysts include a variety of zeolite crystallite sizes and particle properties [120]

[2] BJH: desorption branch

5.3.2 Gases

For each experiment, argon is the inert gas (Air Liquide©). To compare residence time distribution (RTD) with several tracers, we performed the tests with various concentrations of noble gases, He, Ar, and Kr, and gases characteristic of methane partial oxidation to syngas—CO, CH_4, CO_2, O_2, N_2 (all mole %):

1. **Cylinder 1**: Air - 21 % O_2 and 79 % N_2
2. **Cylinder 2**: 15 % CO_2, 15.3 % CO, 19.9 % H_2, 14.7 % CH_4, and the balance argon
3. **Cylinder 3**: 0.987 % CO, 2.05 % He, 1.93 % Kr, 5.00 % O_2, and the balance argon

We chose Cylinder 3 because the gases were inert in the conditions we tested and they covered a wide range of diffusivity (Table 5.2).

Table 5.2 Diffusivities in argon and atomic mass for gases. All diffusivities are calculated with the correlation of Fuller – Schettler – Gidding[151]. This correlation is valid for non-polar gases at 101 kPa.

Gases	D $[cm^2\,s^{-1}]$ $T = 25°C$	D $[cm^2\,s^{-1}]$ $T = 300°C$	molar mass $[g\,mol^{-1}]$
Kr	0.136	0.436	84
CO_2	0.150	0.479	44
O_2	0.194	0.619	32
CO	0.195	0.622	28
CH_4	0.208	0.664	16
He	0.716	2.90	4
H_2	0.796	2.54	2

5.3.3 Micro reactor set-up

We ran all tests in an 8 mm diameter quartz tube 36 cm long (Figure 5.4). Regardless of the bulk density of the sample, we loaded the tube until the tapped bed height reached 18 cm (Table 5.3). Two Brooks mass flow controllers (MFC) maintained a volumetric feed rate to the reactor at 10 mm s^{-1} to 30 mm s^{-1}. A Hiden quadrupole mass spectrometer (MS) with a pulse ion counting (SCEM) detector monitored the effluent concentration on-line[23]. The operating pressure was 6.2×10^{-5} mPa. The capillary was 0.9 m long with a 0.20 mm internal diameter and a heated sheath kept it at 160 °C.

Step injection: The MFC kept a constant stream of argon to the micro-reactor then, at $t = 0$ s, we turned on the MS and at $t = 60$ s, we manually rotated the 4-way valve stem to

Table 5.3 Characteristic RTD experimental operating conditions as function of powder. The powder mass corresponds to that charged to the micro reactor and vibrated until the height was constant—tapped bed height of 18 cm.

Catalyst	Quantity [g]	$10\,\mathrm{mm\,s^{-1}}$ $(N_{\mathrm{Re}} = 6.8)^1$	$30\,\mathrm{mm\,s^{-1}}$ $(N_{\mathrm{Re}} = 20)^1$	Geldart group
FCC	8.19	$4.5 \times U_{\mathrm{mf}}$	$14 \times U_{\mathrm{mf}}$	A
VPOP	9.16	$2.1 \times U_{\mathrm{mf}}$	$6 \times U_{\mathrm{mf}}$	A
VPPC	10.0	$2.0 \times U_{\mathrm{mf}}$	$6 \times U_{\mathrm{mf}}$	A
VPPE	11.9	$2.6 \times U_{\mathrm{mf}}$	$8 \times U_{\mathrm{mf}}$	A
Sand	13.5	$0.77 \times U_{\mathrm{mf}}$	$2.3 \times U_{\mathrm{mf}}$	B

switch from Ar to the tracer gas. After the delay time for the tracer to traverse the system and reach the MS, the effluent concentration increased until reaching a constant value[12].

Pulse injection: The sequence was the same as the step injection but the feed manifold had two 10 mL loops and a 8-way valve (Figure 5.4). We turned the MS on at $t = 0\,\mathrm{s}$ while Ar passed through one sample loop leading to the reactor and tracer filled the second sample loop (and evacuated to exhaust). At $t = 60\,\mathrm{s}$, we rotated the 8-way valve stem and the Ar stream purged the second loop and then entered the reactor. We ensured that the flow configuration on both sides were equal (equal volume of the loop and the same number of valve ports). Another advantage of this system is that the same MFC feeds the reactor and so the volumetric flow rate is exactly the same.

The residence time distribution (RTD) of any system includes contributions from piping to the reactor, the plenum region below the grid, the catalyst, vapour phase above the bed, piping to the analyzer, and finally the analyzer response (unless you measure the input function along the system).[71,145] We minimize the extraneous volumes below and above the catalytic bed to ensure that the contribution to the system variance is mostly due to the reactor. For each set of experiments (step or pulse injection), we measured the RTD below the grid twice, which serves as an inlet boundary condition. The residence time at this point included the time for the gas to pass through the lines and the MS capillary. We substracted this value from the total time metered at the outlet of the reactor. We repeated twice the outlet RTD.

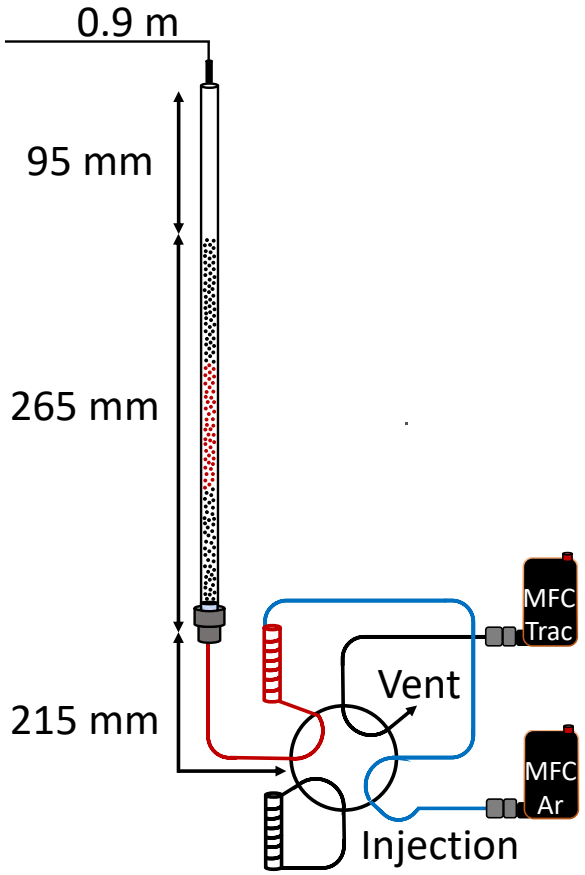

Figure 5.4 Fluidized bed reactor configuration. The quartz tube was 8 mm diameter and 360 mm long. The tapped bed height with all catalyst was 180 mm and it expanded to an average of 265 mm when fluidized. The mass spectrometer capillary was 0.9 mm long and 0.20 mm internal diameter. First, the 8-way valve is in the filling position (not shown) where argon goes to the reactor and the tracer fills a 10 mL sample loop. Then, at time $t = 60$ s, we switch the 8-way valve to the injection position. Argon (blue line) sweeps the tracer (red line) from the loop to the reactor.

5.3.4 Model

For a small deviation from plug flow, the axial dispersion model—analogous to Fick's law[33]—adequately characterizes residence time distributions:

$$\frac{\partial C}{\partial t} + u\frac{\partial C}{\partial z} = \mathcal{D}\frac{\partial^2 C}{\partial z^2} \tag{5.1}$$

where C is the tracer concentration, u is the tracer velocity and $\mathcal{D}$ is the axial dispersion coefficient. In non-dimensional form, we divide through by the ratio of velocity and a characteristic length, Z,:

$$\frac{\partial C}{\partial \theta} + \frac{\partial C}{\partial \xi} = \frac{1}{N_{\mathrm{Pe}}} \frac{\partial^2 C}{\partial \xi^2} \tag{5.2}$$

where $\theta = tu/Z$ (non-dimensional time), $\xi = z/Z$, (non-dimensional length), and $N_{\mathrm{Pe}} = uZ/\mathcal{D}$, the dimensionless Peclet number. The boundary conditions for a closed-open system are[11,71]:

$$C_{0,\xi} = 0, \theta = 0 \; and \; 0 \leq \xi \leq 1 \tag{5.3}$$

$$C_{\theta,0} = \rho_0, \theta > 0 \tag{5.4}$$

$$\frac{\mathrm{d}C_{\theta,1}}{\mathrm{d}\xi} = 0, \theta > 0 \tag{5.5}$$

The exact analytic solution is[71]:

$$G(\theta) = \frac{1}{2} \left[\mathrm{erfc} \sqrt{\frac{N_{\mathrm{Pe}}}{4\theta} (1 - \theta)} + \mathrm{e}^{N_{\mathrm{Pe}}} \mathrm{erfc} \sqrt{\frac{N_{\mathrm{Pe}}}{4\theta} (1 + \theta)} \right] \tag{5.6}$$

The mass spectrometer monitored the concentration of each tracer with time. We subtracted the time it took the tracer to reach the bottom of the reactor and the transit time in the MS capillary from the MS time. We minimized the sum of squares of the error (SSE) between the model predictions and experimental data from the bottom of the leading edge to 80 % of the trailing edge to calculate N_{Pe}. Finally, we normalized the data and the model to reach an area under the curves equal to one.

$$Y = \frac{C_i}{\sum C_i \Delta t} \tag{5.7}$$

The Peclet number characterizes the hydrodynamic of a system and is related to the number of continuous stirred tanks in series (N_{CSTR}):

$$N_{\mathrm{Pe}} = 2(N_{\mathrm{CSTR}} - 1) \tag{5.8}$$

The model is accurate for a step injection and a pulse injection without back-mixing, by-passing, or stagnant zones. For pulse injection, the mean residence time for the continuous

and discrete forms are[33] :

$$\bar{t}_{\text{pulse}} = \frac{\int_0^\infty tC\,\mathrm{d}t}{\int_0^\infty C\,\mathrm{d}t} \cong \frac{\sum t_i C_i \Delta t_i}{\sum C_i \Delta t_i} \tag{5.9}$$

And the variance is[33]:

$$\sigma^2_{\text{pulse}} = \frac{\int_0^\infty t^2 C\,\mathrm{d}t}{\int_0^\infty C\,\mathrm{d}t} - \bar{t}^2_{\text{pulse}} \cong \frac{\sum t_i^2 C_i \Delta t_i}{\sum C_i \Delta t_i} - \bar{t}^2_{\text{pulse}} \tag{5.10}$$

5.4 Results and discussion

5.4.1 Empty tube analysis

The residence time distribution is a function of the stream flow[12]. We compared inlet velocity of $10\,\mathrm{mm\,s^{-1}}$ and $30\,\mathrm{mm\,s^{-1}}$ for a pulse injection in an empty tube (Figure 5.5 – a and b) to isolate its response from that when we load the reactor with catalyst. For all RTD analyses, we fit the the axial dispersion model to experiments with the syngas compounds (CO_2, CO, CH_4, and H_2). When the intlet velocity increases from $10\,\mathrm{mm\,s^{-1}}$ to $30\,\mathrm{mm\,s^{-1}}$, the tracer concentrations of CO_2, CO and CH_4 deviate from axial dispersion model as the trailing edge becomes more prominent (Figure 5.5 – b). The Reynolds number at $10\,\mathrm{mm\,s^{-1}}$ and $30\,\mathrm{mm\,s^{-1}}$ are 6.8 and 20 The flow regime is laminar. Curiously, the model fits the H_2 data perfectly at both velocities. In laminar flow, we would expect a large deviation from the axial dispersion model due to the radial parabolic velocity gradient of the laminar regime; however, for gases in small diameter tubes, the radial diffusion is apparently sufficiently high to minimize concentration gradients, particularly for gases with high diffusivity.

For a perfect plug flow entrance velocity profile, the boundary layer grows until it reaches the parabolic velocity profile. The universal entrance length applies to both Newtonian and non-Newtonian fluids. The distance to reach 99 % of the fully developed centreline velocity, z_{99} is a function of Reynolds number, N_{Re}, and the tube diameter, D_{reactor}[152]:

$$z_{99} = 0.056 N_{\text{Re}} D_{\text{reactor}} \tag{5.11}$$

The entrance lengths at $10\,\mathrm{mm\,s^{-1}}$ and $30\,\mathrm{mm\,s^{-1}}$ (N_{Re}=6.8 and N_{Re}=20.) are 3 mm and 9 mm, which is much smaller than the total length of 360 mm. (Note that Equation 5.11 applies for $N_{\text{Re}} > 200$, but it still demonstrates that the entrance length is short compared to the column length). Thus, the velocity profile along the tube follows the parabolic Hagen-Poiseuille equation[153]:

$$V_{r_s} = V_0(1 - \frac{r^2}{R^2_{\text{reactor}}}) \tag{5.12}$$

where V_r is the axial velocity as a function of radius (r_s), V_0 is the maximum velocity at the centerline, and R_{reactor} is the reactor radius.

At $30\,\text{mm}\,\text{s}^{-1}$, hydrogen is the only compound for which the axial dispersion model fits the experimental data virtually perfectly ($R^2 = 0.998$) (Figure 5.5 –b), which is most likely attributable to its higher molecular diffusivity (at $\mathscr{D} = 0.796\,\text{cm}^2\,\text{s}^{-1}$ compared to CO_2, CO and CH_4 at 0.150 , 0.195 and $0.208\,\text{cm}^2\,\text{s}^{-1}$, respectively), which flushes the wall region at a low gas velocity more rapidly.

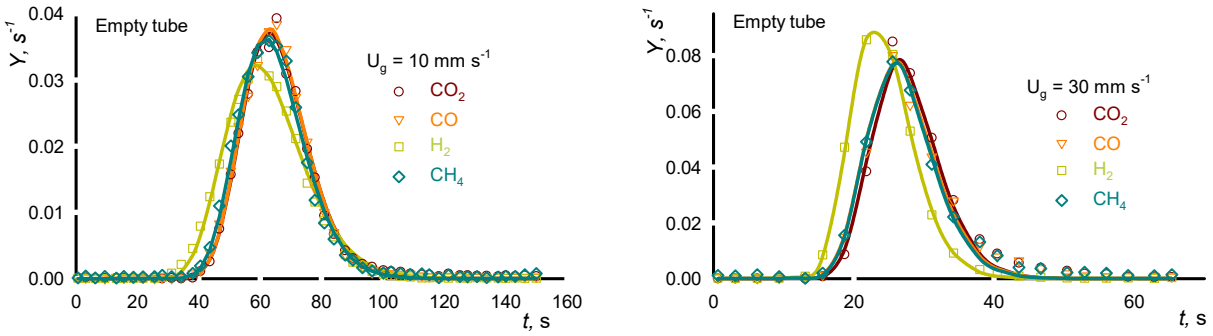

(a) (b)

Figure 5.5 Effect of velocity on RTD for an empty reactor. The curve represents $Y = \frac{C_i}{\sum C_i \Delta t}$ vs time with the area under the curve equal to one. Argon was initially injected in the reactor. At time $t = 0$, we turned the 8-way valve—pulse injection—to substitute argon with a mix of 15 % CO_2, 15 % CO, 20 % H_2, 15 % CH_4 and the balance Ar. The velocity is (a) $10\,\text{mm}\,\text{s}^{-1}$ and (b) $30\,\text{mm}\,\text{s}^{-1}$. The symbols represent the experimental data while the continuous lines are the axial dispersion model. Hydrogen is always the first to come out due to its higher diffusivity. At $30\,\text{mm}\,\text{s}^{-1}$ (b), a tail appears, which is consistent with expectation of a parabolic flow. Because the 1-D plug flow model applies at low gas velocities implies that the radial diffusion of the gases is sufficient to maintain a flat concentration profile. Even at higher gas velocities, the hydrogen diffusivity is high enough to maintain this flat profile.

With the same empty tube conditions for $30\,\text{mm}\,\text{s}^{-1}$, we compared two ways to inject the tracer—pulse and step (Figure 5.5–b and Figure 5.6). The axial dispersion model fits the experimental data well but the uncertainty of the approach to a constant value contributes to the uncertainty in the N_{Pe} For a Heaviside-step function, the standard deviation of the experimental data is on the same order of magnitude as the difference between the signal and the approach to a steady signal, so the uncertainty in identifying at one point the signal

achieves a steady value is much higher that for a step pulse. (Figure 5.6)[12].

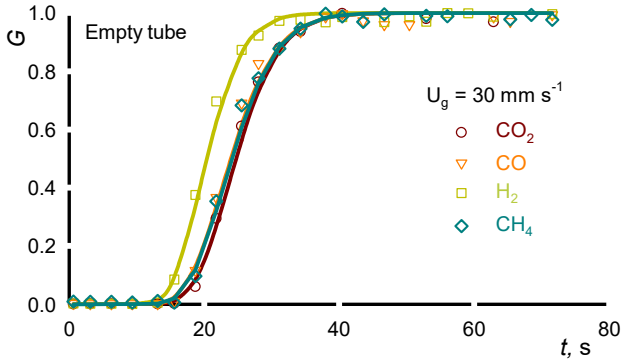

Figure 5.6 RTD of a step injection. The curve represents the concentration of the compounds normalized with respect to their maximum concentration. At time $t = 0$, we rotated the 4-way valve—step injection—to substitute the argon stream with a mix of 15 % CO_2, 15 % CO, 20 % H_2, 15 % CH_4 and a balance of Ar. The velocity was 30 mm s^{-1}. Hydrogen was always the first to come out due to its higher diffusivity.

We compared first and second moments for each pulse tracer injection test 10 and 30 mm s^{-1} (Table 5.4). First, we calculated the mean residence time ($\bar{t}_{in}$) and the variance (σ^2_{in}) at the inlet of the reactor. The values included the time for the gas to pass through the line before the reactor and the MS capillary ($\sigma^2_{in} = \sigma^2_{line} + \sigma^2_{MS}$). Then, the time the peak reaches a maximum (t_{peak}) is the total mean residence time subtracted by the time in the inlet line and MS divided by two ($t_{peak} = \bar{t}_{total} - \bar{t}_{in}/2$). The real mean residence time ($\bar{t}_{real}$) is the value calculated by previously subtracting the time of the inlet. This value represents the mean time for a tracer to pass through the reactor. The variance at the exit (σ^2_{out}) is the spread of the curves[33]. Peclet number (N_{Pe}) is a fitting parameter of the axial dispersion model while $N_{CSTR} = N_{Pe}/2 + 1$.

At 30 mm s^{-1}, the difference (Δ_t) between t_{peak} and $\bar{t}_{real}$ is 2 or 3 s while at 10 mm s^{-1} the value reaches 6 or 7 s for H_2 (Table 5.4). To explain this difference, we compared the residence time distribution at the inlet of the reactor (mass spectrometer + upstream line), and at the outlet for 10 mm s^{-1} and 30 mm s^{-1} in an empty tube (Figure 5.7). At low velocity, the average time that a molecule flows in the reactor is longer than the peak time due to the spread of the curve. Consequently, the variance increases ($< 930\ s^2 vs > 4000\ s^2$). The closer the curve shape approaches the injection time (inlet), the smaller is the difference between the peak and the transit time as we observed at 30 mm s^{-1}. Consequently, the data converge to plug flow behaviour. We observed the same trend for RTD with three Geldart group A powders at 10 and 30 mm s^{-1} (Supplementary file – Table S1).

Table 5.4 Comparison of moments (mean residence time and variance) at the inlet and outlet of the reactor, N_{Pe}, and number of CSTRs in series for an empty tube. Ar was initially injected in the reactor. At $t = 0$, we rotated the 8-way valve (pulse) to substitute argon with a gas mix of 15 % CO_2, 15 % CO, 20 % H_2, 15 % CH_4 and the balance Ar. $\bar{t}_{\mathrm{in}} = \bar{t}_{\mathrm{line}} + \bar{t}_{\mathrm{MS}}$, $\sigma^2_{\mathrm{in}} = \sigma^2_{\mathrm{line}} + \sigma^2_{\mathrm{MS}}$, $t_{\mathrm{peak}} = \bar{t}_{\mathrm{total}} - \bar{t}_{\mathrm{in}}/2$, $\Delta_t = \bar{t}_{\mathrm{real}} - t_{\mathrm{peak}}$, and $N_{\mathrm{Pe}} = 2(N_{\mathrm{CSTR}} - 1)$.

Tracer	$\bar{t}_{in}$ (s)	σ^2_{in} (s^2)	t_{peak} (s)	$\bar{t}_{real}$ (s)	Δ_{t} (s)	σ^2_{out} (s^2)	N_{Pe}	n_{CSTR}	R^2
	Pulse injection - $10\,\mathrm{mm\,s^{-1}}$								
CO_2	23	889	61	67	6	4531	73	38	0.994
CO	22	720	60	66	6	3956	74	38	0.994
H_2	20	544	56	62	6	4523	45	24	0.995
CH_4	31	2151	59	66	7	4701	68	35	0.995
	Pulse injection - $30\,\mathrm{mm\,s^{-1}}$								
CO_2	11	185	28	30	2	931	63	33	0.985
CO	11	186	27	29	2	881	58	30	0.989
H_2	9.2	118	23	25	2	625	58	30	0.998
CH_4	17	672	26	29	3	912	60	31	0.989

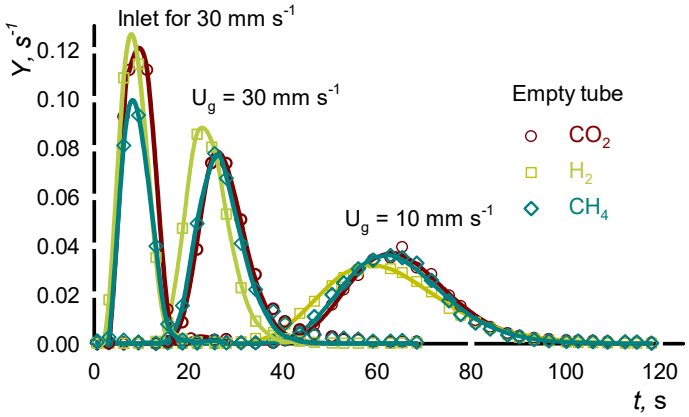

Figure 5.7 Comparison of the residence time distribution at the inlet and outlet of an empty tube. The curve represents $Y = \frac{C_i}{\sum C_i \Delta t}$ vs time with the area under the curve equals one. We measured RTD at the inlet of the reactor to calculate the passage time for gases through the mass spectrometer and the upstream line. We neglected CO because it is indistinguisable from the CH_4 trace.

5.4.2 Porosity analysis with oxygen - Geldart group A

We compared residence time distribution between V-P-O precursor (VPOP), vanadyl pyrophosphate calcined (VPPC), vanadyl pyrophosphate equilibrated (VPPE), and an empty tube at $U_g = 10\,mm\,s^{-1}$ (Figure 5.8–a) and $U_g = 30\,mm\,s^{-1}$ (Figure 5.8–b). All catalysts belong to the Geldart group A powder classification with a mean diameter (d_{50}) of 80(2) , 59(3) and 56.0(1) µm, respectively. At $10\,mm\,s^{-1}$, O_2 exits the reactor first for VPPE followed by VPOP and VPPC simultaneously and finally the empty tube (Figure 5.8–a). Solids in the reactor reduces the empty space, and for this reason, the tracer reaches the MS sooner, the RTD curve for the empty tube is always delayed. The difference between VPPE and VPOP/VPPC is due to porosity and surface area, which is 12 , 22 and $23\,m^3\,g^{-1}$, respectively (Table 5.1). When oxygen is injected into the reactor, it diffuses inside the pores before continuing its path to the exit. Consequently, the mean residence time is longer for catalyst with high surface area and porosity. In this study, VPPE has a surface area half the value of VPOP and VPPC and fewer pores[82]. The real mean residence time ($\bar{t}_{real}$) for VPPE is 55 s compared to 57 s for VPOP and VPPC (Supplementary file Table S1). VPPE equilibrated catalyst operated in the commercial butane oxidation circulating fludized bed for at least 2 years.[154] The commerical process circulated catalyst at a rate of over $1000\,kg\,s^{-1}$ and operated at 400 °C. The tremendous mechanical stresse and thermal stresses (related to local thermal excursions at the oxygen spargers) modified the catalyst so the surface SiO_2 shell changed from a rough porous texture to a glass type morphology with a smoother and rounder shell[82]. As a consequence of the change in porosity, the oxygen exits the reactor 2 seconds sooner with VPPE compared to either VPOP or VPPC.

Overall, when the flow rate increase to $30\,mm\,s^{-1}$, the mean residence time difference between all catalysts is negligible (Figure 5.8–b). Two hypotheses can account for these observations:

1. The gas flow rate is high enough that oxygen passes through the reactor without ever entering the pores;
2. Oxygen feed in the pores, but egresses at the same velocity rate. Then, the residence time distribution is the same as non-porous catalyst.

We highlight the fact that this operational procedure is sufficiently precise to identify differences in the RTD of essentially the same catalyst with a different porosity. For years, engineers have measured the residence time distribution to detect back-mixing or bypassing, understand hydrodynamics, interpret kinetic data, and identify optimal operating conditions. This is sufficiently precise as an on-line diagnostic tool to identify changes in catalyst morphology with time-on-stream in experimental reactors. The porosity analysis introduces a new application for RTDs: An important challenge for fluidized bed and fixed bed catalytic

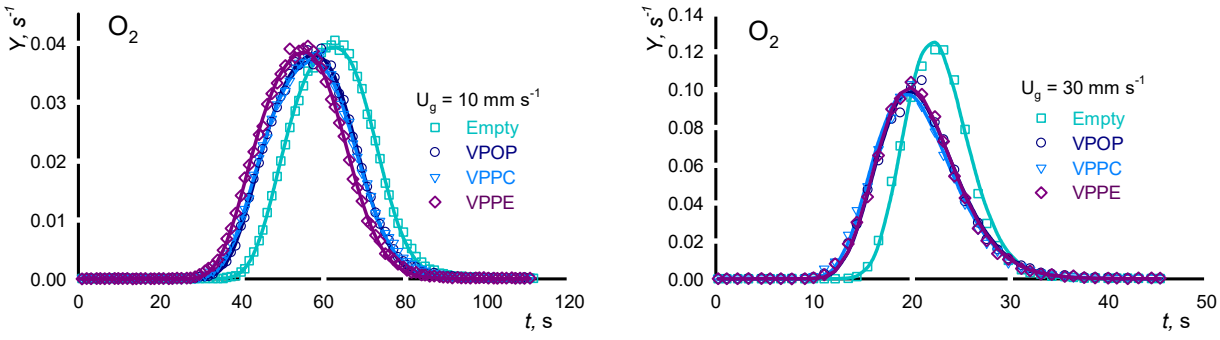

(a) (b)

Figure 5.8 RTD comparison between three catalysts in Geldart group A and empty tube: time vs $Y = \frac{C_i}{\sum C_i \Delta t}$. Argon was initially injected in the reactor at (a) $10\,\mathrm{mm\,s^{-1}}$ and (b) $30\,\mathrm{mm\,s^{-1}}$. The tube was empty or loaded with 9.16 g of VPOP, 10.0 g of VPPC or 11.9 g of VPPE catalysts. At low velocity (a), gas RTD varies in function of porosity. Higher is the porosity, longer the gas will stay inside the vessel. Here, VPOP and VPPC have the same porosity while VPPE is 2 times lower. The RTD at high velocity (b) is the same whatever the catalyst.

processe is catalyst deactivation due to coke build up and sintering, with a subsequent loss in pore volume. An accumulation of carbon in pores reduces reactant contact the active sites, thus decreasing conversion[155]. At a low velocity ($< 2U_{\mathrm{mf}}$), an RTD test can identify the extent of this coking, even under reaction conditions *in-situ*! If a significant delay is observed based on an initial RTD trace, we will be able to detect coking because pores will be blocked by carbon. A characteristic map could be created for a specific reaction to fully understand catalyst deactivation with time. Furthermore, it could be complementary tool for the fluidized-bed TGA system that assess the change in mass during a temperature ramp.[156] This combination could then correctly distinguish between pore loss due to calcination versus coke build-up.

5.4.3 Geldart group A and B powder RTD

The choice RTD tracer depends on the catalyst and environment. Here, we compared RTD of non-porous sand to FCC (fluid catalytic cracking catalyst) with a high porosity, including VPOP, VPPC and VPPE (Geldart Group A powders) The sand belongs to Geldart's group B powder classification which has very low surface area while the surface area of the FCC is 4 times greater than VPOP or VPPC. We consolidated the graphs of the RTD curves by tracer (H_2, CO, CO_2, and CH_4) at $10\,\mathrm{mm\,s^{-1}}$ (Figure 5.9) to better demonstrate differences.

Each graph includes the RTD curve for VPOP, VPPC, VPPE, FCC, sand and empty tube.

For hydrogen (Figure 5.9 – a), $\mathscr{D} = 0.796\,\mathrm{cm^2\,s^{-1}}$, sand (Geldart group B) egresses the reactor first at 23 s followed by all Geldart group A catalysts, and finally the empty tube at 28 s. Carbon dioxide (Figure 5.9 – b), $\mathscr{D}= 0.150\,\mathrm{cm^2\,s^{-1}}$, egresses the reactor 21 s later when FCC is loaded. Additionally, a prominent tail is visible. This is due to (1) high porosity of FCC ($S_\mathrm{a} = 93\,\mathrm{m^2\,g^{-1}}$), (2) chemical interaction — adsorption[28], and (3) the lower diffusivity of CO_2. All these factors combined together provide an important delay in the RTD curve—38 % longer for all CO_2 molecules to exit the reactor with FCC compared to VPP catalysts. We would like to stress that these artifacts are completely independent of the fluid dynamic regime: bubbles, wake, and mass transfer to the emulsion phase are clearly secondary contributions to the dispersion phenomena. For carbon monoxide (Figure 5.9 – c), $\mathscr{D} = 0.195\,\mathrm{cm^2\,s^{-1}}$, the FCC curve is delayed by 10 s compared to sand due to (1) its porosity and (2) chemical interaction between CO_2 and FCC. (Again we are discounting all contributions to dispersion due to bubble-emulsion interactions). Indeed, the four gases are injected at the same time, then FCC adsorbs CO_2 inside the pores all along the reactor. Thus, the total volumetric flow rate (Q) decreases. Consequentially, we also observed a lag in the data for H_2, CO and CH_4 with FCC catalyst. The methane RTD curve, $\mathscr{D} = 0.208\,\mathrm{cm^2\,s^{-1}}$, is very similar to that of CO (Figure 5.9 – d).

We increased the velocity at $30\,\mathrm{mm\,s^{-1}}$ to understand the adsorption behaviour (Figure 5.10). Surprisingly, the RTD is different for each catalyst and the average residence time follows the the order of least porous to most porous except that with FCC the CO_2 tracer egresses last, while it should have been before the empty tube: Sand, VPPE, VPPC, VPOP, empty and FCC. For CO_2 with FCC loaded (Figure 5.10– b), the difference between the other catalysts is only 5 s instead of 20 s at $10\,\mathrm{mm\,s^{-1}}$. Furthermore, the axial dispersion model visually fits the data better ($R^2 = 0.987$). Thus, the adsorption rate at high velocity is lower but still present. Clearly, even if the same quantity of CO_2 adsorbs, the total volumetric flow rate is $3\times$ higher so we would expect that the change in the RTD would be that much lower.

The main trends are:

1. All gas tracers pass through the reactor charged with sand faster because the porosity is lowest. The void fraction is higher with the porous Geldart group A powders and so gas penetrating into the pores delays the signal.
2. RTD curves of the various Geldart group A powders are the same with H_2, while the difference between Geldart group A and B powders is 2 s.
3. Above U_mf, the differences in the RTD increases with increasing gas velocity for each of the powders: At $10\,\mathrm{mm\,s^{-1}}$, the RTD for each gas and each powder are more similar

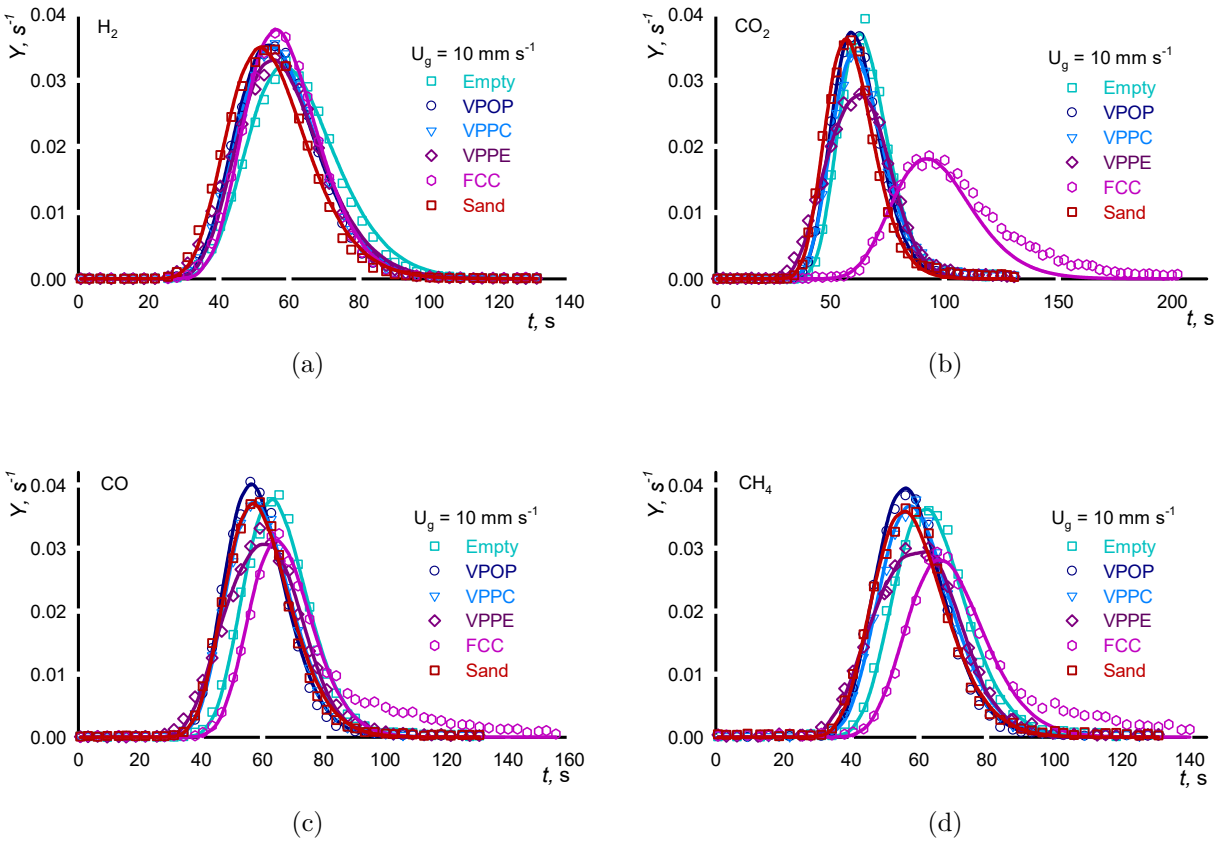

Figure 5.9 Comparison of tracer injected for 5 powders at $10\,\mathrm{mm\,s^{-1}}$: time vs $Y = \frac{C_i}{\sum C_i \Delta t}$. This series of tests included Geldart group A powders—VPOP, VPPC, VPPU, and FCC—and sand, which is a Geldart group B powder. For each catalyst, the mass spectrometer measures the concentration of tracer: (a) hydrogen, (b) carbon dioxide, (c) carbon monoxide, and (d) methane. For hydrogen (a), the RTD overlaps with all catalyst. For carbon dioxide (b), the gas is delayed by 21 seconds with FCC due to a chemical interaction—adsorption. For carbon monoxide (c) and methane (d), a small difference is observed between each catalyst. The gas takes 10 seconds longer to pass through the reactor with FCC, and a tail appears after reaching the maximum.

than they are at $30\,\mathrm{mm\,s^{-1}}$ (Figure 5.9 and 5.10). At short contact times (short pulse length), the ratio of the volume adsorbed to the volumetric flow rate is smaller so the effect is proportionately less evident.

5.4.4 Noble and non-reacting gas tracers

We compared residence time distribution for the FCC with krypton and helium (Figure 5.11–a) to identify bulk gas effects (diffusion, mass transfer across boundaries) and isolate ad-

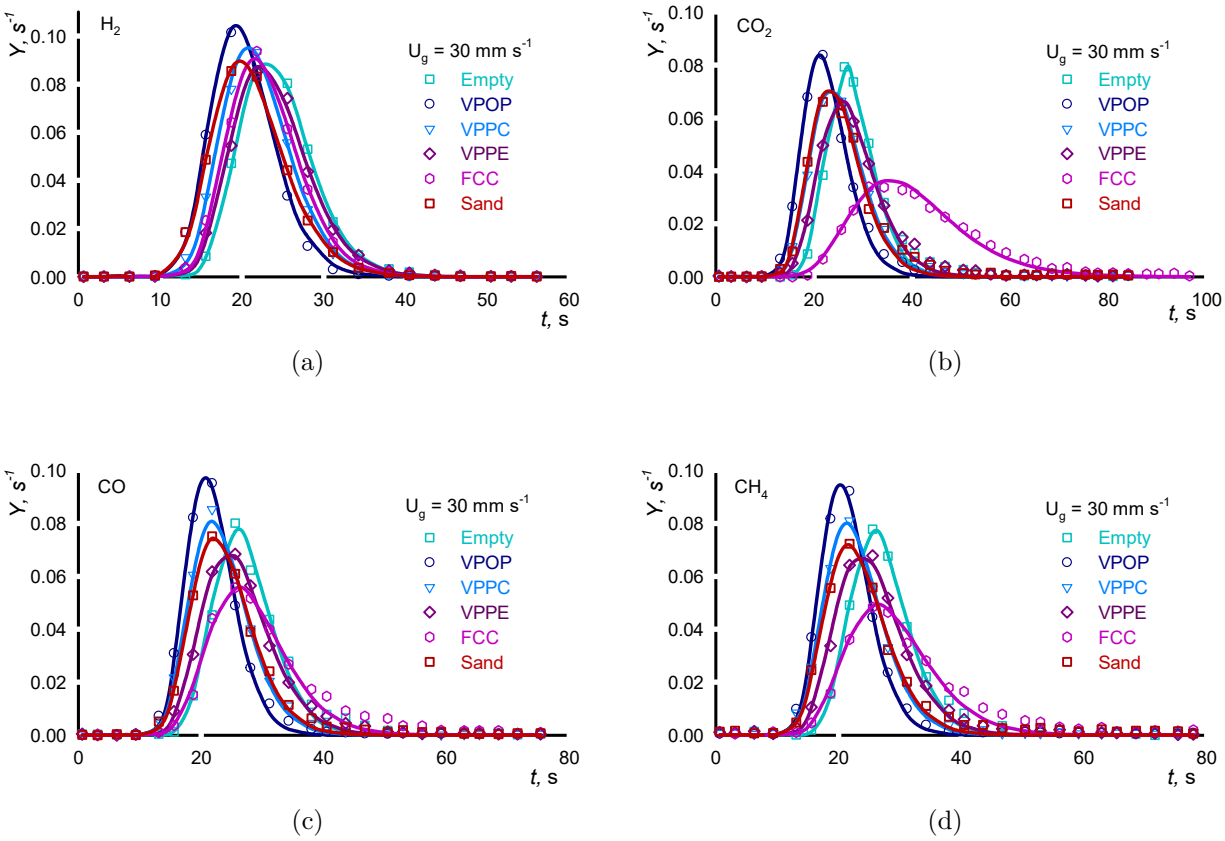

Figure 5.10 Comparison of tracer injected for 5 powders at $30\,\mathrm{mm\,s^{-1}}$: $Y = \frac{C_i}{\sum C_i \Delta x}$ vs time. (a) hydrogen, (b) carbon dioxide (c) carbon monoxide, and (d) methane. At high velocity (30 vs $10\,\mathrm{mm\,s^{-1}}$), the RTD is function of the catalyst. Indeed, each powder has a different residence time distribution.

sorption/reaction effects. Tracers egress the reactor in the same order as their diffusivity coefficient: First, at $t = 27\,\mathrm{s}$, helium ($\mathscr{D} = 0.716\,\mathrm{cm^2\,s^{-1}}$), then at $t = 32\,\mathrm{s}$, CO and O_2 ($\mathscr{D} = 0.195\,,\ 0.194\,\mathrm{cm^2\,s^{-1}}$ respectively), finally, at $t = 35\,\mathrm{s}$, krypton ($\mathscr{D} = 0.136\,\mathrm{cm^2\,s^{-1}}$). For all gases, the axial dispersion model fits the data ($R^2 > 0.98$).

We evaluate the hydrodynamics with carbon monoxide from the gas cylinder containing syngas with 15 % CO and the cylinder with noble gases, oxygen and with 0.987 % CO (Figure 5.11– b). Both CO RTD curves reach the same height (normalized area under the curve equals 1). However, the shape of the curves are distinct: the trace with 15 % CO has an extended tail and the leading edge is delayed by 4 s.

CO_2 adsorption increases the residence time of the tests with the syngas tracer: the cylinder contains 15 % CO_2 and if it were to all adsorb, the volumetric flow rate would drop by 15 %.

The reason for the tail is ambiguous as we could attribute it to either the contribution to the $m/Z = 28$ signal from the CO_2 fragment as it ionizes, or an interaction with CO_2 in the pores, or the most likely cause is related to the signal-to-noise ratio. The MS records 9700 counts for a CO_2 concentration of 15 % (v v^{-1}) while at the same concentration it records 17 800 counts for CO. The CO_2 contribution to the CO signal is less than 18 % but to reach the baseline so quickly requires that we subtract 40 % of the CO_2 signal from the CO signal. This large correction factor is unlikely, furthermore, the methane signal has an appreciable tail but the CO_2 contribution to the the methane m/Z signal is negligible. Since it is unlikely that a methane-CO_2 interaction would be similar to a CO-CO_2 interaction, we also reject this hypothesis for the extensive tail[59]. This leaves us with concentration as a possible explanation: The maximum CO peak height for the tests with syngas was close to 14 000 while it was only 450 for the CO in the noble gas cylinder. The background signal of the syngas was 75 compared to 18 for the noble gas cylinder. So the signal-to-noise ratio was almost an order of magnitude greater for the CO in the cylinder with syngas. The CO concentration in the noble gas cylinder was too low to identify any tail.

Engineers apply RTD to calculate the number of CSTRs and then model reaction kinetics or detect bypassing in vessels. To better understand the vessel hydrodynamics, the RTD must be completed at the actual conditions and with the same gases rather than relying on the response of a single unreacting gas. However, we must consider the signal-to-noise ratio while examining second order effects like tailing.

The conclusions are:

1. Diffusivity affects RTD for porous and non-porous catalyst. Gases with a high diffusivity coefficient means that a molecules spread easily. Thus, the gas will enter the pores as fast as it egresses. Consequently, the MS will detect these species first (Figure 5.5, 5.6, and 5.11). He and H_2 are poor tracers.
2. The tail observed on FCC (Figure 5.9–b) when we injected CO_2, is due to chemical adsorption of CO_2.
3. To measure the RTD precisely, the choice of tracer has to be based on diffusivity coefficients, reactivity, and gases involved. For porous powders, the ratio: tracer diffusivity on reaction gas diffusivity has to be lower than 1.1 For non-porous catalyst, this ratio has to be lower than 1.4

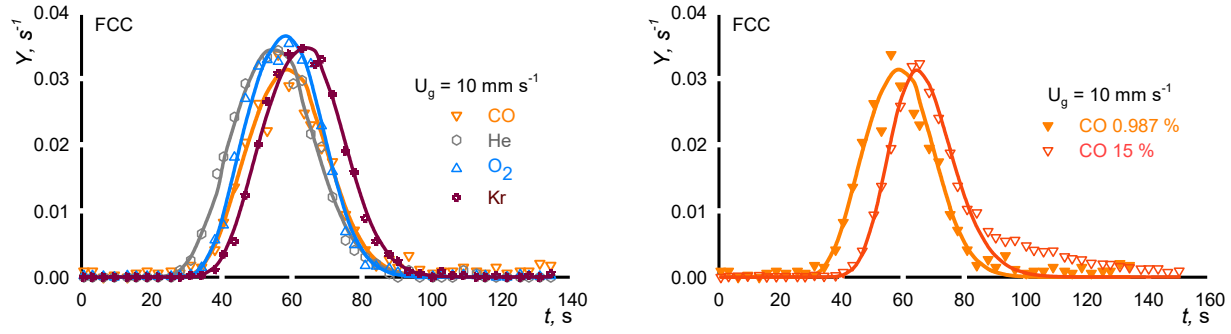

(a) (b)

Figure 5.11 Residence time distribution of FCC at $10\,\mathrm{mm\,s^{-1}}$: time vs $Y = \frac{C_i}{\sum C_i \Delta t}$. (a) At $t = 0$, we rotated the 8-way valve stem to substitute the argon 0.987 % CO, 2.05 % He, 5.00 % O_2, 1.93 % Kr, and the balance Ar. The chromatography effect between each gas to exit the reactor is only due to physical phenomena—diffusivity. (b) CO comparison at 0.987 % and 15 % molar concentration. At 15 %, the CO egresses the reactor 4 s later and presents a tail due to CO_2 included in the bottle. When we inject only non-reactive gases, CO follows the axial dispersion model ($R^2 = 0.970$).

5.5 Conclusion

Residence time distribution is a multifaceted method to characterize the hydrodynamics in vessels. In this study, we built an 8 mm diameter fluidized bed reactor to examine hydrodynamics near U_{mf} with several powders and gas tracers. The technique consists of injecting tracer with a step or pulse injection and meassuring its concentration with a mass spectrometer. The main challenges for this set up included the fragility of the quartz tube particularly around the stainless-steel fitting, the powders that infiltrate the capillary of the MS, and leaks due to fittings. When ambient error enters the MS from the capillary or leaks, m/z at 28 and 32 will increase and compromise the baseline.

We completed well over 500 RTD experiments with Geldart group A powders—VPOP, VPPC, VPPE, and FCC— and sand, a Geldart group B powder. We tested a 7 tracers with varying diffusivities (Kr, CO_2, O_2, CO, CH_4, He, and H_2). To minimize dead zonez and maximize the signal due to the catalyst bed we first measured the RTD below the reactor that accounted for the contribution from the inlet lines and MS. Then, independently, we performed the same procedure, but this time with the MS positioned at the exit. Indeed, if two mass spectrometers are positioned on the reactor at the same time (one at the entrance and the other at the exit of the reactor), the volumetric flow rate along the reactor would

have decreased due to the suction of the MS at the inlet (which is on the order of 20 mL $\min^{-1}$ for the Hiden model). Despite the fact that the measurement would have been instantaneous at the entrance and exit, the uncertainty of the residence time would have been too high.

We established the behaviour of syngas products in an empty tube. An axial dispersion model with a high $N_{\mathrm{Pe}}(< 50)$ characterzies the RTD of hydrogen, which has a high diffusivity ($\mathscr{D} = 0.796\,\mathrm{cm}^2\,\mathrm{s}^{-1}$), even though the flow regime is laminar. Presumably, the radial diffusion is sufficient to minimize concentration gradients. At a $N_{\mathrm{Re}} > 20$, the CO_2, CO, and CH_4 tracers deviate from the axial dispersion.

We compared the RTD of with vanadyl hydrogen phosphate hemihydrate vanadyl pyrophosphate (calcined and equilibrated). At low velocity ($< 2U_{\mathrm{mf}}$), the response to a inpult pulse with VPPE is distinct from VPPC and VPOP: the surface area is half of the the other and it has a 30 % lower pore volume and as a consequence the RTD curve shift towards the right (shorter residence time). This is the first evidence that we know that demonstrates the utility of an RTD experiment to correlate the residence time with morphological changes in catalyst. The logical extension of this idea is to incorporate operando sample loops to identify changes in catalyst behaviour on-line during reaction and in systems with regeneration cycles. This test would elucidate the difference in morphological changes due to sintering and coking.

We compared the RTD with several tracers and powders and demonstrate that at atmospheric temperature, CO_2 adsorbs onto FCC catalyst— the chromatographic effect in which the leading edge is delayed (corresponding to 100 % adsorption) and the trailing edge has an extended tail region. The axial dispersion model is incapable of accounting for this behaviour. Morever, we show that the uncertainty inherent with the Heaviside step function is unable to clearly identify this phenomena.

Thus, three phenomena are predominant in RTD analysis: dispersion, diffusion, and adsorption. The future challenge lies in scaling the methodology for a large system ($D_{\mathrm{reactor}} >$10 cm). Indeed, uniform injection as well as RTD detection uniformly are confrontations that researchers must resolve.

5.6 Acknowledgment

This research was undertaken, in part, thanks to funding from the Canada Research Chairs program and the authors gratefully acknowledge the financial support from the Natural Sciences and Engineering Research Council of Canada (NSERC) and the Canada Foundation for Innovation (CFI).

5.7 Supplementary file

Table 5.5 Comparison of moments (mean residence time and variance) at the inlet and outlet of the reactor, Peclet number, and number of CSTRs in series. The reactor is empty or loaded with VPOP, VPPC, or VPPE. Initially, Ar was initially injected in the reactor. At $t = 0$, we switched the 8-way valve to substitute Ar with air (21 % O_2, 79 % N_2).

Catalyst	$\bar{t}_{in}$ (s)	σ^2_{in} (s^2)	t_{peak} (s)	$\bar{t}_{real}$ (s)	Δ_t (s)	σ^2_{out} (s^2)	N_{Pe}	N_{CSTR}	R^2
	Pulse injection - 10 mm s^{-1}								
Empty	17	333	56	62	6	3894	73	38	0.999
VPOP	18	361	52	57	5	3326	55	29	0.999
VPPC	19	402	52	57	5	3316	52	27	0.999
VPPE	18	363	50	55	5	3061	51	27	0.999
	Pulse injection - 30 mm s^{-1}								
Empty	8.3	73	21	23	2	505	92	47	0.994
VPOP	8.4	75	20	21	1	444	49	26	0.996
VPPC	8.6	77	20	21	1	429	46	24	0.997
VPPE	8.1	70	19	21	2	437	50	26	0.997

CHAPITRE 6 ARTICLE 3: FLUIDIZED BED HYDRODYNAMIC MODELLING OF CO_2 IN SYNGAS: DISTORTED RTD CURVES DUE TO ADSORPTION ON FCC

Ariane Bérard, Bruno Blais, Gregory S. Patience

Journal: AIChE Journal

reçu: 06 octobre 2020 **revisé:** - **accepté:** -

6.1 Abstract

Residence time distribution (RTD) is technique that detects anomalies in the hydrodynamic flow patterns of a vessel, reservoirs, and pipes. We studied the RTD of the gas phase with an 8 mm diameter quartz tube reactor loaded with fluid catalytic cracking catalyst (FCC). We devised a feed manifold to inject a syngas composition—CO_2, CO, CH_4, and H_2—through a 10 mL coiled tube to create a bolus pulse. The FCC catalyst created a chromatographic separation effect: an on-line mass spectrometer sampling at a frequency of close to 2 Hz detected hydrogen first, followed by CO and CH_4 15 s later, and finally another 15 s later CO_2 appears. We fit the axial dispersion model to compare the tracer's behaviour with the ideality—plug-flow. Although the residence time of CO_2 in the reactor is 10 % longer than for CO or CH_4 at 25 °C the difference at 300 °C is negligible. At ambient temperature, the response curve for CO, CH_4, and CO_2 present an extended tail due to adsorption. The fit to the CO_2 data is poor ($R^2 = 0.920$) excluding this phenomenon. We developed a new *tanks-in-series* model based on gas phase, pore volume, and adsorbed species mole balance. We quantify the adsorption and desorption rate for CO, CH_4, and CO_2 as well as the mass transfer between the bulk phase and the pores, and the circulation rate. The optimum result increased the R^2 for CO_2 to 0.986 while H_2, CO, and CH_4 are similar. However, the extended tail is well defined by the new model. These results demonstrated and quantify the effect of dispersion, diffusion, and adsorption on RTD analysis.

keywords: residence time distribution, model, adsorption, diffusion, hydrodynamic

6.2 Introduction

Residence time distribution (RTD) is a fundamental technique applied mainly in mixing, reactor science, biomass and pharmaco-kinetics[7,9,12,18,116]. This method consists of injecting a tracer in a vessel and to measure its concentration with time. Researchers apply RTD for gas[118], solids[17] and liquids[119]. RTD test is more commonly an experimental procedure but researchers are also applying as a post-processing tool for computational fluid dynamics (CFD) results[70,102,129]. Both methods detect back-mixing, dead volume, channeling, and dispersion by comparing against the ideal plug flow model.

RTD of the gas phase in fluidized bed reactors[77] is particularly interesting as the hydrodynamics in these systems comprise several phenomena—bubble phase, emulsion phase, grid regions, and the transport disengagement section above the bed. Indeed, as a function of the tracers injected and the catalyst loaded, RTD analysis differentiates between diffusion, dispersion, and adsorption[12] (Chapitre 5). To describe these phenomena, researchers have developed several models — the one, two or three phases model, the axial dispersion model, the tanks-in-series, and regression model[157].

The one phase model or homogeneous bed model considers exclusively the emulsion phase. This is the case of the axial dispersion model, predominately applied for RTD with the Peclet number ($N_{\mathrm{Pe}} = uZ/\mathcal{D}$) as the prime fitted parameter where $\mathcal{D}$ is the axial dispersion coefficient. The nondimensional form is[69,70,71]:

$$\frac{\partial C}{\partial \theta} + \frac{\partial C}{\partial \xi} = \frac{1}{N_{\mathrm{Pe}}} \frac{\partial^2 C}{\partial \xi^2} \tag{6.1}$$

where C is the concentration, θ is nondimensional time ($\theta = tu/Z$) and ξ is the nondimensional length ($\xi = z/Z$).

To characterize the complex phenomena in fluidized bed, researchers introduce the notions of bubbles, and the mass transfer between bubbles and emulsion—the two phases model. Also, they consider the cloud created by the movement of gas around each bubble[50]. The first approach of the model includes the cloud around the bubble with the emulsion phase[26]. In this case, the mass transfer is between the bubble and the emulsion phase[63]:

$$\frac{dN_{\mathrm{A}}}{dt} = u_{\mathrm{b}} V_{\mathrm{bubble}} \left(\frac{dC_{\mathrm{A,b}}}{dz} \right) = K_{\mathrm{GB}} V_{\mathrm{bubble}} (C_{\mathrm{A}}^{i} - C_{\mathrm{A,b}}) \tag{6.2}$$

Where N_{A} is the mol of A, u_{b} is the bubble rise velocity, V_{bubble} is the volume occupied by the bubble phase, K_{GB} is the interchange coefficient between bubble and emulsion-cloud, C_{A}^{i}

is the concentration of A at gas-particle interface, and $C_{\mathrm{A,b}}$ is the concentration of A in the bubble.

The second approach merges the cloud and the bubble into a single phase and the second phase is the emulsion. The mass transfer balance is[67]:

$$\frac{\mathrm{d}N_A}{\mathrm{d}t} = V_{\mathrm{cloud}} \left(\frac{\mathrm{d}C_{\mathrm{A,c}}}{\mathrm{d}t} \right) = K_{\mathrm{GC}} V_{\mathrm{cloud}} (C_{\mathrm{A,e}} - C_{\mathrm{A,c}}) = k_{\mathrm{GC}} S_{\mathrm{ex,cloud}} (C_{\mathrm{A,e}} - C_{\mathrm{A,c}}) \tag{6.3}$$

where, the index c represents cloud and e represents emulsion, V_{cloud} is the volume occupied by cloud and bubble, K_{GC} is the interchange coefficient between bubble-cloud and emulsion, k_{GC} is the mass transfer coefficient between bubble-cloud and emulsion, and $S_{\mathrm{ex,cloud}}$ is the exterior surface of clouds.

Finally, to approximate reality more closely, the 3-phase model introduces powder physico-chemical properties—porosity, and mass transfer from the gas in the emulsion to the particle surface. First, the flux equation for each phase is[56]:

$$w_{\mathrm{p}} = U_{\mathrm{g,p}} C_{\mathrm{p}} - M_{\mathrm{m,p}} \frac{\partial C_{\mathrm{p}}}{\partial x} \tag{6.4}$$

where w is the mass flux, C is the mass concentration, U_{g} is the gas velocity, and M is the axial mixing coefficient. The index p represents the phases: emulsion (E), bubble (B), or solid (S).

Additionally, the continuity equation for each phase is[56]:

$$\frac{\partial w_{\mathrm{p}}}{\partial x} + \frac{\partial C_{\mathrm{p}}}{\partial t} = r_{\mathrm{p}} \tag{6.5}$$

where r is the reaction rate. To solve equations 6.4 and 6.5 for three phases (E,B, and S), we suppose that the velocity and mixing coefficient of the solid phase is negligible ($u_{\mathrm{S}} = M_{\mathrm{S}} \approx 0$)[56].

The models proposed in the literature for RTD analysis in fluidized bed reactors have limitations:

1. Lack of the gas mass transfer mechanism between the pores inside the catalyst and its surface.
2. In general, reaction concepts are missing. Consequently, when adsorption occurs between the tracer and catalyst. The results diverge from the axial dispersion model.
3. Normally only single tracers are modelled. They may or may not characterize the system correctly (Ar and Kr radioactive gas tracers are excellent tracers but are poor

models for hydrogen or methane). Each gas tracer is modelled independently. The injection of several tracers demonstrates how the hydrodynamics depend on the gas diffusivity (but this is most evident at ambient temperature).

In this article, we analyze the effect of porosity, and Geldart group A and B powders on RTD by injecting a syngas gas composition simultaneously (CO_2, H_2, CO, and CH_4) at ambient temperature and 300 °C. The phenomenon of diffusion and adsorption are the core of RTD analyzes. Then, we develop a new model to account for adsorption of gases on the catalyst since the RTD curve obtained experimentally deviates substantially from idealized flow patterns.

6.3 Experimental

6.3.1 Powders

We compared Fluid Catalytic Cracking Catalyst (FCC) from Total© with sand. They have distinct physico-chemical properties. FCC is a porous Geldart group A powder while sand is non-porous and belongs to the Geldart group B.[158] SEM images demonstrate the spherical shape of FCC and the angular shap of the sand (Figure 6.1). We confirmed the sphericity by applying the Ergun equation ($\phi_{\mathrm{FCC}} = 0.99$ and $\phi_{\mathrm{sand}} = 0.68$) :

$$\frac{\Delta P}{\Delta Z} = \frac{U_{\mathrm{g}}}{\phi d_{\mathrm{p}}} \frac{1-\epsilon_{\mathrm{v}}}{\epsilon_{\mathrm{v}}^3} \left(150(1-\epsilon_{\mathrm{v}}) \frac{\mu}{\phi d_{\mathrm{p}}} + 1.75 \rho_{\mathrm{g}} U_{\mathrm{g}} \right) \tag{6.6}$$

Where ΔP is the pressure drop, ΔZ is the bed height, ϵ_{v} is the void fraction, and μ is the viscosity.

The minimum fluidized velocity (U_{mf}), the bulk density (ρ_b) and the mean particle diameter (d_{50}) are 6, 1.6 and 1.4 times higher respectively for sand compared to FCC (Table 6.1). Inversely, the surface area (S_{A}) measured by BET is 166 times higher for FCC vs sand. However, the Hausner ratio (H_{r}) is similar for both powders. Thus, the hydrodynamic behavior diverges between the two powders since their physical characteristics are different.

6.3.2 Gases

To discern all phenomena (dispersion, diffusion and adsorption), RTD experiments are performed with syngas tracers. The bottle purchased from Air Liquide© contains 15 % CO_2, 15.3 % CO, 19.9 % H_2, 14.7 % CH_4, and the balance N_2. In all studies, the inert gas injected continuously is argon. These gases have a wide range of diffusivity at 25 °C and 300 °C (Table 6.2).

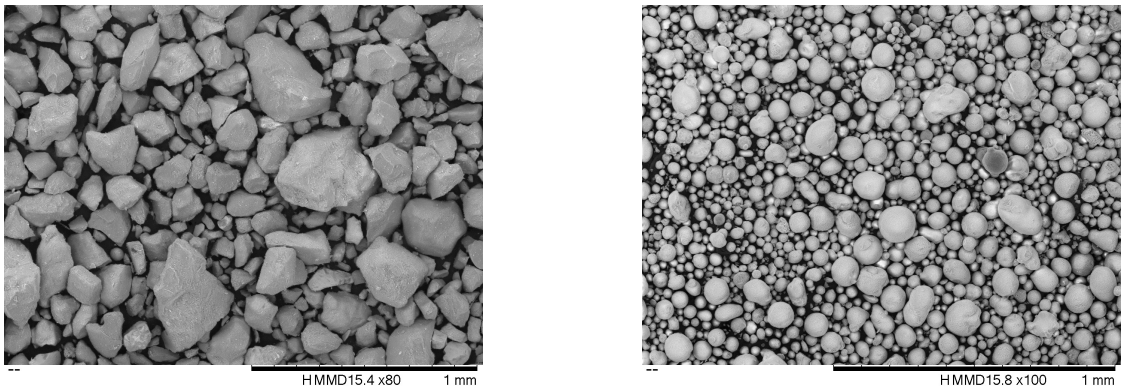

(a) (b)

Figure 6.1 SEM images of the powders: (a) Sand, large cuboid or polygonal particles, (b) FCC, most particles are spheroids.

6.3.3 Micro reactor set-up

The experiments were run at ambient temperature in an 8 mm diameter quartz tube 360 mm long (Figure 6.2). We poured 8.19 g of FCC or 13.5 g of sand to reach, for both, 180 mm tapped bed heights. For all experiments, two Brooks mass flow controllers (MFC) maintained the velocity at $10\,\mathrm{mm\,s^{-1}}$ which represents a Reynolds number (N_{Re}) of 6.8. We installed a Hiden quadrupole mass spectrometer (MS) with a pulse ion counting (SCEM) detector at the exit of the reactor to monitor the tracer concentration *on-line*[23]. The capillary is 0.90 m long, 0.20 mm internal diameter and it is heated at 160 °C. A vacuum pump maintained pressure at 6.2×10^{-5} mPa. A manifold with an 8-way valve and two identical sample loops make up the injection system[12]. Because the the same MFC injects the tracer into the reactor and the lines are identical with the same number of ports on the 8-way valve, the pressure drop across the two lines are identical and we expect only an imperceptible change in pressure when we turn the valve.

The sequence starts with the injection continuously of the inert— argon. Before reaching the reactor, argon passes through the first 10 mL loop. At the same time, the second 10 mL loop fills with tracer (and evacuates to exhaust). After a three minutes purge, we switched the 8-way valve. This corresponds to $t = 0$. The argon stream purges the second sample loop with the syngas tracer and enters the reactor. The stream entering the reactor is always controlled with the same MFC. The MS measured the concentration of all gases simultaneously at 2 Hz for 4 minutes after which we shut off the MS and purge the system with argon for 3 minutes before the beginning another experiment.

For experiments at 300 °C, the reactor is shorter— 32 cm and housed in an electrically heated

Table 6.1 FCC and sand properties[22]. The uncertainties represent standard deviation.

Property	**FCC**	**Sand**	n	**Comments**
Composition	mixed[1]	Silica (SiO_2)	-	-
Geldart Group	A	B	-	-
U_{mf}, $mm\,s^{-1}$	2.2	13	1	-
ρ_b, $kg\,m^{-3}$	874(4)	1328(10)	5	Scott density
	853(19)	1366(27)	5	Poured density
	965(10)	1529(47)	5	Tapped density
	945	1426	1	Hg porosimetry
ρ_p, $kg\,m^{-3}$	1610	2279	1	Hg porosimetry
ρ_{sk}, $kg\,m^{-3}$	2360(2)	2777(5)	10	Gas
ϵ_v	0.44	0.37	1	-
H_r	1.13(3)	1.12(4)	5	Hausner ratio
θ_{angle}, °	24(1)	44(2)	6	Angle of repose
d_{10}, µm	39.4(4)	58(2)	3	Laser diffraction
d_{50}, µm	64.0(6)	87(2)	3	Laser diffraction
d_{90}, µm	104(1)	120(2)	3	Laser diffraction
ϕ	0.99	0.68	1	Ergun equation
S_A, $m^2\,g^{-1}$	93.28	0.56	1	BET
	34.52	0.41	1	BJH[2]
v_{pore}, $mL\,g^{-1}$	0.145	0.003	1	BJH[2]
d_{pore}, nm	38	21	1	BJH[2]

[1] FCC catalysts include a variety of zeolite crystallite sizes and particle properties[120]
[2] BJH: desorption branch

Table 6.2 Diffusivities in argon and atomic mass for gases. All diffusivities are calculated with the correlation of Fuller – Schettler – Gidding[151]. This method is available for non-polar gases at 101.25 kPa.

Gases	$\mathscr{D}$ $[cm^2\,s^{-1}]$ $T = 25°C$	$\mathscr{D}$ $[cm^2\,s^{-1}]$ $T = 300°C$	molar mass $[g\,mol^{-1}]$
CO_2	0.150	0.479	44
CO	0.195	0.622	28
CH_4	0.208	0.664	16
H_2	0.796	2.54	2

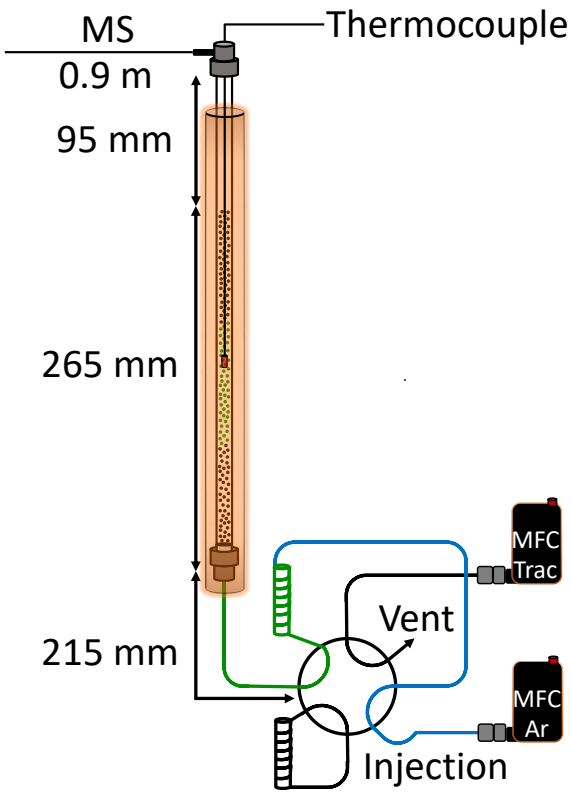

Figure 6.2 Fluidized bed reactor configuration surrounded by a furnace. The quartz tube was 8 mm diameter and 360 mm at 25 °C and or 320 mm at 300 °C. At room temperature, the tapped bed height with all catalyst was 180 mm and it expanded to an average of 265 mm when fluidized. At 300 °C, the tapped bed height is 130 mm. The mass spectrometer (MS) capillary is 0.9 mm long with a 0.20 mm internal diameter. First, the 8-way valve is in the filling position (not shown) where argon goes to the reactor and the tracer fills a 10 mL sample loop. Then, at time $t = 180$ s, we switch the 8-way valve to the injection position. Argon (blue line) sweeps the tracer (green line) from the loop to the reactor.

furnace. The tapped bed height is 13 cm, so 6.50 g of FCC. We only tested FCC to study the effect adsorption at high temperature. All plastic pipes around the reactor were changed for metal while we kept the same lengths and dimensions. We also added a thermocouple to measure the temperature in the catalytic bed. The experimental sequence wass exactly the same.

In accordance with Bérard et al. (2020) we minimized dead volume above and below the catalytic bed to ensure a maximize the contribution to the variance of the reactor [12]. For each set of experiments, we performed two RTD tests at the inlet of the reactor, and two at the outlet. For the axial dispersion model, we subtracted the RTD time at the inlet. For the new model, the entrance data are considered as the initial gas concentration.

6.3.4 Axial dispersion model

We fit experimental data with the the axial dispersion model (Equation 6.1). We applied the boundary conditions for a closed-open system[11,71]:

$$C_{0,\xi} = 0, 0 \leq \xi \leq 1 \tag{6.7}$$

$$C_{\tau,0} = \rho_0, \tau > 0 \tag{6.8}$$

$$\frac{\mathrm{d}C_{\tau,1}}{\mathrm{d}\xi} = 0, \tau > 0 \tag{6.9}$$

The exact analytic solution is[71]:

$$G(\theta) = \frac{1}{2}\left[\mathrm{erfc}\sqrt{\frac{N_{\mathrm{Pe}}}{4\theta}(1-\theta)} + \mathrm{e}^{N_{\mathrm{Pe}}}\mathrm{erfc}\sqrt{\frac{N_{\mathrm{Pe}}}{4\theta}(1+\theta)}\right] \tag{6.10}$$

For each test, we normalized the data to reach an area under the curve equal to one:

$$Y = \frac{C_i}{\sum C_i \Delta t} = 1 \tag{6.11}$$

Then, we subtracted the initial time measured at the inlet of the reactor (MS capillary and inlet lines) to the total time at the exit. We minimized the sum of squares of the error (SSE) between the axial dispersion model and the experimental data to calculate N_{Pe}. Finally, to quantify the difference between the predictions and the data, we calculated the coefficient of determination (R^2).

The model adequately approximates pulse injections (no back-mixing) when we simulate each gas independently but the parameters for each gas are different. So, we developed a new model for multiple gases injection that accounts for the differences and the long tail (due to adsorption).

6.3.5 New Model—Mole balance equation

Reactor RTD analysis includes multiple phases and species particularly for porous solids and flow systems like fluidized beds. The literature often considers an emulsion phase, a bubble phase and at times a cloud phase and a wake. Since the bubble phase is assumed

to have little catalyst, all reaction takes place in the emulsion phase (and cloud and wake). Here, we consider that bubbles form and disintegrate sufficiently rapidly that the gas phase is a continuum. Indeed, researchers achieve 100 % conversion in fluidized bed reactors which implies a rapid mixing between the bubble phase and the other phases. Consequently, this phase is neglected in the new model[159]. We consider catalyst as a distinct phase—solid phase. The third phase is the catalyst surface in its pores on which any species may adsorb. Thus, the new model considers three mole balances—the gas phase moving upwards, gas in the pores that follow the movement of the solids, and the adsorbed species on the catalyst surface (that also follow the solids motion). For the injection of multiple tracers, all gas species are dependent on each other. In fact, if species adsorb on the catalyst pores, this will have the consequence of reducing the total flow rate in the reactor. We included this dependence when we solved the model. The flow chart (Figure 6.3) encompasses the principal steps of solving the model.

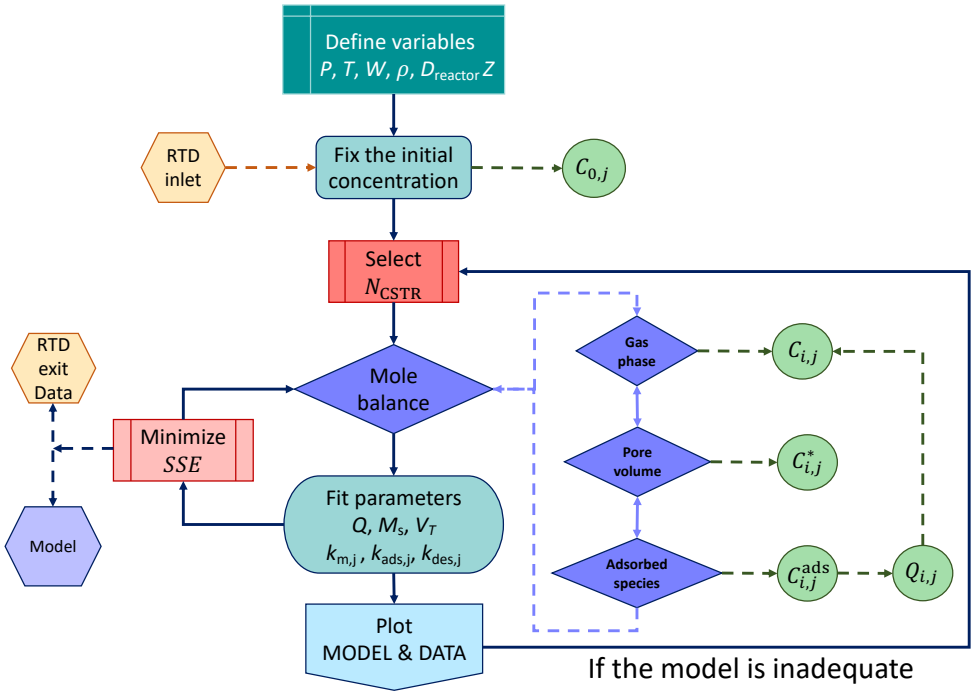

Figure 6.3 Flow chart of the resolution of the new model. Diamonds are equations to solve, hexagons are experimental data, and circles are the result variables for each species j. The model is inadequate if the model peak diverges from the experimental data or the R^2 is smaller compared to the axial dispersion model results. In this case, the number of CSTRs is modified.

Gas phase mole balance

In fluidized beds, when the gas velocity exceeds U_{mf} (minimum fluidization velocity), the pressure drop, ΔP is essentially constant and proportional to the bed density, $\rho_p(1-\epsilon_{\mathrm{v}})$, and the mass of catalyst in the reactor, W:

$$\Delta P = \rho_p(1-\epsilon)gZ = \frac{Wg}{X_{\mathrm{A}}} \tag{6.12}$$

So the molar density, $C_{i,j}$, varies with height, z, according to:

$$C_{i,j} = \frac{P_{i,j}}{RT} = \frac{P_{\mathrm{o}} - \frac{z_{i,j}}{Z}\Delta P}{RT} \tag{6.13}$$

Then, the mole fraction ($y_{i,j}$) for each specie is:

$$y_{i,j} = \frac{C_{i,j}}{\sum_j C_{i,j}} \tag{6.14}$$

As the bed expands, bubbles grow larger but frictional effects are minimal compared to the solids hold-up. Assuming that the pressure drop is negligible introduces an error of as much as 1 % with 10 g of catalyst in a reactor that has a diameter of 8 mm. For deep beds, we include the pressure variation with axial distance.

The volume of the gas phase (V_{g}) is $\epsilon_{\mathrm{v}}V$ while the volume of the gas in the particle phase (V_{p}) is $(1-\epsilon_{\mathrm{v}})\epsilon_{\mathrm{sk}}V$. The mass transfer coefficient—$k_{\mathrm{m},j}$—accounts for molecular diffusion from the gas phase into the catalyst pores and r_j is the adsorption/desorption rate, which is proportional to the number of active sites, V_{A}. A convective term, Q_{rxn}, accounts for mass transfer between the two phases: when a species from the gas phase is in the pore, $C^*_{i,j}$, and adsorbs to a vacant site, V_{V}, on the catalyst surface creating an adsorbed species $C^{\mathrm{ads}}_{i,j}$. This reaction creates a convective flux, that acts like a vaccum. The flux from the bulk gas phase to the pore phase equal to the moles adsorbed. When the desorption rate becomes greater than the adsorption rate, the flux reverses and the convective flux is from the pore to the bulk gas phase. Every reaction, r_j, contributes to the molar flux between the phases at each grid block i, $\tilde{Q}_{\mathrm{rxn},i}$:

$$r^k_{i,j} = \left[k_{ads,j}C^{*,k-1}_{i,j}\left(V_{\mathrm{T}} - C^{\mathrm{ads,k-1}}_{i,j}\right) - k_{des,j}C^{\mathrm{ads,k-1}}_{i,j}\right]W_i V_{\mathrm{pore,i}} \tag{6.15}$$

$$\tilde{Q}_{\mathrm{rxn},i} = \sum_{j=1}^{N_j} r_{i,j}^{k} \tag{6.16}$$

where k_{ads} is the forward reaction—adsorption—and k_{des} is the reverse reaction—desorption. The volumetric flow rate in the axial direction $Q_{i,j}^{k}$ is:

$$Q_{i,j}^{k} = Q_{i-1,j}^{k} + r_{i,j}^{k} \tag{6.17}$$

The axial volumetric flow rate at any height, Q_i, equals the inlet flow rate, Q_{o}, multiplied by the expansion due to the change in pressure plus the sum of the species that have adsorbed or desorbed to that point.

$$Q_i = Q_{\mathrm{o}} \frac{P_{\mathrm{o}}}{P_i} + Q_{i,j}^{k} \tag{6.18}$$

The differential form of the gas phase mole balance is:

$$\frac{\partial C}{\partial t} + U_{\mathrm{g}} \frac{\partial C}{\partial z} = \mathcal{D} \frac{\partial^2 C}{\partial z^2} + k_{\mathrm{m}}(C - C^{*}) + \frac{y_{i,j}^{k-1} \tilde{Q}_{\mathrm{rxn},i}}{V_{\mathrm{g}}} \tag{6.19}$$

With the finite volume approach form, when the adsorption rate is greater than the desorption rate ($k_{\mathrm{ads}} C_i^{*} V_{\mathrm{T}} > k_{\mathrm{des}} C_i^{\mathrm{ads}}$) the mole balance equation for species j in grid block i in the gas phase is:

$$\epsilon_{\mathrm{v}} V \frac{C_{i,j}^{k} - C_{i,j}^{k-1}}{\Delta t} = -Q_i^{k-1} \left(C_{i,j}^{k-1} - C_{i-1,j}^{k-1} \right) - k'_{\mathrm{m,j}} \left(C_{i,j}^{k-1} - C_{i,j}^{*,k-1} \right) - y_{i,j}^{k} \tilde{Q}_{\mathrm{rxn},i} \tag{6.20}$$

where, $k'_{\mathrm{m,j}}$ is a fitting parameter. As gas species, j, adsorbs onto the catalyst surface the accompanying influx of gas from the bulk gas to the pore is the product of the total moles reacted at that grid block multiplied by the mole faction of that species, $\tilde{Q}_{\mathrm{rxn},i}$.

When the adsorption rate is less than the desorption rate, the net flux is from the pore with a mole fraction y^{*} multiplied by the total moles of gas that evolve from the surface during that time step ($k_{\mathrm{ads}} C_i^{*} V_{\mathrm{T}} < k_{\mathrm{des}} C_i^{\mathrm{ads}}$):

$$\epsilon_{\mathrm{v}} V \frac{C_{i,j}^{k} - C_{i-1,j}^{k-1}}{\Delta t} = -Q_i^{k-1} \left(C_{i,j}^{k-1} - C_{i-1,j}^{k-1} \right) - k'_{\mathrm{m,j}} \left(C_{i,j}^{k-1} - C_{i,j}^{*,k-1} \right) + y_{i,j}^{*,k-1} \tilde{Q}_{\mathrm{rxn},i} \tag{6.21}$$

Pore volume mole balance

The hydrodynamics of the gas in the pore as well as the adsorbed species is dictated by the transport of the solids phase. The solids move up predominantly in the centre of the vessel and down along the the walls. This motion is well characterized for spouted beds, riser reactors, and larger sized fluidized beds. This movement ensures isothermal conditions and that the solids are perfectly backmixed. To represent it mathematically, we introduce a solids circulation term, M_s, (convective) in both the upward and downward directions and assume radial uniformity—perfectly backmixed). The mass flux, w_s, equals the quotient of the solids circulation rate and the cross-sectional area. The gas velocity (U_g) is:

$$U_\mathrm{g} = \frac{w_\mathrm{s}}{\rho_\mathrm{p}} = \frac{M_\mathrm{s}}{X_\mathrm{A}\rho_\mathrm{p}} \tag{6.22}$$

where ρ_p is the particle density. The bulk density and skeletal densities are:

$$\rho_\mathrm{b} = \rho_\mathrm{p}(1-\epsilon_\mathrm{v}) \tag{6.23}$$

$$\rho_\mathrm{sk} = \frac{\rho_\mathrm{p}}{1-\epsilon_\mathrm{sk}} \tag{6.24}$$

The convective contribution to the mole balance of the pore phase ($\tilde{Q}_{\mathrm{rxn},i}$) is analogous to that of the the gas phase mole balance. The differential form of the pore volume mole balance is:

$$\frac{\partial C^*}{\partial t} = \mathcal{D}_\mathrm{S}\frac{\partial^2 C^*}{\partial z^2} - k_\mathrm{m}(C-C^*) + W_i\left[k_\mathrm{ads}C^*(C_\mathrm{T}-C^\mathrm{ads}) - k_\mathrm{des}C^\mathrm{ads}\right] \tag{6.25}$$

Where $\mathcal{D}_\mathrm{S}$ is the dispersion coefficient for the solid phase.

when the adsorption rate is greater than the desorption rate ($k_\mathrm{ads}C^*_{i,j}V_\mathrm{T} > k_\mathrm{des}C^\mathrm{ads}_{i,j}$)

$$\begin{aligned}(1-\epsilon_\mathrm{v})\epsilon_{sk}V\frac{C^{k,*}_{i,j}-C^{k-1,*}_{i-1,j}}{\Delta t} &= \frac{M_\mathrm{s}}{\rho_\mathrm{p}}\left(C^{*,k-1}_{i+1,j}-C^{*,k-1}_{i,j}\right) - \frac{M_\mathrm{s}}{\rho_\mathrm{p}}\left(C^{*,k-1}_{i,j}-C^{*,k-1}_{i-1,j}\right)\\ &+ k'_\mathrm{m,j}\left(C^{k-1}_{i,j}-C^{*,k-1}_{i,j}\right) + y^{k-1}_{i,j}\tilde{Q}_{\mathrm{rxn},i} + r^{k-1}_{i,j}\end{aligned} \tag{6.26}$$

and when the desorption rate is greater

$$(1-\epsilon_\mathrm{v})\epsilon_{sk}V\frac{C^{k,*}_{i,j}-C^{k-1,*}_{i-1,j}}{\Delta t} = \frac{M_\mathrm{s}}{\rho_\mathrm{p}}\left(C^{*,k-1}_{i+1,j}-C^{*,k-1}_{i,j}\right) - \frac{M_\mathrm{s}}{\rho_\mathrm{p}}\left(C^{*,k-1}_{i,j}-C^{*,k-1}_{i-1,j}\right)$$

$$+ k'_{\mathrm{m,j}} \left(C_{i,j}^{k-1} - C_{i,j}^{*,k-1} \right) - y_{i,j}^{*,k-1} \tilde{Q}_{\mathrm{rxn},i} + r_{i,j}^{k-1} \tag{6.27}$$

Adsorbed species mole balance

The adsorbed species mole balance resembles the pore volume balance and includes the convective term related to solids motion (M_s) but excludes the gas convection terms (Q_rxn). The differential form of the adsorbed species mole balance is:

$$\frac{\partial C^\mathrm{ads}}{\partial t} = \mathcal{D}_\mathrm{S} \frac{\partial^2 C^\mathrm{ads}}{\partial z^2} + V_\mathrm{pore} \left[k_\mathrm{ads} C^* (C_\mathrm{T} - C^\mathrm{ads}) - k_\mathrm{des} C^\mathrm{ads} \right] \tag{6.28}$$

And, with the finite volume approach is:

$$W_i \frac{C_{i,j}^{ads,k} - C_{i-1,j}^{ads,k-1}}{\Delta t} = -M_\mathrm{s} \left(2C_{i,j}^{ads,k-1} - C_{i,j}^{ads,k-1} - C_{i+1,j}^{ads,k-1} \right) - r_{i,j}^{k-1} \tag{6.29}$$

6.4 Results and discussion

6.4.1 Porosity and Geldart group A, B powders

We analyzed the RTD with a pulse input of a mix of tracers including CO_2, CO, H_2, and CH_4 with FCC (Figure 6.4–a). Diffusivity coefficients for each gas at 25 °C are 0.150 , 0.195 , 0.796 and 0.208 $\mathrm{cm^2\,s^{-1}}$, respectively. Based on previous studies, at high velocity in an empty tube, an extended tail is present (Chapitre 5). To avoid this physical effect, we operated the reactor at $U_\mathrm{g} = 10\,\mathrm{mm\,s^{-1}}$. The surface area of the FCC—Geldart group A powder—is $93\,\mathrm{m^2\,g^{-1}}$. All the gases were superimposed in the empty tube studies, except for H_2 (Chapitre 5). The residence time varied with diffusivity with FCC loaded to the reactor (Figure 6.4–a): At $t = 28\,\mathrm{s}$, hydrogen is first detected, and the axial dispersion model fits the data perfectly ($R^2 = 0.996$); 15 s later the MS begins to detect CO and CH_4 (both have similar diffusivity coefficients). When the trailing edge drops to 80 % of the peak height, the curve deviates from an ideal plug flow and the concentration drops more slowly, which corresponds to a large tail. Finally, another 12 s later, CO_2 appears—the peak height is much smaller and the tail much more pronounced.

The time it takes for the tracer to reach the MS after the valve switch is the same for both the step-input and pulse. But the axial dispersion model fits the step-input pulse data very well compared to the pulse, which demonstrates that its applicability to identify anomalies and flow heterogeneities is poor (Figure 6.5).

We repeated a series of tests with sand—Geldart group B, which has little to no porosity

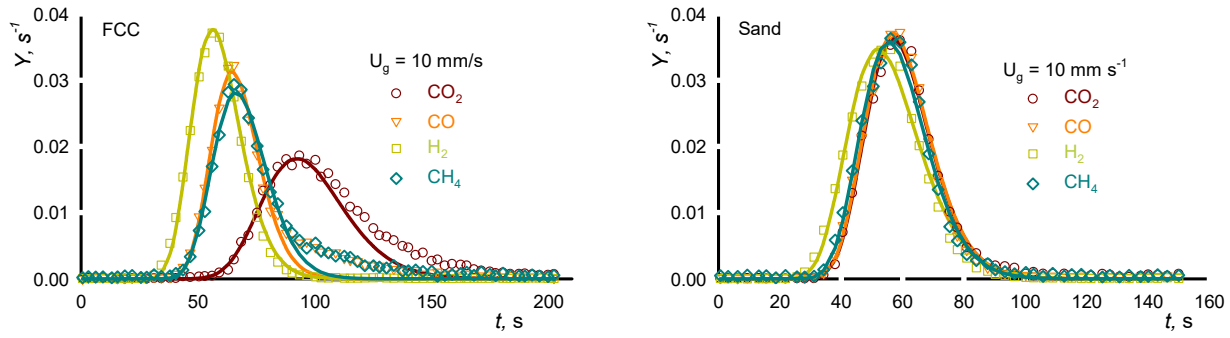

(a) (b)

Figure 6.4 RTD comparison between Geldart group A and B catalyst: time vs $Y = \frac{C_i}{\sum C_i \Delta t}$. The tube was loaded with (a) 8.19 g of FCC – Geldart group A - and (b) 13.5 g of sand – Geldart group B. For FCC (a), the model fits up to the leading edge of the plot, but not the tail where a deviation is observed for CO_2, CO and CH_4. For sand (b), the axial dispersion model fits perfectly the data for all tracers.

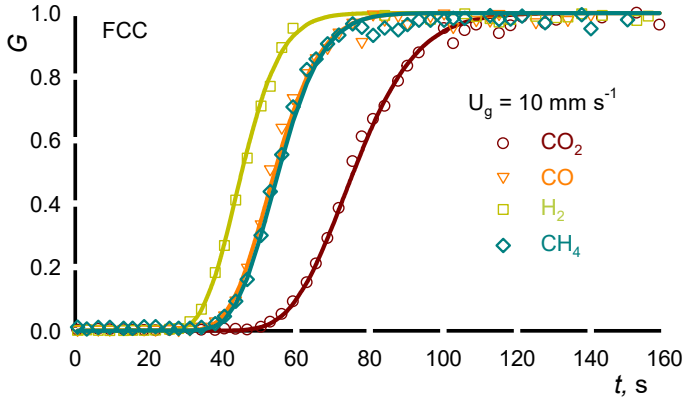

Figure 6.5 RTD for a step injection at 10 mm s^{-1} with 8.19 g FCC. Argon was initially injected. At $t = 0$, we switched the 4-way valve to substitute the Ar with feed gas—CO_2, CO, H_2, CH_4. The dots represent experimental data while the continuous lines are the fitting axial dispersion model. The tail is impossible to detect with a step injection as opposed to the pulse injection.

and an order of magnitude lower surface area—2 $m^2\,g^{-1}$ versus 93 $m^2\,g^{-1}$ (Figure 6.4–b). The RTD curves for CO, CO_2 and CH_4 resemble that of the empty tube (Chapitre 5)—all three curves are superimposed and the axial dispersion model fits the experimental data very well. Hydrogen egressed the reactor first due to his high diffusivity coefficient, which is again consistent with the previous study about empty tube experiments (Chapitre 5).

Analysis of mean residence time ($\bar{t}$) and variance (σ^2) for FCC and sand powders is present in supplementary file.

We attribute the difference between FCC and sand RTD to several factors:

1. **Diffusion**: hydrogen has a diffusivity coefficient four to five times higher than CO, CO_2 and CH_4 (0.796 vs 0.150 to 0.208 $cm^2\,s^{-1}$). Thus, for RTD experiment with FCC and sand, H_2 exit the reactor 10 to 15 s before CO at 10 $mm\,s^{-1}$. Radial diffusion of hydrogen ensures a flat concentration profile so that axial dispersion model fits the experimental data well.
2. **Porosity**: The physico-chemical properties of the gas tracer affect the RTD for porous powders more than for non-porous and the effect increases with longer residence time.
3. **Adsorption**: Diffusivity is insufficient to account for the extended CO_2 tail for the case with FCC: The RTD curve is delayed by 12 seconds after CO and CH_4. We attribute this phenomena to a chromatographic effect where CO_2 ingress into the pores and then interacts/adsorbs to the internal surface. As the tracer passes and the concentration decreases, the driving force reverses and the CO_2 desorbs. This process is on the order of the mixing time of the solids in the bed, which could then extend the residence time (CO_2 adsorbing at the top of the bed is carried down with the solids as the recirculate to the bottom of the reactor[57]).

6.4.2 New model results

For each syngas tracer, we applied the new model (Figure 6.6). We omitted H_2 and resolved simultaneously three mole balances for CO_2, CO, and CH_4. Hydrogen has a high diffusivity coefficient and other phenomena that are unaccounted for with the new model.

First, we calculated the molar concentration at each MS time step and normalized the data to have identical area under the curve for all tracers. The gas concentration detected at the bottom of the reactor (including the entrance lines and the MS capillary) is applied as the initial concentration in the model simulation. To fit the model, we minimized the sum of squares error (SSE) between the data and the new model for all the tracers together (CO_2, CO and CH_4). The parameters adjusted (Table 6.3) are the volumetric flow rate (Q), the circulation flow (M_s), the mass transfer between the bulk phase and pores ($k_{m_{CO_2}}$, $k_{m_{CO}}$, $k_{m_{CH_4}}$, $k_{m_{H2}}$), the adsorption rate ($k_{ads_{CO2}}$, $k_{ads_{CO}}$, $k_{ads_{CH4}}$) and desorption ($k_{des_{CO2}}$, $k_{des_{CO}}$, $k_{des_{CH4}}$). When we reached the highest R^2 for the first three tracers, we fit the hydrogen data by minimizing SSE with the flow rate. We maintained CO_2, CO, and CH_4 parameters. For all tracers, we fitted the first 200 s with an optimal number of CSTR of 40.

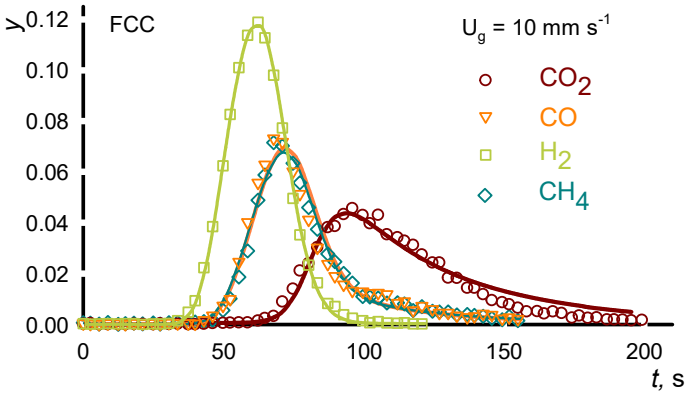

Figure 6.6 New model fitting results for FCC. Same conditions as Figure 6.4. The model predicts dispersion, diffusion, and adsorption phenomena.

Table 6.3 New model parameters adjusted for a pulse injection RTD in a quartz tube loaded with 8.19 g FCC - velocity of 10 mm s^{-1}. M_s is 9.59×10^{-5} for each gases.

Tracer	Q (mL min^{-1})	k_m (s^{-1})	k_{ads} (mol^{-1} s^{-1})	k_{des} (mol^{-1} s^{-1})	V_T (kmol kg^{-1})	R^2
CO_2	19.3	4.8×10^{-7}	31700	124	3.19×10^{-6}	0.986
CO		2.0×10^{-5}	4.92	0.0703		0.970
CH_4		2.1×10^{-5}	4.92	0.0703		0.981
H_2	22.5	3.2×10^{-6}	0	0	0	0.999

The new model predicts the adsorption of CO_2 compared to the axial dispersion model. Indeed, the coefficient of determination (R^2) has a higher value for CO_2 (0.920 vs 0.986), and slightly lower value for CO (0.981 vs 0.986), CH_4 (0.966 vs 0.970), and H_2 (0.995 vs 0.999). However, the R^2 for CO and CH_4 with the new model is due to the difference in height and a slight shift to the right (Figure 6.6) while for the axial dispersion model the low R^2 value is due by the deviation in the descending tail (Figure 6.4—a).

The new model is flexible and adjusts from simple cases, plug flow behaviour, to a complex situation with adsorption. The H_2 molecules, with its small size and its high diffusivity coefficient, exit the reactor first. To compensate for this effect, we increased the flow rate from 19.3 mL min^{-1} to 22.5 mL min^{-1}. To simplify the model, we assumed that carbon monoxide and methane have the same adsorption and desorption rate. Then, only the mass transfer between the bulk phase and the pores is different. Finally, the new model confirms the hypothesis where CO_2 is adsorbed by FCC catalyst and quantify the phenomena. The

desorption rate is 256 times faster than the adsorption rate. The concentration of the vacant site (V_T) equals 3190 nmol g^{-1}. The tail is well represented with this model ($R^2 = 0.986$).

6.4.3 New model—Sensitivity analysis

To analyze the sensitivity of the new model, we varied one parameter at the time while all other variables are at their optimum values. Then we compared the R^2. We analyzed the effect of the number of CSTRs, the time modelling, and the volumetric flow rate. The last one is minimized when we resolved the mole balance equations while n_{CSTR} and time are a chosen value.

Number of CSTRs

We analyzed the effect of the number of CSTRs on the R^2 with three syngas species (Figure 6.7—a) and then consider the hydrogen data independently The R^2 increases reaches a plateau around $n_{CSTR} = 30$ for the three species. At this point, the R^2 of the hydrogen decreases slightly. When we increase n_{CSTR} from 30 to 45 (Figure 6.7—b), the R^2 of CH_4 continues to increase but it reaches a plateau for CO and CO_2. The maximum R^2 for CO_2 is 0.9863 and finally selected 40 CSTRs as the optimum value for parameter estimation.

When we increase the number of CSTR, the RTD curves for CO_2 are higher and slide to the right (Figure 6.7—c). At 40 CSTRs, the height of the fitting curve is the same as the data. At 45 CSTRs, the model deviates from the data at the trailing edge, thus the R^2 is lower. The tails are similar to each curve which confirms that the n_{CSTR} is independent of the slope shape.

Volumetric flow rate

The volumetric flow rate is a measured variable but due to the uncertainty in its value, we take it as a parameter since a small deviation greatly influences the R^2. For example, for CO_2, a variation of 9 % in the flow rate can decrease the R^2 of 83 %. The model is unstable for $Q < 16.455$ mL min^{-1} (which depends on the time step). We fit the data from 16 5 to 30 mL min^{-1}— the injection volumetric flow rate. In general, the R^2 increases up to a maximum and decreases immediately – bell shape (Figure 6.8—a). We expanded the range of the axes to better differentiate between the three species (19—20 mL min^{-1}) – R^2 variation is 5 % (Figure 6.8 —b). At this flow rate zone, the CH_4 decreases while the CO increases. The optimum, where CO crosses CH_4, is 19.5 mL min^{-1}. However, CO_2 reached a maximum at 19.3 mL min^{-1} and then decreased. This is in accordance with the value obtained by

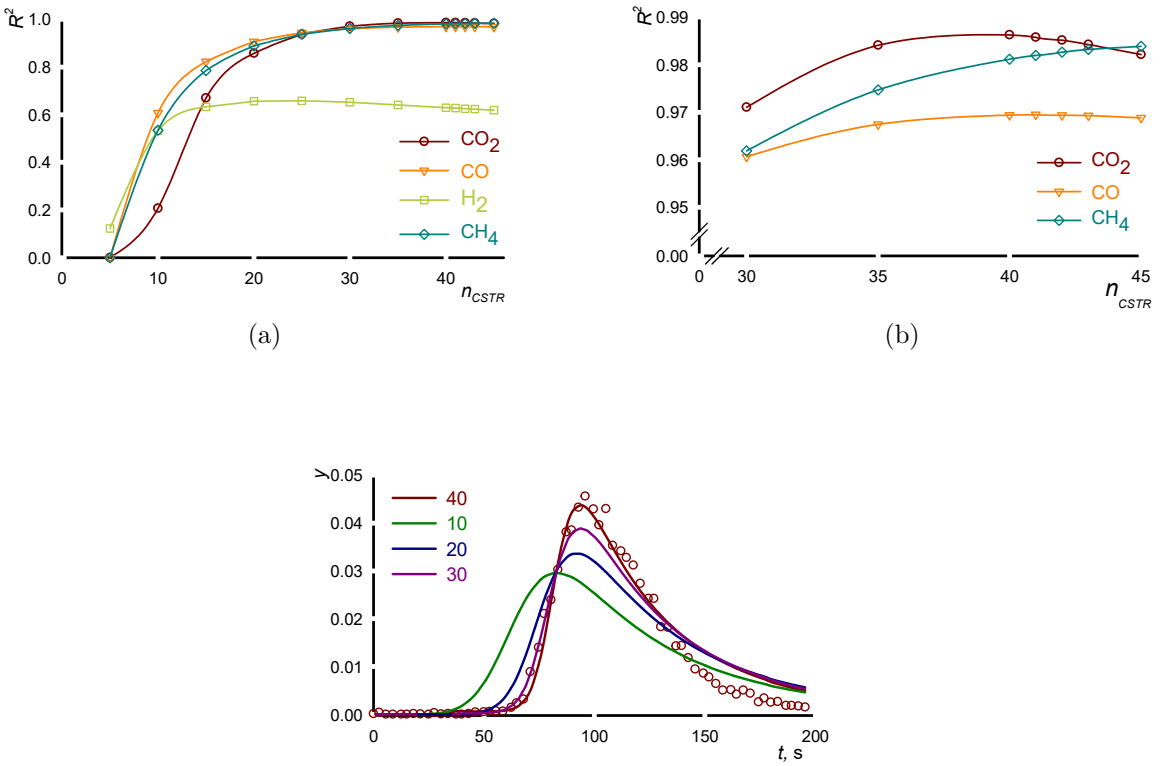

Figure 6.7 Sensitivity analysis on the number of CSTRs. (a) R^2 vs the number of CSTR for the four tracers. (b) Variation of R^2 for CO_2, CO, and CH_4 for $n_{CSTR} = 30$ to 45. (c) RTD curves for CO_2 adsorption on FCC catalyst. The dots are the CO_2 data while the lines are the new model fits with n_{CSTR} from 10 to 40. The optimal value is $n_{CSTR} = 40$.

minimizing the SSE – 19.3 mL min^{-1}.

We plot the RTD curve for CO_2 with the new model and flow rate from 18 to 20 mL min^{-1} (Figure 6.8— c). At 18 mL min^{-1}, the solver becomes unstable with the presence of random peaks. The R^2 decreasing by 10 % with a change of 2 % in the flow rate. With an increase in flow, the curve is shifted to the left and becomes taller. However, the adsorption tail is independent of the flow rate.

Modelling time

The total time from the injection of the tracers until the entire 10 mL pulse exits the reactor is approximately 100 s for H_2, 150 s for CO and CH_4, and 200 s for CO_2. We started the analysis at 110 s due to the instability to resolve under this time (Figure 6.9—a). The R^2 for

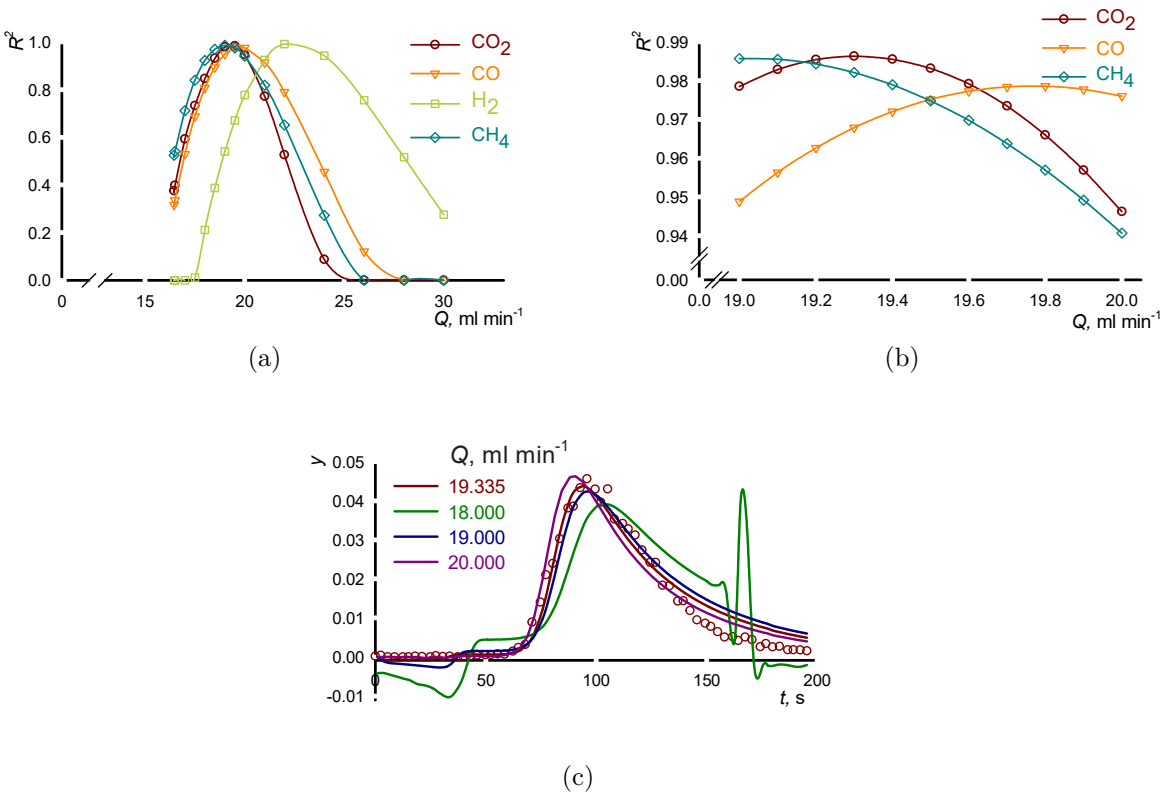

Figure 6.8 Sensitivity analysis of the volumetric flow rate. (a) R^2 vs the flow rate for four tracers. (b) Variation of R^2 for CO_2, CO, and CH_4 for $Q = 19$ to $20\,mL\,min^{-1}$. (c) RTD curves for CO_2 adsorption on FCC catalyst. The flow rate varies from 18 to $20\,mL\,min^{-1}$. The optimal value is $Q = 19.3\,mL\,min^{-1}$.

hydrogen is lower from 120 to 200 s compared to 110 s. This is a common observation when we include time in the modelling beyond which the concentration reaches a steady value[12]. The R^2 is stabilized at 140 s for CO_2, CO and CH_4 (Figure 6.9—b). Indeed, the maximum variation in R^2 for each 10 s is 0.07 % for CO, 0.09 % for CH_4, and 0.11 % for CO_2. Thus, we concluded that from 140 s of modelling time, the model fits the data except for H_2 where its optimum point is at 110 s. It is confirmed with the RTD curve for CO_2 with different time modelling (Figure 6.9—c). At 110 s, the model fit is slightly shifted to the left and the peak is higher.

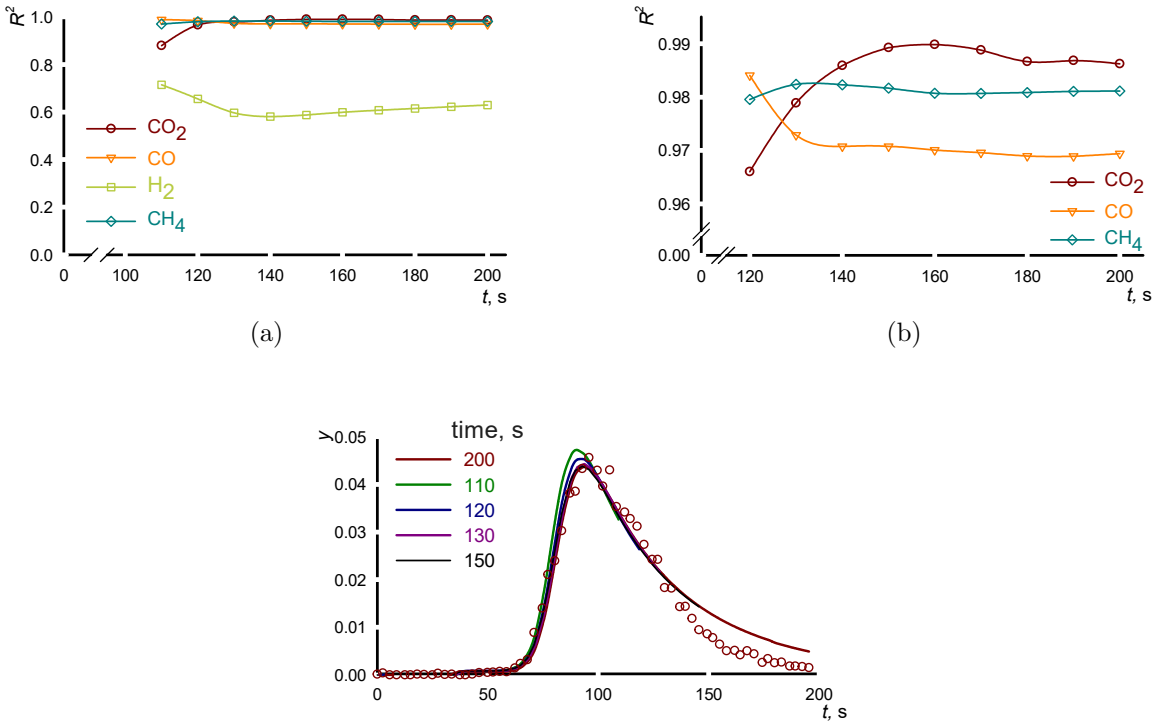

Figure 6.9 Sensitivity analysis of modelling time. (a) R^2 vs the modelling time for the four tracers (b) Variation of R^2 for CO_2, CO, and CH_4 for time = 120 to 200 s. (c) RTD curves for CO_2 adsorption on FCC catalyst. The modelling time is from 110 to 150 s. At 150 s or higher, the fitting results are the same.

6.4.4 Temperature analysis

To confirm the impact of diffusivity on RTD, we compared empty tube, FCC and sand with a pulse injection at 300 °C (Figure 6.10). The syngas tracers—CO_2, CO, CH_4, and H_2—are fed at 10 mm s^{-1}. At this temperature, diffusivity coefficients are 0.479 , 0.622 , 0.664 , and 2.54 cm^2 s^{-1} respectively. The first hypothesis was:

— The larger the difference of diffusivity coefficient is between the gases, the larger will be the delay between each RTD curve.

At 25 °C and 300 °C, the hydrogen diffusivity coefficient is 5 times that of CO_2 and 4 times that of CO and CH_4. According to this hypothesis, the MS should detect H_2 much sooner than the others. However, only hydrogen is slightly advanced compared to CO_2, CO and CH_4, which overlap. Thus, if the ratio (Ex. $H_2/CO = 4$) is kept, the delay between RTD curve will be the same. Curiously, at 300 °C the CO_2 egresses at the same time at the other gases with FCC indicating that adsorption is absent (Figure 6.10–b). Thus we conclude:

1. The experimental technique is capable of identifying the contribution of diffusivity to the RTD when the diffusion coefficient is at least 2 times greater than any other tracer (the curve of the gas with the highest diffusion coefficient shifts to the left). This observation is valid for porous and non-porous powders (Figure 6.10–b,c).
2. Even at 300 °C and 14 $\times U_{\mathrm{mf}}$, the pulse technique is capable of identifying the effect of diffusion coefficient on the RTD (Supplementary file—Figure S2).
3. Small atomic gases like H_2 and He with high diffusivity coefficient will experimentally fit the axial dispersion model for all velocity and temperatures (Figure 6.10).

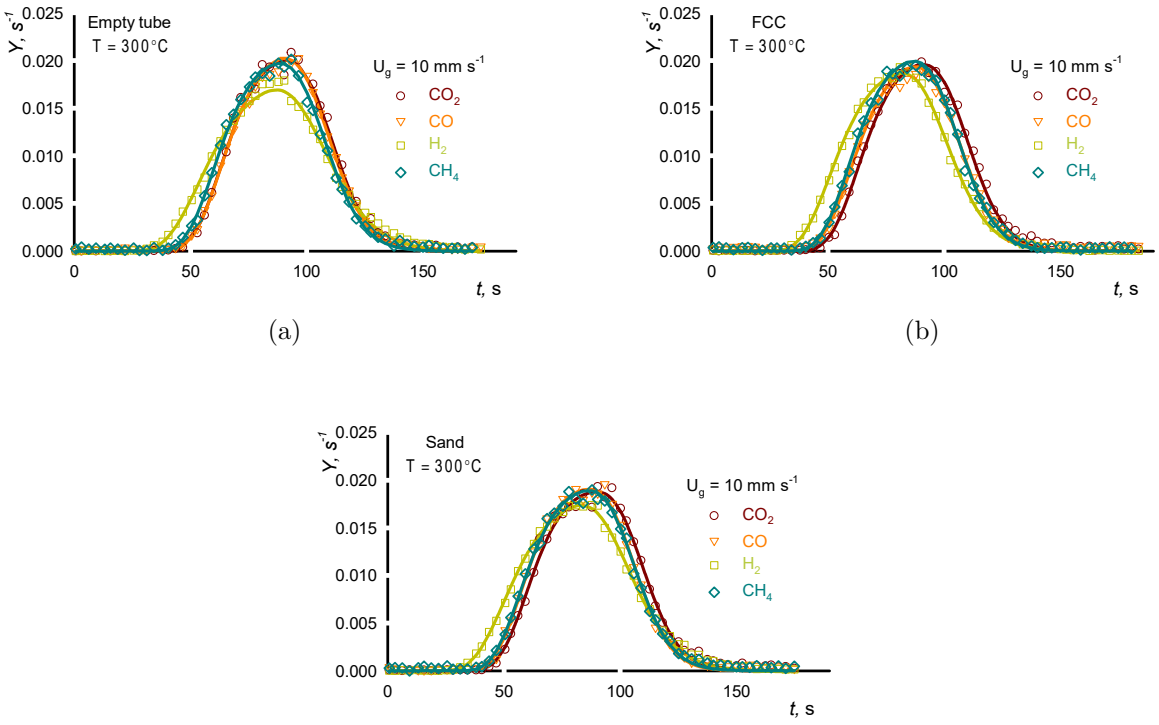

Figure 6.10 Residence time distribution comparison at 300 °C: time vs $Y = \frac{C_i}{\sum C_i \Delta t}$. The quartz tube was (a) empty or loaded with (b) 6.50 g of FCC and (c) 10.7 g of sand. The tapped bed height was 13 cm.

6.5 Conclusion

Residence time distribution is an effective tool to detect bypassing, dead volume, and back mixing. We analyzed gas phase RTD in an 8 mm internal diameter, 36 cm long quartz tube fluidized bed. We injected simultaneously, at $10\,\mathrm{mm\,s^{-1}}$, a syngas mix of gases—CO_2, CO, CH_4 and H_2 and characterized the data with the axial dispersion model. When the reactor is loaded with FCC—a porous catalyst, hydrogen, with its high diffusivity coefficient, egressed the reactor 15 s before CH_4/CO and 27 s before CO_2. Also, an extended tail is observable for CO_2, CO, and CH_4 (more pronounced for CO_2). The axial dispersion model deviates from the experimental data because the model assumes ideal behaviour (R^2 CO_2 = 0.920). We compared the results with a non-porous catalyst—sand. All the RTD curves overlap, except for hydrogen.

We developed a *tanks-in-series* model considering three phase: the gas phase, gas in catalyst pores, and the adsorbed species. We quantify the mass transfer between the bulk phase and the pores (k_m), the circulation rate (M_s), and the real volumetric flow rate (Q). The adsorption rate (k_ads) and desorption rate (k_des) for CO_2 is $31\,719\,\mathrm{mol^{-1}\,s^{-1}}$ and $123.8\,\mathrm{mol^{-1}\,s^{-1}}$ respectively with a concentration of vacant sites of 3.1886×10^{-6} $\mathrm{kmol\,kg^{-1}}$. For CO and CH_4 k_ads and k_des are lower i.e. $4.9201\,\mathrm{mol^{-1}\,s^{-1}}$ and $0.070\,349\,\mathrm{mol^{-1}\,s^{-1}}$. We increased the R^2 from 0.920 with the axial dispersion model to 0.986 with the new model.

To resolve the entire system, we, first, omitted hydrogen due to its 4 to 5 times higher diffusivity coefficient ($\mathscr{D} = 0.796\,\mathrm{cm^2\,s^{-1}}$). We choose 40 CSTRs in series – the optimum value. Then, we minimized the sum of square errors (SSE) on all parameters for CO_2, CO, and CH_4 simultaneously. The total volumetric flow rate (Q) is interdependent of each adsorbed species. Indeed, when a species is adsorbed, Q decreases. Inversely, when a species is desorbed, Q increases.

The new model quantity the adsorption phenomena but has a few limitations. First, the number of CSTRs is fixed at 40 for all the species. However, CO_2 is far from ideal so should have less CSTRs while H_2, with little dispersion, should have several hundred CSTRs. The fact that the model is resolved simultaneously with all the tracers limits required that we better account for the effect of H_2 diffusivity. However, for all practical situations operating at high temperature, differences in diffusivity are unimportant. This highlights the importance of carefully choosing tracers for cold flow studies but at temperatures of 300 °C the physico-chemical properties of the gas tracer species is less critical.

Then, we must set initial values in the Fortran program for all parameters (Table 6.4). If these values are out of the range, the solver will diverge. A substantial amount of time is

required to find this data interval.

Table 6.4 New model limits range for an 8 mm fluidized bed reactor. The other parameters are fixed at their optimum values. Outside this range, the solver diverge.

Parameter	Range
n_{CSTR}	5 to 45
Volumetric flow rate (Q)	16.455 to 30 $\mathrm{mL\,min^{-1}}$
Circulation rate (M_{s})	0.0001 to 0.001 $\mathrm{kg\,s^{-1}}$
$k_{\mathrm{m_{CO_2}}}$	8×10^{-9} to 1×10^{-6}
$k_{\mathrm{m_{CH_4}}}$ et $k_{\mathrm{m_{CO}}}$	0 to 2.2×10^{-5}
$k_{\mathrm{m_{H_2}}}$	0 to 2×10^{-5}
$k_{\mathrm{ads_{CO_2}}}$	18600 to 35050
$k_{\mathrm{ads_{CO}}} = k_{\mathrm{ads_{CH4}}}$	3×10^{-4} to 44
$k_{\mathrm{des_{CO_2}}}$	27 to 144
$k_{\mathrm{des_{CO}}} = k_{\mathrm{des_{CH_4}}}$	8×10^{-6} to 1.1
Vacant site (V_{T})	2.88×10^{-6} to 3.24×10^{-6} $\mathrm{kmol\,kg^{-1}}$
Modelling time	110 to 200 s

Another simplification made to decrease the computational time is to fix the adsorption and desorption rate for CO and CH_4 at the same values ($k_{\mathrm{ads,CO}} = k_{\mathrm{ads,CH4}}$) and ($k_{\mathrm{des,CO}} = k_{\mathrm{des,CH4}}$). This assumption is valid considering extended tail for the 2 species are almost indistinguishable. However, to improve the model, distinct values will account for more of the variance in the experimental data.

6.6 Acknowledgment

This research was undertaken, in part, thanks to funding from the Canada Research Chairs program and the authors gratefully acknowledge the financial support from the Natural Sciences and Engineering Research Council of Canada (NSERC) and the Canada Foundation for Innovation (CFI).

6.7 Supplementary file

6.7.1 Moment analysis

The Peclet number characterizes the hydrodynamic of a system and is related to the number continuous stirred tanks in series (N_{CSTR}):

$$N_{\mathrm{Pe}} = 2(N_{\mathrm{CSTR}} - 1) \tag{6.30}$$

For a pulse injection, the mean residence time for the continuous and discrete forms are[33] :

$$\bar{t}_{\mathrm{pulse}} = \frac{\int_0^\infty tC\,\mathrm{d}t}{\int_0^\infty C\,\mathrm{d}t} \cong \frac{\sum t_i C_i \Delta t_i}{\sum C_i \Delta t_i} \tag{6.31}$$

And the variance is[33]:

$$\sigma^2_{\mathrm{pulse}} = \frac{\int_0^\infty t^2 C\,\mathrm{d}t}{\int_0^\infty C\,\mathrm{d}t} - \bar{t}^2_{\mathrm{pulse}} \cong \frac{\sum t_i^2 C_i \Delta t_i}{\sum C_i \Delta t_i} - \bar{t}^2_{\mathrm{pulse}} \tag{6.32}$$

We compared the moments (Table 6.5) and the inlet injection for FCC and Sand at $10\,\mathrm{mm\,s^{-1}}$. Additionally, we plotted the difference between 10 and $30\,\mathrm{mm\,s^{-1}}$ for FCC a Geldart group A powder (Figure 6.11). For moments, the general trends are:

1. At $10\,\mathrm{mm\,s^{-1}}$, the difference between the peak time and the real average time that a particle pass through the reactor is 6 or 7 s for empty tube, FCC and sand (Table 6.5). The Y value at the peak is $0.04\,\mathrm{s^{-1}}$.
2. At $30\,\mathrm{mm\,s^{-1}}$, the difference (Δ_t) is 2 or 3 s and Y value at the peak is $0.09\,\mathrm{s^{-1}}$.
3. If Y value ($Y = \frac{C_i}{\sum C_i \Delta t}$) at the peak is lower than $0.04\,\mathrm{s^{-1}}$ ($10\,\mathrm{mm\,s^{-1}}$) or $0.09\,\mathrm{s^{-1}}$ ($30\,\mathrm{mm\,s^{-1}}$), the data deviate from the axial dispersion model. Consequently, the variance is over $5000\,\mathrm{s^2}$ for $10\,\mathrm{mm\,s^{-1}}$ and over $850\,\mathrm{s^2}$ for $30\,\mathrm{mm\,s^{-1}}$. It is the case for FCC at 10 and $30\,\mathrm{mm\,s^{-1}}$ for all gases except hydrogen.

Table 6.5 Comparison of moments (mean residence time and variance) at the inlet and outlet of the reactor, Peclet number, and number of CSTRs in series. The tube is loaded with FCC or sand. Ar was initially injected in the reactor at 10 mm s^{-1}. $\bar{t}_{\text{in}} = \bar{t}_{\text{line}} + \bar{t}_{\text{MS}}$, $\sigma^2_{\text{in}} = \sigma^2_{\text{line}} + \sigma^2_{\text{MS}}$, $t_{\text{peak}} = \bar{t}_{\text{total}} - \bar{t}_{\text{in}}/2$, $\Delta_t = \bar{t}_{\text{real}} - t_{\text{peak}}$, and $N_{\text{Pe}} = 2(N_{\text{CSTR}} - 1)$.

Tracer	$\bar{t}_{in}$ (s)	σ^2_{in} (s^2)	t_{peak} (s)	$\bar{t}_{real}$ (s)	Δ_t (s)	σ^2_{out} (s^2)	N_{Pe}	N_{CSTR}	R^2
	FCC								
CO_2	23	866	100	107	7	12170	56	29	0.937
CO	22	720	72	78	6	6907	80	41	0.983
H_2	20	545	53	60	7	3761	58	30	0.996
CH_4	31	2173	75	81	6	7465	68	35	0.970
	Sand								
CO_2	24	975	55	62	7	4151	59	31	0.993
CO	22	720	54	61	7	3919	58	30	0.992
H_2	21	552	49	55	6	3159	40	21	0.993
CH_4	33	2308	52	61	9	3956	55	29	0.993

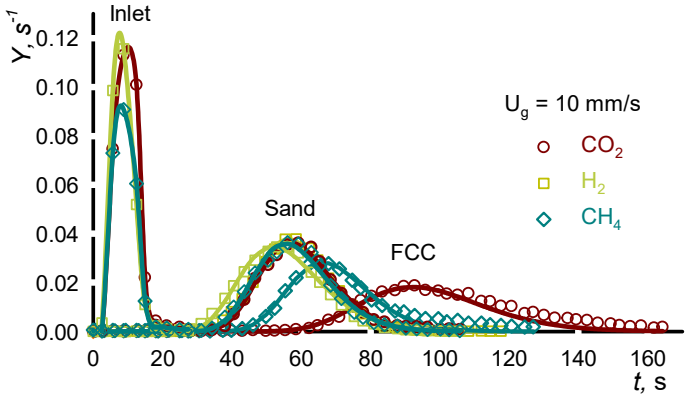

Figure 6.11 Comparison of the residence time distribution at the inlet and outlet at 10 mm s^{-1}. The curve represents $Y = \frac{C_i}{\sum C_i \Delta t}$ vs time with the area under the curve equals one. The quartz reactor is loaded with 8.19 g FCC or 13.2 g sand. We measured RTD at the inlet of the reactor to calculate the transit time for gases through the mass spectrometer and the upstream line. The data for FCC deviate from the axial dispersion model (presence of a tail) while for sand the data fit perfectly.

6.7.2 Temperature analysis

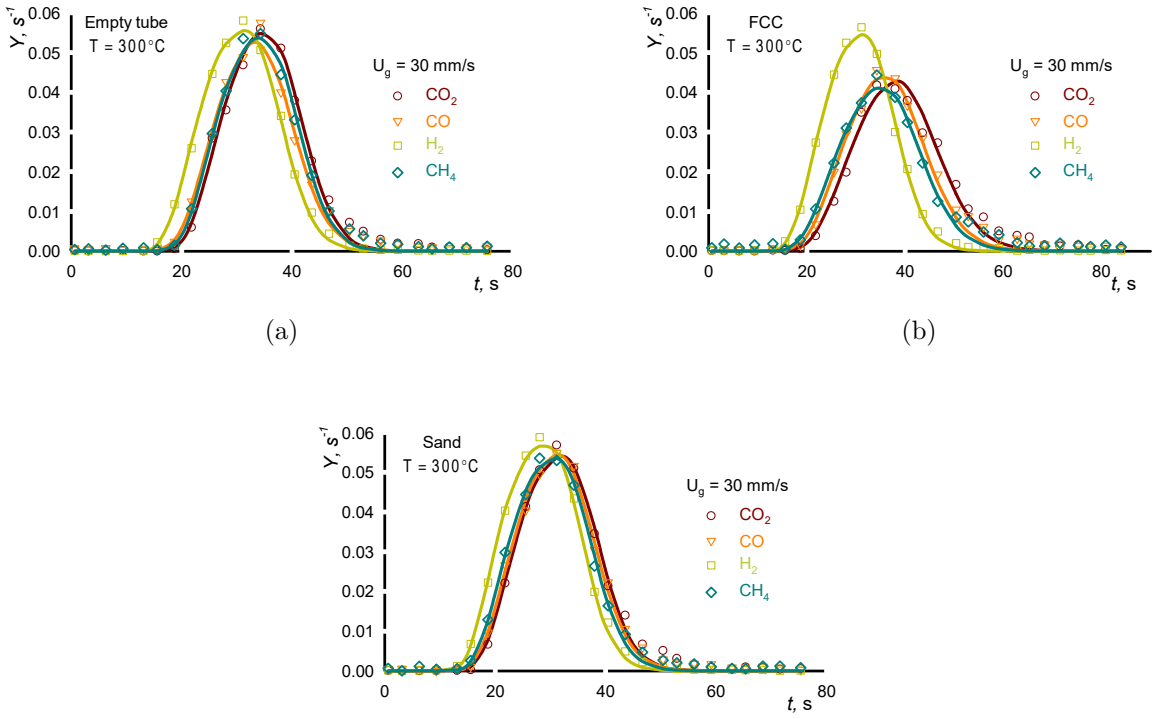

Figure 6.12 Residence time distribution comparison at 300 °C: $Y = \frac{C_i}{\sum C_i \Delta x}$ vs time. The quartz tube was (a) empty or loaded with (b) 6.50 g of FCC and (c) 10.7 g of sand. The tapped bed height was 13 cm. At higher velocity (30 vs 10 mm s^{-1}), diffusivity affect the RTD specially with FCC powder. Each distribution is separate from each other.

6.7.3 Statistical analysis

For each gas, we plotted the RTD data from the MS versus the fitting with the axial dispersion model (ADM) and the new model (Figure 6.13). Thus, the deviation of the models from the data is visible.

For CO_2 with the ADM (Figure 6.13—(a)), the rising curve fits the data while the downward curve is not linear that show a deviation from the data. It is the section where the extended tail is present on the RTD curve (adsorption). The R^2 is low, i.e. 0.920. With the new model (Figure 6.13—(b)), the R^2 increased considerably to 0.986. Dots from the upward and downward sections are both closer to the regression line (grey dotted lines). A small deviation at downward is still perceptible, but less predominant than the ADM.

For CO with the ADM (Figure 6.13—(c)), the dots are near the linear regression except at the end of the downward curve. In this section (0 to 0.013), the ADM deviates from the data. This has the effect of decreasing R^2 to 0.946. With the new model (Figure 6.13—(d)), the deviation section is now linear and R^2 increase to 0.970.

CH_4 behaviour is similar to CO with the ADM. However, with CH_4 (Figure 6.13—(e)), the dots are aligned in a straight line, and only deviates at the end of the downward slope. Thus, the R^2 is 0.979. With the new model (Figure 6.13—(f)), any major deviation is visible, but the dots are further from the central line, particularly from zero to half the upward curve. Nevertheless, the R^2 increases to 0.986.

Finally, both models fit greatly hydrogen ($R^2 \geq 0.99$) (Figure 6.13—(g),(h)). However, with the new model the dots are just a little bit closer to the regression line.

Thus, for all gases, the new model presents a better fit with the data compared to the axial dispersion model.

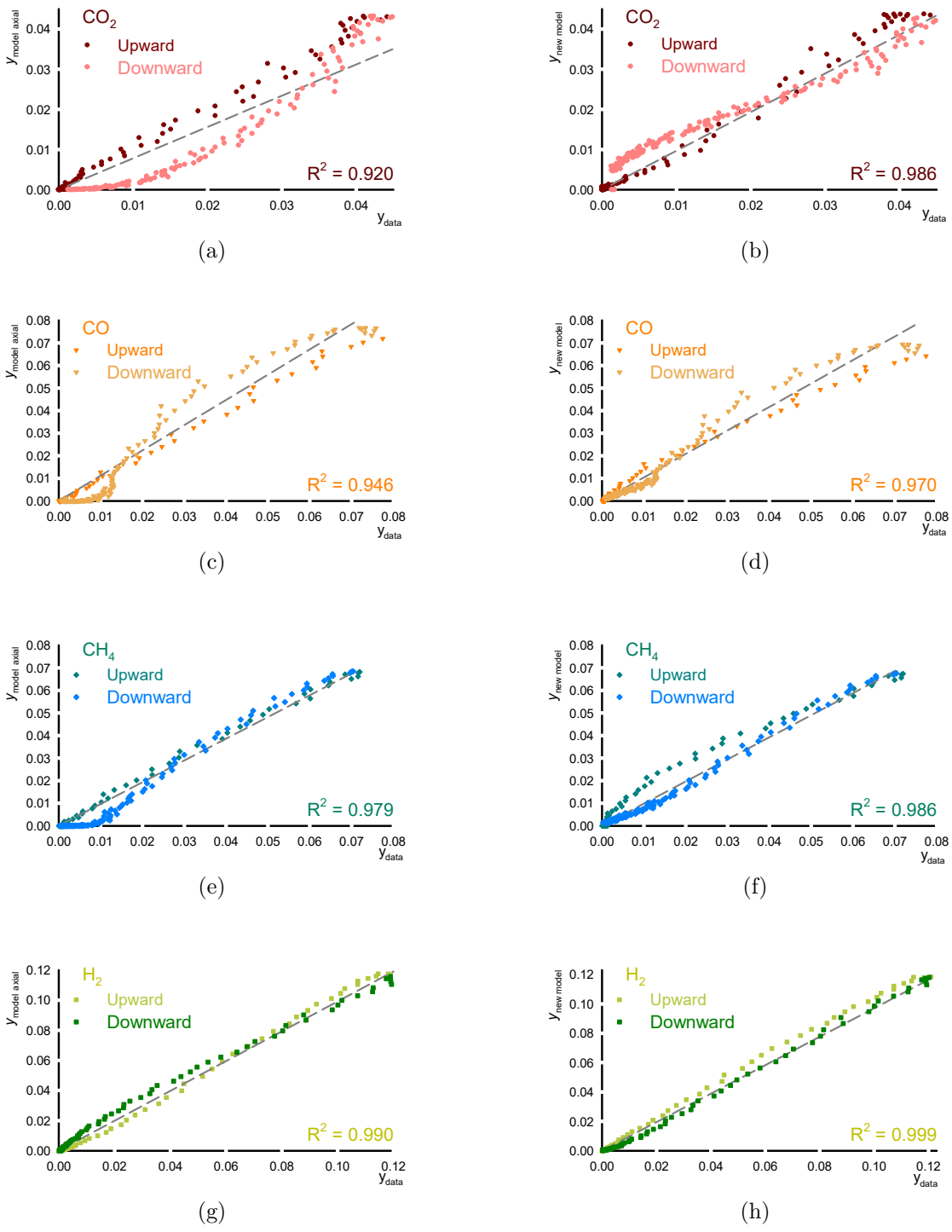

Figure 6.13 RTD data vs model fitting for each gas. The 2 colours represent the upward and downward of the RTD curve. The grey dotted line is the linear regression of all the data and crossing (0,0). (a), (c), (e), (g) are the axial dispersion model for CO_2, CO, CH_4, and H_2, respectively. (b), (d), (f), (h) are the new model. For all gases, we increased the coefficient of determination (R^2) with the new model.

CHAPITRE 7 ARTICLE 4: EXPERIMENTAL METHODS IN CHEMICAL ENGINEERING: UNRESOLVED CFD-DEM

Ariane Bérard, Gregory S. Patience, Bruno Blais

Journal: The Canadian Journal of Chemical Engineering

reçu: 29 juillet 2019 **revisé:** 20 septembre 2019 **accepté:** 7 octobre 2019

7.1 Abstract

CFD-DEM combines computational fluid dynamics (CFD), which solves the equation of motion of gas or liquids, with the discrete element method (DEM), a simulation technique based on a Lagrangian description of particle motion that predicts the flow of granular matter and powders. Resolved CFD-DEM solves the transport equations with CFD at a scale smaller than the particle diameter (d_p), assuming no-slip on the particle surface to couple the phases. The fluid solver scale is coarser than d_p in unresolved CFD-DEM and virtual mass, drag, and other solid-fluid forces couple the phases. Resolved CFD-DEM is more accurate, but is orders of magnitude more computationally intensive. Unresolved CFD-DEM predicts solid distribution, pressure loss, mass flow rate, and dense and dilute phase flow patterns when the solid to fluid and fluid to solid coupling between the fluid phase and the solid phase are non-trivial. Researchers apply CFD-DEM to predict gas-fluid dynamics of fluidized beds, spouted beds, hoppers, cyclones, costal erosion, and rock slides. Open source codes, commercial software, and parallel computer architectures have accelerated its adoption in pharmaceutical, agro-industrial, and reactor design. Current research targets improving the solid-fluid coupling strategies and multiphysics problems including heat transfer, mass transfer, and chemical reactions within or at the surface of the particles. The field has grown to over 200 indexed articles per year (Web of Science) in 2018. This article is part of a special series dedicated to experimental methods in chemical engineering that reviews the most important concepts, applications, and limitations of each technique.

keywords: computational fluid dynamics, discrete element method, hydrodynamic forces, unresolved, simulation

7.2 Introduction

Particle technology and granular matter represent 40 % of the value added to the chemical industry, including fluidized beds, spouted beds, dryers, solid-liquid reactors, and dispersed solid-fluid flow.[160] In the latter, the gas or liquid is the continuous phase while the particulate phase is structurally autonomous, like in pneumatic conveying. In fixed bed reactors and porous media the particles are structurally connected.[5] We define granular matter as particulate systems in which the effective diameter, $d_\mathrm{p} > 1\,\mu\mathrm{m}$.[161] At this scale Brownian motion due to thermal agitation is negligible and the forces acting on the particles are non-stochastic. Traditional CFD methods apply to immobile granular matter systems like porous media. Dispersed solid-fluid flows refer to the general case where the particles flow freely and the fluid accelerates particle motion.

Scale separation adds complexity to modelling disperse solid-liquid flows. Particle-fluid and particle-particle interactions at the d_p length scale affect structures at the process length scale such as macroscopic flow patterns and the generation of voids.[162] CFD-DEM combines computational fluid dynamics (CFD) with the discrete element method (DEM) to predict the dynamics of dispersed solid-fluid flows.

Resolved CFD-DEM (Figure 7.1—a) discretizes the fluid domain to the particle scale and resolves the flow around each particle. The no-slip boundary condition at the particle surface couples the two phases.[163,164,165,166,167,168,169] Using state of the art high-performance computing infrastructure and solving the flow constitutive equations at the particle scale limits the number of particles in the system to the order of 300 000.[170] When the Navier-Stokes equations are solved using the Lattice Boltzmann method, a minimum of 8 lattice nodes per particle diameter are required to ensure accuracy.[171] Discretization of the Navier-Stokes equations by finite volume[172] or finite element[168,169] are equally limited. The no-slip boundary condition requires an immersed boundary or fictitious domain to avoid the remeshing the solution at each time step, which can degrade accuracy and increase computational time.[173]

Unresolved CFD-DEM (Figure 7.1—b) solves the volume-averaged Navier-Stokes equations for the fluid at a scale greater than the particle dimension and accounts for the solid phase with DEM. Several particles occupy the same fluid mesh cell (or element). Explicit expressions couple the two phases for each solid-liquid interaction force: drag, virtual mass, Saffman lift, and Magnus lift, for example.[174]

Resolved CFD-DEM is more accurate than unresolved CFD-DEM because it fully accounts for the flow around each particle without additional models to couple the particle and fluid phases. However, it is an order of magnitude more computationally intensive: the largest

systems studied with 24 756 cores on a tier 0 high performance computer only have 350 000 particles.[170] Unresolved CFD-DEM resolves the flow at a coarser scale and simulates systems with more than 50 million particles.[175] Furthermore, it runs on smaller computer architectures: a 12 core workstation resolves 200 s of a 150 000 particle solid-liquid mixing operation in a month.[173] Unresolved has additional complexity due to the coupling procedure between the DEM and the CFD.

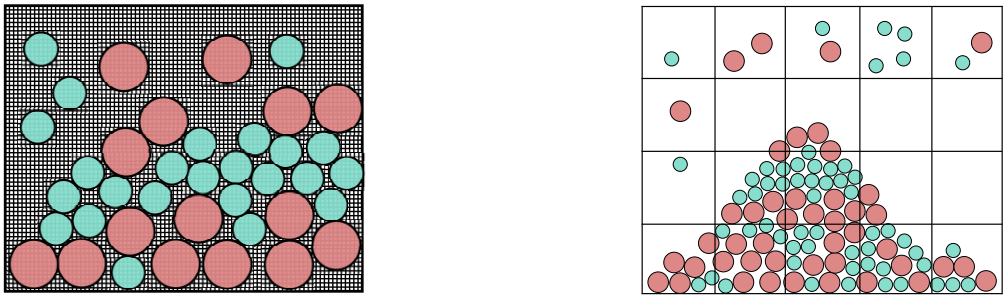

(a) (b)

Figure 7.1 Comparison CFD-DEM. (a) In resolved CFD-DEM, we discretize the fluid mesh to a smaller scale than the particle. (b) whereas in unresolved CFD-DEM, the fluid mesh is coarser than the particle.

Here, we review unresolved CFD-DEM, introduce the underlying equations, and discuss its numerical implementation. We then examine applications of the method and highlight the current challenges it faces. The main goal of this tutorial review is to understand the fundamentals behind CFD-DEM as a first approach. It is one of a series of articles dedicated to chemical engineering experimental methods.[133] Although it is not an experimental method per se, researchers and engineers apply CFD-DEM to predict the solid-fluid flows of fluidized beds[176,177,178] and spouted bed reactors,[179,180,181] dispersion and diffusion of airborne dust,[182,183] separation of particulate matter and air in cyclones,[184,185] drying woods chips,[186,187] food,[188], suspension of solid particles in agitated vessels,[189,190,191,192] pneumatic conveying,[193] and granulation.[194]

7.3 Method and numerical implementation

Unresolved CFD-DEM solves the fluid flow equations at a scale larger than that of the individual particles, while accounting for their effect on the fluid. To calculate the void fraction and the solid-fluid momentum exchange, we project the volume and the forces resulting from the solid-fluid interactions onto the CFD mesh. Then, from the fluid velocity, $\boldsymbol{u}$, the particle velocity, $\boldsymbol{v}$, the fluid density, ρ, and the fluid dynamic viscosity, μ, we calculate the

solid-fluid forces at the centre of mass of the particles. A pointwise description is applied for the particles. This projection (like a local volume filtering technique)[195] leads to a volume averaged form of the Navier-Stokes (VANS) equations.[174,196] In order to handle the particle-particle and particle-geometry collisions, we apply the soft-sphere discrete element method (DEM).[197,198,199]. These two models, which operate independently, are coupled at regular intervals—for instance at each CFD iteration—and the positions and velocities of the particles are applied to update the solid-fluid coupling (Figure 7.2).

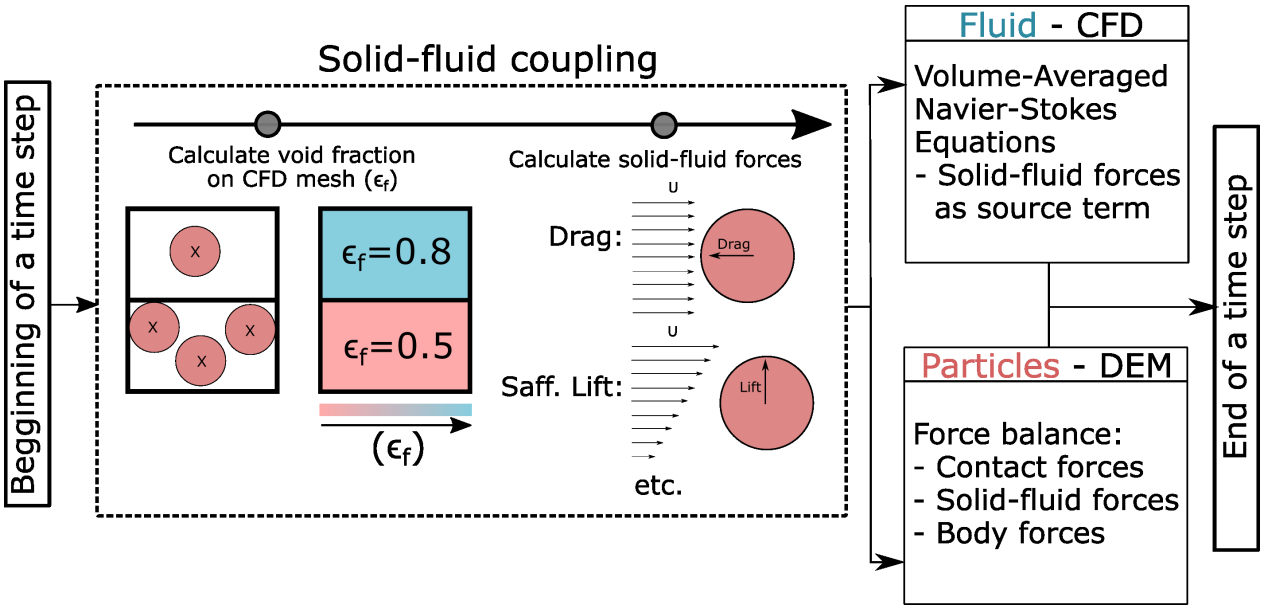

Figure 7.2 Portrait of an unresolved CFD-DEM iteration. First, we project the position of the particles onto the CFD mesh and calculate the void fraction ϵ_v. Then, from the fluid velocity, $\boldsymbol{u}$, the particle velocity, $\boldsymbol{v}$, the fluid density, ρ, and the fluid dynamic viscosity, μ, we calculate the solid-fluid forces at the centre of mass of the particles. These forces are source terms in the volume-averaged Navier-Stokes (VANS) equation in the CFD solver for the fluid and within the force balance of the DEM solver for the particles.

7.3.1 Governing equations for the solid-phase (DEM)

The discrete element method (DEM) tracks the position and velocity of each particle and handles collisions by allowing small overlaps (<5% d_p) between spheres. It decomposes the overlap into normal and tangential directions with contact models that contain elastic and dissipative components, which account for inelastic particle-particle collisions.[197,198,199] As a result of Newton's second law of motion, the governing equations motion of particle i

become[199]:

$$\frac{\mathrm{d}\boldsymbol{x}_i}{\mathrm{d}t} = \boldsymbol{v}_i \tag{7.1}$$

$$m_i \frac{\mathrm{d}\boldsymbol{v}_i}{\mathrm{d}t} = \sum_j \boldsymbol{f}_{c,ij} + \sum_w \boldsymbol{f}_{c,iw} + \sum_k \boldsymbol{f}_{nc,ik} + \boldsymbol{f}_{pf,i} + \boldsymbol{f}_{g,i} \tag{7.2}$$

$$I_i \frac{\mathrm{d}\boldsymbol{\omega}_i}{\mathrm{d}t} = \sum_j \left(\boldsymbol{M}_{c,ij} + \boldsymbol{M}_{r,ij}\right) + \sum_w \left(\boldsymbol{M}_{c,iw} + \boldsymbol{M}_{r,iw}\right) \tag{7.3}$$

where m_i and I_i are the mass and the moment of inertia of a particle i, $\boldsymbol{f}_{c,ij}$ is the force exerted at the contact point between two particles i and j, $\boldsymbol{f}_{c,iw}$ is the force exerted at the contact point between a particle i and a wall section w belonging to the geometry, $\boldsymbol{f}_{nc,ik}$ is a non-contact force on particle i due to particle k, such as electro-static, Van der Waals forces or cohesive forces (eg, liquid bridges), $\boldsymbol{f}_{pf,i}$ is a particle-fluid interaction force (eg, due to CFD coupling), and $\boldsymbol{f}_{g,i}$ is a body force acting on the particles (eg, gravity or a magnetic field). Finally, $\boldsymbol{M}_{c,ij}$ and $\boldsymbol{M}_{r,ij}$ are respectively the contact torque and rolling friction torque applied on particle i due to its collision with particle j, and $\boldsymbol{M}_{c,iw}$ and $\boldsymbol{M}_{r,iw}$ the same torque components but for collisions between particle i and a wall section.

The contact forces between two particles (or a particle and a wall segment) are split into normal and tangential elastic and dissipative components[199]:

$$\boldsymbol{f}_{c,ij} = k_{n,ij} \left\|\boldsymbol{\delta}_{n,ij}\right\|^a \boldsymbol{\delta}_{n,ij} + \gamma_{n,ij} \left\|\boldsymbol{\delta}_{n,ij}\right\|^b \dot{\boldsymbol{\delta}}_{n,ij} + k_{t,ij} \left\|\boldsymbol{\delta}_{n,ij}\right\|^c \boldsymbol{\delta}_{t,ij} + \gamma_{t,ij} \left\|\boldsymbol{\delta}_{n,ij}\right\|^d \dot{\boldsymbol{\delta}}_{t,ij} \tag{7.4}$$

where $k_{n,ij}$ and $k_{t,ij}$ are the normal and tangential stiffness coefficients, $\gamma_{n,ij}$ and $\gamma_{t,ij}$ are the normal and tangential damping coefficients, $\boldsymbol{\delta}_{n,ij}$ and $\boldsymbol{\delta}_{t,ij}$ are the normal and tangential overlaps, and $\dot{\boldsymbol{\delta}}_{n,ij}$ and $\dot{\boldsymbol{\delta}}_{t,ij}$ are their derivatives with respect to time. The exponents a, b, c, and d depend on the contact model. For linear contact models they are zero.

The expressions relating $k_{n,ij}$, $k_{t,ij}$, $\gamma_{n,ij}$, and $\gamma_{t,ij}$ to the material properties and the overlaps depend on the contact model.[199] The equations for DEM are integrated in time using a velocity-Verlet scheme or a similar, preferrably symplectic, time integration scheme.

7.3.2 Governing equations for the fluid flow (CFD)

The volume-averaged Navier-Stokes equation takes into account the fact that the volume that can be occupied by the fluid within each cell (or element) depends on the volume of solid particles that occupies it. For example, a fluid that goes from a region with few particles and a void fraction (ϵ_v) close to 1, must accelerate if it enters a region concentrated with particles (ex: $\epsilon_\mathrm{v} = 0.5$) in order to ensure that the fluid mass is conserved through the continuity

equation. The main differences between various forms of the VANS equations discussed in the literature lie in the treatment of the stress tensor of the fluid and the solid-fluid coupling.[174]

The two general sets of VANS equations—form A and B— are mathematically equivalent, but assume a discretized the pressure gradient and stress divergence differently. For all forms of the VANS equations, the continuity equation is:

$$\frac{\partial}{\partial t}\left(\epsilon_{\mathrm{v}}\right)+\nabla\cdot\left(\epsilon_{\mathrm{v}}\boldsymbol{u}\right)=0 \tag{7.5}$$

where ϵ_{v} is the void fraction and $\boldsymbol{u}$ is the fluid velocity. When we compare this equation to the traditional continuity equation of the incompressible Navier-Stokes equation:

$$\nabla\cdot\boldsymbol{u}=0 \tag{7.6}$$

we see that the presence of a time-dependent and/or a space-dependent void fraction leads to a non-divergence free velocity field to ensure mass conservation. Rewriting Equation (7.5), we see that the divergence of the velocity is:

$$\nabla\cdot\boldsymbol{u}=-\boldsymbol{u}\cdot\nabla\epsilon_{\mathrm{v}}-\frac{\partial}{\partial t}\left(\epsilon_{\mathrm{v}}\right) \tag{7.7}$$

This has further consequences in pressure correction schemes in finite volume approaches.

The formulation of the equation for the momentum conservation differs between models A and B.

Form A:

$$\rho_f\left(\frac{\partial}{\partial t}\left(\epsilon_{\mathrm{v}}\boldsymbol{u}\right)+\nabla\cdot\left(\epsilon_{\mathrm{v}}\boldsymbol{u}\otimes\boldsymbol{u}\right)\right)=-\epsilon_{\mathrm{v}}\nabla p+\epsilon_{\mathrm{v}}\nabla\cdot\left(\boldsymbol{\tau}_f\right)-\boldsymbol{F}_{pf}^{A}+\rho_f\epsilon_{\mathrm{v}}\boldsymbol{g} \tag{7.8}$$

$$\boldsymbol{F}_{pf}^{A}=\frac{1}{\Delta V}\sum_{i}^{n_p}\left(\boldsymbol{f}_{pf,i}-\boldsymbol{f}_{\nabla p,i}-\boldsymbol{f}_{\nabla\cdot\boldsymbol{\tau},i}\right) \tag{7.9}$$

Form B:

$$\rho_f\left(\frac{\partial}{\partial t}\left(\epsilon_{\mathrm{v}}\boldsymbol{u}\right)+\nabla\cdot\left(\epsilon_{\mathrm{v}}\boldsymbol{u}\otimes\boldsymbol{u}\right)\right)=-\nabla p+\nabla\cdot\left(\boldsymbol{\tau}_f\right)-\boldsymbol{F}_{pf}^{B}+\rho_f\epsilon_{\mathrm{v}}\boldsymbol{g} \tag{7.10}$$

$$\boldsymbol{F}_{pf}^{B}=\frac{1}{\Delta V}\sum_{i}^{n_p}\boldsymbol{f}_{pf,i} \tag{7.11}$$

with

$$\boldsymbol{f}_{pf,i} = \boldsymbol{f}_{d,i} + \boldsymbol{f}_{\nabla p,i} + \boldsymbol{f}_{\nabla\cdot\boldsymbol{\tau},i} + \boldsymbol{f}_{\mathrm{vm},i} + \boldsymbol{f}_{B,i} + \boldsymbol{f}_{\mathrm{Saff},i} + \boldsymbol{f}_{\mathrm{Mag},i} \tag{7.12}$$

where $\boldsymbol{F}_{\mathrm{pf}}$ is the momentum transfer term between the fluid and the solid phase, $V_{p,i}$ is the volume of particle i, n_{p} is the number of particles, and $\boldsymbol{f}_{pf,i}$ is the individual force acting on a particle i due to the presence of the surrounding fluid.

Forms A and B are generic and are mathematically equivalent. However, they differ in the way in which we implement incompressibility. In form A, ϵ_{v} multiplies the pressure gradient, which leads to a different pressure equation when compared to the standard Navier-Stokes equations. This form can lose hyperbolicity, in which case the solutions obtained are non-physical (see the Appendix).[200,201]

Form B accounts for the pressure force applied on the particles at the previous time step in the momentum coupling term ($\boldsymbol{F}_{\mathrm{pf}}$), if the coupling between the phases is explicit (which is generally always the case). Mathematically, this is equivalent to adding the factor ϵ_{v} in front of the pressure gradient. However, discretely, form A and B lead to a different pressure equation. In form A, the ϵ_{v} factor is taken into account on the continuous equation and alters the Poisson equation for pressure; whereas, in form B, it is lumped with the momentum coupling term. Remember that the pressure in the incompressible Navier-Stokes equations, and also the incompressible VANS equations, is instantly defined as a function of the velocity field and is, mathematically, a Lagrangian multiplier to impose mass conservation.[202] Consequently, applying the previous pressure to calculate subsequent pressure may induce numerical instabilities.

Both forms give results that are theoretically equivalent.[174] We conclude that the choice of form A and form B only affects the numerical discretization of the equations: mathematically, they describe the same physics. Forms A and B are generic and applicable to any concentration, $N_{\mathrm{Re_p}}$, and flow regime.

7.3.3 Solid-fluid coupling: Calculation of the void fraction

An important step in the solid-fluid coupling is the projection of the particle volume and solid-fluid force onto the CFD mesh to define the fluid volume fraction ϵ_{v} and calculate the momentum exchange term $\boldsymbol{F}_{\mathrm{pf}}$. For this projection, the scheme must ensure mass conservation and produce a ϵ_{v} field, wherein the CFD simulation is stable while having an acceptable computational cost. The resulting projection scheme depends on the approach applied to project the particles, but also on the location (nodal or cell-centered) where the void fraction

ϵ_v is stored. If the scheme is cell-centered (ie, cell-centered finite volume), the void-fraction that corresponds to the cell will define the void fraction field. If the scheme is nodal/vertex-centered (ie, vertex-centered finite volume or finite element), the nodal void fraction values from the values within the cell are defined by a weighing procedure or using the dual of the mesh.

The standard method proposed in the literature, the particle counting method, is to assign the full volume of a particle to a fluid cell (or element) if the centroid of that particle resides in the cell (Figure 7.3).[203] This method predicts the hydrodynamics for cases where $\frac{d_p}{\Delta x} \leq 3$, with Δx the characteristic size of the cells. However, when $\frac{d_p}{\Delta x}$ is small, as is the case when the mesh size is decreased or when the simulation domain contains narrow sections, the volume fractions become discontinuous.

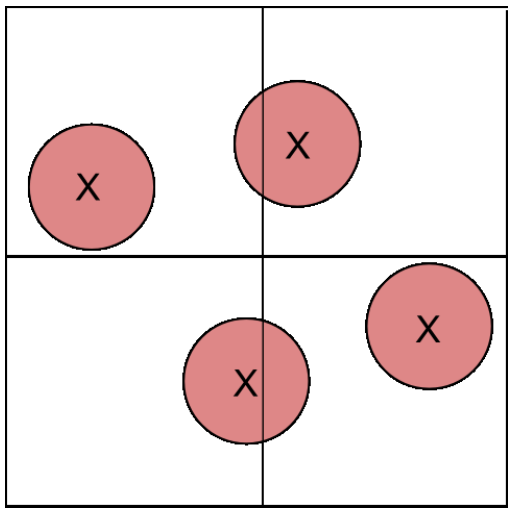

Figure 7.3 2D simplified illustration of the particle counting method for the projection of particles onto a CFD grid. In this method, the volume of a particle is attributed to a CFD cell if the centroid of the particle lies in the cell

Alternatives to the particle counting method include:

- the concentration blob (or particle cloud)[203,204];
- the conservative concentration blob (or conservative particle cloud)[203];
- the moment preserving approach (M_4' method)[203,205];
- the two-grid formulation[206]; and
- the divided approach.[2,173,207]

In the concentration blob, the particle volume $V_{p,i}$ is associated with a blob function:

$$V_{p,i} = A_i f(\boldsymbol{x} - \boldsymbol{x}_i, R_{w,i}) \tag{7.13}$$

where A_i is the amplitude of the blob function, $R_{w,i}$ is the blob radius, $\boldsymbol{x}$ is a coordinate in space, $\boldsymbol{x}_i$ is the position of the particle centroid, and f is a weighing function. The concentration blob generally implements a Gaussian or Gaussian-like weight function to continuously spread the volume of the particle over a larger radius $R_{w,i}$. The amplitude A_i must be chosen such that the integral over the whole weighting function is equal to the particle volume. With the appropriate weighting function, this method leads to a continuous void fraction field. It only conserves mass if the integral of the weight function over the domain is exact. However, this integral is generally carried out using a quadrature, which introduces numerical integration error. The conservative blob rescales the amplitude to ensure that mass is conserved discretely. For both methods, if the value of the weight function f is not zero outside of the particle (for $|\boldsymbol{x} - \boldsymbol{x}_i| > \frac{d_p}{2}$), the mass is not conserved close to the domain boundaries.

In the Gaussian projection preserving moments, the particle volume is distributed on a stencil of cells (eg, 64) that surround the cell of interest using an interpolation function that satisfies mass conservation and preserves the first moment of the discrete population of particles.[203] This approach is unusual in CFD-DEM.

To calculate the void fraction, the two-grid formulation establishes a coarser grid than the CFD mesh. This allows the fluid to be solved at a fine scale while maintaining a mesh sufficiently large ($\frac{\Delta x}{d_p} > 3$) to ensure that the particle counting approach leads to a well-defined ϵ_v.

The divided approach subdivides the projected particle into regions of equal volumes (eg, 27 sub-regions), each of which is represented by a point that is located on the mesh in order to calculate the void fraction and the momentum exchange term. This approach has the advantage of conserving mass while smoothing the void fraction and the momentum exchange term. The points are generally chosen as the points of a given quadrature (eg, Gauss quadrature) in a spherical domain (Figure 7.4).

Researchers often calculate the void fraction and the momentum exchange term by counting the particle or using the divided approach following by the smoothing of the resulting fields. Three smoothing techniques include:

— parabolic filtering[173];
— darning socks[204]; and
— trajectory smoothing.[208]

Parabolic filtering applies a parabolic diffusion equation to smooth a variable $\boldsymbol{\xi}$ such as void

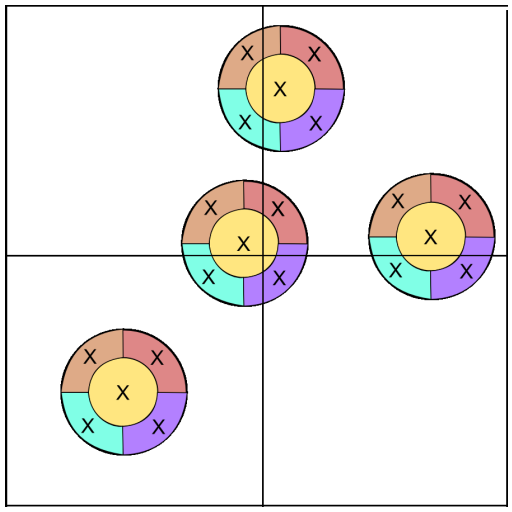

Figure 7.4 2D simplified illustration of the divided approach for the projection of particles onto a CFD grid with 5 points (or regions) per particle. Adapted from Blais et al (2016) [173]

fraction or momentum exchange [173]:

$$\frac{\partial \boldsymbol{\xi}}{\partial t} = \nabla^2 \left(\frac{\lambda^2}{\Delta t_{CFD}} \boldsymbol{\xi} \right) \tag{7.14}$$

where ξ is the field to be smoothed, Δt_{CFD} is the time step of the simulation, and λ is a length scale that is about the same size as d_p or the Δx. This approach leads to diffusion of the coupling terms to cells that have not seen particles. The darning socks approach fixes holes or oscillation in the void fraction field that are generated by the discrete character of the particles. When holes are detected in cells that have neighbours that contain particles, a fraction of the particle volume and the momentum exchange term is transferred from the neighbour to the cell. This process is conservative and does not smear the exchange fields to non-physical locations. However, it is mesh dependent since the darning process only considers the neighbouring cells.

Finally, trajectory smoothing applies a kernel to smooth the projection on the trajectory of the particle. This leads to a conservative projection that only smears the exchange fields and void fraction on the actual trajectory of the particles in a mesh independent way.

The standard particle counting approach, sock darning and conservative blob, are best, because they conserve mass and momentum with a well-established volume fraction field. [203,204] The divided approach, which subdivides a particle by the weight of Gauss, which is then projected by the standard method, only refines the standard method and has the same advantages while being endowed with better behaviour when Δx decreases. The two-grid method

generally gives superior results, but is more complex to implement and difficult to generalize in the case of unstructured meshes. The trajectory smoothing method is a promising approach since it smooths the fields to physical locations (the particle trajectory) in a mesh-independent fashion.[208] However, this method is very recent and its impact on complex CFD-DEM is not yet fully assessed.

Projection methods that are conservative, have smooth time derivative, are mesh-independent, and are uncomputationally intensive to calculate are lacking. Projection methods remains an active research topic. Smoothing the exchange fields that are calculated and the novel trajectory smoothing appear to alleviate issues related to the projection of the particle. However, the state of the art has yet to coalesce around a single robust, generic, and accurate strategy to accurately project the the exchange field, especially for small mesh cells ($\frac{\Delta x}{d_p} < 3$).

7.3.4 Solid-fluid coupling: Hydrodynamics forces

According to Equation (7.15) the interaction between particle and fluid leads to hydrodynamics forces such as: drag force ($\boldsymbol{F}_{\mathrm{D}}$), virtual mass force ($\boldsymbol{F}_{\mathrm{Vm}}$), Basset force ($\boldsymbol{F}_{\mathrm{Basset}}$), lift force (Saffman ($\boldsymbol{F}_{\mathrm{Saff}}$), and Magnus ($\boldsymbol{F}_{\mathrm{Mag}}$)) and undisturbed flow ($\boldsymbol{F}_{ud}$). The latter includes pressure forces ($\boldsymbol{F}_{\mathrm{p}}$) and viscous shear ($\boldsymbol{F}_{\tau}$). The particle-fluid interaction forces ($\boldsymbol{f}_{pf,i}$) are:

$$\sum \boldsymbol{f}_{pf,i} = \boldsymbol{F}_{\mathrm{D}} + \boldsymbol{F}_{p} + \boldsymbol{F}_{\emptyset} + \boldsymbol{F}_{\mathrm{Vm}} + \boldsymbol{F}_{\mathrm{Basset}} + \boldsymbol{F}_{\mathrm{Saff}} + \boldsymbol{F}_{\mathrm{Mag}} \tag{7.15}$$

or:

$$\boldsymbol{f}_{pf,i} = \boldsymbol{f}_{d,i} + \boldsymbol{f}_{\nabla p,i} + \boldsymbol{f}_{\nabla \cdot \boldsymbol{\tau},i} + \boldsymbol{f}_{\mathrm{vm},i} + \boldsymbol{f}_{B,i} + \boldsymbol{f}_{\mathrm{Saff},i} + \boldsymbol{f}_{\mathrm{Mag},i} \tag{7.16}$$

Each hydrodynamic force is caused by different factors. Some of them are only present in an unsteady state system (Table 7.1).

Drag force

Drag is the force a particle experiences as a fluid passes around it, neglecting acceleration—$F_{\mathrm{drag,ss}}$:

$$F_{\mathrm{drag,ss}} = \frac{1}{2}\rho_f C_{\mathrm{D}} A |\boldsymbol{u} - \boldsymbol{v}|(\boldsymbol{u} - \boldsymbol{v}) \tag{7.17}$$

Table 7.1 Hydrodynamic forces[2,3]

Forces	Source	Unsteady force
Drag	Relative velocity between particle and fluid and presence of neighboring particles	
Pressure	Pressure gradient	
Shear	Shear stress	
Virtual mass	Particle acceleration in the fluid phase	√
Basset	Viscous effect, instability on the boundary layer	√
Lift - Magnus	Particle rotation due to particles contact or rebound to a wall, assymetric pressure distribution	
Lift - Saffman	Non-uniform shear velocity field leading to pressure difference around the particle	

where C_{D} is the drag coefficient, which depends on particle shape, orientation, Reynolds number, $N_{\mathrm{Re_p}}$, Mach number (when $N_{\mathrm{Ma}} > 0.6$ the flow is sonic), turbulence, and evaporating or burning droplets. C_{D} drops at the critical Reynolds number, normally around 3×10^6, due to boundary layer effects but varies with the relative turbulence intensity. Several definitions of the drag coefficient were developed as a function of the $N_{\mathrm{Re_p}}$ and drag model (Table 7.2). Most of the correlations are based on Navier-Stokes equations such as the Ergun drag force model. Alternatively, Rong and Beestra established their model following Lattice-Boltzman simulations (LBM). Avoid limiting values of each parameter when choosing a drag model to ensure continuity.

The Rong drag model[209] accurately characterizes drag for multi-particle systems (Table 7.3,7.4) and applies over a large range of Reynolds numbers and fluid volume fractions ($0.37 < \epsilon_f < 1$). The Rong drag model together with Ergun equation include the β factor, which is a function of $N_{\mathrm{Re_p}}$ and ϵ_f. However, β depends on the model. Most commercial software combines the Ergun and Wen and Yu expression to evaluate the drag force. In the case $\epsilon_f = 0.4$, these two model predictions diverge notably.

Table 7.2 Drag coefficient equation applied with drag model

Drag model	C_{D}	$N_{\mathrm{Re,p}}$
Stokes (1851)[210]	$C_D = \dfrac{24}{N_{\mathrm{Re}}}$	$N_{\mathrm{Re}} < 1$
Oseen (1927)[211]	$C_D = \dfrac{24}{N_{\mathrm{Re}}}\left(1 + \dfrac{3}{16}N_{\mathrm{Re}}\right)$	$N_{\mathrm{Re}} < 5$
Schiller-Naumann (1933)[212]	$C_{\mathrm{D}} = \begin{cases} 24(1 + 0.15N_{\mathrm{Re,p}}^{0.687})/N_{\mathrm{Re,p}} \\ 0.44 \end{cases}$	$N_{\mathrm{Re,p}} \leq 1000$
Ergun-Wen and Yu (1952)[213,214]		$N_{\mathrm{Re,p}} > 1000$
Gidaspow (1994)[201]		Newton's law
Huilin-Gidaspow (2006)[215]		
Ingebo (1956)[216]	$C_{\mathrm{D}} = \dfrac{27}{N_{\mathrm{Re}}^{0.84}}$	droplet motion in combustion
Torobin & Gauvin (1961)[217]	$C_{\mathrm{D}} = 0.3\left(\dfrac{N_{\mathrm{Re,p}}}{N_{\mathrm{Re_c}}}\right)^{-3}$	$0.9N_{\mathrm{Re_c}} < N_{\mathrm{Re}} < N_{\mathrm{Re,m}}$ critical condition
Hadamard-Rybczynnski (1978)[218]	$C_{\mathrm{D}} = \dfrac{24}{N_{\mathrm{Re}}}\dfrac{1 + 2/3\bar{\mu}}{1 + \bar{\mu}}$	$N_{\mathrm{Re}} < 1$ shear stress induces internal motion
Syamlal-O'brien (1989)[219]	$C_{\mathrm{D}} = \left(0.63 + \dfrac{4.8}{\sqrt{N_{\mathrm{Re,p}}/v_t}}\right)^2$	-
Cheng (2009)[220]	$C_{\mathrm{D}} = \dfrac{24}{N_{\mathrm{Re,p}}}(1 + 0.27N_{\mathrm{Re,p}})^{0.43} + 0.47\left[1 - \exp\left(-0.04N_{\mathrm{Re,p}}^{0.38}\right)\right]$	$N_{\mathrm{Re,p}} \leq 2 \times 10^5$
Rong (2013)[209]	$C_{\mathrm{D}} = \left(0.63 + \dfrac{4.8}{\sqrt{N_{\mathrm{Re,p}}}}\right)^2$	-

The Hill-Koch-Ladd (HKL) model[222] is specific to fluidized beds and accurate over a narrow range of Reynolds numbers ($40 < N_{\mathrm{Re_p}} > 120$). Benyahia et al[223] extended the range of HKL's model to fit all $N_{\mathrm{Re_p}}$ and solids void fractions. Beetstra's model[224] accounts for polydisperse systems such as fluidized beds operating at $N_{\mathrm{Re_p}} < 1000$ and porosities less

Table 7.3 Drag force empirical correlations - part 1

Drag model	$\boldsymbol{F}_D$
Rong[209]	$\boldsymbol{F}_D = \frac{1}{8} C_D d_{p,i}^2 \rho_f \lvert\boldsymbol{u} - \boldsymbol{v_i}\rvert (\boldsymbol{u} - \boldsymbol{v_i}) \epsilon_f^{2-\beta(\epsilon_f, N_{\mathrm{Re}})}$ $\beta(\epsilon_f, N_{\mathrm{Re}}) = 2.65(\epsilon_f + 1) - (5.3 - 3.5\epsilon_f)\epsilon_f^2 e^{-\frac{(1.5 - \log N_{\mathrm{Re}}^2}{2}}$ $N_{\mathrm{Re}} = \frac{\rho_f d_{p,i} \lvert\boldsymbol{u} - \boldsymbol{v_i}\rvert}{\mu_f}$
Ergun[213] Wen and Yu[214]	$\boldsymbol{F}_D = \beta_{pf} \frac{(\boldsymbol{u} - \boldsymbol{v})}{\rho_f}$ $\beta_{pf} = \begin{cases} 150 \frac{(1-\epsilon_f)^2}{\epsilon_f} \frac{\mu_f}{(\phi_p d_p)^2} + 1.75(1-\epsilon_f) \frac{\rho_f}{\phi_p d_p} \lvert\boldsymbol{u} - \boldsymbol{v}\rvert & \epsilon_f \leq 0.8 \\ \frac{3}{4} C_D \frac{\lvert\boldsymbol{u}-\boldsymbol{v}\rvert \rho_f (1-\epsilon_f)}{d_p} \epsilon_f^{-2.7} & \epsilon_f > 0.8 \end{cases}$
Di Felice[221]	$\boldsymbol{F}_D = f(\epsilon_f) \boldsymbol{F_{D0}}$ $f(\epsilon_f) = \epsilon_f^{-(\alpha+1)}$ where $\alpha = 3.7 - 0.65 \exp\left[-(1.5 - \log N_{\mathrm{Re_p}})^2/2\right]$ $\boldsymbol{F_{D0}} = \frac{1}{2} \rho_f C_D A_\perp (\boldsymbol{u} - \boldsymbol{v}) \lvert\boldsymbol{u} - \boldsymbol{v}\rvert$
Hill-Koch-Ladd[222] (HKL)	$\boldsymbol{F}_D = A \frac{(1-\epsilon_f)^2}{\epsilon_f} + B(1-\epsilon_f) N_{\mathrm{Re_p}}$ $A = \begin{cases} 180 & \epsilon_f < 0.6 \\ \frac{18\epsilon_f^3(1+3)(1-\epsilon_f)^{1/2}/\sqrt{2} + 135(1-\epsilon_f)/64 + 16.14(1-\epsilon_f)}{1 - 0.681(1-\epsilon_f) - 8.48(1-\epsilon_f)^2} & \epsilon_f > 0.6 \end{cases}$ $B = 0.6057\epsilon_f^2 + 1.908\epsilon_f^2(1-\epsilon_f) + 0.209\epsilon_f^{-3}$ $N_{\mathrm{Re_p}} = \frac{\epsilon_f \rho_f d_{p,i} \lvert\boldsymbol{u} - \boldsymbol{v_i}\rvert}{\mu_f}$
Benyahia et al.[223]	$\boldsymbol{F}_D = \boldsymbol{F}_0 + \boldsymbol{F}_1 N_{\mathrm{Re}}$ $\boldsymbol{F}_0 = \begin{cases} (1-w)\epsilon_f^2 [\frac{1 + 3\sqrt{\frac{\epsilon_s}{2}} + 2.11\epsilon_s \ln \epsilon_s + 17.9\epsilon_s}{1 + 0.681\epsilon_s - 11\epsilon_s^2 + 15.4\epsilon_s^3}] + w(10\frac{\epsilon_s}{\epsilon_f}) & \epsilon_s < 0.4 \\ 10\frac{\epsilon_s}{\epsilon_f} & \epsilon_s \geq 0.4 \end{cases}$ $\boldsymbol{F}_1 = \begin{cases} 0.467\epsilon_f^3\epsilon_s + 0.0183\epsilon_f^3 & \epsilon_s < 0.095 \\ 0.033\epsilon_f^3 + 0.106\epsilon_s\epsilon_f^3 + 0.0116/\epsilon_f^2 & \epsilon_s \geq 0.095 \end{cases}$ $w = e^{[-10(0.4-\epsilon_s)/\epsilon_s]}$
Beestra et al.[224]	$\boldsymbol{F}_D = A \frac{(1-\epsilon_f)^2}{\epsilon_f} + B(1-\epsilon_f) N_{\mathrm{Re_p}}$ $A = 180 + 18 \frac{18\epsilon_f^4(1 + 1.5\sqrt{1-\epsilon_f})}{1-\epsilon_f}$ $B = \frac{0.31(\epsilon_f^{-1} + 3\epsilon_f(1-\epsilon_f) + 8.4 N_{\mathrm{Re_p}}^{-0.343})}{1 + 10^{3(1-\epsilon_f)} N_{\mathrm{Re_p}}^{2\epsilon_f - 2.5}}$

than 0.9. Simulation results for monodisperse systems are substantially different compared to the Ergun equation, but similar to the Hill, Koch, and Ladd expression for $N_{\mathrm{Re_p}} < 120$.

Table 7.4 Drag force empirical correlations - part 2

Drag model	$\boldsymbol{F}_D$
Chen et al.[225]	$\boldsymbol{F}_D = \frac{10\epsilon_s}{(1-\epsilon_s)^2} + \frac{10\epsilon_s}{1-1.14\epsilon_s^{0.3}} + \frac{0.413 N_{\mathrm{Re}}}{24(1-\epsilon_s)^2}[A]$ $A = \frac{-0.058(1-\epsilon_s)^{-4} + 2.16(1-\epsilon_s) + 23\epsilon_s(1-\epsilon_s) + 8.4 N_{\mathrm{Re}}^{-0.343}}{1 + 10^{3\epsilon_s} N_{\mathrm{Re}}^{(-0.5-2\epsilon_s}}$
Gidaspow et al.[201] Huilin-Gidaspow[215]	$\boldsymbol{F}_D = \frac{\beta_{pf}(\boldsymbol{u}-\boldsymbol{v})}{\rho_f}$ $\beta_{pf} = \begin{cases} 150\frac{(1-\epsilon_f)^2\mu_f}{\epsilon_f d_p^2} + 1.75[(1-\epsilon_f)\frac{\rho_f}{d_p}\lvert\boldsymbol{u}-\boldsymbol{v}\rvert] & \epsilon_f \le 0.8 \\ \frac{3}{4}\frac{C_D\lvert\boldsymbol{u}-\boldsymbol{v}\rvert\rho_f(1-\epsilon_f)}{d_p}\epsilon_f^{-2.7} & \epsilon_f > 0.8 \end{cases}$ $\beta_{pf} = \varphi\frac{3C_D\epsilon_s\rho_f\lvert\boldsymbol{u}-\boldsymbol{v}\rvert}{4d_p}\epsilon_f^{-2.65} + (1-\varphi)\times[150\frac{\epsilon_s^2\mu_f}{\epsilon_f d_p^2} + 1.75\frac{\rho_f\epsilon_s}{d_p}\lvert\boldsymbol{u}-\boldsymbol{v}\rvert]$ $\varphi = \frac{arctan[150\times 1.75(\epsilon_s - 0.8)]}{\pi} + 0.5$
Syamlal-O'Brien[219]	$\boldsymbol{F}_D = \frac{\beta_{pf}(\boldsymbol{u}-\boldsymbol{v})}{\rho_f}$ $\beta_{pf} = \frac{3}{4}\frac{\epsilon_s\epsilon_f\rho_f}{v_t^2 d_p}C_D(\frac{N_{\mathrm{Re_s}}}{v_t})\lvert\boldsymbol{u}-\boldsymbol{v}\rvert$ $v_t = 0.5(A - 0.06N_{\mathrm{Re_p}}) + \sqrt{(0.06N_{\mathrm{Re_p}})^2 + 0.12N_{\mathrm{Re_p}}(2B-A) + A^2}$ $\begin{cases} A = \epsilon_f^4.14 \quad B = 0.8\epsilon_f^4.14 & \epsilon_f \le 0.85 \\ A = \epsilon_f^4.14 \quad B = \epsilon_f^4 2.65 & \epsilon_f > 0.85 \end{cases}$
Schiller-Naumann[212]	$\boldsymbol{F}_D = \frac{C_D N_{\mathrm{Re}}}{24}$

For a continuous distribution, the Huilin-Gidapsow model should be considered to avoid inconstancy for β_{pf} at ϵ_p equals 0.2.[226] The Syamlal-O'Brien drag model includes terminal velocity, which is pertinent to fluidized beds.[219]

Undisturbed flow

Undisturbed flow includes forces due to pressure gradients (F_p) and shear stress (F_τ) and is present when particles are subject to gravity and acceleration in fluid. In a fluidized bed reactor, particle-particle friction and particle-wall friction contribute to the pressure drop due to the mass of particles. They are non-negligible for liquid-solid systems when the density ratio is around 1 or when the surrounding fluid is viscous.[5,227]

The undisturbed flow forces are:

$$F_{ud} = F_p + F\tau \tag{7.18}$$

Then, the pressure force on a single particle is[228]:

$$F_p = -V_p(\frac{\partial p}{\partial x}) = -\frac{1}{6}\pi d_p^3 \nabla P_g \tag{7.19}$$

and, the shear stress force is[228]:

$$F_\tau = V_p(\frac{\partial \tau_k}{\partial x_k}) = -\frac{\pi}{6} d_p^3 \nabla \cdot \tau \tag{7.20}$$

Basset force

Basset force, also known as the history term or force, accounts for the temporal delay in the boundary layer surrounding the particle created when the relative velocity changes with time. This viscous effect depends on the historical acceleration of the particle where the unsteady force is created on the particle due to the generation of the boundary layer. It only applies for unsteady flow as a virtual mass force[5,227] and is generally negligible with gaseous systems or when particle acceleration is low. Furthermore, we can neglect the Basset force if[229,230]:

$$\begin{cases} \frac{\rho_f}{\rho_s} \sim 10^{-3} & \text{for } (\frac{\mu}{\rho_f \omega d_p^2})^2 > 6 \\ \frac{\rho_f}{\rho_s} < 0.002 \\ \omega \tau_V < 0.5 \end{cases} \tag{7.21}$$

(7.22)

The most common model is based on the integral of past particle acceleration[231]:

$$F_{\text{Basset}} = \frac{3}{2} d_p^2 \sqrt{\pi \rho_f \mu_f} [\int_{t_0}^{t} \frac{(\boldsymbol{u} - \boldsymbol{v})}{\sqrt{t - t'}} dt' + \frac{(\boldsymbol{u} - \boldsymbol{v})_0}{\sqrt{t}}] \tag{7.23}$$

Virtual, added, or apparent mass force

Virtual mass force is the force a particle exerts on a fluid that is going slower.[5] It is equivalent to adding a virtual mass to a sphere, from where the name is derived. This transient force only occurs in an unsteady flows system. Like the Basset force, it is negligible if the relative

velocity between the particle and the fluid are equal.[227] The general form of function for relative acceleration is[232]:

$$\boldsymbol{F}_{vm,i} = \frac{\rho_f V_d}{2}\left(\frac{d\boldsymbol{u_i}}{dt} - \frac{d\boldsymbol{v_i}}{dt}\right) \tag{7.24}$$

An alternative form is[233]:

$$\boldsymbol{F}_{V_m} = C_{V_m} V_p \rho_f \frac{(\dot{\boldsymbol{u}} - \dot{\boldsymbol{v}})}{2} \tag{7.25}$$

with,

$$C_{V_m} = 2.1 - \frac{0.132}{(0.12 + \boldsymbol{A}_c^2)} \tag{7.26}$$

and,

$$\boldsymbol{A}_C = \frac{(\boldsymbol{u} - \boldsymbol{v})^2}{d_p \frac{d(\boldsymbol{u}-\boldsymbol{v})}{dt}} \tag{7.27}$$

Lift force

Lift forces are due to either particle rotation, gradients in the velocity profile, or to the shape of the particles. In the latter case, they depend on the orientation of the particles with respect to the flow (Figure 7.5). For irregularly shaped particles, the pressure difference on an asymmetrical surface and the deviation of the centre of pressure from geometric centres are the two factors causing lift force.[4]

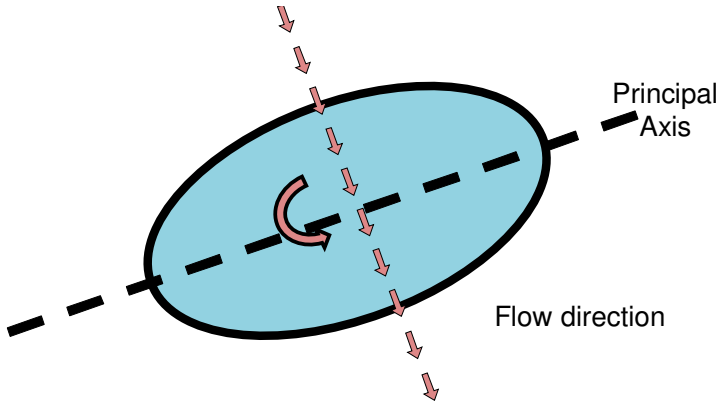

Figure 7.5 Lift force on a non-spherical regular shape particle (disks and spheroids)

One model assumes that the lift force is proportional to drag force:

$$F_L = \frac{1}{2} C_L \rho_f \boldsymbol{u}^2 A_p \tag{7.28}$$

where, C_L is the lift coefficient (Table 7.5).

Table 7.5 Lift coefficient [4]

Equations	Conditions	ref.
$C_L = C_D \sin^2\alpha \cdot \cos\alpha$	Newton law region	[234]
$C_L = C_D \dfrac{\sin^2\alpha \cdot \cos\alpha}{0.65 + 40 N_{\mathrm{Re}}^{0.72}}$	$30 < N_{\mathrm{Re}} < 1500$	[235]
$C_L = (\dfrac{b_1}{N_{\mathrm{Re_p}}^{b_2}} - \dfrac{b_3}{N_{\mathrm{Re_p}}^{b_4}}) \sin(\alpha)^{b_5 + b_6 N_{\mathrm{Re_p}}^{b_7} \cos(\alpha)^{b_8 + b_9 N_{\mathrm{Re_p}}^{b_{10}}}}$	all particle shapes, N_{Re} and incident angle	[236]

Alternately, lift forces can be separated in to Saffman type and Magnus type forces (Figure 7.2).

Saffman lift force

A particle undergoes a Saffman force when a velocity gradient across the surface creates a pressure distribution. The highest velocity region corresponds to the lowest pressure and conversely the lowest velocity to the highest pressure. This gradient generates a net lift force on spheres, and can induce rotation for non-spherical particles. [5] Several models characterize the Saffman lift force as a function of $N_{\mathrm{Re_p}}$ (Table 7.6).

Magnus lift force

Magnus force is developed by a pressure differential present on the surface of the particle where the velocity gradient is due to rotation. [5,227] The model of this force is mainly a function of the velocity of the particle ($\boldsymbol{v}$) and the fluid ($\boldsymbol{u}$) and the particle rotation ($\boldsymbol{\omega}_p$) (Table 7.7).

Table 7.6 Saffman force expressions[5]

Model	Equations	Conditions	ref.
Saffman	$F_{saff} = 1.6\mu_f d_p \lvert \boldsymbol{u_i} - \boldsymbol{v_i} \rvert \sqrt{N_{\mathrm{Re_G}}}$	$N_{\mathrm{Re}} << \sqrt{N_{\mathrm{Re_G}}}$	
(1968)	$N_{\mathrm{Re_G}} = \dfrac{d_p^2}{\boldsymbol{v_c}} \dfrac{d\boldsymbol{u}}{dy}$	$N_{\mathrm{Re}} << 1$	[237,238]
	$F_{saff,i} = 1.61 d_p^2 (\mu_f \rho_f)^{0.5} \lvert \omega_{f,i} \rvert^{-0.5} [\varepsilon_{ijk} (\boldsymbol{u_j} - \boldsymbol{v_j}) \omega_{f,k}]$	$N_{\mathrm{Re_G}} << 1$	
Mei	$F_{saff,i} = C_S 1.61 d_p^2 (\mu_f \rho_f)^{0.5} \lvert \omega_{f,i} \rvert^{-0.5} [\varepsilon_{ijk} (\boldsymbol{u_j} - \boldsymbol{v_j}) \omega_{f,k}]$		
(1992)	$C_S = (1 - 0.3314\beta^{1/2}) \exp(-\dfrac{N_{\mathrm{Re}}}{10}) + 0.3314\beta^{1/2}$	$N_{\mathrm{Re}} \leq 40$	[239]
	$C_S = 0.0524 (\beta N_{\mathrm{Re}})^{1/2}$	$N_{\mathrm{Re}} > 40$	
	$\beta = \dfrac{d_p}{2 \lvert \boldsymbol{u_i} - \boldsymbol{v_i} \rvert} \lvert \omega_{f,i} \rvert$		

Table 7.7 Magnus force expressions[5]

Equations	Conditions	ref.
$F_{Mag,i} = \dfrac{\pi}{8} d_p^3 \rho_f [\varepsilon_{ijk} \omega_{p,j} (\boldsymbol{v_k} - \boldsymbol{u_k})]$	N_{Re} the order of unity	[240]
$F_{Mag,i} = \dfrac{\pi}{8} d_p^3 \rho_f \omega_p (\boldsymbol{v} - \boldsymbol{u})$	If the rotation vector is normal to the relative velocity vector	[240]
$F_{Mag} = \dfrac{1}{2} \rho_f A_p C_{LR} \lvert \boldsymbol{v} - \boldsymbol{u} \rvert (\boldsymbol{v} - \boldsymbol{u})$		[240]
$C_{LR} = \dfrac{d_p \omega_p}{\lvert \boldsymbol{u} - \boldsymbol{v} \rvert} = 2\Omega$		[240]
$C_{LR} = min(0.5, 0.5\Omega)$		[241]
$C_{LR} = 0.45 + (2\Omega - 0.45) \exp(-0.075 \Omega^{0.4} N_{\mathrm{Re}}^{0.7})$	$\begin{cases} 1 < \Omega < 6 \\ 10 < N_{\mathrm{Re}} < 140 \end{cases}$	[242]

7.4 Applications

Researchers apply CFD-DEM to predict the behaviour of particles and the dynamics of fluids in a large spectrum of unit operations:[4]

— fluidized beds[176,177,178,243,244,245];
— spouted beds[179,180,181,246,247,248];
— mixing[173,190,191,249,250,251];
— sedimentation and sediment transport[252,253,254,255];
— pneumatix conveying[193,256,257,258,259];

— dryers[186,187,188,260]; and
— cyclones.[184,185]

WoS indexed 695 articles that mention CFD-DEM in the search function *topic* from 2016 up until May 2019, which is much lower than spectroscopic techniques, which appear 50 000 times per year.[133] Of these articles, 397 are associated with chemical engineering followed by mechanics (78), mechanical engineering (58), multi-disciplinary material science (54), and energy and fuels (53). This is one of the few topics that chemical engineers share more with mechanical engineers compared to chemists.[261] These articles appear in 221 journals and proceedings of which *Powder Technology* published 20 % (138 of the 695). *Chemical Engineering Science* published 54 articles, while only 4 other journals published more than 20: *Advanced Powder Technology* (28), *AIChE Journal* (22), *Particuology* (22), and *Chemical Engineering Research & Design* (20).

We created a bibliometric map of the co-occurrences of 107 keywords mentioned most in these articles with VOSViewer (Figure 7.6).[14,262] The red cluster with 25 keywords includes flow, particles, and multi-phase flow. All of the other clusters have from 11 to 16 keywords: The green cluster relates to gas-solid flow and granular flow; major topics in the blue cluster include fluidized beds (FB), dynamics, and segregation; packed beds and reactors are subjects of the yellow cluster; spheres, direct numerical simulation, and drag force are most prominent in the magenta cluster; systems and granular materials are the most frequent keywords in the light blue cluster; and heat transfer, particle systems, and fluidization are the main subjects of the teal coloured cluster.

We review two families of operations (fluidized beds and mixing) characteristic of chemical engineering that highlight the capacity of CFD-DEM to simulate gas-solid and liquid-solid flows. Furthermore, they demonstrate that CFD-DEM predicts local quantities like fluid and granular flow patterns, macroscopic quantities—pressure drop, residences time, mixing time, axial diffusion—and local granular flow patterns.

7.4.1 Fluidized bed and spouted bed reactors

CFD-DEM highlight operational problems that may arise when changing conditions—start-up, shut-down, gas velocity, species concentration, pressure, or temperature. Simulations gauge the agglomeration strength between particles in the bed but, equally importantly, in cyclone diplegs where the cohesive forces are higher due to the much lower d_{p}. CFD-DEM models demonstrated that higher pressure retards the agglomeration rate.[263] Coupling CFD-DEM with heat transfer and kinetic models also explores the heat distribution and concentration gradients that are particularly sensitive in the grid region and at the cooling

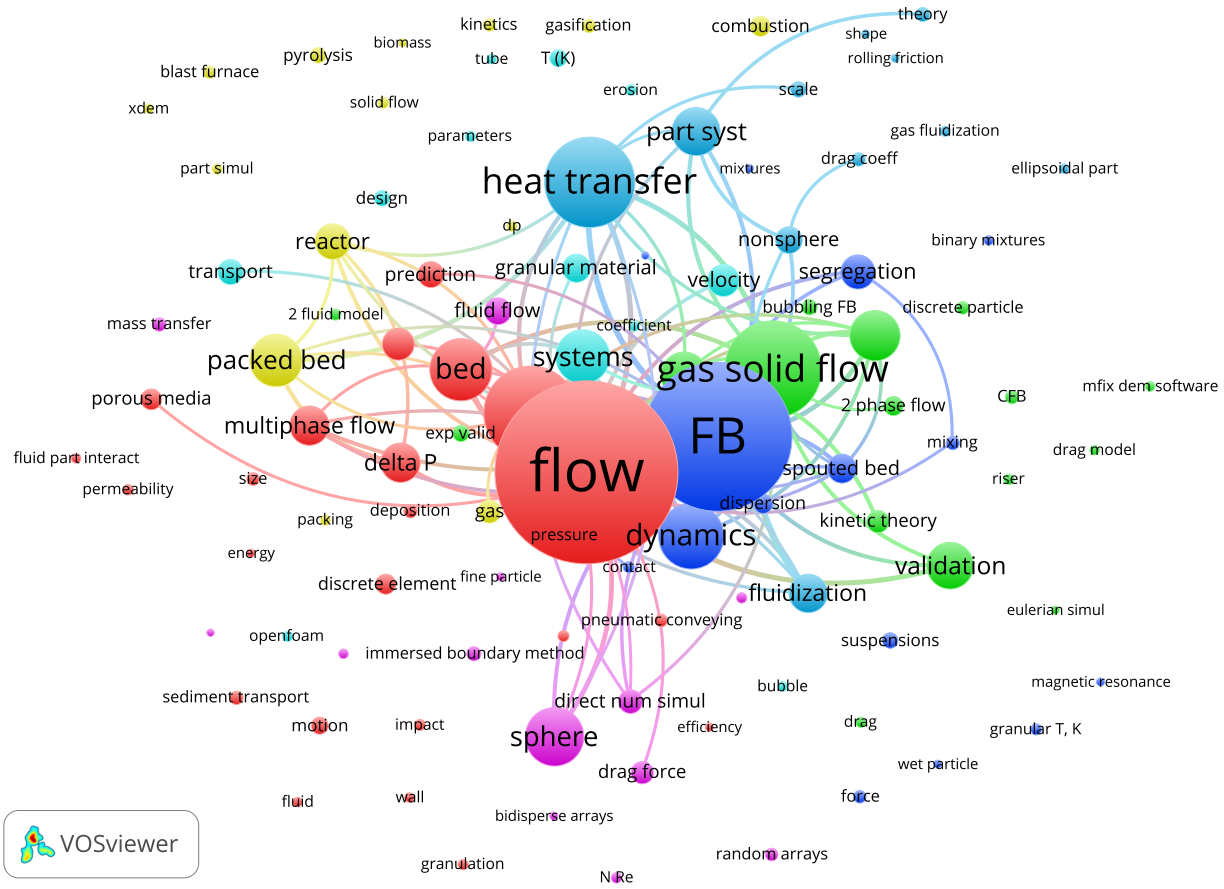

Figure 7.6 Bibliometric map of 107 keywords from 695 articles WoS indexed from 2016 to mid-2019 with with CFD-DEM as a topic.[14,133,262] VosViewer software grouped the keywords of these articles into 7 clusters (denoted by colour). The proximity of the circles indicates how closely they are related and the size is proportional to how often authors list the word as a keyword The size of the circle and font are proportional to the number of articles and the largest circles for each cluser are: flow (188 articles), gas-solids flow (100), fluidized beds (FB-153), packed beds (54), spheres (60), systems (56), and heat transfer (93). The smallest circles for each category are efficiency (9 articles), Eulerian simulation (9), fluidized beds (FB-153), packed beds (54), spheres (60), systems (56), and heat transfer (93). Lines represent citation links.

coils.[264]

Ever more research has been dedicated to modelling spouted beds by CFD-DEM.[246,265,266,267] Gas enters spouted bed reactors through a single hole at the base and develops a conic velocity profile in the bed unless constrained by a draft tube. Recent studies on spouted bed instability accurately described recurrent problems like spout deflection and have quantitatively characterized the voidage distribution and particle momentum profile.[268] Like for

traditional fluidized beds, researchers study heat transfer with CFD-DEM,[247] the hydrodynamics of non-spherical particles,[266] and the mixing.[265]

Figure 7.7 shows the CFD-DEM simulation of the fluidization of 200 000 FCC particles in an 8 mm cylindrical fluidized bed. This simulation was carried out using the open source CFDEM framework and illustrates typical results with unresolved CFD-DEM.[269]

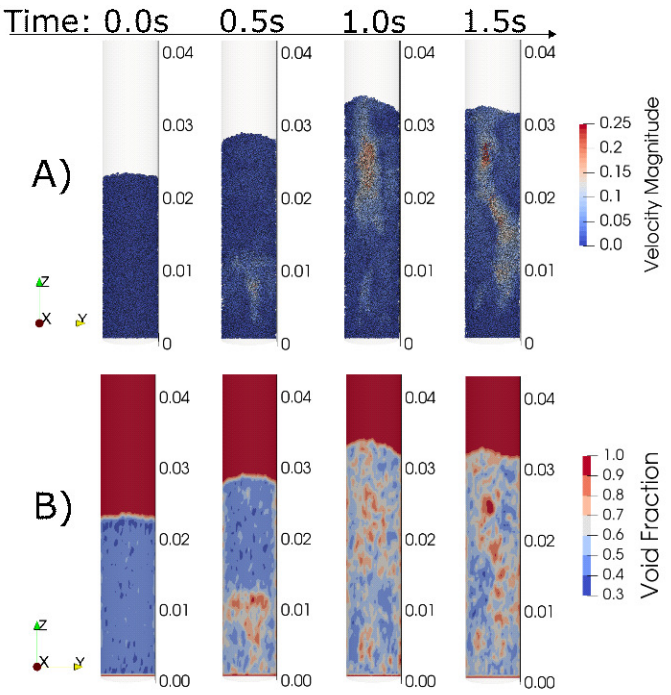

Figure 7.7 CFD-DEM simulation of the fluidization of 200 000 FCC particles in a 8 mm diameter cylindrical fluidized bed reactor: A, individual particle velocity; and B, void fraction profile. Under the simulation condition, the bed undergoes fluidization and unsteady bubbles are formed as the bed expands

7.4.2 Solid-liquid mixing

Solid-liquid mixing is a unit operation in which agitated vessels suspend particles in a fluid. Despite their apparent simplicity and wide commercial application in pharmaceuticals, minerals, and food processing, predicting power consumption and the impeller speed to suspend particles requires experimentation: a priori agitated vessel design remains an art except for the most basic impeller geometry and particle size distributions. Unresolved CFD-DEM predicts the just-suspended speed, the fraction of suspended particles, and particle concentration for both the laminar and the early turbulent regimes.[173,190,191]

The sliding and rolling friction coefficients were the only DEM parameters that alter the fraction of suspended particles, but only at velocities for which complete suspension is unreachable. Figure 7.8 illustrates CFD-DEM model predictions of particle distribution and velocity for a viscous solid-liquid system operating at 100 rpm, 250 rpm, and 350 rpm.[173]

Researchers apply unresolved CFD-DEM to study turbulent solid-liquid mixing. The particle size distribution and the initial state of the particle bed influence the solution long after initiating agitation. Furthermore, polydisperse systems take longer to reach steady-state.[250,251,255]

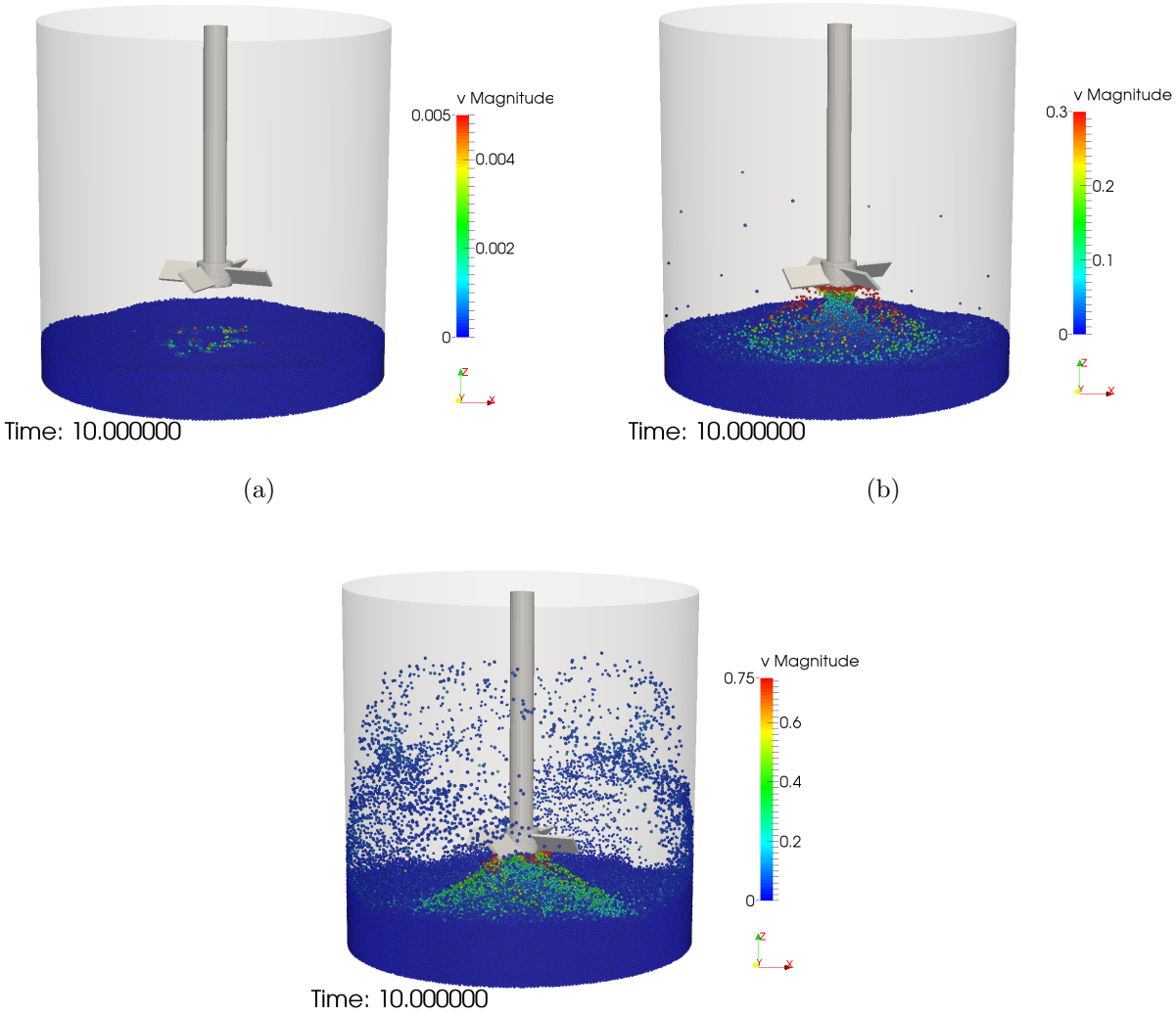

Figure 7.8 Unresolved CFD-DEM simulation of a viscous liquid-solid mixing tank operating at: (a) 100 rpm, (b) 250 rpm, and (c) 350 rpm.

7.5 Uncertainty and limitations

The Lagrangian nature of DEM and the fact that it tracks the position and the velocity of each particle induces a limitation on the number of particles and the size of the systems that can be simulated. Even leveraging HPC, it is seldom possible to simulate more than 10^8 particles within a reasonable clock time (ie, a week). Most simulations generally contain up to the order of 10^6 particles. This limits the size of the systems that can be investigated. Although this is a limitation shared by pure DEM, this is exacerbated in CFD-DEM due to the added cost of the CFD solver for the VANS equations, but also due to the need to couple the CFD and the DEM for each individual particle, which induces additional computational overhead. Coarse graining, which consists of reducing the number of particles by agglomerating particles into parcels, is a promising active field of research, which can achieve good accuracy for some flow configurations at a greatly reduced computational cost.[270]

Since the solid-fluid forces such as drag and their dependency on the void fraction and $N_{\mathrm{Re_p}}$ must be modelled, the accuracy of DEM simulation depends on the validity of these expressions. Although the effect of the void fraction and of the $N_{\mathrm{Re_p}}$ on drag is well-known, it is unclear how those two factors affect the Saffman and Magnus lift and the virtual mass.

The projection of the particles onto the CFD mesh remains an active topic of research. There is a need for a projection method that leads to a continuously differentiable (in space and time) void fraction and momentum exchange term.

Turbulence modelling, a phenonema not discussed in this article, is also an open challenge. Steady CFD-DEM simulations are illogical, and as such, unsteady Reynolds averaged Navier-Stokes (URANS), large eddy simulations (LES), or direct numerical simulations (DNS) must be employed.

Since URANS models the entire turbulence cascade, additional correlations are necessary to account for unresolved turbulence on solid-fluid interactions like drag. Large eddy simulations suffer from the same predicament, but to a lesser degree since they resolve the larger flow scales. However, they require finer meshes, which in turn can be problematic for the projection of the particle information.

Similarly, unresolved CFD-DEM poorly characterizes suspension rheology.[173] Since the flow field is unresolved around the particles, the additional momentum dissipation due to the disturbance of the flow created by the particle has to be modelled by incorporating a viscosity model. To correct the suspension viscosity, the Krieger-Dougherty[271] model is applied with the local value of the solid fraction $(1 - \epsilon_{\mathrm{v}})$.[173] It remains unclear whether this process can be generalized to all liquid-solid flows.

Unresolved CFD-DEM contains a number of model parameters linked to DEM. Some of these parameters —the density (ρ_i), the Young's modulus (E_i), the Poisson ratio (ν_i), and the shear modulus (G_i)—are based on material properties. However, parameters such as the coefficients of sliding and rolling friction (μ_s and μ_r), as well as the coefficient of restitution (e) depend on surface properties (ie, roughness) and on the shape of the particles. In DEM, these parameters need to be calibrated for each type of powder and, in some cases, for each flow configuration. In some solid-fluid flows modelled by CFD-DEM, these parameters affect results but to a lesser extent than in pure DEM.

Furthermore, the models for solid-fluid forces (eg, drag) are based on correlations that are valid in a limited range of $N_{\mathrm{Re_p}}$ and ϵ_{v}. These introduce additional modelling uncertainties that are process dependent. Work remains to establish the uncertainties linked to these correlations. Although unresolved CFD-DEM remains an active research area, it has already demonstrated that it is one of the most accurate, robust and versatile approaches to simulate solid-fluid flows in processes encountered in chemical engineering.

7.6 Conclusion

Computational fluid dynamics coupled with discrete element methods (unresolved CFD-DEM) is a simulation technique based on a Lagrangian description of particle motion and a Eulerian description of fluid motion that predicts solid-fluid flows. For fluid flow (CFD), the equations are governed by the volume-averaged Navier Stokes (VANS). These equations consider the volume fraction occupied by the fluid within each cell depends on the volume of solid particles.

For the solid-phase (DEM), the translational and rotational motion of each particle is governed by Newton's second law of motion. Each particle is tracked and the overlap during the collision is decomposed into normal and tangential directions and introduced to contact models. The latter included elastic and dissipative components, which allow the treatment of inelastic particle-particle collision.

Solid-fluid coupling is the core of unresolved CFD-DEM. This includes calculating fluid void fraction by projecting the particle volume and solid-fluid force onto the Eulerian mesh. This projection must ensure mass conservation, stability of the CFD simulation, and a reasonable computational cost. Moreover, solid-fluid coupling involves hydrodynamics forces, which are all possible forces between fluid and solid. For all the systems, drag, the force due to the pressure gradient, and the shear stress are always involved. For unsteady systems, systems with sharp velocity gradients or rotating particles, including virtual mass, Basset and lift

(Saffman and Magnus) forces may be required.

Coupling CFD and DEM is an active field of research that already predicts the hydrodynamics of a large number of applications such as fluidized beds, spouted beds, and solid-liquid mixing. It is a predictive tool that allows researchers to have a new perspective on the physical behaviour of solid-fluid systems, while being cost-effective. Although there are still challenges, such as decreasing the computational time, improving the robustness and the accuracy of the solid-fluid coupling, and extending the approach to fully multiphysics simulations, this simulation technique has a promising future.

7.7 Appendix A

Consequences of the loss of hyperbolicity of conservation equations

This short demonstration shows the importance of preserving the hyperbolic character of a conservation law in order to preserve its stability. One may refer to Toro's book [272] for a more rigorous definition of hyperbolic systems and for complementary information.

Without loss of generality, we consider a 1D hyperbolic system for a conservation law:

$$\frac{\partial \boldsymbol{y}}{\partial t} + \mathcal{A}(\boldsymbol{y})\frac{\partial \boldsymbol{y}}{\partial x} = 0 \tag{7.29}$$

with $\boldsymbol{y} \in \mathbb{R}^n$ et $\mathcal{A} \in \mathbb{R}^{n\times n}$. As long as the system preserves its hyperbolicity, the eigenvalues of $\mathcal{A}$ are real. If the systems looses hyperbolicity, matrix $\mathcal{A}$ possesses complex eigenvalues.

Since the convection matrix $\mathcal{A}$ is a real matrix, its complex eigenvalues are necessarily conjugate. We can illustrate the consequence of these conjugate eigenvalues by applying a model equation for the transport of a complex scalar (ie, a wave).

We consider a given the advection of a complex scalar:

$$\partial_t(\alpha) + \lambda\frac{\partial \alpha}{\partial x} = 0 \tag{7.30}$$

with $\alpha, k \in \mathbb{C}$. The solution to this hyperbolic problem can be written in the form of a wave solution of the form $e^{i(\omega t - kx)}$ with $\omega \in \mathbb{C}$ and $k \in \mathbb{R}$. This is like solving the problem in Fourier space with ω a pulse and k a wave number. With this consideration, we find that ω and k verify:

$$i\omega = i\lambda k \tag{7.31}$$

Given the real nature of k, we find that:

$$Re(\omega) = Re(\lambda)k \tag{7.32}$$

$$Im(\omega) = Im(\lambda)k \tag{7.33}$$

which gives a solution of the form $e^{i(Re(\lambda)kt-kx)-Im(\omega)t}$. Therefore, if the imaginary part of ω is positive, the solution will be stable, otherwise, it will be unstable and this instability will grow exponentially.

We go back to the case of our general hyperbolic system with a real convection matrix $\mathcal{A}$. We have seen that a loss of hyperbolicity of the system implied the presence of complex conjugate eigenvalues. In this case, one eigenvalue in each of the pair of conjugate complex eigenvalues will have a negative imaginary part leading to exponential instability. We therefore conclude with this example that loss of hyperbolicity of a system directly leads to the loss of stability.

CHAPITRE 8 SIMULATION DE LA RTD DANS UN RÉACTEUR À LIT FLUIDISÉ PAR CFD-DEM

Nous avons débuté une simulation par CFD-DEM identique aux conditions d'opération en laboratoire. La CFD-DEM s'applique bien à notre réacteur, puisqu'il est de petite taille et donc, le temps de calcul peut être acceptable selon la taille des particules employées. Jusqu'à présent, dans la littérature, aucune étude RTD sur la phase gazeuse en CFD-DEM dans un réacteur à lit fluidisé n'a été produite. L'objectif est de construire une simulation robuste permettant de simuler les expériences en laboratoire. Ainsi, de nouvelles conditions d'opération ou même une mise à l'échelle de notre montage en laboratoire pourront se faire rapidement par CFD-DEM. Pour se faire, les grandes étapes pour la simulation sont :

1. Construction du micro-réacteur;
2. Initialisation des particules par DEM — insérer les particules dans le réacteur;
3. Couplage de la CFD avec la DEM et étude de l'hydrodynamique;
4. Ajout de la RTD — injection d'un traceur et mesure de sa concentration à la sortie.

8.1 Maillage du micro-réacteur

Le microréacteur a un diamètre de 8 mm et une longueur de 36 cm. Celui-ci est modélisé en 3 dimensions sous forme d'un cylindre. Le maillage est séparé en 200 cellules sur la longueur et comprend 20 cellules de courbure et 10 cellules en profondeur. Ainsi, le total est de 40 000 cellules (Figure 8.1). Ce maillage a été choisi après des tests monophasique où il a été montré qu'il était capable de bien reproduire l'écoulement dans le réacteur. Compte tenu des faibles vitesse de gaz (<30 mm/s) et de la faible longueur charactéristique du réacteur (8mm), l'écoulement monophasique dans le micro-réacteur est laminaire. Conséquemment, ce maillage est largement suffisant pour bien décrire le comportement de la phase gazeuse. La figure 8.2 présente le profil axial de l'écoulement monophasique.

8.2 Condition de la DEM — phase solide

Deux catalyseurs sont envisagés pour l'étude RTD par CFD-DEM. Tout d'abord, le sable, qui a un diamètre moyen (d_{50}) de 87 µm (Tableau 8.1). Il a été choisi pour sa grande taille comparée aux autres catalyseurs étudiés. Cependant, le sable est considéré sphérique dans la simulation, ce qui n'est pas le cas en réalité. En effet, l'image produite par microscopie

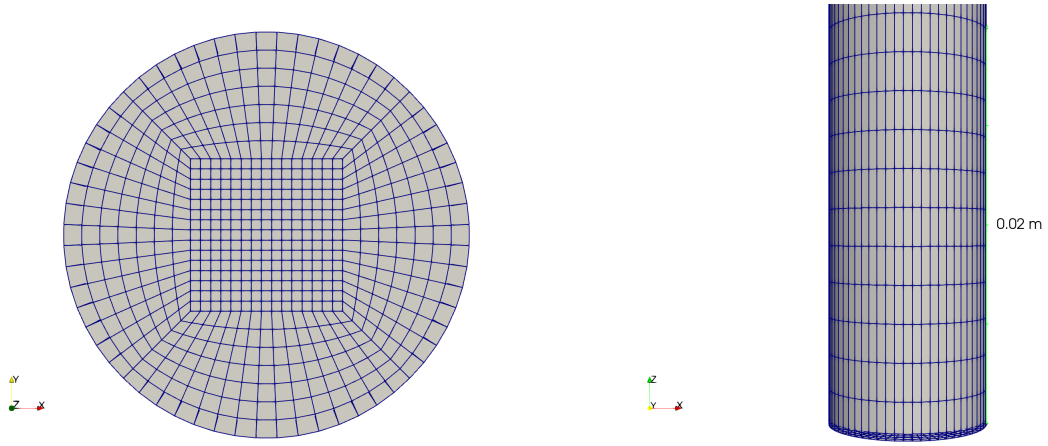

(a) (b)

Figure 8.1 Maillage employé pour le volet CFD. (a) Coupe axiale (de normale $\boldsymbol{z}$) (b) Coupe transversale (de normale $\boldsymbol{y}$)

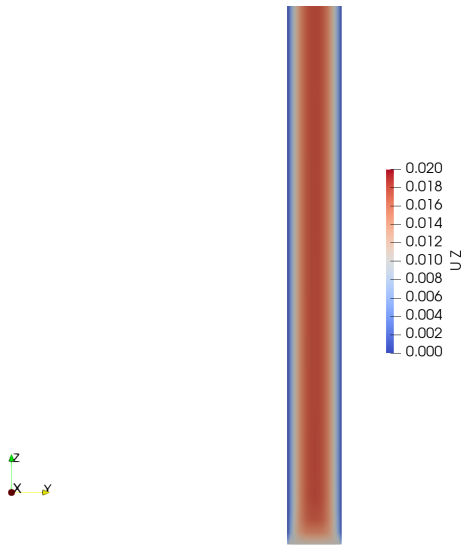

Figure 8.2 Profil de vitesse axiale dans le micro-réacteur.

électronique à balayage (SEM) démontre sa forme polygonale (Figure 8.3). C'est pour cette raison que le FCC a été choisi comme deuxième catalyseur. Cette poudre est plus fine ($d_{50} = 64\,\mu m$) et demandera un temps de calcul plus élevé, mais sa forme est parfaitement sphérique ($\phi = 0.99$). De plus, il est intéressant de comparer deux poudres de groupe Geldart différent (A et B).

La distribution de la taille des particules (PSD) a été mesurée expérimentalement par diffraction laser. Par la suite, pour la simulation, les particules ont été distribuées en fonction de leur pourcentage massique (Tableau 8.2). Au total, la CFD-DEM comprend 7 tailles de particules par poudre. De plus, nous posons l'hypothèse que les sphères sont pleines à l'intérieur et donc que la porosité est nulle. Cette hypothèse est juste pour le sable qui a une aire de surface (S_A) de $0.56\,m^2\,g^{-1}$, mais pas pour le FCC où $S_A = 93\,m^2\,g^{-1}$.

8.3 Condition de la CFD — phase gazeuse

La partie CFD est consacrée aux fluides. L'argon est l'inerte qui fluidise le lit de catalyseur en continu. Puis, à un temps $t = 0$, un volume fini d'un traceur, soit l'oxygène, sera injecté. Ce traceur a été choisi, car aucune interaction avec le sable et le FCC n'est observée. Trois vitesses seront comparées soit 10, 20 et $30\,mm\,s^{-1}$. La masse volumique (ρ) est considérée constante puisque l'écoulement est non compressible (tableau 8.3).

Le volet CFD emploie une méthode de type volumes finis pour simuler la phase gazeuse à l'aide d'*OpenFoam*. Un schéma d'interpolation centré d'ordre deux est employé. De sucroît, le couplage semi-implicite entre la pression et la vitesse est réalisé à l'aide d'une méthode de prédicteur-correcteur de type PISO (*Pressure-Implicit with Splitting of Operators*)

Tableau 8.1 Caractéristique du sable et du FCC simulé par CFD-DEM

	Sable	FCC
ρ_b ($kg\,m^{-3}$)	1328	874
d_{10} (µm)	58	39.4
d_{50} (µm)	87	64.0
d_{90} (µm)	120	104

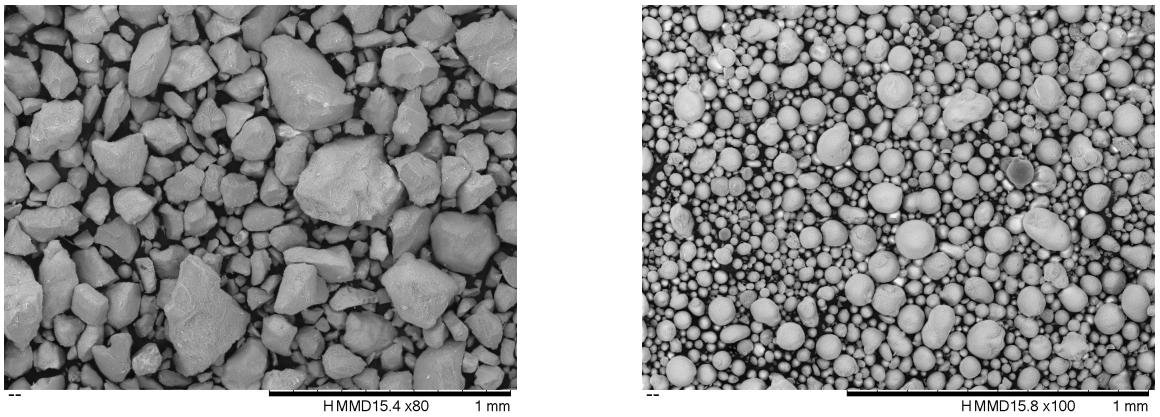

(a) (b)

Figure 8.3 Image SEM des poudres. (a) Sable, grosses particules cuboïdes ou polygonales. (b) FCC, la plupart des particules sont des sphères.

Tableau 8.2 Distribution selon le pourcentage massique des particules de sable et de FCC simulé par CFD-DEM

Sable		FCC	
d_p (µm)	Pourcentage massique	d_p (µm)	Pourcentage massique
68	9.90 %	40	13.3 %
89	13.8 %	83	17.1 %
101	18.4 %	101	9.53 %
116	17.1 %	116	9.10 %
133	12.7 %	143	17.2 %
164	15.4 %	187	16.8 %
230	12.4 %	246	17.1 %

Tableau 8.3 Caractéristique des phase gazeuses simulées par CFD-DEM à 22 °C et 1 bar

	Argon	Oxygène
ρ (kg m^{-3})	1.63	1.31
$\mu_\mathrm{dynamique}$ (Pa s)	2.243×10^{-5}	2.050×10^{-5}
$\mu_\mathrm{cinématique}$ (m^2 s^{-1})	1.376×10^{-5}	1.571×10^{-5}

8.4 Résultats préliminaires

8.4.1 Initialisation des particules

La première étape est d'insérer dans le réacteur un nombre défini de particules. L'objectif est d'atteindre un niveau de 18 cm de catalyseur ce qui est la hauteur exacte ajoutée en laboratoire soit 13.5 g de sable ou 8.19 g de FCC. Nous avons donc inséré jusqu'à 9 millions de particules dans le haut du réacteur à un taux de 500 000 particules par 100 000 itérations (Figure 8.4–a). Une fois insérées, en raison de la gravité, les particules tomberont avec une certaine vitesse jusqu'à ce qu'elles atteignent le fond (Figure 8.4–b).

8.4.2 Résultats préliminaire pour un plus faible nombre de particules

Une première vague de simulation ont été lancées pour mesurer la capacité du modèle CFD-DEM à prédire la vitesse minimale de fluidisation pour un plus faible nombre de particules (1.5 cm de poudre). La Figure 8.5 présente des profiles d'écoulements et de fraction volumique typique obtenu dans ce type de simulation.

La Figure 8.6 montre que le modèle est capable dans ces circonstances de reproduire la vitesse minimale de fluidization pour les particules de sable. Ces résultats sont très encourageant, car ils démontrent que le modèle est fondementalement approprié. Cependant, le coût de calcul, somme-toute important, pour 1/12 des particules laisse présager un fort coût pour le lit complet, malgré sa petite taille.

8.5 Étapes suivantes pour poursuivre le projet

L'objectif final de ce projet est de comparer la RTD pour le FCC et le sable en injectant par pulse 10 mL d'oxygène. Le tout sera fait pour 3 vitesses de gaz différentes. Les étapes restantes sont :

1. Initialisation des particules
   (a) FCC (0.25, 3, 5 et 10 millions de particules)
2. Couplage CFD-DEM
   (a) Sable : 10, 20 et 30 $\mathrm{mm\,s^{-1}}$
   (b) FCC : 10, 20 et 30 $\mathrm{mm\,s^{-1}}$
3. Étude RTD : ajouter l'injection de 10 mL du traceur (O_2) et mesurer la concentration à la sortie.

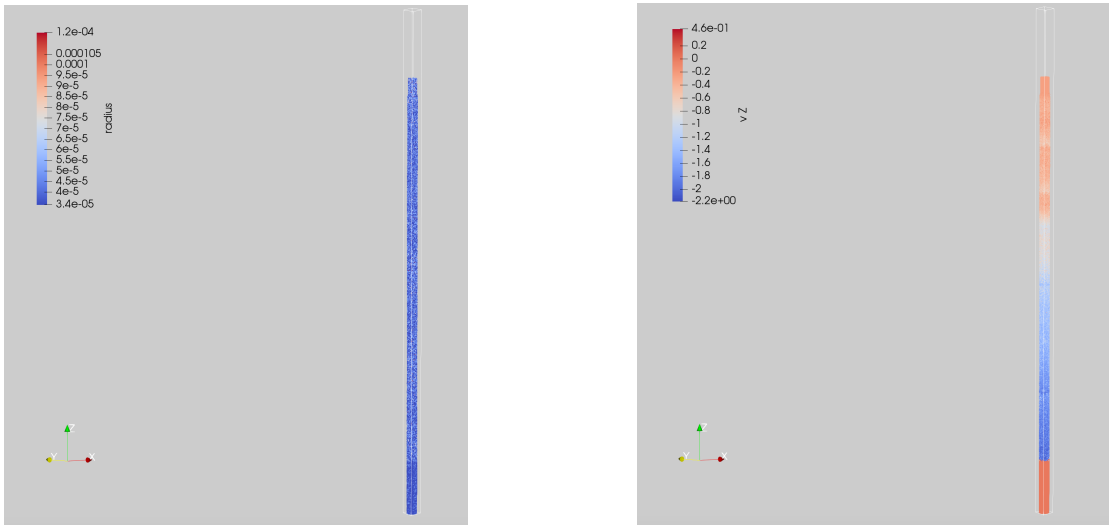

(a) (b)

Figure 8.4 Initialisation de 9 millions de particules dans le microréacteur (a) Distribution des particules en fonction de leur rayon. (b) Distribution en fonction de la vitesse axiale dans le réacteur. Les particules sont insérées dans le haut du réacteur (vitesse nulle) et, par gravité, vont se diriger avec une certaine vitesse vers le bas. Finalement, les particules atteignent l'extrémité et se stabilisent pour former le lit de catalyseur

4. Comparaison de la simulation CFD-DEM avec les essais en laboratoire

La difficulté rencontrée lors de la simulation par CFD-DEM est plutôt au niveau du temps de calcul. Par exemple, pour initier 9 millions de particules, cela prend 5 jours de calcul avec 240 processeurs. L'ampleur de la tâche a été sous-estimée au départ, mais ces résultats préliminaires sont de bon augure pour la suite. Des recherches supplémentaires sont nécessaires.

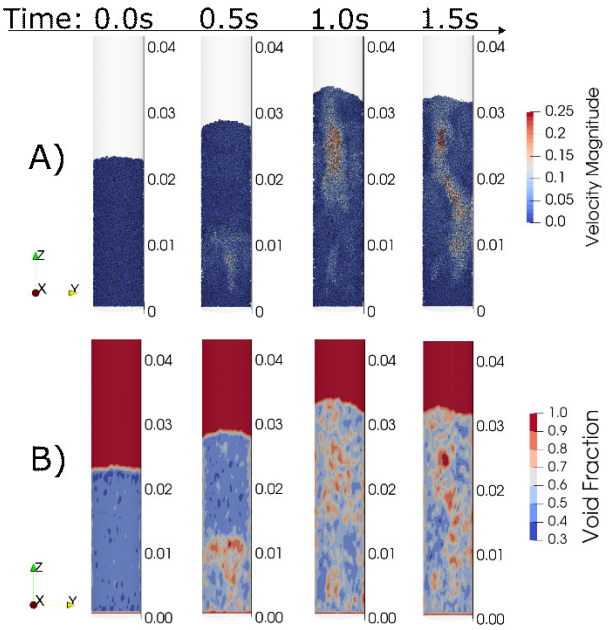

Figure 8.5 Simulation CFD-DEM de la fluidisation de 200 000 particules de FCC dans le micro-reacteur : A, Vitesse des particules ; B, profile de fraction de vide.

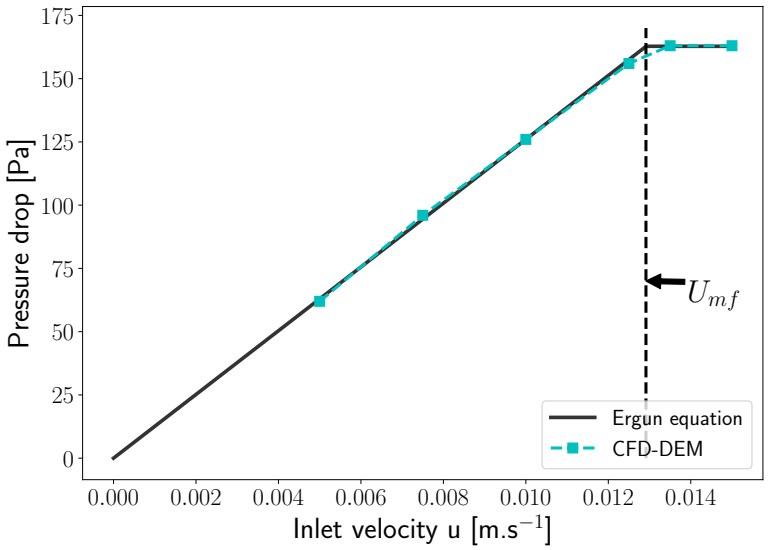

Figure 8.6 Perte de charge dans le micro-réacteur pour 1.5 cm de poudre. Les résultats pour la perte de charge sont comparés à la loi d'Ergun. La barre verticale indique la vitesse minimale de fluidisation mesurée expérimentalement.

CHAPITRE 9 DISCUSSION GÉNÉRALE

9.1 Développement de la méthodologie RTD

Les articles *Experimental Methods in Chemical Engineering : Residence time distribution – RTD* et *Residence Time Distribution in Fluidized Beds : Diffusion, Dispersion, and Adsorption* ont permis d'améliorer la méthodologie des études RTD. En effet, la littérature était limitée au niveau de la procédure. Les points nouveaux apportés à la méthodologie des analyses RTD de la phase gazeuse dans un réacteur à lit fluidisé sont :

1. Pour obtenir le temps moyen exact ($\bar{t}$), tout volume autre que le lit catalytique doit être minimisé (ligne, spectromètre de masse, entrée, sortie, injection) (Chapitre 4).
2. Pour détecter tout type d'anomalies ou de déviation par rapport au comportement idéal *plug flow*, l'injection de type *pulse* est à prioriser (Chapitre 5).
3. Plus le débit volumique est élevé ($27 \times U_{\mathrm{mf}}$), plus la répétabilité des essais RTD sera faible. Donc, il est primordial d'augmenter son nombre d'expérience si la vitesse est élevée (Chapitre 4).
4. La fréquence d'acquisition des données par le spectromètre de masse doit être au maximum de 24 Hz. À une valeur plus élevée, trop de bruit est présent (Chapitre 4).
5. Le coefficient de diffusion ($\mathscr{D}$) du traceur choisi doit être similaire au gaz impliqué dans le système étudié. Ce critère est particulièrement sensible lorsque le catalyseur est poreux (Chapitre 5).
6. Les essais RTD sont grandement influencés si le catalyseur est poreux. Un phénomène d'adsorption peut être observé ce qui aura un impact sur l'ensemble des gaz présents. En effet, l'adsorption fera diminuer le débit volumique total et donc augmentera le temps de résidence moyen ($\bar{t}$). Donc, des conditions d'opération identiques doivent être utilisées (Chapitre 5 et 6).
7. La température influence le phénomène d'adsorption. Par contre, la différence causée par la diffusion est toujours présente. Donc, il est primordial que la température soit la même que le système étudié (Chapitre 6).
8. Un protocole étape par étape avec la durée de chaque étape a été développé pour quatre vitesse (10, 20, 30 et 60 $\mathrm{mm\,s^{-1}}$) (Chapitre 4).

9.2 Développement d'un modèle RTD

La seconde contribution est le développement d'un modèle RTD présenté dans l'article : *Fluidized bed hydrodynamic modelling of CO_2 in syngas : Distorted RTD curve due to adsorption on FCC*. Ce nouveau modèle est valide lorsqu'un ou plusieurs traceurs sont injectés simultanément dans un réacteur à lit fluidisé. Le tableau 9.1 présente les différences entre la littérature, c'est-à-dire le modèle par dispersion axiale, et le modèle développé dans ce projet. La nouveauté la plus importante est que la résolution considère la dépendance des traceurs. En effet, le CO_2 est adsorbé dans les pores du catalyseur FFC ce qui a pour effet de diminuer le débit volumique total du système. Il en est de même pour le CO et le CH_4. Cette variation du débit est prise en compte dans le nouveau modèle.

Tableau 9.1 Comparaison du modèle de dispersion axiale (littérature) et du nouveau modèle développé

Critère	Modèle de dispersion axiale[69,71]	Nouveau modèle RTD (Chapitre 6)
Nombre de phases	1 seul phase – émulsion	3 phases : *bulk*, catalyseur et la surface intérieure des pores
Nombre de traceurs	chaque traceur est résolu indépendamment	Tous les traceurs sont résolus dépendamment des uns aux autres
Phénomène inclus dans le modèle	Dispersion, diffusion, convection	Dispersion, diffusion, convection et adsorption
Type de résolution	Solution analytique Minimisation de SSE[1]	Approche par volume fini Minimisation de SSE[1]
Provenance du modèle	Analogie avec la loi de Fick	Bilan molaire

[1] SSE : Erreur des sommes aux carrés

9.3 Développement de la CFD-DEM

Malgré le fait que l'étude de la simulation CFD-DEM présente seulement des résultats préliminaires, ceux-ci sont de bon augure pour la suite. En effet, il a été possible d'insérer 9 millions de particules dans le microréacteur ainsi qu'étudier le profil de vitesse pour 200 000 particules. La vitesse minimale de fluidisation est cohérente avec celle obtenue en laboratoire.

9.4 Difficultés rencontrées lors du projet

9.4.1 Expérience RTD en laboratoire

Les expériences en laboratoire amènent son lot de défis. Tout d'abord, un problème récurrent était l'étanchéité du système. En effet, le réacteur étant en quartz, celui-ci est très fragile. Donc, il fallait être extrêmement délicat lorsqu'il était serré. Les férules étaient en plastique pour les expériences à température ambiante. Donc, il était plus simple de serrer sans briser le réacteur. Par contre, à 300 °C, il fallait avoir des férules en métal. Plus de 10 réacteurs ont été brisés au cours des expériences. L'étanchéité du système est primordiale, car des gaz toxiques sont injectés — CO_2, CO, CH_4, Kr, H_2. De plus, le spectromètre de masse (MS) aspire les gaz. Donc, si une légère fuite est présence, le MS détectera immédiatement et les résultats seront erronés.

Un autre défi était de minimiser l'espace à la sortie du réacteur (entre le lit de catalyseur et l'embout du MS), sans faire entrer les particules à l'intérieur du capillaire du MS (qui aspire continuellement). Ce problème arrivait fréquemment lorsque le FCC était employé, car son diamètre moyen était de 64 µm. À des valeurs élevées de débit volumique, la fluidisation était plus intense et emportait le catalyseur directement dans le capillaire (Figure 4.22). Il était donc nécessaire de le changer, ce qui est une tâche délicate et risquée pour le spectromètre de masse – la poussière pouvant entrer dans le quadrupole. De plus, il fallait attendre 24 h pour le démarrage de la pompe et pour obtenir des valeurs exactes. C'est pour cette raison que les débits changent entre l'article de revue de la RTD (Chapitre 4) et celle sur les traceurs (Chapitre 5). Il existe un filtre pouvant être ajouté à l'embout du MS. Par contre, celui-ci ralentit le temps de résidence, ce qu'il voulait être évité dans notre situation.

Les essais à haute température ont causé beaucoup de problèmes. En effet, tout le système devait être modifié pour supporter de haute température. Toutes les lignes étaient initialement en plastique et ont été changées en métal avec exactement les mêmes dimensions physiques. Le plus complexe était de réussir à fermer le haut et le bas du réacteur avec des boulons sans briser le tube de quartz. Un serrement de trop et le réacteur était brisé et jeté. De plus, l'obtention d'une température uniforme était difficile, car les gaz entraient dans le réacteur à la température ambiante et prenaient un certain temps avant de chauffer. Pour contrer cela, nous avons rajouté de la laine de verre pour élever le lit de catalyseur. Une température uniforme a été obtenue, mais une erreur s'est ajoutée à la RTD, car le volume avant le lit catalytique a été augmenté (Figure 9.1).

Finalement, le plus grand défi fut d'obtenir une méthodologie étape par étape pour obtenir des résultats répétables. En effet, chaque geste effectué a été analysé pour diminuer au maxi-

(a)

(b)

Figure 9.1 Essai expérimental à haute température. Réacteur à lit fluidisé en quartz, vide avec un distributeur en laine de verre. (a) Le réacteur est installé dans un four pouvant atteindre 1000 °C. (b) Rapprochement sur le distributeur de laine de verre plus épais pour avoir une température uniforme dans le réacteur.

mum les erreurs. Un protocole a été créer pour l'ensemble des essais RTDs (Annexe 4.7.1 – Chapitre 4). Il propose un temps exact pour chaque étape de la mesure RTD, ce qui n'a jamais été fait ou vu dans la littérature.

9.4.2 Modèle RTD

Le nouveau modèle RTD a été codé en 3 programmes : Fortran, Microsoft Excel et MatLab. Finalement, le code Fortran a été choisi pour sa vitesse d'exécution — moins d'une minute pour résoudre. Par contre, il est difficile à comprendre, il demande une connaissance en Fortran et il n'est pas simple d'utilisation. L'Excel est simple et convivial, mais il demande un ordinateur puissant, car son temps de résolution varie entre 10 et 15 minutes. Finalement, l'essai avec le code MatLab a été catastrophique. Le temps de résolution dépassait les 15 minutes et n'incluait pas toutes les caractéristiques du modèle. C'est pour cette raison que celui-ci a été laissé de côté.

Au départ, un fichier Excel a été produit pour chaque traceur indépendamment. Chaque fichier était très lourd à résoudre et contenait beaucoup de liaisons inutiles. Par la suite, un second fichier Excel a été créé, plus épuré et minimisant les liaisons et les variables à résoudre. Malgré cela, il était tout de même difficile à compiler. Ainsi, le code Fortran était la solution à adopter.

9.4.3 Simulation par CFD-DEM

La plus grande difficulté de la simulation CFD-DEM est le temps de calcul pour atteindre l'objectif. Celui-ci ainsi que l'ensemble de ce projet ont été sous-estimés au départ. C'est pour cette raison que les résultats obtenus sont que préliminaires. Par contre, ceux-ci sont prometteurs et une suite est à venir.

CHAPITRE 10 CONCLUSION

10.1 Synthèse des travaux

Ce projet de doctorat a permis de développer une méthodologie pour l'analyse du temps de résidence de la phase gazeuse d'un réacteur à lit fluidisé de 8 mm de diamètre.

Tout d'abord, la revue de littérature *Experimental Methods in Chemical Engineering : Reactors – fluidized Beds* (Annexe A) a mis en lumière les défis qui ont été rencontrés lors des expériences en laboratoire. Nous avons défini les caractéristiques physiques minimales nécessaires lors d'une publication qui fait intervenir des catalyseurs. Ces caractéristiques (vitesse minimale de fluidisation, masse volumique, fraction de vide, ratio de Hausner, angle de repos, la distribution de la taille des particules, la sphéricité et l'aire de surface) sont devenues essentielles dans les articles subséquents. De plus, nous avons démontré les nombreuses applications en génie chimique : la gazéification, la pyrolyse, la combustion, la capture du CO_2, et les procédés impliquant la biomasse. Les limitations d'un réacteur à lit fluidisé sont principalement reliées à l'hydrodynamique soit la maximisation du contact gaz-solide et la minimisation du contournement du gaz. C'est pourquoi l'analyse RTD est primordiale pour ce type de réacteur. Les régimes de fluidisation ont été définis dans cette revue. Puis, ils ont été analysés par la RTD dans le second article de revue de littérature : *Experimental Methods in Chemical Engineering : Residence Time Distribution – RTD* (Chapitre 4).

Ce second article comporte plus de 500 essais RTD. L'objectif principal était de développer une méthodologie précise pour les expériences RTD en laboratoire. Tout d'abord, le modèle de dispersion axial incluant les conditions frontières fermé-fermé, ouvert-ouvert et ceux appliqués dans ce projet : fermé-ouvert a été présenté. La solution analytique de ce modèle a permis de comparer tous nos résultats subséquents avec un comportement idéal *plug-flow*. Les trois moments : temps de résidence moyen ($\bar{t}$), la variance (σ^2) et l'asymétrie (s^3) ont été définis et appliqués dans l'article sur les traceurs gazeux (Chapitre 5). Les expériences ont permis d'améliorer la méthodologie des essais RTD au niveau de la fréquence d'acquisition des données du spectromètre de masse, la répétabilité, le type de valve et par le fait même d'injection, la minimisation des volumes morts et l'analyse des données avec le modèle de dispersion axiale. Finalement, quatre traceurs (CO_2, CO, H_2 et CH_4) ont été injectés simultanément par *pulse* et par échelon dans le réacteur contenant du FCC. Les courbes RTD résultantes présentaient une queue prolongée pour le CO_2, CO et CH_4 dans la pente descendante. Cela indique la présence d'adsorption. De plus, l'hydrogène, ayant un coefficient de diffusion plus élevé ($\mathscr{D} = 0.796\,\mathrm{cm\,s^{-1}}$), quitte le réacteur en avance. Ces résultats non

attendus ont poussé l'étude vers l'article suivant.

Le troisième article, *Residence Time Distribution : Adsorption, Dispersion, and Diffusion* est basé sur plus de 300 essais RTD expérimentaux dans un réacteur de 8 mm de diamètre et 36 cm de hauteur. Tout d'abord 3 catalyseurs de la même provenance, mais ayant des porosités différentes, ont été comparés. Il s'agit du précurseur (VPOP), du vandyle pyrophosphate calciné (VPPC) et équilibré (VPPE). À faible vitesse ($2U_{\mathrm{mf}}$), le VPPE quitte le réacteur en avance. En effet, sa plus faible porosité empêche le gaz d'entrer dans les pores et donc diminue son temps de résidence. L'étude du phénomène de cokage *In-situ* par RTD est une piste à explorer. Puis, le phénomène de diffusion a été étudié en injectant des gaz nobles non réactifs ayant des coefficients de diffusivité différent (Kr et He). De plus, le cylindre de gaz contenait du CO et O_2 pour des expériences futures. Ce cylindre a été conçu précisément dans le but de n'obtenir aucun chevauchement lors de l'acquisition des données avec le spectromètre de masse. Les résultats démontrent que les gaz quittent le réacteur en ordre décroissant de leur coefficient de diffusivité. Par la suite, quatre nouveaux traceurs (CO_2, CO, H_2 et CH_4) contenus dans une même bouteille ont été injectés dans le réacteur à lit fluidisé remplit de FCC — Geldart groupe A, poreux – et de sable — Geldart groupe B, non poreux. C'est ainsi que l'impact sur la RTD causé par la porosité, l'adsorption et la diffusion a été démontré simultanément. Le modèle de dispersion axiale ne concordait pas avec les résultats. C'est pour cette raison que l'article qui a suivi se penche sur cette découverte.

Le quatrième article, *Fluidized bed hydrodynamic modelling of CO_2 in syngas : Distorted RTD curve due to adsorption on FCC*, propose un nouveau modèle RTD permettant de résoudre simultanément quatre traceurs (CO_2, CO, H_2 et CH_4). En effet, il a été démontré que ceux-ci étaient dépendants entre eux : le CO_2 est adsorbé à l'intérieur des pores du FCC, ceci entraine une diminution du débit total dans le réacteur. L'adsorption se produit aussi pour le CH_4 et le CO. Ce nouveau modèle a permis de mettre en lumière et d'expliquer en profondeur le phénomène d'adsorption. Finalement, à haute température ($T = 300\,^{\circ}\mathrm{C}$), aucune adsorption du CO_2, CO et CH_4 n'est observé.

Le dernier article, *Experimental Methods for Chemical Engineering : Unresolved CFD-DEM*, est une revue de littérature sur la CFD-DEM. Les équations gouvernant la phase solide, soit la DEM, proviennent de la seconde loi de Newton. Celles gouvernant le fluide, soit la CFD, sont les équations de Navier-Stokes en fonction du volume moyen (VANS). Puis, les équations dictant le couplage CFD-DEM sont les forces hydrodynamiques qui incluent la force de traînée, les forces d'écoulements non perturbés (pression, cisaillement), la force de Basset, la force de masse virtuelle, et la portance. Les applications en génie chimique sont nombreuses : lit fluidisé, mélange, séchage, cyclones, convoyeur pneumatique, et bien d'autres.

La limitation principale de cette technique est le temps de calcul, ce qui limite la taille des systèmes à simuler. De plus, plusieurs propriétés physiques et propriétés de surface doivent être connues pour obtenir une simulation qui s'approche le plus de la réalité.

Le dernier objectif de ce projet était d'explorer la simulation CFD-DEM en concevant un réacteur à lit fluidisé de 8 mm de diamètre et 36 cm de hauteur pour les essais RTD. Nous avons réussi à insérer 9 millions de particules. De plus, le profil de vitesse pour 200 000 particules à démontrer que la vitesse minimale de fluidisation (U_{mf}) simulée par CFD-DEM et celle mesurée en laboratoire était identique. Ces résultats préliminaires sont de bon augure pour la suite des recherches.

10.2 Limitations de la solution proposée

La méthodologie développée dans l'article *Experimental Methods in Chemical Engineering : Residence Time Distribution – RTD* est valide dans plusieurs conditions. En effet, toutes les analyses faites sur les instruments annexes au réacteur (spectromètre de masse et les valves) sont exactes pour tout type de réservoirs ou réacteurs, mais uniquement dans l'intervalle de débit sélectionné (10 et 60 $\mathrm{mm\,s^{-1}}$) et à température ambiante. Pour ce qui est de l'étude sur l'effet des traceurs (CO_2, CO, H_2 et CH_4), les résultats sont valides dans un réacteur à lit fluidisé de 8 mm remplit de FCC, avec un débit de 10 $\mathrm{mm\,s^{-1}}$, et à 25 °C.

La concentration des gaz a été mesurée à l'aide du spectromètre de masse. Aucun autre détecteur a été employé, ce qui limite les résultats. En effet, le spectromètre de masse utilisé était très précis et nouveau. Des variations dans les résultats, selon la précision du détecteur manipulé, pourraient être perceptibles.

Une des expériences RTD faisait intervenir une bouteille de gaz ayant des concentrations très faibles : 0.987 % CO, 2.05 % He, 1.93 % Kr, 5.00 % O_2, et la balance de l'argon. Le choix de ces traceurs était primordial, car nous voulions que ceux-ci soient tous indépendants lors de la mesure à l'aide du spectromètre de masse (pas de chevauchement). De plus, cette bouteille de gaz a été conçue pour des travaux futurs où nous voulons expérimenter la RTD avec une réaction $CO + O_2 \rightarrow CO_2$. La problématique est que la concentration est tellement faible que lors de la détection avec le MS, le bruit est quasiment aussi important que la concentration mesurée. Pour obtenir une bouteille avec une concentration plus élevée pour chaque composant, il fallait débourser 20 000 $ et atteindre 6 mois. Donc, les expériences ont été limitées et seulement quelques essais avec un nouveau capillaire ont été faits.

Le nouveau modèle RTD a été codé en Fortran et donc des connaissances sur le sujet sont nécessaires pour l'utiliser. Ceci est une limitation dans le cas où le code veut être partagé

entre chercheurs. L'alternative dans le fichier Excel serait plus conviviale, mais demande un ordinateur très puissant pour résoudre plusieurs traceurs simultanément. La plus grande problématique avec le code Fortran est que les conditions initiales posées doivent être proches de la réalité. Dans le cas contraire, la résolution devient instable et aucun résultat n'est obtenu. Puis, le modèle ne prend pas en considération les situations où un des traceurs à un coefficient de diffusivité très éloigné des autres. Celui-ci devra être résolu indépendamment. Finalement, seulement le mélange de CO_2, CO, H_2 et CH_4 a été confronté au nouveau modèle.

La simulation CFD-DEM est limitée par le temps de calcul. Ainsi, malgré la petite taille du réacteur, il sera nécessaire de diminuer la quantité de catalyseur pour obtenir des résultats. Cela n'est pas un problème, puisque des essais RTD en laboratoire ont été faits avec une hauteur de lit de catalyseur de 11.6 cm au lieu de 18 cm. Donc, il sera possible de comparer l'expérimentation à la simulation CFD-DEM.

10.3 Améliorations et projet futures

À la suite des résultats obtenus dans ce projet de doctorat, plusieurs nouvelles interrogations se sont posées. Une étude du temps de résidence *traditionnelle* se fait à l'aide d'un traceur non réactif. Or, en se basant sur les expériences effectuées, les résultats proposent que les traceurs gazeux sont dépendants les uns les autres et influenceront la RTD. À titre d'exemple, le CO était présent dans 2 bouteilles de gaz et n'avait pas le même temps de résidence en compagnie ou en absence du CO_2 (adsorption). Ainsi, pour la suite, une étude avec des gaz qui réagissent (exemple : oxydation du CO en CO_2) serait intéressante. Cette étude est spécialement conçue pour des systèmes gazeux où plusieurs gaz sont impliqués simultanément.

D'autre part, le projet était très limité au réacteur à lit fluidisé de 8 mm de diamètre. Différentes conditions d'opérations devront être appliquées pour élargir l'intervalle des résultats. Les essais subséquents devront contenir une étude plus approfondie sur la température, la pression, la taille du réacteur et par le fait même la mise à l'échelle. Des études sur les réacteurs à lits fixes seraient aussi à envisager.

Les résultats obtenus dans l'article *Residence Time Distribution : Dispersion, Diffusion, and Adsorption* ont démontré l'effet de la porosité entre le VPOP, VPPC, et VPPE sur la RTD. Une voie à explorer serait l'application de la RTD pour détecter le phénomène de cokage dans les réacteurs à lit fluidisé. En effet, la méthodologie proposée est suffisamment précise pour détecter lorsque les pores d'un catalyseur sont fermés. Ainsi, il serait possible d'analyser, en continu, le cokage directement dans le réacteur en injectant un traceur par *pulse*. Les avantages sont que les résultats sont simultanés et que la réaction n'a pas besoin d'être

arrêtée. Une étude plus approfondie sur le sujet est primordiale.

Il a été démontré dans l'article *Fluidized Bed Hydrodynamic Modelling of CO_2 in Syngas : Distorted RTD Curves Due to Adsorption on FCC* que la température jouait un rôle sur la présence d'adsorption du CO_2 sur le FCC. À haute température (300 °C), aucune adsorption n'était présente. Or, il serait intéressant de refaire les mêmes expériences, mais à basse température soit environ 5 °C. Les deux objectifs seraient de déterminer l'influence de la température sur (1) l'adsorption du CO2 ainsi que sur (2) la différence de diffusivité entre les traceurs.

Puis, le modèle RTD est présentement sous forme d'un code Fortran ou d'un fichier Excel. Il serait intéressant de proposer une solution sur Python pour améliorer la vitesse d'exécution tout en assurant une compréhension simple pour l'utilisateur. De plus, pour valider l'efficacité du modèle dans d'autres conditions, des études RTDs avec un second mélange de gaz adsorbable seraient pertinentes. Dans le même ordre d'idée, des analyses RTD sur la phase liquide pourraient être envisagées pour ensuite être analysées par le nouveau modèle. Cela augmentera significativement les limites d'utilisation du modèle.

Finalement, la simulation CFD-DEM est à poursuivre. L'étude hydrodynamique pour un plus grand nombre de particules et pour le FCC est à faire. De plus, pour simuler la RTD, l'injection d'un traceur gazeux par *pulse* est à développer.

RÉFÉRENCES

[1] W. Resnick et R. White, "Mass transfer in systems of gas and fluidized solids," *Chemical Engineering Progress*, vol. 45, p. 377–390, 1949.

[2] C. Kloss *et al.*, "Models, algorithms and validation for open source DEM and CFD–DEM," *Progress in Computational Fluid Dynamics, an International Journal*, vol. 12, n°. 2, p. 140–152, 2012.

[3] S. Al-Arkawazi *et al.*, "Modeling the hydrodynamic forces between fluid–granular medium by coupling dem–cfd," *Chemical Engineering Research and Design*, vol. 117, p. 439–447, 2017.

[4] W. Zhong *et al.*, "DEM/CFD–DEM Modelling of Non–spherical Particulate Systems : Theoretical Developments and Applications," *Powder Technology*, vol. 302, p. 108–152, 2016.

[5] C. T. Crowe *et al.*, "Multiphase Flows with Droplets and Particles, Second Edition." CRC Press, 2011.

[6] R. MacMullin et M. Weber, "The theory of short-circuiting in continuous flow mixing vessels in series and the kinetics of chemical reactions in such systems," *Transactions of American Institute of Chemical Engineers*, vol. 31, n°. 2, p. 409–458, 1935.

[7] S. Magdalena et P. M. Synowiec, "Study of fluid dynamic conditions in the selected static mixers part ii-determination of the residence time distribution," *Canadian Journal of Chemical Engineering*, vol. 95, p. 2410–2422, 2017.

[8] X. Wang *et al.*, "Mathematical modelling of residence time distribution in tubular loop reactors," *Canadian Journal of Chemical Engineering*, vol. 95, p. 1101–1108, 2017.

[9] M. Escotet-Espinoza *et al.*, "Effect of tracer material properties on the residence time distribution (rtd) of continuous powder blending operations. part i of ii : Experimental evaluation," *Powder Technology*, vol. 342, p. 744–763, 2019.

[10] A. Macchi *et al.*, "Experimental methods in chemical engineering : Micro reactors," *The Canadian Journal of Chemical Engineering*, vol. 97, n°. 11, p. 2383–2394, 2019.

[11] L. Lapidus et N. R. Amundson, "Mathematics of adsorption in beds. vi. the effects of longitudinal diffusion in ion exchange and chromatographic columns," *Journal of Physical Chemistry*, vol. 56, p. 984–987, 1952.

[12] A. Bérard, B. Blais et G. S. Patience, “Experimental methods in chemical engineering : Residence time distribution—RTD,” *Canadian Journal of Chemical Engineering*, vol. 98, n°. 4, p. 848–867, 2020.

[13] C. Analytics, “Web of science core collection.”

[14] N. J. van Eck et L. Waltman, “Software survey : Vosviewer, a computer program for bibliometric mapping,” *Scientometrics*, vol. 84, p. 523–538, 2010.

[15] H. Fogler, “Elements of chemical reaction engineering.” Michigan : Prentice-Hall, 1986.

[16] X. Guo, Y. Fan et L. Luo, “Residence time distribution on flow characterisation of multichannel systems : Modelling and experimentation,” *Experimental Thermal and Fluid Science*, vol. 99, p. 407–419, 2018.

[17] J. Zhang et G. Xu, “Scale-up of bubbling fluidized beds with continuous particle flow based on particle-residence-time distribution,” *Particuology*, vol. 19, p. 155–163, 2015.

[18] C. W. Chan *et al.*, “Particle velocities and their residence time distribution in the riser of a cfb,” *Powder Technology*, vol. 203, n°. 2, p. 187–197, 2010.

[19] J. Adeosun et A. Lawal, “Residence-time distribution as a measure of mixing in t-junction and multilaminated/elongational flow micromixers,” *Chemical Engineering Science*, vol. 65, n°. 5, p. 1865–1874, 2010.

[20] E. Georget *et al.*, “Residence time distributions in a modular micro reaction system,” *Journal of Food Engineering*, vol. 116, n°. 4, p. 910–919, 2013.

[21] F. Yazdanpanah *et al.*, “Effectiveness of purging on preventing gas emission buildup in wood pellet storage,” *The Canadian Journal of Chemical Engineering*, vol. 93, n°. 6, p. 1024–1032, 2015.

[22] M. Menendez *et al.*, “Experimental methods in chemical engineering : Reactors–fluidized beds,” *The Canadian Journal of Chemical Engineering*, vol. 97, n°. 9, p. 2383–2394, 2019.

[23] P. Perreault, E. Robert et G. S. Patience, “Experimental methods in chemical engineering : Mass spectrometry–ms,” *The Canadian Journal of Chemical Engineering*, vol. 97, n°. 5, p. 1036–1042, 2019.

[24] P. V. Danckwerts, “Continuous flow systems : Distribution of residence times,” *Chemical Engineering Science*, vol. 2, n°. 1, p. 1–13, 1953.

[25] M. J. Lorences *et al.*, "Fluid bed gas rtd : Effect of fines and internals," *Powder Technology*, vol. 168, nº. 1, p. 1–9, 2006.

[26] W. Yang, "Handbook of fluidization and fluid-particle systems." Pittsburgh, Pennsylvania, U.S.A. : Marcel Dekker, Inc., 2003, p. 850.

[27] G. Khaled *et al.*, "Simplified correlations of axial dispersion coefficient and porosity in a solid–liquid fluidized bed adsorber," *Experimental Thermal and Fluid Science*, vol. 88, p. 317–325, 2017.

[28] A. Karau *et al.*, "The influence of particle size distribution and operating conditions on the adsorption performance in fluidized beds," *Biotechnology and Bioengineering*, vol. 55, nº. 1, p. 54–64, 1997.

[29] S. D. Kim, H. S. Kim et J. H. Han, "Axial dispersion characteristics in three–phase fluidized beds," *Chemical Engineering Science*, vol. 47, nº. 13, p. 3419–3426, 1992.

[30] J. Kim, G. Han et C. Yi, "Axial dispersion of gas in a circulating fluidized bed," vol. 19, nº. 3, p. 491–494.

[31] R. W. Breault, "A review of gas–solid dispersion and mass transfer coefficient correlations in circulating fluidized beds," *Powder Technology*, vol. 163, nº. 1, p. 9 – 17, 2006.

[32] L. Godfroy, J. Chaouki et F. Larachi, "Position and velocity of a large particle in a gas/solid riser using the radioactive particle tracking technique," *The Canadian Journal of Chemical Engineering*, vol. 77, nº. 2, p. 253–261, 1999.

[33] O. Levenspiel, "Chemical reaction engineering." Toronto : John Wiley & Sons, 1999.

[34] F. Wei *et al.*, "Axial and lateral dispersion of fine particles in a binary–solid riser," *The Canadian Journal of Chemical Engineering*, vol. 76, nº. 1, p. 19–26, 1998.

[35] G. Amos, M. Rhodes et H. Mineo, "Gas mixing in gas—solids risers," *Chemical Engineering Science*, vol. 48, nº. 5, p. 943 – 949, 1993.

[36] R. Alkhaddar *et al.*, "Residence time distribution of a model hydrodynamic vortex separator," *Urban Water*, vol. 3, nº. 1, p. 17 – 24, 2001.

[37] Y. Gao, F. J. Muzzio et M. G. Ierapetritou, "A review of the residence time distribution (rtd) applications in solid unit operations," *Powder Technology*, vol. 228, p. 416 – 423, 2012.

[38] G. McKay, M. Otterburn et J. Aga, "Intraparticle diffusion process occuring during adsorption of dyestuffs," *Water Air Soil Pollut*, vol. 26, p. 381–390, 1987.

[39] S. Sie, "Intraparticle diffusion and reaction kinetics as factors in catalyst particle design," *The Chemical Engineering Journal and the Biochemical Engineering Journal*, vol. 53, n°. 1, p. 1 – 11, 1993.

[40] B. Crittenden et T. W. J., "Adsorption technology and design." Butterworth–Heinemann, 1998.

[41] E. N. Fuller, P. D. Schettler et J. C. Giddings, "New method for prediction of binary gas–phase diffusion coefficients," *Industrial & Engineering Chemistry*, vol. 58, n°. 5, p. 18–27, 1966.

[42] R. fowler, "The mathematical theory of non–uniform gases," *Nature*, vol. 144, n°. 1, p. 993–995, 1939.

[43] P. D. Neufeld, A. R. Janzen et R. A. Aziz, "Empirical equations to calculate 16 of the transport collision integrals for the lennard-jones (12–6) potential," *The Journal of Chemical Physics*, vol. 57, n°. 3, p. 1100–1102, 1972.

[44] C. R. Wilke et C. Y. Lee, "Estimation of diffusion coefficients for gases and vapors," *Industrial & Engineering Chemistry*, vol. 47, n°. 6, p. 1253–1257, 1955.

[45] J. H. Arnold, "Studies in diffusion, i–estimation of diffusivities in gaseous systems," *Industrial & Engineering Chemistry*, vol. 22, n°. 1, p. 1091, 1930.

[46] J. O. Hirschfelder, R. B. Bird et E. L. Spotz, "The transport properties of gases and gaseous mixtures. ii." *Chemical Reviews*, vol. 44, n°. 1, p. 205–231, 1949.

[47] E. N. Fuller, P. D. Schettler et J. C. Giddings, "New method for prediction of binary gas-phase diffusion coefficients," *Industrial & Engineering Chemistry*, vol. 58, n°. 5, p. 18–27, 1966.

[48] R. L. Adams et J. R. Welty, "A gas convection model of heat transfer in large particle fluidized beds," *AIChE Journal*, vol. 25, n°. 3, p. 395–405, 1979.

[49] J. C. Chen, J. R. Grace et M. R. Golriz, "Heat transfer in fluidized beds : design methods," *Powder Technology*, vol. 150, n°. 2, p. 123 – 132, 2005.

[50] A. Drinkenburg et K. Rietema, "Gas transfer from bubbles in a fluidized bed to the dense phase—i. theory," *Chemical Engineering Science*, vol. 27, n°. 10, p. 1765 – 1774, 1972.

[51] H. Vreedenberg, “Heat transfer between a fluidized bed and a horizontal tube,” *Chemical Engineering Science*, vol. 9, n°. 1, p. 52 – 60, 1958.

[52] A. B.R. et G. L.R., “Heat transfer to horizontal tube in shallow fluidized beds,” dans *National Heat Transfer Conference*, St–Louis, USA, 1976.

[53] M. Leva et M. Grummer, “A correlation of solids turnovers in fluidized systems,” *Chem. Eng. Progr.*, vol. 48, n°. 6, p. 307 – 313, 1952.

[54] V. Borodulya *et al.*, “Heat transfer between a surface and a fluidized bed : consideration of pressure and temperature effects,” *International Journal of Heat and Mass Transfer*, vol. 34, n°. 1, p. 47 – 53, 1991.

[55] L. Wender et G. T. Cooper, “Heat transfer between fluidized–solids beds and boundary surfaces–correlation of data,” *AIChE Journal*, vol. 4, n°. 1, p. 15–23, 1958.

[56] D. Wippern *et al.*, “Characterization of fluidized bed reactors with gas tracer measurements,” *Chemical Engineering Communications*, vol. 10, n°. 4–5, p. 307–330, 1981.

[57] J. Yates et J. Constants, “Residence time distributions in a fluidised bed in which gas adsorption occurs : stimulus–response experiments,” *Chemical Engineering Science*, vol. 28, n°. 6, p. 1341–1347, 1973.

[58] P. R. Kasten et N. R. Amundson, “An elementary theory of adsorption in fluidized beds. mathematics of adsorption in beds.” *Industrial & Engineering Chemistry*, vol. 42, n°. 7, p. 1341–1346, 1950.

[59] A. Reichhold et H. Hofbauer, “Internally circulating fluidized bed for continuous adsorption and desorption,” *Chemical Engineering and Processing : Process Intensification*, vol. 34, n°. 6, p. 521–527, 1995.

[60] J. Fan *et al.*, “Research on reactive adsorption desulfurization over ni zno sio2 al2o3 adsorbent in a fixed fluidized bed reactor,” *Industrial & Engineering Chemistry Research*, vol. 49, n°. 18, p. 8450–8460, 2010.

[61] P. Menoud, L. Cavin et A. Renken, “Modelling of heavy metals adsorption to a chelating resin in a fluidized bed reactor,” *Chemical Engineering and Processing : Process Intensification*, vol. 37, n°. 1, p. 89 – 101, 1998.

[62] P. Ammendola, F. Raganati et R. Chirone, “Co2 adsorption on a fine activated carbon in a sound assisted fluidized bed : Thermodynamics and kinetics,” *Chemical Engineering Journal*, vol. 322, p. 302 – 313, 2017.

[63] D. Kunii et O. Levenspiel, “Fluidization engineering,” dans *Fluidization Engineering (Second Edition)*, second edition éd., D. Kunii et O. Levenspiel, édit. Boston : Butterworth–Heinemann, 1991, p. 1 – 491.

[64] N. Frossling, “The evaporation of falling drops,” dans *The Evaporation of Falling Drops*, D. Kunii et O. Levenspiel, édit. Harwell, England : U.K.A.E.A. Research Group, Atomic Energy Research Establishment, 1963, p. 1–59.

[65] W. Ranz, “Friction and transfer coefficients for single particles and pack beds,” *Chemical Engineering Progress*, vol. 48, n°. 5, p. 247 – 253, 1952.

[66] J. F. Davidson et D. Harrison, “Fluidised particles,” dans *Fluidised particles*, U. P. Cambridgde, édit. Cambridge : University Press, 1963.

[67] B. Partridge et R. P.N., “Chemical reaction in a bubbling gas fluidised bed,” *Trans. Inst. Chem. Engrs.*, vol. 44, p. 335–348, 1966.

[68] S. Sit et J. Grace, “Effect of bubble interaction on interphase mass transfer in gas fluidized beds,” *Chemical Engineering Science*, vol. 36, n°. 2, p. 327 – 335, 1981.

[69] K. A. Hweij et F. Azizi, “Hydrodynamics and residence time distribution of liquid flow in tubular reactors equipped with screen-type static mixers,” *Chemical Engineering Journal*, vol. 279, p. 948–963, 2015.

[70] L. Hua, J. Wang et J. Li, “Cfd simulation of solids residence time distribution in a cfb riser,” *Chemical Engineering Science*, vol. 117, p. 264–282, 2014.

[71] G. Patience, “Circulating fluidized beds : Hydrodynamics and reactor modelling,” Thesis, 1990.

[72] S. Mahmoudi, J. Seville et J. Baeyens, “The residence time distribution and mixing of the gas phase in the riser of a circulating fluidized bed,” *Powder Technology*, vol. 203, n°. 2, p. 322 – 330, 2010.

[73] T. Salmi et J. J. Romanainen, “A novel exit boundary condition for the axial dispersion model,” *Chemical Engineering and Processing : Process Intensification*, vol. 34, n°. 4, p. 359 – 366, 1995.

[74] J. Wehner et R. Wilhelm, “Boundary conditions of flow reactor,” *Chemical Engineering Science*, vol. 6, n°. 2, p. 89 – 93, 1956.

[75] O. Levenspiel et W. Smith, "Notes on the diffusion-type model for the longitudinal mixing of fluids in flow," *Chemical Engineering Science*, vol. 6, n°. 4, p. 227–235, 1957.

[76] F. A. G. H. W. W. M. T. Li, Norman N., dans *Advanced Membrane Technology and Applications*. John Wiley & Sons, 2008.

[77] S. Geng *et al.*, "Conditioning micro fluidized bed for maximal approach of gas plug flow," *Chemical Engineering Journal*, vol. 351, p. 110–118, 2018.

[78] W. Letzsch, *Fluid Catalytic Cracking (FCC) in Petroleum Refining*. Cham : Springer International Publishing, 2015, p. 261–316.

[79] K. L. M. Sels, Bert F., "Y zeolites as a major component of fcc catalysts : Main challenges in the modification thereof," dans *Zeolites and Zeolite–Like Materials*. Elsevier, 2016.

[80] M. S. Rigutto, R. van Veen et L. Huve, "Chapter 24 – zeolites in hydrocarbon processing," dans *Introduction to Zeolite Science and Practice*, ser. Studies in Surface Science and Catalysis, J. Čejka *et al.*, édit. Elsevier, 2007, vol. 168, p. 855.

[81] M. J. Lorences *et al.*, "Butane oxidation to maleic anhydride – kinetic modeling and byproducts," *Industrial & Engineering Chemistry Research*, vol. 42, n°. 26, p. 6730–6742, 2003.

[82] N. F. Dummer *et al.*, "Structural evolution and catalytic performance of dupont v-p-o/ sio2 materials designed for fluidized bed applications," *Applied Catalysis A : General*, vol. 376, p. 47–55, 2010.

[83] R. Contractor *et al.*, "A new commercial scale process for n–butane oxidation to maleic anhydride using a circulating fluidized bed reactor," dans *New Developments in Selective Oxidation II*, ser. Studies in Surface Science and Catalysis, V. C. Corberán et S. V. Bellón, édit. Elsevier, 1994, vol. 82, p. 233 – 242.

[84] ——, "Butane oxidation to maleic anhydride over vanadium phosphate catalysts," *Catalysis Today*, vol. 1, n°. 1, p. 49 – 58, 1987.

[85] W. D. J. Cowan, Jack C., "5.1.1.1 physical and chemical properties of silica," dans *Water–Formed Scale Deposits*. Knovel, 1976.

[86] S. M. O. T. J. Pannala, Sreekanth, "10.2 application of cfbs," dans *Computational Gas–Solids Flows and Reacting Systems – Theory, Methods and Practice*. IGI Global, 2011.

[87] W.-C. Yang, dans *Fluidization, Solids Handling, and Processing–Industrial Applications*. William Andrew Publishing/Noyes, 1998.

[88] C. Schaschke, “fluidized catalytic cracker unit (fccu),” dans *Dictionary of Chemical Engineering*. Oxford University Press, 2014.

[89] S. Kawamura et Y. Suezawa, “Mechanism of gas flow in a fluidized bed at low pressure,” *Kagaku Kogaku*, vol. 25, n°. 1, p. 524, 1961.

[90] W. J. Thiel et O. E. Potter, “Slugging in fluidized beds,” *Industrial & Engineering Chemistry Fundamentals*, vol. 16, n°. 2, p. 242–247, 1977.

[91] I. Iliuta *et al.*, “Residence time distribution of the liquid in gas–liquid cocurrent upflow fixed–bed reactors,” *Chemical Engineering Science*, vol. 51, n°. 20, p. 4579–4593, 1996.

[92] A. Rodrigues, L. Zuping et J. Loureiro, “Residence time distribution of inert and linearly adsorbed species in a fixed bed containing "large–pore” supports : applications in separation engineering,” *Chemical Engineering Science*, vol. 46, n°. 11, p. 2765–2773, 1991.

[93] A. Bérard, G. S. Patience et B. Blais, “Experimental methods in chemical engineering : Unresolved cfd-dem,” *The Canadian Journal of Chemical Engineering*, vol. 98, n°. 2, p. 424–440, 2020.

[94] B. Lan *et al.*, “Long-time coarse-grained cfd-dem simulation of residence time distribution of polydisperse particles in a continuously operated multiple-chamber fluidized bed,” *Chemical Engineering Science*, vol. 219, p. 115599, 2020.

[95] S. Wang *et al.*, “Cfd-dem study of the effect of ring baffles on system performance of a full-loop circulating fluidized bed,” *Chemical Engineering Science*, vol. 196, p. 130 – 144, 2019.

[96] P. Khomwachirakul *et al.*, “Simulation of flow and drying characteristics of high-moisture particles in an impinging stream dryer via cfd-dem,” *Drying Technology*, vol. 34, n°. 4, p. 403–419, 2016.

[97] K. Chen *et al.*, “Cfd simulation of particle residence time distribution in industrial scale horizontal fluidized bed,” *Powder Technology*, vol. 345, p. 129 – 139, 2019.

[98] P. Khongprom *et al.*, “Axial gas and solids mixing in a down flow circulating fluidized bed reactor based on cfd simulation,” *Chemical Engineering Science*, vol. 73, p. 8–19, 2012.

[99] D. V. Kalaga *et al.*, “Liquid phase axial mixing in solid–liquid circulating multistage fluidized bed : Cfd modeling and rtd measurements,” *Chemical Engineering Journal*, vol. 191, p. 475 – 490, 2012.

[100] M. Goldschmidt, R. Beetstra et J. Kuipers, “Hydrodynamic modelling of dense gas-fluidised beds : comparison and validation of 3d discrete particle and continuum models,” *Powder Technology*, vol. 142, n°. 1, p. 23 – 47, 2004.

[101] S. Rodríguez-Rojo et M. Cocero, “Supercritical fluidized bed modeling,” *The Journal of Supercritical Fluids*, vol. 50, n°. 1, p. 54 – 60, 2009. [En ligne]. Disponible : http://www.sciencedirect.com/science/article/pii/S0896844609001181

[102] T. Li *et al.*, “Numerical investigation of gas mixing in gas-solid fluidized beds,” *AIChE Journal*, vol. 56, n°. 9, p. 2280–2296, 2010.

[103] D. J. Patil, M. van Sint Annaland et J. Kuipers, “Gas dispersion and bubble-to-emulsion phase mass exchange in a gas-solid bubbling fluidized bed : A computational and experimental study,” *International Journal of Chemical Reactor Engineering*, vol. 1, n°. 1, 2003.

[104] T. Li *et al.*, “Mixing of secondary gas injection in a bubbling fluidized bed,” *Chemical Engineering Research and Design*, vol. 87, n°. 11, p. 1451 – 1465, 2009.

[105] J. Wang, W. Ge et J. Li, “Eulerian simulation of heterogeneous gas–solid flows in cfb risers : Emms-based sub-grid scale model with a revised cluster description,” *Chemical Engineering Science*, vol. 63, n°. 6, p. 1553 – 1571, 2008.

[106] A. Pandit et J. Joshi, “Pressure drop in fixed, expanded and fluidized beds packed columns and static mixers - a unified approach,” *Reviews in Chemical Engineering*, vol. 14, n°. 4-5, p. 321 – 371, 1998.

[107] J. JB, “Solid-liquid fluidised bebs : Some design aspects,” *Chemical Engineering Research and Design*, vol. 61, n°. 3, p. 143–161, 1983.

[108] K. Luo *et al.*, “Computational fluid dynamics–discrete element method investigation of pressure signals and solid back-mixing in a full-loop circulating fluidized bed,” *Industrial & Engineering Chemistry Research*, vol. 56, n°. 3, p. 799–813, 2017.

[109] J. Li et J. Kuipers, “Effect of pressure on gas–solid flow behavior in dense gas-fluidized beds : a discrete particle simulation study,” *Powder Technology*, vol. 127, n°. 2, p. 173

– 184, 2002. [En ligne]. Disponible : http://www.sciencedirect.com/science/article/pii/S003259100200116X

[110] Y. Zhao *et al.*, "Eulerian-lagrangian simulation of distinct clustering phenomena and rtds in riser and downer," *Particuology*, vol. 8, n°. 1, p. 44–50, 2010.

[111] X. Ku, T. Li et T. Lovas, "Cfd–dem simulation of biomass gasification with steam in a fluidized bed reactor," *Chemical Engineering Science*, vol. 122, p. 270 – 283, 2015.

[112] Y.-Q. Zhuang *et al.*, "CFD–DEM modeling of gas–solid flow and catalytic MTO reaction in a fluidized bed reactor," *Computers & Chemical Engineering*, vol. 60, p. 1–16, 2014.

[113] S. Bellan *et al.*, "A cfd-dem study of hydrodynamics with heat transfer in a gas-solid fluidized bed reactor for solar thermal applications," *International Journal of Heat and Mass Transfer*, vol. 116, p. 377 – 392, 2018.

[114] G. S. Patience, J. Chaouki et F. Berruti, "Chapter 10 - gas phase hydrodynamics in circulating fluidized bed risers," dans *Advances in Engineering Fluid Mechanics : Multiphase Reactor and Polymerization System Hydrodynamics*, N. P. Cheremisinoff, édit. Burlington : Gulf Professional Publishing, 1996, p. 255 – 296.

[115] J. Li *et al.*, "Hydraulic performance of winpak-c modular catalytic structured packing," *Canadian Journal of Chemical Engineering*, vol. 94, p. 556–564, 2016.

[116] P. Wojewodka, R. Aranowski et C. Jungnickel, "Residence time distribution in rapid multiphase reactors," *Journal of Industrial and Engineering Chemistry*, vol. 69, p. 370–378, 2019.

[117] D. A. Sievers et J. J. Stickel, "Modeling residence-time distribution in horizontal screw hydrolysis reactors," *Chemical Engineering Science*, vol. 175, p. 396–404, 2018.

[118] R. Andreux *et al.*, "Hydrodynamic and solid residence time distribution in a circulating fluidized bed : Experimental and 3d computational study," *Chemical Engineering and Processing : Process Intensification*, vol. 47, n°. 3, p. 463–473, 2008.

[119] M. Dulle, H. Ozcoban et C. Leopold, "The effect of different feed frame components on the powder behavior and the residence time distribution with regard to the continuous manufacturing of tablets," *International Journal of Pharmaceutics*, vol. 555, p. 220–227, 2019.

[120] L. Vinnett *et al.*, "The use of radioactive tracers to measure mixing regime in semi-autogenous grinding mills," *Minerals Engineering*, vol. 115, p. 41–43, 2018.

[121] M. V. de Velden, J. Baeyens et K. Smolders, "Solids mixing in the riser of a circulating fluidized bed," *Chemical Engineering Science*, vol. 62, n°. 8, p. 2139–2153, 2007. [En ligne]. Disponible : http://www.sciencedirect.com/science/article/pii/S0009250907000395

[122] G. S. Patience, J. Chaouki et G. Kennedy, "Solids residence time distribution in cfb reactors," dans *Circulating Fluidized Bed Technology III*, P. Basu, M. Horio et M. Hasatani, édit. Oxford : Pergamon Press, 1990, p. 599–604.

[123] R. Bader, J. Findlay et T. M. Knowlton, "Gas-solid flow patterns in a 30.5 cm diameter circulating fluidized bed," dans *Circulating Fluidized Bed Technology II*, P. Basu et J. F. Large, édit. New York : Pergamon Press, 1988, p. 123–137.

[124] D. Bai *et al.*, "Residence time distributions of gas and solids in a cfb," dans *Fluidization VII*, O. E. Potter et D. J. Nicklin, édit. New York : Engineering Foundation, 1990, p. 195–202.

[125] D. C. Chesonis *et al.*, "Hydrodynamics and mixing of solids in a recirculating fluidized bed," *Industrial & Engineering Chemistry Research*, vol. 29, n°. 9, p. 1785–1792, 1990.

[126] A. Lyngfelt et B. Leckner, "Residence time distribution of sorbent particles in a circulating fluidized bed boiler," *Powder Technology*, vol. 70, p. 285–292, 1992.

[127] J. Yerushalmi et A. Avidan, "High velocity fluidization," dans *Fluidization*, R. C. J. F. Davidson et D. Harrison, édit. London : Academic Press, 1985, p. 225–229.

[128] F. Berruti *et al.*, "Hydrodynamics of circulating fluidized bed risers : A review," *The Canadian Journal of Chemical Engineering*, vol. 73, n°. 5, p. 579–602, 1995.

[129] Z. Zou *et al.*, "Cfd simulation of solids residence time distribution in a multi-compartment fluidized bed," *Chinese Journal of Chemical Engineering*, vol. 25, n°. 12, p. 1706–1713, 2017.

[130] S. G. Taylor, "Conditions under which dispersion of a solute in a stream of solvent can be used to measure molecular diffusion," *Proceedings of the Royal Society London*, vol. A225, p. 473–477, 1954.

[131] E. T. van der Laan, "Notes on the diffusion-type model for longitudinal mixing in flow (o. levenspiel and w. k. smith)," *Chemical Engineering Science*, vol. 7, p. 187, 1958.

[132] R. Voncken, D. Holmes et H. den Hartog, "Fluid flow in turbine-stirred, baffled tanks–iii : Dispersion during circulation," *Chemical Engineering Science*, vol. 19, n°. 3, p. 209–213, 1964.

[133] G. S. Patience, "Experimental methods in chemical engineering : Preface," *Canadian Journal of Chemical Engineering*.

[134] ——, "Experimental methods and instrumentation for chemical engineers." Amsterdam, Netherlands : Elsevier B.V., 2017.

[135] L. Hua et J. Wang, "Residence time distribution of particles in circulating fluidized bed risers," *Chemical Engineering Science*, vol. 186, p. 168–190, 2018.

[136] S. Deshmukh *et al.*, "Development of a membrane-assisted fluidized bed reactor–1–gas phase backmixing and bubble-to-emulsion phase mass transfer using tracer injection and ultrasound experiments," *Industrial and Engineering Chemistry Research*, vol. 44, n°. 16, p. 5955–5965, 2005.

[137] S. Rodriguez-Rojo, N. Lopez-Valdezate et M. J. Cocero, "Residence time distribution studies of high pressure fluidized bed of microparticles," *The Journal of Supercritical Fluids*, vol. 44, n°. 3, p. 433–440, 2008.

[138] Y. Li *et al.*, "A novel quasi plug-flow reactor design for enzymatic hydrolysis of cellulose using rheology experiment and cfd simulation," *The Canadian Journal of Chemical Engineering*, vol. 96, n°. 3, p. 770–778, 2018.

[139] J. Li et H. Weinstein, "An experimental comparison of gas backmixing in fluidized beds across the regime spectrum," *Chemical Engineering Science*, vol. 44, n°. 8, p. 1697–1705, 1989.

[140] D. Geldart et A. Abrahamsen, "Homogeneous fluidization of fine powders using various gases and pressures," *Powder Technology*, vol. 19, n°. 1, p. 133–136, 1978.

[141] J. Baeyens et D. Geldart, "An investigation into slugging fluidized beds," *Chemical Engineering Science*, vol. 29, n°. 1, p. 255–265, 1974.

[142] L. Blas *et al.*, "Numerical modeling of oxygen carrier performances ($NiO/NiAl_2O_4$) for chemical–looping combustion," *Energies*, vol. 10, n°. 7, p. 864, 2017.

[143] W. Engisch et F. Muzzio, "Using residence time distributions (rtds) to adress the traceability of raw materials in continuous pharmaceutical manufacturing," *J. Pharm. Innov.*, vol. 11, p. 64–81, 2016.

[144] P. A. Reyniers *et al.*, "Computational fluid dynamic design of jet stirred reactors for measuring intrinsic kinetics of gas–phase and gas–solid reactions," *International Journal of Chemical Kinetics*, vol. 48, n°. 9, p. 556–569, 2016.

[145] S. Boroun et F. Larachi, "Residence time distribution of passive scalars in magnetic nanofluid poiseuille flow under uniform rotating magnetic fields," *Chemical Engineering Science*, vol. 224, p. 115770, 2020.

[146] R. Shinnar et D. Rumschitzki, "Tracer experiments and rtd's in heterogeneous reactor analysis and design," *AIChE Journal*, vol. 35, n°. 10, p. 1651–1658, 1989.

[147] P. Biloen *et al.*, "On the activity of fischer–tropsch and methanation catalysts : A study utilizing isotopic transients," *Journal of Catalysis*, vol. 81, n°. 2, p. 450–463, 1983.

[148] G. S. Patience et R. E. Bockrath, "Butane oxidation process development in a circulating fluidized bed," *Applied Catalysis A : General*, vol. 376, n°. 1, p. 4–12, 2010.

[149] G. S. Patience *et al.*, "Pressure calcination of vpo catalyst," *Industrial & Engineering Chemistry Research*, vol. 46, n°. 13, p. 4374–4381, 2007.

[150] R. Bardestani, G. S. Patience et S. Kaliaguine, "Experimental methods in chemical engineering : specific surface area and pore size distribution measurements—bet, bjh, and dft," *Canadian Journal of Chemical Engineering*, vol. 97, n°. 11, p. 2781–2791, 2019.

[151] N. Vargaftik, "Handbook of [physical] [properties] of [liquids] and [gases]." Springer–Verlag Berlin Heidelberg, 1975.

[152] A. K. Mehrotra et G. S. Patience, "Unified entry length for newtonian and power–law fluids in laminar pipe flow," *Canadian Journal of Chemical Engineering*, vol. 68, n°. 4, p. 529–533, 1990.

[153] A. Ostadfar, "Chapter 1 – fluid mechanics and biofluids principles," dans *Biofluid Mechanics*, A. Ostadfar, édit. Academic Press, 2016, p. 1–60.

[154] G. S. Patience et E. Bordes-Richard, "International VPO workshop : Preface," *Applied Catalysis A : General*, vol. 376, n°. 1–2, p. 1–3, 2010.

[155] G. Berhault, "Chapter 10 – metal sulfides : Novel synthesis methods and recent developments," dans *New Materials for Catalytic Applications*, V. I. Parvulescu et E. Kemnitz, édit. Amsterdam : Elsevier, 2016, p. 313–360.

[156] N. Saadatkhah *et al.*, “Experimental methods in chemical engineering : Thermogravimetric Analysis—tga,” *Canadian Journal of Chemical Engineering*, vol. 98, n°. 1, p. 34–43, 2020.

[157] W.-C. Yang, “Bubbling fluidized beds,” dans *Handbook of fluidization and fluid-particle systems*, W.-C. Yang, édit. New York : Marcel Dekker, 2003, ch. 3, p. 63–121.

[158] D. Geldart, “Types of gas fluidization,” *Powder Technology*, vol. 7, p. 285–292, 1973.

[159] G. S. Patience *et al.*, “Oxidation kinetics of carbon deposited on cerium–doped fepo4 during dehydration of glycerol to acrolein,” *Chemical Engineering & Technology*, vol. 35, n°. 9, p. 1699–1706, 2012.

[160] B. J. Ennis *et al.*, “Particle Technology : The legacy of neglect in the United-States,” *Chemical Engineering Progress*, vol. 90, n°. 4, p. 32–43, 1994.

[161] P. G. de Gennes, “Reflections on the mechanics of granular matter,” *Physica A : Statistical Mechanics and Its Applications*, vol. 261, n°. 3, p. 267–293, 1998.

[162] M. van der Hoef *et al.*, “Numerical simulation of dense gas solid fluidized beds : A multiscale modeling strategy,” *Annual Review of Fluid Mechanics*, vol. 40, n°. 1, p. 47–70, 2008.

[163] J. J. Derksen, “Flow–induced forces in sphere doublets,” *Journal of Fluid Mechanics*, vol. 608, p. 337–356, 2008.

[164] ——, “Direct meso–scale simulations of fibres in turbulent liquid flow,” *Canadian Journal of Chemical Engineering*, vol. 88, n°. 4, p. 677–681, 2010.

[165] A. J. C. Ladd, “Numerical simulations of particulate suspensions via a discretized boltzmann – equation .1. theoretical foundation,” *Journal of Fluid Mechanics*, vol. 271, p. 285–309, 1994.

[166] ——, “Numerical simulations of particulate suspensions via a discretized boltzmann – equation .2. numerical results,” *Journal of Fluid Mechanics*, vol. 271, p. 311–339, 1994.

[167] A. Ladd et R. Verberg, “Lattice–boltzmann simulations of particle–fluid suspensions,” *Journal of Statistical Physics*, vol. 104, n°. 5–6, p. 1191–1251, 2001.

[168] R. Glowinski *et al.*, “A distributed lagrange multiplier/fictitious domain method for particulate flows,” *International Journal of Multiphase Flow*, vol. 25, n°. 5, p. 755–794, 1999.

[169] ——, “A fictitious domain approach to the direct numerical simulation of incompressible viscous flow past moving rigid bodies : Application to particulate flow,” *Journal of Computational Physics*, vol. 169, n°. 2, p. 363–426, 2001.

[170] C. Rettinger *et al.*, “Fully resolved simulations of dune formation in riverbeds,” dans *International Supercomputing Conference*. Springer, 2017, p. 3–21.

[171] A. ten Cate *et al.*, “Particle imaging velocimetry experiments and lattice Boltzmann simulations on a single sphere settling under gravity,” *Physics of Fluids*, vol. 14, n°. 11, p. 4012–4025, 2002.

[172] A. Hager *et al.*, “Parallel resolved open source CFD–DEM : Method, validation and application,” *Journal of Computational Multiphase Flows*, vol. 6, n°. 1, p. 13–28, 2014.

[173] B. Blais *et al.*, “A semi–implicit immersed boundary method and its application to viscous mixing,” *Computers and Chemical Engineering*, vol. 85, 2016.

[174] Z. Y. Zhou *et al.*, “Discrete particle simulation of particle-fluid flow : Model formulations and their applicability,” *Journal of Fluid Mechanics*, vol. 661, p. 482–510, 2010.

[175] J. Capecelatro, O. Desjardins et R. O. Fox, “Effect of domain size on fluid–particle statistics in homogeneous, gravity-driven, cluster-induced turbulence,” *Journal of Fluids Engineering*, vol. 138, n°. 4, p. 041301, 2015.

[176] P. Pepiot et O. Desjardins, “Numerical analysis of the dynamics of two– and three–dimensional fluidized bed reactors using an Euler–Lagrange approach,” *Powder Technology*, vol. 220, p. 104–121, 2012.

[177] D. Jajcevic *et al.*, “Large–scale CFD–DEM simulations of fluidized granular systems,” *Chemical Engineering Science*, vol. 98, p. 298–310, 2013.

[178] F. Alobaid, J. Ströhle et B. Epple, “Extended CFD/DEM model for the simulation of circulating fluidized bed,” *Advanced Powder Technology*, vol. 24, n°. 1, p. 403–415, 2013.

[179] X. Yang *et al.*, “Numerical simulation of mixing characteristics of trace sample and bed material in micro fluidized bed reaction analyzer (in chinese),” *J. Chem. Ind. Eng.*, vol. 65, p. 3323–3330, 2014.

[180] V. Salikov *et al.*, “Characterization and CFD–DEM modelling of a prismatic spouted bed,” *Powder Technology*, vol. 270, p. 622–636, 2015.

[181] C. Goniva *et al.*, “Influence of rolling friction on single spout fluidized bed simulation,” *Particuology*, vol. 10, n°. 5, p. 582–591, 2012.

[182] W. Cheng *et al.*, “The diffusion and pollution mechanisms of airborne dusts in fully–mechanized excavation face at mesoscopic scale based on CFD–DEM,” *Process Safety and Environmental Protection*, vol. 104, p. 240–253, 2016.

[183] H. Yu *et al.*, “Mechanisms of dust diffuse pollution under forced–exhaust ventilation in fully–mechanized excavation faces by CFD–DEM,” *Powder Technology*, vol. 317, p. 31–47, 2017.

[184] K. W. Chu *et al.*, “Cfd–dem modelling of multiphase flow in dense medium cyclones,” *Powder Technology*, vol. 193, p. 235–247, 2009.

[185] ——, “CFD–DEM simulation of the gas–solid flow in a cyclone separator,” *Chemical Engineering Science*, vol. 66, p. 834–847, 2011.

[186] V. Scherer *et al.*, “Coupled DEM–CFD simulation of drying wood chips in a rotary drum – Baffle design and model reduction,” *Fuel*, vol. 184, p. 896–904, 2016.

[187] F. Sudbrock *et al.*, “Convective drying of agitated silica gel and beech wood particle beds—experiments and transient dem–cfd simulations,” *Drying Technology*, vol. 33, n°. 15–16, p. 1808–1820, 2015.

[188] J. Azmir, Q. Hou et A. Yu, “Discrete particle simulation of food grain drying in a fluidised bed,” *Powder Technology*, vol. 323, p. 238–249, 2018.

[189] B. Blais *et al.*, “Development of an unresolved cfd–dem model for the flow of viscous suspensions and its application to solid liquid mixing,” *Journal of Computational Physics*, vol. 318, p. 201–221, 2016.

[190] ——, “Cfd–dem simulations of early turbulent solid-liquid mixing : Prediction of suspension curve and just–suspended speed,” *Chemical Engineering Research and Design*, vol. 123, p. 388–406, 2017.

[191] B. Blais et F. Bertrand, “Cfd–dem investigation of viscous solid–liquid mixing : Impact of particle properties and mixer characteristics,” *Chemical Engineering Research and Design*, vol. 118, p. 270–285, 2017.

[192] M. Lassaigne *et al.*, “Experimental investigation of the mixing of viscous liquids and non–dilute concentrations of particles in a stirred tank,” *Chemical Engineering Research and Design*, vol. 108, p. 55–68, 2016.

[193] T. Brosh et A. Levy, "Modeling of Heat Transfer in Pneumatic Conveyer Using a Combined DEM–CFD Numerical Code," *Drying Technology*, vol. 28, n°. 2, p. 155–164, 2010.

[194] J. Neuwirth *et al.*, "CFD–DEM study and direct measurement of the granular flow in a rotor granulator," *Chemical Engineering Science*, vol. 86, p. 151–163, 2013.

[195] J. Capecelatro et O. Desjardins, "An Euler–Lagrange strategy for simulating particle-laden flows," *Journal of Computational Physics*, vol. 238, p. 1–31, 2013.

[196] T. Anderson et R. Jackson, "A fluid mechanical description of fluidized beds," *Ind. Engng. Chem. Fundam.*, vol. 6, p. 527–539, 1967.

[197] "DEM-based models for the mixing of granular materials," *Chemical Engineering Science*, vol. 60, n°. 8, p. 2517–2531, 2005.

[198] "Discrete particle simulation of particulate systems : Theoretical developments," *Chemical Engineering Science*, vol. 62, n°. 13, p. 3378–3396, 2007.

[199] B. Blais *et al.*, "Experimental methods in chemical engineering : Discrete element method—dem," *Canadian Journal of Chemical Engineering*, vol. 97, p. 1964–1973, 2019.

[200] J. X. Bouillard, R. W. Lyczkowski et D. Gidaspow, "Porosity distributions in a fluidized–bed with an immersed obstacle," *American Institute of Chemical Engineers Journal*, vol. 35, n°. 6, p. 908–922, 1989.

[201] D. Gidaspow, "Multiphase flow and fluidization : continuum and kinetic theory descriptions." Academic press, 1994.

[202] J. H. Ferziger et M. Perić, "Computational methods for fluid dynamics." Springer Berlin, 1996.

[203] J. Marshall et K. Sala, "Comparison of methods for computing the concentration field of a particulate flow," *International Journal of Multiphase Flow*, vol. 56, p. 4–14, 2013.

[204] S. Pirker, D. Kahrimanovic et C. Goniva, "Improving the applicability of discrete phase simulations by smoothening their exchange fields," *Applied Mathematical Modelling*, vol. 35, n°. 5, p. 2479–2488, 2011.

[205] J. Monaghan, "Extrapolating b splines for interpolation," *Journal of Computational Physics*, vol. 60, n°. 2, p. 253–262, 1985.

[206] S. Deb et D. K. Tafti, “A novel two grid formulation for fluid–particle systems using the discrete element method,” *Powder Technology*, vol. 246, p. 601–616, 2013.

[207] C. Goniva *et al.*, “An open source CFD–DEM perspective,” dans *Proceedings of OpenFOAM Workshop, Göteborg*, 2010, p. 22–24.

[208] A. S. Simonsen *et al.*, “Trajectory integrated smoothening of exchange fields for discrete phase simulations,” *Computers & Fluids*, vol. 186, p. 15–23, 2019.

[209] L. Rong, K. Dong et A. Yu, “Lattice–boltzmann simulation of fluid flow through packed beds of uniform spheres : Effect of porosity,” *Chemical Engineering Science*, vol. 99, p. 44–58, 2013.

[210] G. Stokes, “On the effect of internal friction of fluids on the motionn of a pendulum,” *Mathematical and Physics Papers*, vol. 3, n°. 1, p. 1880–1905, 1851.

[211] C. Oseen, “Hydrodynamik.” Leipzig, 1927.

[212] L. Schiller et Z. Naumann, “A drag coefficient correlation.” *Z. Ver. Deutsch. Ing.*, vol. 77, n°. 13–14, p. 318–320, 1933.

[213] S. Ergun, “Fluid flow through packed columns,” *Chem. Eng. Prog.*, vol. 48, p. 1179–1184, 1952.

[214] C. Wen et Y. Yu, “A generalized method for predicting the minimum fluidization velocity,” *American Institute of Chemical Engineers Journal*, vol. 12, p. 610–612, 1966.

[215] L. Huilin *et al.*, “Hydrodynamic simulation of gas–solid flow in a riser using kinetic theory of granular flow,” *Chemical Engineering Journal*, vol. 95, n°. 1, p. 1–13, 2003.

[216] R. Ingebo, “Drag coefficients for droplets and solid spheres in clouds accelerating in airstreams,” *NACA TN*, vol. 3762, 1956.

[217] L. Torobin et W. Gauvin, “The drag coefficients of single spheres moving in steady and accelerated motion in a turbulent fluid,” *American Institute of Chemical Engineers Journal*, vol. 7, n°. 4, p. 615–619, 1961.

[218] R. Clift, J. Grace et M. Weber, “Bubbles, drops and particles.” San Diego : Academic Press, 1978.

[219] M. Syamlal et T. J. O’Brien, “Computer simulation of bubbles in a fluidized bed,” *AIChE Symposium Series*, vol. 85, n°. 270, p. 22–31, 1989.

[220] N.-S. Cheng, "Comparison of formulas for drag coefficient and settling velocity of spherical particles," *Powder Technology*, vol. 189, n°. 3, p. 395–398, 2009.

[221] R. Di Felice, "The voidage function for fluid–particle interaction systems," *Int. J. Multiphase Flow*, vol. 20, p. 153–159, 1994.

[222] D. L. Koch et R. J. Hill, "Inertial effects in suspension and porous–media flows," *Annual Review of Fluid Mechanics*, vol. 33, n°. 1, p. 619–647, 2001.

[223] S. Benyahia, M. Syamlal et T. J. O'Brien, "Extension of hill–koch–ladd drag correlation over all ranges of reynolds number and solids volume fraction," *Powder Technology*, vol. 162, n°. 2, p. 166–174, 2006.

[224] R. Beetstra, M. van der Hoef et J. A. M. Kuipers, "Drag force of intermediate reynolds number flow past mono– and bidisperse arrays of spheres," *American Institute of Chemical Engineers Journal*, vol. 53, p. 489–501, 2007.

[225] Y. Chen, J. R. Third et C. Müller, "A drag force correlation for approximately cubic particles constructed from identical spheres," *Chemical Engineering Science*, vol. 123, p. 146–154, 2015.

[226] G. Liu *et al.*, "Cfd–dem simulation of liquid–solid fluidized bed with dynamic restitution coefficient," *Powder Technology*, vol. 304, p. 186–197, 2016.

[227] H. Zbib, "Hydrodynamics analysis of a liquid–solid fluidized bed via cfd–dem simulations, stability analysis, and tomography," Thèse de doctorat, Ryerson University, 2016.

[228] H. Zhu *et al.*, "Discrete particle simulation of particulate systems : Theoretical developments," *Chemical Engineering Science*, vol. 62, n°. 13, p. 3378–3396, 2007.

[229] D. Voir et E. Michaelides, "The effect of the history term on the motion of rigid spheres in a viscous fluid," *Int. J. Multiphase Flow*, vol. 20, n°. 547, 1994.

[230] A. Hjelmfelt et L. Mockros, "Motion of discrete particles in a turbulent fluid," *App. Sci. Res.*, vol. 16, n°. 149, 1966.

[231] P. A. Moreno-Casas et F. A. Bombardelli, "Computation of the basset force : recent advances and environmental flow applications," *Environmental Fluid Mechanics*, vol. 16, n°. 1, p. 193–208, 2016.

[232] T. R. Auton, J. Hunt et M. Prud'homme, "The force exerted on a body inn ann inviscid unsteady nonnuniform rotational flow," *Journal of Fluid Mechanics*, vol. 197, n°. 1, 1988.

[233] F. Odar et W. S. Hamilton, "Forces on a sphere accelerating in a viscous fluid," *Journal of Fluids Mechanics*, vol. 18, n°. 2, p. 302–314, 1964.

[234] J. Hoerner, "Fluid–dynamics drag," *Hoerner Fluid Dynamics*, 1965.

[235] M. Mandø et L. Rosendahl, "On the motion of non–spherical particles at high reynolds number," *Powder Technology*, vol. 202, n°. 1, p. 1–13, 2010.

[236] M. Zastawny *et al.*, "Derivation of drag and lift force and torque coefficients for non–spherical particles in flows," *International Journal of Multiphase Flow*, vol. 39, p. 227–239, 2012.

[237] P. Saffman, "The lift on a small sphere in a slow shear flow," *Journal of Fluid Mechanics*, vol. 22, n°. 2, p. 385–400, 1965.

[238] ——, "Corrigendum to « the lift on a small sphere in a slow shear flow »," *Journal of Fluid Mechanics*, vol. 31, n°. 3, p. 624, 1968.

[239] R. Mei, "An approximate expression for the shear lift on a spherical particle at finite reynolds number," *Int. J. Multiphase Flow*, vol. 18, n°. 1, p. 145–147, 1992.

[240] S. Rubinow et J. Keller, "The transverse force on spinning sphere moving in a viscous fluid," *Journal of Fluid Mechanics*, vol. 11, n°. 3, p. 447–459, 1961.

[241] T. Tanaka, K. Yamagata et Y. Tsuji, "Experiment onn fluid forces on a rotating sphere and spheroid," *Proc. Second KSME–JSME Fluids Engr. Conf.*, vol. 1, p. 366, 1990.

[242] B. Oesterlé et B. Dinh, "Experiments on the lift of a spinning sphere in a range of intermediate reynolds numbers," *Experiments in Fluids*, vol. 25, n°. 1, p. 16–22, 1998.

[243] T. Li *et al.*, "CFD–DEM study of effect of bed thickness for bubbling fluidized beds," *Particuology*, vol. 10, n°. 5, p. 532–541, 2012.

[244] A. Di Renzo et F. P. Di Maio, "Homogeneous and bubbling fluidization regimes in DEM–CFD simulations : Hydrodynamic stability of gas and liquid fluidized beds," *Chemical Engineering Science*, vol. 62, n°. 1–2, p. 116–130, 2007.

[245] T. Tsuji, K. Yabumoto et T. Tanaka, "Spontaneous structures in three–dimensional bubbling gas–fluidized bed by parallel DEM–CFD coupling simulation," *Powder Technology*, vol. 184, n°. 2, p. 132–140, 2008.

[246] C. Wang *et al.*, "Simulation of gas–solid flow in rectangular spouted bed by coupling cfd–dem and les," *Can. J. Chem. Eng.*, vol. 92, n°. 8, p. 1488–1494, 2014.

[247] ——, "Numerical simulation of gas–solid heat transfer behaviour in rectangular spouted bed," *Can. J. Chem. Eng.*, vol. 93, n°. 11, p. 2077–2083, 2015.

[248] M. Saidi *et al.*, "Numerical and experimental investigation of hydrodynamic characteristics of a slot–rectangular spouted bed," *Can. J. Chem. Eng.*, vol. 94, n°. 2, p. 332–339, 2016.

[249] M. Schrader *et al.*, "Design of a cfd–dem–based method for mechanical stress calculation and its application to glass bead–enhanced cultivations of filamentous lentzea aerocolonigenes," *Biochemical Engineering Journal*, vol. 148, p. 116–130, 2019.

[250] J. Derksen, "Simulations of dense agitated solid–liquid suspensions – Effects of the distribution of particle sizes," *Chemical Engineering Science*, vol. 189, p. 56–64, 2018.

[251] J. J. Derksen, "Eulerian–Lagrangian simulations of settling and agitated dense solid–liquid suspensions – achieving grid convergence," *American Institute of Chemical Engineers Journal*, vol. 64, n°. 3, p. 1147–1158, 2018.

[252] R. Sun et H. Xiao, "CFD–DEM simulations of current–induced dune formation and morphological evolution," *Advances in Water Resources*, vol. 92, p. 228–239, 2016.

[253] ——, "SediFoam : A general–purpose, open–source CFD–DEM solver for particle–laden flow with emphasis on sediment transport," *Computers & Geosciences*, vol. 89, p. 207–219, 2016.

[254] J. Derksen, "Assessing Eulerian–Lagrangian simulations of dense solid–liquid suspensions settling under gravity," *Computers & Fluids*, vol. 176, p. 266–275, 2018.

[255] J. J. Derksen, "Eulerian-Lagrangian simulations of settling and agitated dense solid-liquid suspensions - achieving grid convergence," *American Institute of Chemical Engineers Journal*, vol. 64, n°. 3, p. 1147–1158, 2018.

[256] S. Kuang, M. Zhou et A. Yu, "CFD–DEM modelling and simulation of pneumatic conveying : A review," *Powder Technology*, n°. 22, 2019.

[257] T. Brosh, H. Kalman et A. Levy, "DEM simulation of particle attrition in dilute–phase pneumatic conveying," *Granular Matter*, vol. 13, n°. 2, p. 175–181, 2011.

[258] F. Zhou *et al.*, "CFD–DEM simulation of the pneumatic conveying of fine particles through a horizontal slit," *Particuology*, vol. 16, p. 196–205, 2014.

[259] S. B. Kuang *et al.*, "Application of periodic boundary conditions to CFD–DEM simulation of gas–solid flow in pneumatic conveying," *Chemical Engineering Science*, vol. 93, p. 214–228, 2013.

[260] A. Hobbs, "Simulation of an aggregate dryer using coupled CFD and DEM methods," *International Journal of Computational Fluid Dynamics*, vol. 23, n°. 2, p. 199–207, 2009.

[261] G. S. Patience, C. A. Patience et F. Bertrand, "Chemical engineering research synergies across scientific categories," *Canadian Journal of Chemical Engineering*, vol. 96, p. 811–820, 2018.

[262] Clarivate Analytics, "*Web of Science Core Collection*, accessed on 15 may 2019, http ://apps.webofknowledge.com," 2019.

[263] Z. Mansourpour, N. Mostoufi et R. Sotudeh-Gharebagh, "A mechanistic study of agglomeration in fluidised beds at elevated pressures," *Canadian Journal of Chemical Engineering*, vol. 91, n°. 3, p. 560–569, 2013.

[264] S. Wang *et al.*, "Cfd–dem simulation of heat transfer in fluidized beds : Model verification, validation, and application," *Chemical Engineering Science*, vol. 197, p. 280–295, 2019.

[265] S. Yang *et al.*, "Cfd–dem simulation of the spout–annulus interaction in a 3d spouted bed with a conical base," *Canadian Journal of Chemical Engineering*, vol. 92, n°. 6, p. 1130–1138, 2014.

[266] B. Ren *et al.*, "Numerical simulation of spouting of cylindroid particles in a spouted bed," *Canadian Journal of Chemical Engineering*, vol. 92, n°. 5, p. 928–934, 2014.

[267] X. Bao, W. Du et J. Xu, "An overview on the recent advances in computational fluid dynamics simulation of spouted beds," *Canadian Journal of Chemical Engineering*, vol. 91, n°. 11, p. 1822–1836, 2013.

[268] Y. Yue *et al.*, "Particle–scale study of spout deflection in a flat–bottomed spout fluidized bed," *Chemical Engineering Science*, vol. 205, p. 121–133, 2019.

[269] C.-O. S. C. CFDEM, "Dem and cfd," *URL : http ://www. cfdem. com*, 2015.

[270] L. Lu *et al.*, "Assessment of different coarse graining strategies to simulate polydisperse gas–solids flow," *Chemical Engineering Science*, vol. 179, p. 53–63, 2018.

[271] I. M. Krieger et T. J. Dougherty, "A mechanism for non–Newtonian flow in suspensions of rigid spheres," *Transactions of The Society of Rheology (1957–1977)*, vol. 3, n°. 1, p. 137–152, 1959.

[272] E. F. Toro, "Riemann solvers and numerical methods for fluid dynamics : a practical introduction." Springer Science & Business Media, 2013.

[273] D. Kunii et O. Levenspiel, "Fluidization engineering." Amsterdam : Elsevier, 2013.

[274] B. Azeem *et al.*, "Nutrient release characteristics and coating homogeneity of biopolymer coated urea as a function of fluidized bed process variables," *Canadian Journal of Chemical Engineering*, vol. 95, p. 849–862, 2017.

[275] D. King, "Estimation of dense bed voidage in fast and slow fluidized beds of fcc catalyst, in *Fluidization VI*." Oxford : J.R. Grace and L.W. Shemilt and M.A. Bergougnou, Eds., Engineering Foundation, 1989, p. 1–8.

[276] G. S. Patience et R. E. Bockrath, "Drift flux modelling of entrained gas–solids suspensions," *Powder Technology*, vol. 190, p. 412–425, 2009.

[277] J. F. Richardson et W. Zaki, "Fluidization of solid particles in liquids," *Chemical Engineering Progress*, vol. 32, p. 35, 1954.

[278] H. T. Bi *et al.*, "A state–of–the–art review of gas–solid turbulent fluidization," *Chemical Engineering Science*, vol. 55, p. 4789–4825, 2000.

[279] J. Wang *et al.*, "From bubbling to turbulent fluidization : Advanced onset of regime transition in micro–fluidized beds," *Chemical Engineering Science*, vol. 66, p. 2001–2007, 2011.

[280] A. Chehbouni *et al.*, "Effets de differents parametres sur les vitesses de transition de la fluidisation en regime turbulent," *Canadian Journal of Chemical Engineering*, vol. 73, n°. 1, p. 41–50, 1995.

[281] M. Saidi *et al.*, "Numerical and experimental investigation of hydrodynamic characteristics of a slot-rectangular spouted bed," *The Canadian Journal of Chemical Engineering*, vol. 94, n°. 2, p. 332–339, 2016.

[282] M. A. Fakhari *et al.*, "Experimental study of simultaneous removal of co2 and so2 in a spouted bed reactor," *Canadian Journal of Chemical Engineering*, vol. 95, p. 1150–1155, 2017.

[283] G. Tonetto, J. Atias et H. de Lasa, "Fcc catalysts with different zeolite crystallite sizes : acidity, structural properties and reactivity," *Applied Catalysis A : General*, vol. 270, p. 9–25, 2004.

[284] A. Anantharaman, R. A. Cocco et J. W. Chew, "Evaluation of correlations for minimum fluidization velocity (u_{mf}) in gas–solid fluidization," *Powder Technology*, vol. 323, p. 454–485, 2018.

[285] J. Yu *et al.*, "Isothermal differential characteristics of gas–solid reaction in micro–fluidized bed reactor," *Fuel*, vol. 103, p. 29–36, 2013.

[286] ASTM D7743-12, "Standard test method for measuring the minimum fluidization velocities of free flowing powders, astm international," 2012.

[287] M. Leturia *et al.*, "Characterization of flow properties of cohesive powders : A comparative study of traditional and new testing methods," *Powder Technology*, vol. 253, p. 406–423, 2014.

[288] J. M. Rodriguez, T. Edeskar et S. Knutsson, "Particle shape quantities and measurement techniques–a review," *Electronic Journal of Geotechnical Engineering*, vol. 18, n°. Bundle A, p. 169–198, 2013.

[289] I. Gibson *et al.*, "An examination of wen and yu's formula for predicting the onset of fluidisation," *Chemical Engineering Research and Design*, vol. 135, p. 103–111, 2018.

[290] L. Li et W. Ma, "Experimental study on the effective particle diameter of a packed bed with non–spherical particles," *Transport in Porous Media*, vol. 89, p. 35–48, 2011.

[291] J. Liu, J. R. Grace et X. Bi, "Novel multifunctional optical-fiber probe : I. development and validation," *AIChE Journal*, vol. 49, n°. 6, p. 1405–1420, 2003. [En ligne]. Disponible : https://aiche.onlinelibrary.wiley.com/doi/abs/10.1002/aic.690490607

[292] H. Zhang *et al.*, "A novel calibration procedure for a fiber optic solids concentration probe," *Powder Technology*, vol. 100, n°. 2, p. 260 – 272, 1998.

[293] J. Groen *et al.*, "Local bubble porperties in 40 and 80 cm diameter fluidized beds," *AIChE Symp. Ser.*, vol. 93, p. 147, 1997.

[294] H. T. Bi, "A critical review of the complex pressure fluctuation phenomenon in gas–solids fluidized beds," *Chemical Engineering Science*, vol. 62, n°. 13, p. 3473 – 3493, 2007.

[295] J. Ruud van Ommen *et al.*, "Optimal placement of probes for dynamic pressure measurements in large-scale fluidized beds," *Powder Technology*, vol. 139, n°. 3, p. 264 – 276, 2004.

[296] N. Ellis *et al.*, "Hydrodynamics of turbulent fluidized beds of different diameters," *Powder Technology*, vol. 141, n°. 1, p. 124 – 136, 2004.

[297] S. Malcus, G. Chaplin et T. Pugsley, "The hydrodynamics of the high-density bottom zone in a cfb riser analyzed by means of electrical capacitance tomography (ect)," *Chemical Engineering Science*, vol. 55, n°. 19, p. 4129 – 41 388, 2000.

[298] S. Liu *et al.*, "Electrical capacitance tomography for gas-solids flow measurement for circulating fluidized beds," *Flow Measurement and Instrumentation*, vol. 16, n°. 2-3, p. 135–144, 2005.

[299] J. S. Lin, M. M. Chen et B. T. Chao, "A novel radioactive particle tracking facility for measurement of solids motion in gas fluidized beds," *AIChE Journal*, vol. 31, n°. 3, p. 465–473, 1985.

[300] L. Godfroy, G. S. Patience et J. Chaouki, "Radial hydrodynamics in risers," *Industrial & Engineering Chemistry Research*, vol. 38, n°. 1, p. 81–89, 1999.

[301] R. Mabrouk *et al.*, "Scale effects on fluidized bed hydrodynamics," *International Journal of Chemical Reactor Engineering*, vol. 3, n°. 1, 2005. [En ligne]. Disponible : https://www.degruyter.com/view/journals/ijcre/3/1/article-ijcre.2005.3.1.1263.xml.xml

[302] S. Sanaei *et al.*, "Hydrodynamic characteristics of gas–solid fluidization at high temperature," *The Canadian Journal of Chemical Engineering*, vol. 88, n°. 1, p. 1–11, 2010.

[303] N. Mostoufi, G. Kennedy et J. Chaouki, "Decreasing the sampling time interval in radioactive particle tracking," *The Canadian Journal of Chemical Engineering*, vol. 81, n°. 1, p. 129–133, 2003.

[304] P. Agarwal, A. S. Hull et K. S. Lim, "Chapter 12—digital image analysis techniques for the study of bubbling fluidized beds, in *Non–Invasive Monitoring of Multiphase*

Flows." Amsterdam : J. Chaouki and F. Larachi and M. P. Duduković, Eds., Elsevier Science B.V., 1997, p. 407–455.

[305] I. Julian, J. Herguido et M. Menendez, "Particle mixing in a two–section two–zone fluidized bed reactor. experimental technique and counter–current back–mixing model validation," *Industrial & Engineering Chemistry Research*, vol. 52, p. 13 587–13 596, 2013.

[306] J. Westerweel, "Fundamentals of digital particle image velocimetry," *Measurement Science and Technology*, vol. 8, n°. 12, p. 1379–1392, 1997.

[307] J. de Jong *et al.*, "Development and validation of a novel digital image analysis method for fluidized bed particle image velocimetry," *Powder Technology*, vol. 230, p. 193 – 202, 2012.

[308] N. Herzog *et al.*, "A comparative study of different cfd-codes for numerical simulation of gas–solid fluidized bed hydrodynamics," *Computers & Chemical Engineering*, vol. 39, p. 41 – 46, 2012.

[309] J. R. Grace et F. Taghipour, "Verification and validation of cfd models and dynamic similarity for fluidized beds," *Powder Technology*, vol. 139, n°. 2, p. 99 – 110, 2004.

[310] T. Kan, V. Strezov et T. J. Evans, "Lignocellulosic biomass pyrolysis : A review of product properties and effects of pyrolysis parameters," *Renewable and Sustainable Energy Reviews*, vol. 57, p. 1126 – 1140, 2016.

[311] S. Rönsch *et al.*, "Review on methanation – from fundamentals to current projects," *Fuel*, vol. 166, p. 276 – 296, 2016. [En ligne]. Disponible : http://www.sciencedirect.com/science/article/pii/S0016236115011254

[312] Y. Niu, H. Tan et S. Hui, "Ash-related issues during biomass combustion : Alkali-induced slagging, silicate melt-induced slagging (ash fusion), agglomeration, corrosion, ash utilization, and related countermeasures," *Progress in Energy and Combustion Science*, vol. 52, p. 1 – 61, 2016. [En ligne]. Disponible : http://www.sciencedirect.com/science/article/pii/S0360128515300216

[313] N. Koike *et al.*, "Upgrading of pyrolysis bio-oil using nickel phosphide catalysts," *Journal of Catalysis*, vol. 333, p. 115 – 126, 2016. [En ligne]. Disponible : http://www.sciencedirect.com/science/article/pii/S0021951715003504

[314] Z. Chao *et al.*, "Modelling of binary fluidized bed reactors for the sorption-enhanced steam methane reforming process," *The Canadian Journal of Chemical Engineering*, vol. 95, n°. 1, p. 157–169, 2017. [En ligne]. Disponible : https://onlinelibrary.wiley.com/doi/abs/10.1002/cjce.22602

[315] M. Kaarsholm *et al.*, "Phosphorous modified zsm–5 : Deactivation and product distribution for mto," *Chemical Engineering Science*, vol. 62, n°. 18–20, p. 5527–5532, 2007.

[316] J. F. Davidson, "Symposium on fluidisation discussion," *Trans. Inst. Chem. Eng.*, vol. 39, p. 230–232, 1961.

[317] I. Julian *et al.*, "Use of α-shapes for the measurement of 3d bubbles in fluidized beds from two-fluid model simulations," *Powder Technology*, vol. 288, p. 409 – 421, 2016.

[318] A. Gianetto *et al.*, "Fluid catalytic cracking catalyst for reformulated gasolines. kinetic modeling," *Industrial & Engineering Chemistry Research*, vol. 33, n°. 12, p. 3053–3062, 1994.

[319] N. Saadatkhah *et al.*, "Spray dried SiO_2 WO_3/TiO_2 and SiO_2 vanadium pyrophosphate core–shell catalysts," *Powder Technology*, vol. 316, p. 434–440, 2017.

[320] D. Carnevali *et al.*, "Gas–phase fructose conversion to furfural in a microfluidized bed reactor," *ACS Sustainable Chemistry & Engineering*, vol. 6, n°. 4, p. 5580–5587, 2018.

[321] T. Ghaznavi, C. Neagoe et G. S. Patience, "Partial oxidation of d–xylose to maleic anhydride and acrylic acid over vanadyl pyrophosphate," *Biomass and Bioenergy*, vol. 71, p. 285–293, 2014.

[322] D. C. Boffito *et al.*, "Biofuel synthesis in a capillary fluidized bed," *Catalysis Today*, vol. 237, n°. 16, p. 13–17, 2014.

[323] D. C. Boffito, G. B. Manrique et G. S. Patience, "One step cracking/transesterification of vegetable oil : Reaction–regeneration cycles in a capillary fluidized bed," *Energy Conversion and Management*, vol. 103, p. 958–964, 2015.

[324] S. Lotfi, D. C. Boffito et G. S. Patience, "Gas–phase partial oxidation of lignin to carboxylic acids over vanadium pyrophosphate and aluminum–vanadium–molybdenum," *ChemSusChem*, vol. 8, n°. 20, p. 3424–3432, 2016.

[325] M. Dalil *et al.*, "Transient acrolein selectivity and carbon deposition study of glycerol dehydration over WO_3/TiO_2 catalyst," *Chemical Engineering Journal*, vol. 270, p. 557–563, 2015.

[326] C. Briens *et al.*, "Effect of interactions between spray jets on liquid distribution in a fluidized bed," *Canadian Journal of Chemical Engineering*, vol. 95, p. 680–687, 2017.

[327] J. Kopyscinski, T. J. Schildhauer et S. M. A. Biollaz, "Employing catalyst fluidization to enable carbon management in the synthetic natural gas production from biomass," *Chemical Engineering & Technology*, vol. 32, n°. 3, p. 343–347, 2009.

[328] S. Geng *et al.*, "Methane decomposition kinetics over fe2o3 catalyst in micro fluidized bed reaction analyzer," *Industrial & Engineering Chemistry Research*, vol. 57, p. 8413–8423, 2018.

[329] S. Samih *et al.*, "Development of a microwave thermogravimetric analyzer and its application on polystyrene microwave pyrolysis kinetics," *Journal of Analytical and Applied Pyrolysis*, vol. 130, p. 209–215, 2018.

[330] S. Samih et J. Chaouki, "Development of a fluidized bed thermogravimetric analyzer," *AIChE Journal*, vol. 61, n°. 1, p. 84–89, 2015.

[331] M. Latifi et J. Chaouki, "A novel induction heating fluidized bed reactor : Its design and applications in high temperature screening tests with solid feedstocks and prediction of defluidization state," *AIChE Journal*, vol. 61, n°. 5, p. 1507–1523, 2015.

[332] P. Leclerc, J. Doucet et J. Chaouki, "Development of a microwave thermogravimetric analyzer and its application on polystyrene microwave pyrolysis kinetics," *Journal of Analytical and Applied Pyrolysis*, vol. 130, p. 209–215, 2018.

[333] F. Wang *et al.*, "Distinctive hydrodynamics of a micro fluidized bed and its application to gas–solid reaction analysis," *Energy & Fuels*, vol. 32, p. 4096–4106, 2018.

[334] T. Zhou *et al.*, "Study on the combustion and nox emission characteristics of low rank coal in a circulating fluidized bed with post–combustion," *Canadian Journal of Chemical Engineering*, vol. 95, p. 2333–2340, 2017.

[335] L. Dong *et al.*, "Kinetic characteristics of the particles in a dense–phase pulsed fluidized bed for dry beneficiation," *Canadian Journal of Chemical Engineering*, vol. 95, p. 1133–1140, 2017.

[336] M. Latifia, F. Berruti et C. Briens, "Jiggle bed reactor for testing catalytic activity of olivine in bio–oil gasification," *Powder Technology*, vol. 316, p. 400–409, 2017.

[337] D. Barletta et M. Poletto, "Aggregation phenomena in fluidization of cohesive powders assisted by mechanical vibrations," *Powder Technology*, vol. 225, p. 93–100, 2012.

[338] Y. Liu, H. Ohara et A. Tsutsumi, "Pulsation–assisted fluidized bed for the fluidization of easily agglomerated particles with wide size distributions," *Powder Technology*, vol. 316, p. 388–399, 2017.

[339] C. G. Visconti *et al.*, "Kinetics of low–temperature fischer–tropsch synthesis on cobalt catalysts : Are both slurry autoclave and tubular packed–bed reactors adequate to collect relevant data at lab–scale ?" *Canadian Journal of Chemical Engineering*, vol. 94, p. 685–695, 2016.

[340] D. C. Boffito *et al.*, "How do you write and present research well ? 10-state the uncertainty, but not too precisely," *Canadian Journal of Chemical Engineering*, vol. 94, p. 1425–1430, 2016.

ANNEXE A REVUE DE LITTÉRATURE SUR LES RÉACTEURS À LIT FLUIDISÉ

Revue de littérature tiré de : *Experimental Methods in Chemical Engineering : Reactors - Fluidized Beds*[22]

Industry relies on fluidized beds to synthesize chemicals (acrylonitrile, maleic anhydride, titanium dioxide, vinyl chloride)—combust coal, dry powders, and treat waste. Fluidized bed folklore declares that they are hard to scale-up and the gas phase is backmixed. Commercial failures that disregard standard design criteria around powder management, gas/solids injection, and mixing reinforce this belief. However, engineers select fluidized beds for processes that are impractical with conventional technologies to achieve economies of scale for highly exothermic, endothermic, or explosive reactions, for catalysts that deactivate in seconds (or minutes), and for chemistry that requires multiple dosing cycles. Failures are more frequent for these challenging applications. For this reason, researchers study reaction kinetics in fixed beds despite internal mass transfer limitations and axial and radial temperature and concentration gradients.

Fluidized bed hydrodynamics vary with powder properties (particle diameter, size distribution, density, sphericity), operating conditions (gas density, viscosity, temperature, pressure), reactor geometry (diameter, height, mass, grid geometry). The minimum fluidization velocity (U_{mf}) is a property that identifies the transition from the fixed bed regime to the fluidized bed regime and equals the gas velocity at which the upward drag force equals the weight of the powder. At the experimental scale, fluidized beds operate isothermally, solids are completely backmixed, and the gas phase is close to plug flow ($U_{\mathrm{g}} < 3U_{\mathrm{mf}}$). Here, we describe the relationship between powder properties and fluidization quality, list experimental techniques, describe recent applications, and gas phase hydrodynamics and uncertainties.

Introduction

Engineers select fluidized beds to achieve economies of scale for catalytic reactions that are highly exothermic, endothermic, or explosive, for catalysts that deactivate in seconds and minutes, and for chemistry that requires multiple dosing cycles (redox reactions). Together with catalysis, other applications include combustion, filtration of particles, drying, and coating of solid particles.[273,274] Despite the many advantages of the fluidized bed, researchers are reluctant to study kinetics in these reactors, instead favouring fixed bed reactors. Fluid beds

operate isothermally while radial and axial temperature gradients complicate interpreting fixed bed kinetic data ; intraparticle mass transfer resistance is orders of magnitude lower in fluidized bed powders because of the smaller particle size (although, researchers grind pellets to a smaller size to study kinetics in fixed beds) ; solids are completely backmixed, while in fixed beds the oxidation state or coking varies axially and radially ; we sample solids on-line in a fluidized bed but is problematic in fixed beds. However, fixed beds are easier to operate and the gas phase approaches plug flow, while bubbles and solids circulation complicates interpreting kinetic data in a fluidized bed. Furthermore, fluidized beds require more attention with respect to catalyst synthesis and reactor design—grids configuration, cyclones, and filters.

This article is part of a special series dedicated to experimental methods in chemical engineering, each of which first summarizes the general principles of the method, describes the practical aspects, identifies the applications, and finally identifies sources of errors and uncertainty.[133] Here, we highlight the motivation of operating fluidized beds as a means to measure reaction kinetics and discuss fluidization regimes, particle technology, instrumentation, uncertainty, and gas phase hydrodynamics. The predominant research clusters, derived from the keywords of a bibliometric analysis of 4300 articles published in 2016 and 2017, include : pyrolysis and gasification, biomass, combustion and CO_2 capture, simulation, coal, and systems.

Fluidization regimes

In gas-solid fluidized beds, when the pressure drop across the bed exceeds the weight of the bed, the bed continues to expand with increasing gas velocity, and bubble frequency increases. Bed expansion depends on the particle properties and,[158] was the first to classify powders into four categories according to their particle size and density (Figure A.1, bottom). Geldart group A powders, like fluid catalytic cracking catalyst (FCC), are aeratable and the target d_p is on the order of 70 µm with a bulk density of 1000 kg m^{-3}. Sand is a typical group B powder with bulk densities and a particle size of 50 % higher (and more) versus group A powders. Group C powders are cohesive and research in this area is expanding to be able to characterize nanoparticles in catalysis, pharmaceutical, and agronomy—flour and cement are examples of cohesive powders with a lower particle size and density than group A. The group D powders have the greatest particle diameter and generally exceed 1000 µm. Their applications in fluidized bed reactors are limited.

Geldart group A powders reach the minimum fluidization velocity, U_{mf}, and then begin to bubble at velocities approximately $2 \times U_{mf}$ and more. Group B powders transition from the

fixed bed regime immediately to the bubbling regime. Group C powders develop cracks and the bed stratifies. Fluidizing these powders requires an external force like vibration. Gas flows preferentially through a central column that has a porosity greater than 0.98 (Figure A.1, top).

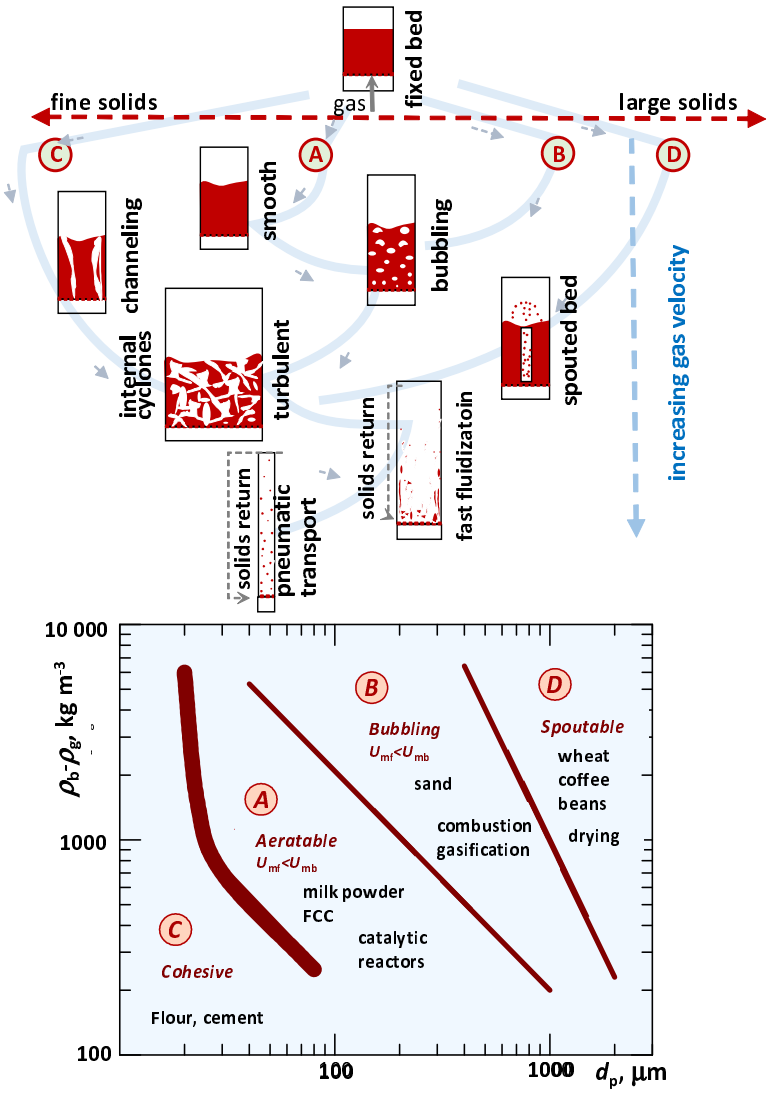

Figure A.1 Sketches showing how the gas velocity determines fluidization regimes for Geldart type A, B, C, and D powders (top), and the Geldart classification diagram (bottom). Adapted from[158] and[273].

Bed expansion and porosity of gas-solids systems depend on superficial velocity, U_g, particle properties, and vessel geometry. The bed expands with increasing fluid velocity to the point where the gas suspends the solids entirely and the upward drag force equals the apparent weight of the bed (the minimum fluidization velocity) : the pressure drop, ΔP, equals the mass of powder in the bed, W (Figure A.2).

Neglecting friction, buoyancy, and interparticle forces, ΔP is the product of the suspension density, ρ, vertical distance between two points, Δz, and gravitational constant.

$$\Delta P = \rho g \Delta z \tag{A.1}$$

The mass of powder in the bed equals the density times the cross-sectional area, X_{A}, and height

$$W = \rho X_{\mathrm{A}} \Delta z \tag{A.2}$$

so, the maximum pressure drop is a function of catalyst mass and geometry.

$$\Delta P = g \frac{W}{X_{\mathrm{A}}} \tag{A.3}$$

The measured pressure drop is slightly below that calculated from Equation (A.3) (green line in Figure A.2) because of the wall and interparticle forces. The pressure drop below the minimum fluidization velocity respects the Ergun equation :

$$\frac{\Delta P}{\Delta Z} = \frac{U_{\mathrm{g}}}{\phi d_{\mathrm{p}}} \frac{1-\epsilon_{\mathrm{v}}}{\epsilon_{\mathrm{v}}^3} \left(150(1-\epsilon_{\mathrm{v}}) \frac{\mu}{\phi d_{\mathrm{p}}} + 1.75 \rho_{\mathrm{g}} U_{\mathrm{g}} \right) \tag{A.4}$$

where U_{g} is the superficial gas velocity, ϵ_{v} is the void fraction, d_{p} is the average particle diameter, μ is the fluid viscosity, ρ_{g} is the gas density, and ϕ is the sphericity.

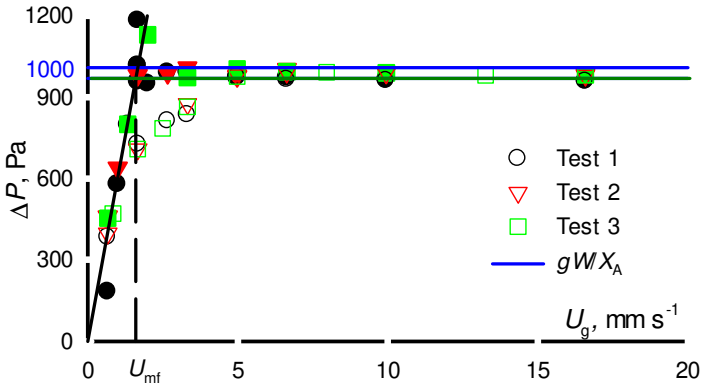

Figure A.2 Fluidization curve for fluid catalytic cracking catalyst (FCC—Geldart group A powder). The hollow symbols represent the pressure drop while increasing the gas flow rate from zero (descending), while the ascending filled symbols represent the pressure drop while increasing the gas velocity. The intersection of the linear portion of the descending pressure drop line (black line starting at (0,0)) and the horizontal descending green line is the the minimum fluidization velocity, U_{mf}.

Although the bed expands to its maximum height near U_{mf}, bubbles appear up to $U_{\mathrm{mb}} = 2 \times U_{\mathrm{mf}}$ and more for aeratable particles like flour—Geldart group A. For powders like sand that have a higher bulk density and/or larger average particle size, d_{p}, $U_{\mathrm{mb}} = U_{\mathrm{mf}}$ (Figures A.1 and A.3).[158] Bubbles transport a volume of gas that corresponds to to the excess gas that fluidizes the best at U_{mf}. The choice of the reactor diameter affects the value of U_{mf} (Figures A.3a and A.3b). We compared the fluidization of two reactors—internal diameter 8 mm, microreactor, and 22 mm. The same height of sand, 30 cm, was kept for the two reactors. The average of U_{mf} for the microreactor is 125 % higher than the other. The values procured with the larger reactor concord with a recent study with a similar reactor and sand powder.[77] So, wall effects in a microreactor have an important influence on the U_{mf} value.

Above U_{mf}, the bed acts like a fluid :

a) the surface of the bed remains horizontal when the vessel is tilted ;

b) the solids bed height equalizes when two vessels are fluidized above U_{mf} operating at the same U_{g} ;

c) the solid empties through a hole in the wall ; and

d) a solid object will float or sink in a fluidized bed depending if its density is greater than or less than the operating bed density, ρ.

The mass flux carried upward through the spout increases with gas velocity and a fountain forms as the solids escape the bed. For group A and B powders, bubbles disintegrate and form streamers that coalesce and break apart at a high frequency in the turbulent fluidization regime (Figure A.1, top). Cyclones are sufficient to return the solids to the bed, but at higher gas velocities, the solids entrainment rate becomes unmanageable with cyclones and additional vessels are required to circulate the solids back to the bed. The higher fluidization regimes are known as fast fluidization and pneumatic conveying. In gas-solids systems, the bed porosity, ϵ_{gs}, increases with gas velocity according to :

$$\epsilon_{\mathrm{gs}} = \frac{U_{\mathrm{g}} + 1}{U_{\mathrm{g}} + a} \tag{A.5}$$

where a equals 2 for FCC powder and is 1.7 for the vanadium pyrophosphate catalyst.[275,276] For liquid–solids systems, bed porosity, ϵ_{ls}, increases to the power $1/n$ with velocity, u_{l} :[277]

$$\frac{u_{\mathrm{l}}}{u_{\mathrm{i}}} = \epsilon_{\mathrm{ls}}^{n} \tag{A.6}$$

where u_{i} is a parameter and n depends on particle properties, vessel diameter, and Reynolds' terminal velocity. Applications include ion-exchange and biological reactions with immobili-

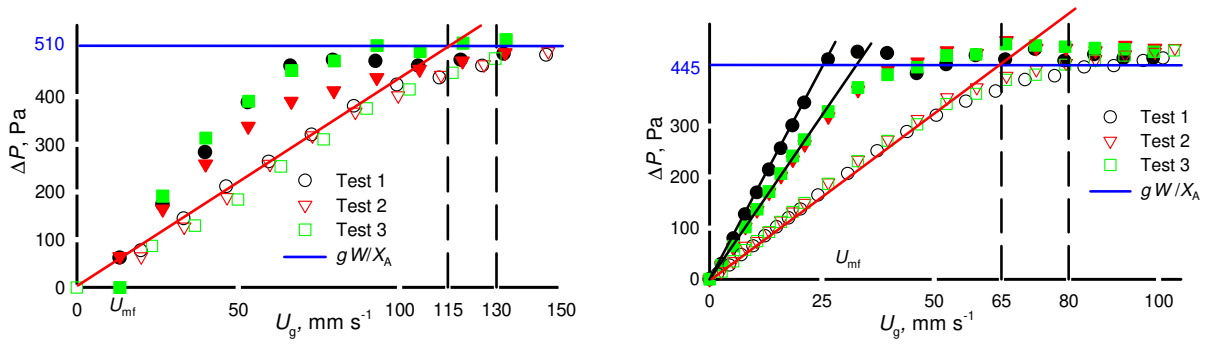

(a) (b)

Figure A.3 Fluidization curves for sand (Geldart group B powder). The intersection of the diagonal red line starting from (0,0) with the horizontal line (representing the weight of the solids) approximates U_{mf} : (a) 8 mm ID reactor with $115\,\mathrm{mm\,s^{-1}} < U_{\mathrm{mf}} < 130\,\mathrm{mm\,s^{-1}}$; and (b) 22 mm ID reactor with $65\,\mathrm{mm\,s^{-1}} < U_{\mathrm{mf}} < 80\,\mathrm{mm\,s^{-1}}$.

zed cells.[?]

The turbulent fluidization regime favours heat and mass transfer while maintaining plug flow like gas-phase hydrodynamics. The critical velocity, U_{c}, differentiates the bubbling regime from turbulent regime and researchers estimate its value via visual observation, bed expansion, absolute and differential pressure fluctuations, local solid fraction fluctuations and the heterogeneity index.[278,279] Based on a soft-sphere discrete particle model, U_{c} depends on reactor diameter, D_{reactor} and the Archimedes number, N_{Ar} :[279,280]

$$\frac{U_{\mathrm{c}}}{\sqrt{gD_{\mathrm{t}}}} = 0.463 N_{\mathrm{Ar}}^{0.145} \tag{A.7}$$

where

$$N_{\mathrm{Ar}} = \frac{d_{\mathrm{p}}^3 \rho_{\mathrm{g}} (\rho_{\mathrm{p}} - \rho_{\mathrm{g}}) g}{\mu^2} \tag{A.8}$$

Most commercial catalytic reactors operate with Geldart group A powders, whereas pyrolytic and thermal reactions operate with group B powders. Interest in cohesive powders is increasing as more research groups attempt to work with nano-particles and large reactors may operate with coarse group D powders, often in spouted beds.[281,282] To characterize the reaction kinetics of catalysts, most fluidized bed reactors operate in the bubbling regime and often within 2–3 $\times\, U_{\mathrm{mf}}$.

Powder characterization

Every paper that works with fluidized beds must describe the particle properties (Table A.1). This basic data helps readers understand the context of the work at a glance and includes minimum fluidization velocity, particle density, and size distribution (PSD). Papers describing a catalyst must include specific surface area, s_A, specific pore volume, v_{pore}, and pore diameter, d_{pore}.

Table A.1 Powder properties. Fifteen graduate students and interns generated the database. They conducted the tests with no prior instruction and repeated U_{mf} and density measurements at least 3 times. †FCC catalysts include a variety of compositions and particle properties[283]

Property	FCC†		Sand		n	Comment
	value	s	value	s		
U_{mf} [mm s^{-1}]	2.2	0.7	120	10	3	$D_{reactor} = 8$ mm
ρ_b [kg m^{-3}]	905	10	1445	52	70	Scott density
	911	15	1407	26	48	poured density
	1003	32	1537	39	48	tapped density
	945		1426		1	Hg porosimetry
ρ_p [kg m^{-3}]	1610		2279		1	Hg porosimetry
ρ_{sk} [kg m^{-3}]	2360	2	2665	1	9	gas pycnometer
ϵ_v	0.44		0.37		1	
H_r	1.10	0.04	1.09	0.03	48	Hausner ratio
θ_{ang} [°]	25	7	29	5	45	angle of repose
d_{10} [µm]	34.5	0.1	200	10	3	laser diffraction
d_{50} [µm]	55.7	0.6	306	9	3	laser diffraction
d_{90} [µm]	89	1	467	9	3	laser diffraction
ϕ	0.99		0.68		1	Ergun equation
s_A [m^2 g^{-1}]	237		0.56		1	BET
	27		0.41		1	BJH
v_{pore} [mL g^{-1}]	0.22	1	0.003		1	BET
d_{pore} [nm]	3.1	1	21		1	BET, BJH

U_{mf}—**minimum fluidization velocity**— Since 1950, researchers have developed 100 correlations to predict how it varies with particle properties, operating conditions, and reactor geometry.[284] This property is the basis for many hydrodynamic models. We select operating superficial velocity, U_g, as a function of U_{mf}.[285] Below U_{mf}, the bed is analogous to a fixed bed. To achieve sufficiently high mixing and heat transfer rates,

while maintaining small bubbles and minimizing bypassing, we recommend operating U_g at least $> 1.5 \times U_{mf}$ (but higher gas velocities might be appropriate for Geldart A powders versus Geldart B powders). In small diameter reactors ($D_t < 0.1\,m$, for example) bubbles coalesce to form slugs that take up the entire cross-section with increase U_g. The effect of slugs on gas-solids contacting is uncertain.

The ASTM standard details a method to measure U_{mf} but despite the detailed procedure, predictions of the 100 correlations vary by over an order of magnitude.[286] Sixteen graduate students measured the U_{mf} for FCC powder in a 8 mm diameter quartz tube with ambient air as the fluidizing gas. The mean minimum fluidization velocity was $2.2\,mm\,s^{-1}$ with an uncertainty $\Delta_{Umf} = 32\,\%$. Selecting the slope of the ascending pressure drop curve for group B powders has an uncertainty of 16 %, which translates to a velocity of $5\,mm\,s^{-1}$ close to an order of magnitude greater than FCC.

Bulk Density, ρ_b, defines how much solids will fit into a given reactor volume. We poured 100–150 g of powder into a 100 mL graduated cylinder and measured the mass on a high precision balance to determine the poured density. It correlates well with both the Scott density and bulk density from mercury porosimetry. The standard deviation was lower than ±2 % except for the Scott density of the sand that was ±5 % due to a large dispersion in his shape (Figure A.4).

Particle density, ρ_p, is the basis of correlations to characterize fluidized bed hydrodynamics, including: bed void fraction (ϵ_v, ϵ_{mf}), particle terminal velocity (V_t), minimum fluidization velocity, and slip velocity ($U_{sl} = U_g - V_t$). The particle density is:

$$\rho_p = \frac{\rho_b}{1 - \epsilon_v} \tag{A.9}$$

Skeletal density, ρ_{sk}, is the true density of the material without intra and interparticle voids and we calculate it from the bulk density and intra particle void fraction, ϵ_{sk}:

$$\rho_{sk} = \frac{\rho_p}{1 - \epsilon_{sk}} \tag{A.10}$$

This is the true density of the solid and we measure it with Hg and gas porosimetry. High pressure forces Hg into connected channels and pores:

$$d_{pore} = -4\gamma \cos\theta_c / P \tag{A.11}$$

where d_{pore} is the pores diametre, γ is the surface tension of Hg, θ_c is the contact angle, and P is the applied pressure: Hg penetrates 3 nm pores at 40 MPa.

Hausner ratio, H_r, is the quotient of the poured density to the tapped density, $H_r =$

$\rho_{\text{poured}}/\rho_{\text{tapped}}$. Values greater than 1.4 indicate that the powder is cohesive and thus the flowability will be poor (Geldart group C powder), while values less than 1.25 ensure that the powder flows freely (group A powders).[287] After measuring the poured density in the 100 mL graduated cylinder, we tapped the side of the glass cylinder with a pen or wooden handled brush until the solids no longer compacted. Like for the poured density, the tapped density standard deviation was ±2 %. The Hausner ratio was within ±3 %.

Angle of repose, θ_{r} , is another measure of flowability. When powder piles up on a flat surface, it forms a cone and the angle it forms with respect to the horizontal plane is called the angle of repose. The coefficient of static friction, μ_{s}, equals $\tan\theta_{\text{r}}$. In this test, powder poured out of a graduated cylinder a couple of cm from the table top until the diameter of the circle it formed reached 100 mm. The angle of repose of the FCC was higher than for the sand with a similar standard deviation, so we expect that the FCC would flow better.

PSD—Particle size and distribution— is a parameter equally important as density to classify powders. Catalytic reactors operate best with 70 µm powders, a wide particle size distribution, and as much as 35 % fines (20 µm $< d_{\text{p}} <$ 44 µm).[148] Depending on the application, we assign a particle diameter based on either a number mean or a mass mean. Since the distribution is equally as important as the diameter, we include d_{10}, d_{50}, d_{90}, the particle diameter at which 10 % have a diameter less than this value, the median particle diameter with respect to mass, and the diameter at which 10 % of the particles have a larger diameter, respectively.

Sphericity, ϕ, is a coefficient we apply to a particle diameter that represents how much its geometry deviates from a perfect sphere: $\phi = 1$ for spheres and $\phi = 0.84$ for cubes. Catalysts in fluidized beds become rounded with time, but in experimental reactors with short run times, they are more often angular polyhedrons (cuboids). Researchers synthesize catalysts, form pellets, then break up the pellets to 60 µm to 200 µm. FCC catalyst is spray dried and so its shape is spherical and ϕ approaches 1 (Figure A.4a), while the sand is a mixture of angular chunks and rounded particles, so ϕ is less than 0.9 (Figure A.4b). The crushed particles have angular shapes and a full characterization considers sphericity, surface texture, and particle corner roundness.[288] We derive ϕd_{p} from the descending data of U_{mf} tests: Ergun's equation (Equation A.4) applies in the fixed bed regime below U_{mf} and since:

$$\frac{150\mu(1-\epsilon_{\text{v}})}{\phi d_{\text{p}}} >> 1.75\rho_{\text{g}}U_{\text{g}}, \tag{A.12}$$

then:

$$\phi d_{\mathrm{p}} = 12.2 \left[\frac{U_{\mathrm{g}}}{\mathrm{d}P/\mathrm{d}z} \frac{(1-\epsilon_{\mathrm{v}})^2}{\epsilon_{\mathrm{v}}^3} \mu \right]^{1/2} \tag{A.13}$$

and the uncertainty (see section *Sources of error*) is (assuming that $\Delta\mu$ is zero):

$$\frac{\Delta_{\phi d_{\mathrm{p}}}}{\phi d_{\mathrm{p}}} = \sqrt{\left(\frac{1}{2}\frac{\Delta_{U\mathrm{g}}}{U_{\mathrm{g}}}\right)^2 + \left(\frac{1}{2}\frac{\Delta_{\mathrm{d}P/\mathrm{d}z}}{\mathrm{d}P/\mathrm{d}z}\right)^2 + \left(\frac{\Delta_{(1-\epsilon_{\mathrm{v}})}}{(1-\epsilon_{\mathrm{v}})}\right)^2 + \left(\frac{3}{2}\frac{\Delta_{\epsilon}}{\epsilon_{\mathrm{v}}}\right)^2} \tag{A.14}$$

We define sphericity as the ratio of the surface area of a sphere that has the same volume of the particle, A_{sp}, to the surface area of the particle, A_{p}:

$$\phi = \frac{A_{\mathrm{sp}}}{A_{\mathrm{p}}} = \frac{\pi^{\frac{1}{3}}(6V_{\mathrm{p}})^{\frac{2}{3}}}{A_{\mathrm{p}}} \tag{A.15}$$

For a wide range of particle types and sizes, the sphericity is a function of ϵ_{mf}:[214]

$$\frac{1-\epsilon_{\mathrm{mf}}}{\phi^2\epsilon_{\mathrm{mf}}^3} = 11; \quad \frac{1}{\phi\epsilon_{\mathrm{mf}}^3} = 14 \tag{A.16}$$

A better correlation for irregular shaped sieved alumina is ($\phi = 0.77$):[289]

$$\frac{1-\epsilon_{\mathrm{mf}}}{\phi^2\epsilon_{\mathrm{mf}}^3} = 12.2 \tag{A.17}$$

For irregular shaped particles and mixtures of particle shapes (spheres and cylinders, for example) and sizes, the ideal particle size is the product of the shape factor and the Sauter mean diameter, d_{sv}.[290] So, to apply the Ergun equation, we substitute ϕd_{p} with the Sauter mean diameter—the ratio of the particle volume, V_{p}, and particle surface area, A_{p}:

$$d_{\mathrm{sv}} = 6\frac{V_{\mathrm{p}}}{A_{\mathrm{p}}} \tag{A.18}$$

Surface area, s_{A}, is the property that researchers maximize to ensure that molecules from the gas phase adequately contact the active phase. Bulk catalysts have lower surface than catalysts grafted to zeolites and other high surface area supports. Changes in surface area with time correlate with changes in the catalyst performance. Hg ($d_{\mathrm{pore}} > 300\,\mathrm{nm}$) and N_2 ($d_{\mathrm{pore}} < 300\,\mathrm{nm}$) porosimetry measure surface area.

Pore volume, v_{pore}, like surface area is an excellent indicator of how micro pores change with conditions (as well as d_{pore}). These characteristics are measured in parallel with the surface area.

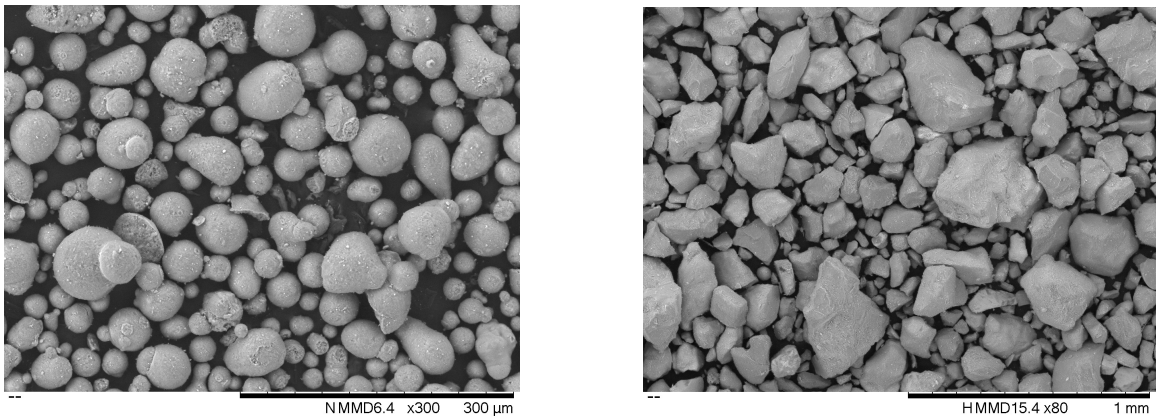

(a) (b)

Figure A.4 SEM image of catalyst: (a) FCC, most particles are spheroids but some are fractured and others form agglomerates; and (b) sand, the larger particles are cuboids while some of the smaller particles are spheroids.

Characterization techniques

Chemical engineers scale-up fluidized bed reactors to commercial scale and so rather than studying these reactors as an analytical technique, they are the object of study. The analytical techniques to study the hydrodynamic conditions include (Table A.2):

Optical probes inserted in the bed measure reflected or transmitted light intensity. When the probe is larger than the particle, it detects all particles and evaluates solids concentration. When the probe is smaller than the particle diameter, it estimates velocity.

Pressure measurements are easy, inexpensive, and widely applied in experimental and commercial facilities. Time averaged pressure difference at two heights assesses bed density, while sampling at high frequency determines fluidization quality.

Tomography is a non-intrusive technique that reconstructs the distribution of the phases and the bed cross-section, slice-by-slice. The principle is based on discriminating between the physical properties of the phases. Electric capacitance tomography (ECT) differentiates the solids phase from the gas based on the powder's dielectric constant: electrodes around the bed circumference measure capacitance. NaI scintillating detectors measure photons transmitted through the bed in x-ray and γ-ray tomography, which is slower than ECT but has a higher spatial resolution.

Particle tracking identifies the position of tracer particles with time. Tracers match either the fluid properties (continuous phase) or the particle properties (dispersed

Table A.2 Fluidized bed measurement techniques

Technique	Principle	Observations
Optical probes[291,292,293]	fibres immersed in bed	calibration problematic
Pressure[294,295,296]	ΔP between two point	applied in industry time-averaged or time-resolved
Tomography[297,298]	Electric capacitance (ECT) (dielectric particles)	fast temporal resolution high T or P excluded poor spatial resolution image reconstruction
	X/γ-ray tomography (RPT)	photons travel through bed slower than ECT better spatial resolution than ECT
Particle[299,300,301] tracking[302,303]	radioactive particles multiple γ-detectors	computer automated (CARPT) characterizes 3D beds
Optics[304,305]	optical, magnetic phosphorescent particles	requires digital image analysis
Image analysis[306,307?]	particle image velocimetry	transparent, 2D, or dilute systems digital image analysis extracts data

phase). In radioactive particle tracking (RPT), NaI scintillator detectors surround the vessel. To construct images from data generated with phosphorescent, optical, or magnetic particles requires digital image analysis (DIA) software.

Particle image velocimetry (PIV): Ultrafast high resolution cameras record images of an illuminated bed. DIA software identifies particles and bubbles displacement from one image to the next. The analysis includes pattern recognition algorithms to treat the data statistically to derive the hydrodynamic parameters.

Computational fluid dynamics (CFD) develops models to predict fluid-particle interactions.[308] Advances in computational resources have accelerated resolving the fluid dynamic equations, but challenges regarding CFD validation remain.[309]

Applications

In 2016 and 2017, fluidized beds appeared in 4135 articles indexed by the Web of Science Core Collection (WoS).[13] VOSViewer generated a bibliometric from the keywords of these articles (Figure A.5) and identified five clusters of research:[14] gasification and pyrolysis (blue), combustion and CO_2 capture (red), simulation and hydrodynamics (green), biomass (or-

ange), and coal (magenta). WoS assigned almost half the articles to the chemical engineering category (1953), followed by energy & fuels (1497), environmental engineering (407), environmental sciences (340), and thermodynamics (307). Surprisingly, physical, multidisciplinary, and applied chemistry have so few articles with fluidized beds even though these categories have the greatest synergy with chemical engineering (other than energy & fuels).[261] However, the distribution is consistent with the instrumentation and mathematical bibliographic map that clusters fluidized beds with modelling rather than either particle technology or catalyst characterization.[133]

Powder Technology published 310 articles related to fluidized beds, followed by *Energy & Fuels* (266), *Fuel* (159), *Chemical Engineering Journal* (125), and *International Journal of Hydrogen Energy* (115). The three top cited manuscripts were reviews of lignocellulosic biomass pyrolysis (with 146 citations),[310] then methanation (128 citations),[311] and ash generated from biomass combustion (98 citations).[312] The top 11 cited publications were reviews and the *Journal of Catalysis* published the most cited article (49 citations), which applied nickel phosphide catalysts to upgrade pyrolysis bio-oil.[313] During this period *Can. J. Chem. Eng.* published 22 articles on fluidized beds and the top 3 concentrated on modelling: hydrodynamics of slot-rectangular spouted beds,[281] sorption enhanced steam methane reforming in binary fluidized beds,[314] and scale-up dimensionless groups derived from non-invasive measurements.[?] The three articles in *Can. J. Chem. Eng.* belong to the green cluster and were cited much less than the review articles in the blue, red, and orange clusters that are in the centre of the network.

Uncertainty

The solids phase in fluidized beds is perfectly backmixed to some extent, radial concentration gradients are negligible, and the bed operates isothermally. These characteristics simplify interpreting kinetic data compared to fixed beds, which have thermal, axial, and radial concentration gradients.[315] The largest uncertainty around fluidized bed reactors as an analytical technique is the gas-solids contacting. Gas passes through the bed as bubbles at velocities, U_b, several times greater than the superficial gas velocity (Figure A.6).

$$U_\mathrm{b} = 0.71\sqrt{g d_\mathrm{b}} \tag{A.19}$$

where d_b is the bubble diameter. Bubbles are formed near the distributor, grow, coalesce, collapse, and erupt at the bed surface. They drag a wake of solids upward and reacting species traverse a cloud of circulating gas around the bubble.[316] An 8 mm bubble rises at

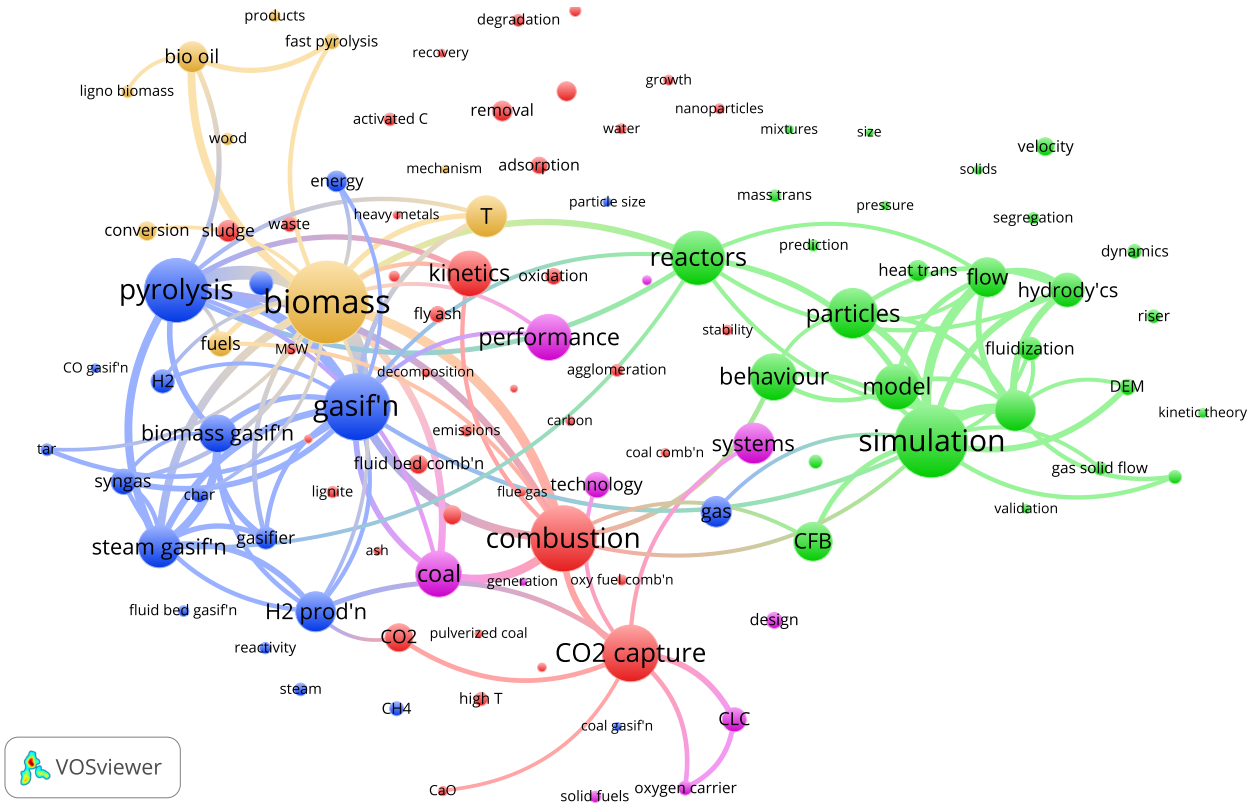

Figure A.5 Bibliometric map of keywords. VOSViewer generated the network from 4300 articles WoS indexed in 2016 and 2017.[13,14] The number of occurrences of each keyword is proportional to the size of the font and circle. Biomass appeared in 465 articles, followed by simulation (408), gasification (377), combustion (372), and pyrolysis (361). The fewest occurrences of the top 100 keywords include ash (48) and heavy metals (48), which belong to the smallest circles and font size. Colour clusters are topics that are closely related and the linked lines are subjects.

$20\,\mathrm{mm\,s^{-1}}$, which is an order of magnitude higher than U_{mf} of the FCC powder.

Bubbles, gas bypassing, and the notion that the gas phase is backmixed have limited the adoption of fluid bed reactors as a tool to measure catalytic reaction kinetics, despite their superior solids mass transfer and heat transfer characteristics.

CFD modelling characterizes the bubble hydrodynamics in both 2-D and 3-D (Figure A.6).[317] The configuration in the figure is a two-zone two-section fluidized bed with a second feed midway up the bed and a change in the cross section in a middle point at this point. The bubble growth here is different than conventional reactors with a single feed point at the entrance and a constant cross-section. While 2-D experimental studies demonstrate how bubbles change with height,[305] 3-D CFD simulation predictions shows that the bubble size in a 3-D bed will have a different evolution.[317]

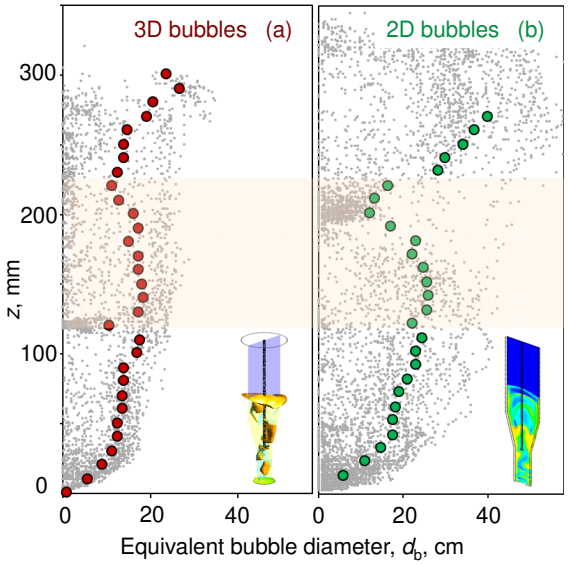

Figure A.6 CFD model of a two-zone two-section fluidized bed reactor: (a) 3-D; and (b) 2-D. The gas velocity at the grid is $2.5 \times U_{\mathrm{mf}}$ and $D_{\mathrm{t}} = 4\,\mathrm{cm}$. The upper zone diameter is 8 cm and begins 12 cm above the grid. The flow rate through the sparger to the upper section (beige section of the image), feeds enough gas so the velocity in the flanged section is the same in the straight section below —$U_{\mathrm{g}}/U_{\mathrm{mf}} = 2.5$. The red dots in (a) and the green dots in (b) represent the mean bubble size along the vertical axis. The gray dots represent individual bubble sizes derived from the simulation. The images in the bottom right of each figure depict the CFD simulations based on the alpha-shape method.

Limitations

For catalytic reactions, the major impediment of fluidized bed process development is synthesizing and testing catalysts, and characterizing gas phase hydrodynamics—particularly maximizing gas-solids contacting and minimizing bypassing. High throughput tandem reactors test hundreds of compositions and reaction conditions in a matter of a week. Operating micro-fluidized beds ($D_t < 10\,\text{mm}$) requires at minimum 1 g of solids although more catalyst is better. In reactors, from 5 mm to 21 mm in diameter, the gas phase is close to plug flow in shallow beds with an expanded bed height of 20 mm.[77] The riser simulator is a microreator that suspends catalyst and recirculates gas at a high rate to maintain differential conditions in the bed but high overall conversion.[318]

The fluidization characteristics—bed expansion, bubble size, and flow characteristics—are superior with rounded particles, which are produced in spray dryers. However, the yield in small scale spray dryers is much less than 50 % so producing a precious metal catalyst becomes expensive.[319] To achieve an attrition resistant catalyst requires a micronization step to reduce the primary particle size to 2 µm.[148] Mechanical stresses at 2–3 $\times$ U_{mf} are insufficient to attrit zeolites, alumina, silica, or TiO_2 supports, but unsupported catalysts require binders even at these low velocities. More binder ensures the integrity of the catalyst when the bed operates above $50\,\text{mm}\,\text{s}^{-1}$.

Highly exothermic or endothermic processes, explosive reactions, and vapourizing/reacting liquid streams are more challenging in fixed beds compared to fluidized beds. Atomizing non-volatile compounds—fructose,[320] xylose,[321] vegetable oil,[322,323] lignin,[324] glycerol,[325] and bitumen[326]—through spargers into micro-fluidized beds requires high gas velocities ($5\,\text{m}\,\text{s}^{-1}$ to $20\,\text{m}\,\text{s}^{-1}$), which attrit even supported catalysts. Heating the gas to reaction conditions is a limiting factor, and so solids backmixing and higher gas velocities heat the atomized droplets faster. Despite the excellent thermal characteristics, in the CO methanation reaction, a temperature gradient of 100 °C formed from the grid to 10 mm above.[327] Furthermore, agglomerates form around the sparger exit from the atomized liquid solution when the temperature or the injection velocity is too low.[321]

Because of the degrees of freedom, researchers adapt fluidized bed geometry, particle properties, and gas and solids injection to suit the needs of the process. Pulsing methane through a sparger into a micro-fludized bed, rather than switching the feed to the grid between methane and Ar is an example of changing the feed gas configuration to improve performance.[328] The injection configuration modifies the velocity profile and voidage around the nozzle. Despite extensive experimental modifications—on-line pulse feeding, on-line mass spectrometry, controlled micro-injection of reacting solids species—it remains unclear if micro-reactors maintain

isothermal differential conditions: the similarity between kinetic parameters in thermal gravimetric analysis and micro-reactors is no guarantee.[285] Other micro-fluidized bed geometries combine micro-fluidized beds with additional mixing techniques and unconventional heating methods:[329] Fluidized beds have been adapted as thermal gravimetric analyzers (TGA) that operate up to 1200 °C with 5 g of catalyst while measuring weight loss.[156,330] To achieve high heating rates, these reactors were equipped with either micro-wave heating or induction heating.[331,332]

Most of the work in fluidized beds is dedicated to pyrolysis, combustion, gasification, and reduction, which require adding solids to the bed as it operates.[333?] Transporting solids between the reaction and regeneration zones—circulating fluidized beds—is a common configuration to identify process conditions for scale up for coal combustion and to examine NO_x emissions, for example.[334] Rather than circulating solids between two vessels, the two-zone fluidized bed circulates solids vertically in the same vessel.[305] In vortex fluidized beds, gas injected tangentially to a cylindrical chamber rotates and operates at higher bed densities—higher gas-solid slip velocities. Pulsating the air flow changes the size and number of the bubbles and decreases solids backmixing while increasing bed density.[335] A jiggle bed reactor is an example where mixing is introduced mechanically rather than through external gas flow. A pneumatic actuator lifts the reactor (or grid) up at a frequency to suspend the bed and thus also operates at high slip velocities.[336] Cohesive group C powders fluidize best with mechanical agitation in which aggregates form and the bed expands like a group A or group B powder.[337] Pulsating gas to the grid is another mechanical technique to fluidize wet particles with a wide size distribution.[338]

Sources of Error

A kinetic reaction model is a composite calculation that depends on a half-dozen physicochemical measurements—temperature (mulitple), pressure, flow rate, species composition—each of which introduces error. For any function, f, the uncertainty, Δ, is:

$$\Delta f^2 = \left(\frac{\partial f}{\partial x_1}\Delta_{x1}\right)^2 + \left(\frac{\partial f}{\partial x_2}\Delta_{x2}\right)^2 + \ldots + \left(\frac{\partial^2 f}{\partial x_n}\Delta_{xn}\right)^2 \tag{A.20}$$

When f is a product of factors, $f = \beta_0 x_1^{\beta_1} x_2^{\beta_2} \ldots x_n^{\beta^n}$:

$$\frac{\Delta_f}{f} = \sqrt{\sum_{i=1}^{n}\left(\frac{\beta_i}{x_i}\Delta_{x_i}\right)^2} \tag{A.21}$$

and when it is a sum of factors, $f = \beta_0 x_1^{\beta_1} + x_2^{\beta_2} + \ldots + x_n^{\beta^n}$:

$$\Delta_f = \sqrt{\sum_{i=1}^{n} \left(\beta_i \Delta_{x_i}\right)^2}. \tag{A.22}$$

For the reaction, A $\rightarrow$ B, conversion, X_A, is:

$$X_\mathrm{A} = \frac{y_\mathrm{A,in} - y_\mathrm{A,out}}{y_\mathrm{A,in}} \tag{A.23}$$

$$= \frac{y_\mathrm{B}}{y_\mathrm{A,in}} \tag{A.24}$$

where y_i is the molar fraction of species i. The resulting uncertainty in conversion, ΔX_A, is:

$$\frac{\Delta_{X_\mathrm{A}}}{X_\mathrm{A}} = \sqrt{\left(\frac{\Delta_{y_\mathrm{B}}}{y_\mathrm{B}}\right)^2 + \left(\frac{\Delta_{y_\mathrm{A,in}}}{y_\mathrm{A,in}}\right)^2} \tag{A.25}$$

Operating a reactor under differential kinetics (conversion less than 20 % but closer to 10 %) reduces the uncertainty of the hydrodynamic regime: conversion is relatively independent of whether the reactor is perfectly backmixed or in plug flow. However, instrument error becomes the dominant factor: assuming a gas chromatograph measures concentration at $\Delta_y = 0.01$, then, when $X = 10\,\%$, $\Delta_X = 10\,\%$, but at $X = 90\,\%$, $\Delta_X = 1.5\,\%$.

The uncertainty in X of n repeated measurements is the product of the coverage factor ($t-$value at a significance level α and a confidence level of $1 - \alpha$, which we usually assume 0.95) and the standard error of the mean. ($s_X/\sqrt{n}$)

$$\Delta_X = t(\alpha, n-1)\frac{s_X}{\sqrt{n}} \tag{A.26}$$

Assuming the reaction is first order in species concentration A, the rate constant, k_o at reference temperature T_o at a contact time τ_c (V/Q) is:

$$k_\mathrm{o} = -\frac{1}{\tau_\mathrm{c}} \ln\left(1 - X\right) \tag{A.27}$$

and the corresponding uncertainty is:

$$\left(\frac{\Delta_{k\mathrm{o}}}{k_\mathrm{o}}\right)^2 = \left(\frac{\Delta_\tau}{\tau_\mathrm{c}}\right)^2 + \left(\frac{\Delta_X}{(1-X)\ln\left(1-X\right)}\right)^2 \tag{A.28}$$

The reaction rate, k, at any temperature with respect to k_o and uncertainty are:

$$k = -\frac{k_\mathrm{o}}{\tau_\mathrm{c}} \exp\left[-\frac{E\mathrm{a}}{R}\left(\frac{1}{T} - \frac{1}{T_\mathrm{o}}\right)\right] \ln\left(1 - X\right) \tag{A.29}$$

$$\left(\frac{\Delta_k}{k}\right)^2 = \left(\frac{\Delta_\tau}{\tau_\mathrm{c}}\right)^2 + \left(\frac{\Delta_X}{(1-X)\ln\left(1-X\right)}\right)^2 + \left(\frac{\Delta_{k\mathrm{o}}}{k_\mathrm{o}}\right)^2 + \left(\frac{\Delta_{E\mathrm{a}}}{R}\left[\frac{1}{T} - \frac{1}{T_\mathrm{o}}\right]\right)^2 + \left(\frac{E_\mathrm{a}\Delta_T}{RT^2}\right)^2 \tag{A.30}$$

To assess the influence of each factor on Δ_k, we assume a reactor operating at 350 °C in plug flow and vary Δ_{Ea}, Δ_X, and Δ_T, individually (Figure A.7):

$\Delta_{Ea} = 100\,\mathrm{J\,mol^{-1}}$**:** $\Delta_k < 1\,\%$, when $T = T_\mathrm{o} + 350\,^\circ\mathrm{C}$

$\Delta_{Ea} = 1000\,\mathrm{J\,mol^{-1}}$**:** $\Delta_k < 1\,\%$, when $T = T_\mathrm{o} + 50\,^\circ\mathrm{C}$

$\Delta_T = 7\,^\circ\mathrm{C}$**:** $\Delta_k = 10\,\%$

$\Delta_X = 1\,\%$**:** $\Delta_k < 4\,\%$, when $30\,\% < X < 90\,\%$

$\Delta_X = 2\,\%$**:** $\Delta_k < 8\,\%$, when $30\,\% < X < 90\,\%$

The contribution to Δ_k is greater for temperature (Δ_T) and conversion (Δ_X) compared to E_a. To derive kinetics in fixed beds, researchers dilute catalyst with inert solids, operate in long narrow reactors ($L > 800\,\mathrm{mm}$ and $D_\mathrm{t} > 11\,\mathrm{mm}$, for example),[339] and dilute the reactants. These measures are necessary to maintain isothermal conditions because radial and/or axial temperature gradients of just $\pm 7\,^\circ\mathrm{C}$ contribute to an uncertainty of 10 % to Δ_k/k. Whereas, operating at low conversion facilitates interpreting the data from the point of view of hydrodynamics: it introduces error with respect to uncertainty. Reactors operating in a range of conversion from 30 % to 90 % minimize the error of Δ_k/k. Beyond this range, the uncertainty increases above 4 and 8 % at $\Delta_x = 0.01$ and $\Delta_x = 0.02$, respectively.

Researchers who carry 5 significant figures for E_a overstate the certainty in their model: a confidence interval of $49\,000\,\mathrm{J\,mol^{-1}} < E_\mathrm{a} < 51\,000\,\mathrm{J\,mol^{-1}}$ only contributes 1 % to Δ_k/k at a temperature difference of $\Delta T = 50\,^\circ\mathrm{C}$ and 6 % at $\Delta T = 350\,^\circ\mathrm{C}$.[340] For the interval $49\,900\,\mathrm{J\,mol^{-1}} < E_\mathrm{a} < 50\,100\,\mathrm{J\,mol^{-1}}$ Δ_k/k is less than 1 % even when the system operates 350 °C above the reference temperature, T_o (Figure A.7).

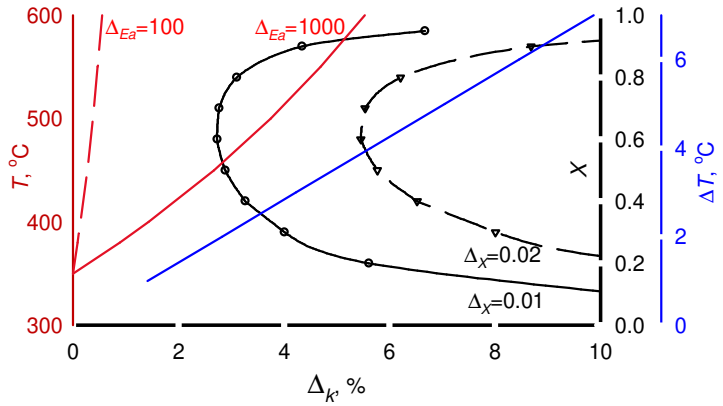

Figure A.7 Uncertainty in k, Δ_k, as a function of conversion ($\Delta_X = 0.01$, solid black line with open circles and $\Delta_X = 0.02$ (dashed black line with open triangles), temperature (Δ_T blue line), and activation energy ($\Delta_{Ea} = 1000\,\mathrm{J\,mol^{-1}}$ solid red line and $\Delta_{Ea} = 100\,\mathrm{J\,mol^{-1}}$ dashed red line) (Eq. (A.30)). Base case reactor conditions: catalyst operating in plug flow at 350 °C and $E_\mathrm{a} = 50\,\mathrm{kJ\,mol^{-1}}$.

Gas-phase hydrodynamics

Tracer studies detect gas bypassing and characterize the overall flow pattern—plug flow and number of continuous stirred tank reactors (n_CSTR)—but a reactive tracer measures gas-solids contact efficiency.[25,68,77] The convection-dispersion model assumes at dimensionless time $\theta = 0$ ($\theta = tU_\mathrm{g}/L$), the concentration of tracer $\rho(0,\xi) = \rho(0,0)$ for $0 < \xi < 1$ ($\xi = z/L$):

$$\frac{\partial\rho}{\partial\theta} + \frac{\partial\rho}{\partial\xi} = \frac{1}{N_\mathrm{Pe}}\frac{\partial^2\rho}{\partial\xi^2} \tag{A.31}$$

where $N_\mathrm{Pe} = U_\mathrm{g}L/\mathcal{D}$, the Peclet number (the inverse of which[33] refers to as the dispersion number) and $\mathcal{D}$ is the dispersion. A standard set of boundary conditions assumes $\rho(\theta,0) = 1$ at $\xi = 0$ and $\partial\rho(\theta,\xi)/\partial\xi = 0$ at $\xi = 1$. The exact solution is:[11]

$$\frac{\rho(\theta,1)}{\rho(\theta,0)} = G(\theta) = \frac{1}{2}\left[\mathrm{erfc}\left(\sqrt{\frac{N_\mathrm{Pe}}{4\theta}}\,(1-\theta)\right) + \mathrm{e}^{N_\mathrm{Pe}}\mathrm{erfc}\left(\sqrt{\frac{N_\mathrm{Pe}}{4\theta}}\,(1+\theta)\right)\right] \tag{A.32}$$

For low extents of dispersion:[33]

$$\frac{\rho(\theta,1)}{\rho(\theta,0)} = \sqrt{\frac{N_\mathrm{Pe}}{4\pi}}\exp\left[-(1-\theta)^2\frac{N_\mathrm{Pe}}{4}\right] \tag{A.33}$$

We measured the RTD of the FCC catalyst in an 8 mm quartz tube loaded with 9.15 g. Two

mass flow controllers fed Ar and air to a 4-way valve that led directly to the reactor. A Hiden mass spectrometer (MS) monitored the effluent at a frequency of up to 40 Hz and we noted the time ($\theta = 0$) when we switched the valve from argon to air. However, at a high sample frequency the percent standard deviation from one signal to the other was 10 %, so we reduced it to 10 Hz and reduced the standard deviation to 3 %.

We measured the concentration just below the reactor to assess $\rho_{\theta,0}$. Rather than a perfect Heaviside input pulse, the MS began recording a signal about 3.5 s after the valve switch, and it took several seconds for the signal to reach a steady value. The breakthrough curves are sharp and reach a steady value within 4 s after detecting the tracer gas (Figure A.8). The mean residence time with solids is shorter than an empty tube because it occupies volume. Since the solids are porous, the residence time is longer than what we expect based on the bulk density and particle density alone. For the empty $N_{\mathrm{Pe}} = 165$, and for the tube with solids, it is about 35. At $20\times U_{\mathrm{mf}}$, slugs occupied the whole cross-section and the bed height oscillated by 20 % of the total bed length. At $10\times U_{\mathrm{mf}}$, the bed height oscillated 10 % of the total bed length and seldom did bubbles coalesce to form slugs or occupy the entire area.

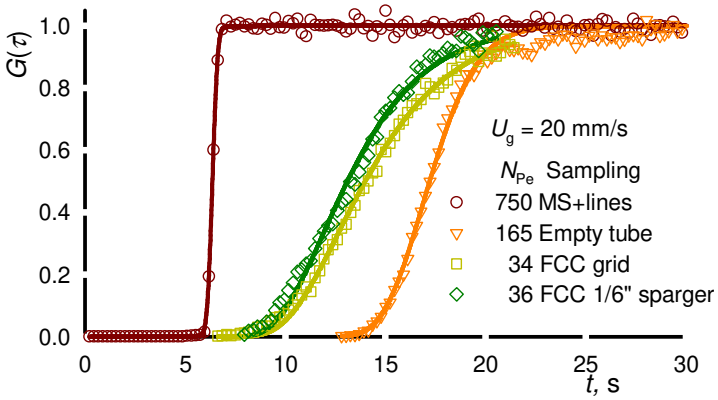

Figure A.8 Residence time distribution of a 8 mm ID fluidized bed of FCC operating at $6 \times U_{\mathrm{mf}}$. The quartz tube operated with 9.15 g of catalyst and when fluidized it occupied 60 % of the reactor volume.

A hydrodynamic model assuming 5 n_{CSTR} and accounting for the contributions of the MS, entrance region, and exit fit the experimental breakthrough curve best. In a 45 mm fluidized bed with Geldart group A powders, n_{CSTR} dropped from 39 to 5 with an increase in gas velocity from U_{mf} to $6\times U_{\mathrm{mf}}$, which is equivalent to a drop in N_{Pe} of 77 to 9 ($N_{\mathrm{Pe}} = 2n_{\mathrm{CSTR}} - 2$).

Kinetic Modelling

Establishing the predominant gas and solids flow regime reduces the error in estimating kinetic rate constants and activation energies. For fixed beds, we assume the gas phase is in plug flow, so the rate constant is derived according to Equation ((A.29)). Rate constants are insensitive to the assumed ideal flow pattern when reactors operate below 20 % conversion, but low conversion translates to higher uncertainty (Figure A.7). The general equation of conversion for a first order reactor operating with n_{CSTR} is:

$$k = \frac{n}{\tau_{\mathrm{c}}}\left[(1-X)^{-\frac{1}{n}} - 1\right] \tag{A.34}$$

$$N_{\mathrm{Da}} = n\left[(1-X)^{-\frac{1}{n}} - 1\right] \tag{A.35}$$

where N_{Da} is the Damkohler number. The error in k (or $N_{\mathrm{Da}} = k\tau_{\mathrm{c}}$), assuming a plug flow gas phase versus a series of 10 perfectly mixed tanks in series, $n_{\mathrm{CSTR}} = 10$, is 5 % when the reactor operates at 87 % conversion and increases to 10 % at 98.5 % (Figure A.9). With $n_{\mathrm{CSTR}} = 5$, typical of reactors operating at $U_{\mathrm{g}} > 10 \times U_{\mathrm{mf}}$, the error is 5 % at 40 % conversion, and 10 % at 65 % conversion. Experimental designs to derive kinetics require that factors cover the widest possible operating ranges, which implies gas velocities near U_{mf} and $10\times, 20 \times U_{\mathrm{mf}}$. To minimize the error in kinetic modelling this wide range of gas velocities might introduce, either the reactor must operate below 50 % conversion, or the hydrodynamic model must account for the change in n_{CSTR} as a function of U_{g}.

Selectivity in fixed bed reactors is higher compared to fluidized beds and the difference is greater for thermally sensitive compounds. *n*-Butane combusts at high temperature and pressure (0.5 MPa, for example). It is more easily than maleic anhydride, and so selectivities in both reactor types are similar. Acrylic acid, on the other hand, reacts with oxygen at much lower temperatures than propylene and thus selectivities are higher in fixed bed reactors. The solids backmixing, rather than the gas phase flow pattern, is presumably the largest contributor to the lower selectivity as the catalyst carries interstitial and intraparticle gas downwards allowing the product more time to react with gas phase oxygen.

Bubbles in micro-fluidized beds can only grow as large as the diameter of the vessel (slugs). However, gas in the slugs contact the solids phase as they pass through and as the particles rain down when the slugs collapse. Bubbles grow larger than 100 mm and more in larger diameter reactors with Geldart B powders and so the gas bypasses through high velocity bubbles. We account for mass transfer resistance in the rate equation with the term $k_{\mathrm{m}}a_{\mathrm{m}}$,

where k_m is the mass transfer coefficient and a_m is the superficial area:

$$r_\mathrm{A} = \frac{1}{1/k + 1/(k_\mathrm{m} a_\mathrm{m})} C_\mathrm{A} \tag{A.36}$$

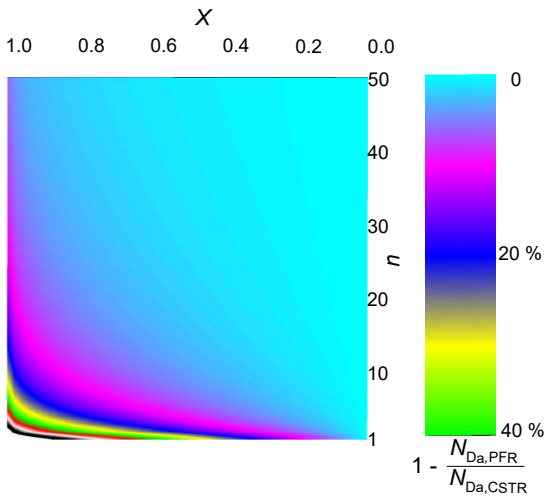

Figure A.9 Plug flow versus n_CSTR gas phase reactor model. The colours represent the % relative difference between the predicted N_Da of a fixed bed versus n_CSTR model ($N_\mathrm{Da} = k\tau_\mathrm{c}$). The N_Da number for $n_\mathrm{CSTR} = 50$ at 63 % conversion is 1 % greater than the plug flow N_Da and at 95 % conversion it is greater by 3 %. $N_\mathrm{Da} = 0.223$ at 20 % conversion in a plug flow reactor, while it equals 0.25 in an CSTR—a 10 % relative difference.

Conclusion

Fluidized beds are versatile and effective reactors to study kinetics, pyrolyze biomass, combust coal, dry solids, and gasify waste. The solids in the bed are completely backmixed and it operates isothermally with much lower hot spots compared to fixed beds. The gas phase hydrodynamics in small reactor diameters approach plug flow with $n_\mathrm{CSTR} > 10$ even for $U_\mathrm{g} > U_\mathrm{mf}$. The factors to consider when designing and operating fluid beds include: the fluidization regime (bubbling, slugging, turbulent, spouting), geometry, operating conditions, and particle properties—Geldart powder classification, U_mf, density, Hausner ratio, angle of repose, PSD, sphericity, and surface area. The principal techniques to characterize the bed behaviour are particle tracking, tomography, pressure measurements, optical probes, CFD, and PIV. Despite the scale-up and operation challenges of fluidized bed reactors compared to fixed bed, this technology will continue to dominate the market in challenging applications that involved multiple phases, explosive feedstocks, highly exothermic or endothermic

reactions, and processes where catalysts deactivate and coke. The future for the technology will expand at both ends of the particle size spectrum—from the synthesis and handling of nanoscale powders to treating heterogeneous feedstocks with multiple fluid phases—municipal solids, electronic waste, end-of-life polymers, and lignocellulosics. Converting organic waste to high value chemicals while recycling glass and metals will contribute to society's desire for the cradle to grave (re-use) circular economy.

Acknowledgements

The authors thank H. Li, Z. Ma, T. N. Eran, M. G. Rigamonti, R. Vazquez, A. D'Oliveira, M. Ferreiro-Gonzalez, Y.-X. Song, N. Saadatkhah O. Chub, M. Bindes, Y. Zhuang, M. Sharifian, and N. F. Rosli for measuring the powder properties of the FCC and sand. H. Li measured the particle and bulk density with the mercury intrusion porosimeter. B. A. Patience collected the data from WoS and created the VoSViewer bibliographic map.

ANNEXE B DÉMARCHE DE LA RÉSOLUTION DU MODÈLE DE DISPERSION AXIALE

D'une manière générale, chaque condition expérimentée consiste en 12 expériences RTD. Deux essais sont faits à l'entrée du réacteur et deux à la sortie du réacteur. Puis, trois débits volumiques sont nécessaires : 30, 40, 50 ou 60 $\mathrm{mL\,min^{-1}}$.

Durant une expérience RTD, le spectromètre de masse enregistre à une fréquence de 4 Hz la concentration (en compte) de chaque traceur. Le fichier Excel obtenu contient le temps en millisecondes et la concentration de chaque traceur. Tel qu'expliqué précédemment, certaines molécules en s'ionisant se chevauchent et la concentration lue par le MS est erronée. Donc, la première étape consiste à calculer les valeurs réelles.

Étape 1 : Calculer les concentrations réelles (C) enregistrées par le MS (C_{MS})

Cette étape est uniquement nécessaire lorsque la bouteille contenant le CO_2, CO, H_2 et CH_4 est employé.

$$C_{\mathrm{CO_2}} = C_{\mathrm{MS_{CO_2}}} \tag{B.1}$$

$$C_{\mathrm{CO}} = C_{\mathrm{MS_{CO}}} - 0.114 C_{\mathrm{CO_2}} \tag{B.2}$$

$$C_{\mathrm{CH_4}} = C_{\mathrm{MS_{CH_4}}} - 0.085 C_{\mathrm{CO_2}} - 0.009 C_{\mathrm{CO}} \tag{B.3}$$

$$C_{\mathrm{H_2}} = C_{\mathrm{MS_{H_2}}} - 0.03 C_{\mathrm{CH_4}} \tag{B.4}$$

Étape 2 : Calculer le temps réel seconde (t_{rel}) à partir du temps enregistré par le MS (t_{MS})

$$t_{\mathrm{rel,i+1}} = \frac{t_{\mathrm{MS,i+1}} - t_{\mathrm{MS,i}}}{1000} \tag{B.5}$$

Puis, la prochaine étape consiste à supprimer le temps que prend le gaz à entrer dans le réacteur et à atteindre le MS. Ce temps a été mesuré grâce aux essais expérimentaux à l'entrée du réacteur.

Les courbes sont normalisées dans le but d'obtenir une aire sous la courbe égale à 1. Ainsi, il est plus simple, visuellement, de voir les déviations du modèle de dispersion axiale.

Étape 3 : Calculer le temps entre chaque prise de données (Δt)

$$\Delta t_i = t_{\text{rel,i}} - t_{\text{rel,i}-1} \tag{B.6}$$

Étape 4: Calculer l'aire sous la courbe (C_{aire})

$$C_{\text{aire,i}} = C_i \times \Delta t_i \tag{B.7}$$

$$C_{\text{aire}} = \sum C_i \times \Delta t_i = \sum C_{\text{aire,i}} \tag{B.8}$$

Étape 5 : Calculer la courbe E – Levenspiel [33]

$$E_i = \frac{C_i}{C_{\text{aire}}} \tag{B.9}$$

Ainsi, l'aire sous la courbe est égale à 1, soit $\sum E_i \Delta t = 1$

Les prochaines étapes permettent de mesurer les deux moments : le temps de résidence moyen ($\bar{t}$) et la variance (σ^2).

Étape 6: Calculer le temps de résidence ($\bar{t}$) [33]

$$\bar{t} = \frac{\sum t_{\text{rel,i}} C_i \Delta t_i}{\sum C_i \Delta t_i} = \frac{V_{\text{réacteur}}}{Q} \tag{B.10}$$

Où $V_{\text{réacteur}}$ est le volume du réacteur et Q le débit volumique.

Étape 7: Calculer la variance (σ^2) [33]

$$\sigma^2 = \frac{\sum t_{\text{rel,i}}^2 C_i \Delta t_i}{\sum C_i \Delta t_i} - \bar{t}^2 \tag{B.11}$$

Les prochaines étapes permettent de résoudre la solution analytique du modèle de dispersion axiale pour ainsi calculer le nombre de Péclet (N_{PE}). Il est nécessaire de définir les valeurs initiales pour le volume du réacteur, le nombre de Péclet et le temps de résidence moyen ($\bar{t}_{\text{res}}$).

Étape 8: Calculer le temps adimensionnel (θ)

$$\theta_i = \frac{t_{\text{rel,i}}}{\bar{t}_{\text{res}}} \tag{B.12}$$

Où $\bar{t}_{\text{res}}$ est le temps moyen de résidence résolue à l'aide du modèle de dispersion axiale.

Étape 9 : Calculer $G(\theta)_i$

$$G(\theta)_i = 0.5 \left(\text{ERFC} \left(\left(\frac{\sqrt{N_{\text{Pe}}}}{2} \right) \left(\frac{1 - \theta_i}{\sqrt{\theta_i}} \right) \right) \right) \tag{B.13}$$

$$+ \exp(N_{\text{Pe}}) \times \text{ERFC} \left(\left(\frac{\sqrt{N_{\text{Pe}}}}{2} \right) \left(\frac{1 + \theta_i}{\sqrt{\theta_i}} \right) \right)$$

Où,

$$\text{ERFC}(x) = \frac{2}{\sqrt{\pi}} \int_x^\infty e^{-t^2} dt \tag{B.14}$$

Step 10: Calculer χ

Si,

$$t_{\text{rel,i}} > \frac{V_{\text{réacteur}}}{Q} \tag{B.15}$$

Alors,

$$\chi_i = \frac{\theta_i - \left(\frac{V_{\text{réacteur}}}{Q}\right)}{\bar{t}_{\text{res}}} \tag{B.16}$$

Sinon,

$$\chi_i = 0 \tag{B.17}$$

Étape 11 : Calculer $G(\chi_i)$

Si,

$$t_{\text{rel,i}} > \tau > \frac{V_{\text{réacteur}}}{v} \tag{B.18}$$

Alors,

$$G(\chi)_i = 0.5\left(\text{ERFC}\left(\left(\frac{\sqrt{N_{\text{Pe}}}}{2}\right)\left(\frac{1-\chi_i}{\sqrt{\chi_i}}\right)\right)\right) \tag{B.19}$$

$$+\exp(N_{\text{Pe}}) \times \text{ERFC}\left(\left(\frac{\sqrt{N_{\text{Pe}}}}{2}\right)\left(\frac{1+\chi_i}{\sqrt{\chi_i}}\right)\right)$$

Où τ est le temps de résidence théorique.

Étape 12: Calculer les concentrations du modèle (C_{model}) par pas de temps

$$C_{\text{model,i}} = G(\theta)_i - G(\chi)_i \tag{B.20}$$

Étape 13 : Calculer le SSE

$$\text{SSE}_i = \left(C_i - C_{\text{model,i}}\right)^2 \tag{B.21}$$

$$\text{SSE} = \sum \left(C_i - C_{\text{model,i}}\right)^2 \tag{B.22}$$

La somme du SSE se fait du moment où la courbe RTD commence son ascension jusqu'à 20 % dépasser le maximum (le sommet de la courbe).

Étape 14 : Minimisation du SSE

La dernière étape consiste à minimiser la valeur du SSE à l'aide du Solveur Excel. L'objectif est de minimiser la cellule du SSE en variant le volume du réacteur, le temps de résidence moyen et le nombre de Péclet. Le mode de résolution est GRG non linéaire.

Étape 15 : Production de graphique

Finalement, il suffit de tracer sur un graphique les données expérimentales avec des points et le modèle de dispersion axiale avec une ligne continue.

ANNEXE C CODE FORTRAN DU NOUVEAU MODÈLE

Voici le code Fortran utilisé pour résoudre le nouveau modèle. Le texte en bleu représente les commentaires.

```
C gfortran - Wall - ggdb3 - std = legacy - ffpe - trap = invalid,zero,overflow -o RTD RTD-AR7.FOR 2 > log
REAL P(101,100),Y1(101),X1(100)
EXTERNAL FUNK
COMMON/BK1/ Y_IN (4,90000),Y_I (4,600),Y_E (4,600),YFIT(99,600)
COMMON/BK2/ DT,DZ,DIA,PI,NT,NZ,NP,NT_INC, NT_DATA
COMMON/BK3/ V(20),QR(4),RKA(4),RKD(4),CIRC,A1,VT
COMMON/BK4/ NPARM,NDATA,JEXP,IRLNCNT,IPARM(20)
COMMON/BK5/ RHO_B, RHO_P, RHO_SC, EPSILON, VOL_SK, EPS_T, EPS_SK
COMMON/BK6/ Q_MLMIN, W_CAT, VOL, VOL_CAT, VOL_P, XA
COMMON/BK7/ T_LAB, P_LAB, RHOG_LAB, DELTA_P, HEIGHT
COMMON/BK8/ R2(6)
COMMON/BKGB/ A(10000)
COMMON/RHS/ D(1000),X(1000)
COMMON/EQUT/ EPGB,IGB,IERR,IFRST,N,M
OPEN(UNIT=10,FILE='RTD _ AR6.F10',STATUS='OLD')
OPEN(UNIT=11,FILE='RTD _ AR1.F11',STATUS='OLD')
OPEN(UNIT=20,FILE='C.F20',STATUS='UNKNOWN')
OPEN(UNIT=21,FILE='C.F21',STATUS='UNKNOWN')
OPEN(UNIT=22,FILE='C.F22',STATUS='UNKNOWN')

IRLNCNT = 0
CALL DATA

IF(NPARM.GT.0) THEN
DO 21 I = 1,NPARM
X1(I) = V(IPARM(I))
P(1,I) = V(IPARM(I))
Y1(1) = FUNK(X1)
IDUM = -1
```

```
DO 23 I = 2,NPARM+1
DO 22 J = 1,NPARM
RANDOM = RAN0(IDUM)
IF(RANDOM.EQ.0.5) RANDOM = RAN0(IDUM -J)
X1(J) = P(1,J)*(0.97 + RANDOM/20.)
P(I,J) = X1(J)
CONTINUE
Y1(I)=FUNK(X1)
CONTINUE
CALL AMOEBA(P,Y1,MP,NP,NPARM,FTOL,FUNK,ITER)
ENDIF

WRITE(6,*)'HERE 1'
CALL RNITIAL
WRITE(6,*)'HERE 2'

CALL CSTR
WRITE(6,*)'HERE 3',NT_DATA,YFIT(1,NT_DATA),YFIT(5,NT_DATA)
CALL OUTDATA
CALL MULTR2
WRITE(6,600)(R2(IP),IP=1,NP),(X(IPARM(I)),I=1,NPARM)
600 FORMAT(4X,'R2',12(2X,G12.5))
STOP
END

**************************************************************
FUNCTION FUNK(X1)
REAL X1(100)
COMMON/BK1/ Y_IN(4,90000),Y_I(4,600),Y_E(4,600),YFIT(99,600)
COMMON/BK2/ DT,DZ,DIA,PI,NT,NZ,NP,NT_INC,NT_DATA
COMMON/BK3/ V(20),QR(4),RKA(4),RKD(4),CIRC,A1,VT
COMMON/BK4/ NPARM,NDATA,JEXP,IRLNCNT,IPARM(20)
COMMON/BK5/ RHO_B,RHO_P,RHO_SC,EPSILON,VOL_SK,EPS_T,EPS_SK
COMMON/BK8/ R2(6)
IRLNCNT = IRLNCNT + 1
IF(IRLNCNT.GT.260) THEN
```

```
WRITE(6,*)'Did I get here',IRLNCNT
WRITE(6,610)(R2(IP),IP=1,NP),(X1(IPARM(I)),I=1,NPARM)
WRITE(6,611)(IPARM(I),I=1,NPARM)
FORMAT(4X,'R2',8(2X,G12.5))
FORMAT(4X,'N_parameters',6(2X,i3))
CALL OUTDATA
CALL MULTR2
STOP
ENDIF
DO 50 IP = 1,NPARM
V(IPARM(IP)) = X1(IP)
CONTINUE

DO 52 IP = 1,NP
DO 51 IT = 1,NT_DATA
YFIT(IP,IT) = 0.0
YFIT(IP+NP,IT)=0.0
CONTINUE
YFIT(9,IT) = 0.
YFIT(10,IT) = 0.
CONTINUE

CALL RNITIAL
CALL CSTR

CALL MULTR2
SUM_R2 = 0.
DO 53 IP = 1,NP
SUM_R2 = SUM_R2 + R2(IP)
CONTINUE
FUNK = FLOAT(NP) - SUM_R2
FUNK = 3. - R2(4) - R2(2) - R2(3)
FUNK = 2. - R2(4) - R2(3)
FUNK = 1. - R2(1)
WRITE(,600)IRLNCNT,(X1(IP),IP=1,NPARM),FUNK
WRITE(6,600)IRLNCNT,(R2(IP),IP=1,4),(X1(IP),IP=1,NPARM),FUNK
```

```
600 FORMAT(1X,I6,1X,10(G12.5,1X))
RETURN
END
```

CALCULATION - EXPLICIT

```
SUBROUTINE CSTR
DIMENSION Y(4,201),Y0(4,201),C(4,201),C0(4,201),RHOG(201)
DIMENSION V(4,201),V0(4,201),RXN(4,201),QRXN(201),Q_G(201) !,UG(600),VC(600)
COMMON/BK1/ Y_IN(4,90000),Y_I(4,600),Y_E(4,600),YFIT(99,600)
COMMON/BK2/ DT,DZ,DIA,PI,NT,NZ,NP,NT_INC,NT_DATA
COMMON/BK3/ VAR(20),QR(4),RKA(4),RKD(4),CIRC,A1,VT
COMMON/BK5/ RHO_B,RHO_P,RHO_SC,EPSILON,VOL_SK,EPS_T,EPS_SK
COMMON/BK6/ Q_MLMIN,W_CAT,VOL,VOL_CAT,VOL_P,XA
COMMON/BK7/ T_LAB,P_LAB,RHOG_LAB,DELTA_P,HEIGHT
DO 45 IT = 1,NT_DATA
DO 44 IP = 1,NP
YFIT(IP,IT)= 0.0
YFIT(IP+4,IT)=0.0
CONTINUE
YFIT(9,IT) = 0.0
YFIT(10,IT) = 0.0
YFIT(11,IT) = 0.0
YFIT(12,IT) = 0.0
YFIT(13,IT) = 0.0
CONTINUE

DELTA_Z = HEIGHT/FLOAT(NZ)
DO 47 IZ = 1,NZ
DO 46 IP = 1,NP
Y(IP,IZ) = 0.0000000001 (mole fraction)
Y0(IP,IZ) = 0.0000000001 (mole fraction)
C(IP,IZ) = 0.0000000001 (mole fraction)
C0(IP,IZ) = 0.0000000001 (mole fraction)
V(IP,IZ) = 0.000000000000001 (kmol kg)
V0(IP,IZ) = 0.000000000000001 (bar)
```

```
RXN(IZ,IZ) = 0. (kmol kg)
CONTINUE
CONTINUE

QR(3) = QR(2)
RKA(3) = RKA(2)
RKD(3) = RKD(2)
Q_KMOLS = Q_MLMIN/60.*RHOG_LAB/1000000. (kmol s^-1)
Q_V = CIRC*EPS_SK/RHO_P (m^3 s^-1 - flow rate of gas in particles
VOL_IZ = VOL/FLOAT(NZ)
VOL_P = VOL_CAT*EPS_SK/FLOAT(NZ)
W_IZ = W_CAT/FLOAT(NZ)
THETA_V = DT/W_IZ

P_IZ = P_LAB + DELTA_P/FLOAT(NZ)/2.
DO 48 IZ = NZ,1,-1
RHOG(IZ) = P_IZ/0.08314/T_LAB (kmol m^-3
P_IZ = P_IZ + DELTA_P/FLOAT(NZ)
Q_G(IZ) = Q_KMOLS
CONTINUE

TIME =-DT/2.
ITT = 0
IT_REF = 0
DO 56 IT = 1,NT
TIME = TIME + DT
IT_REF = IT_REF + 1
DO 50 IZZ = 1,NZ
Q_G(IZZ) = Q_G(IZZ) + RXN(IZZ)
DO 49 IPP = 1,NP
Y0(IPP,IZZ)= Y(IPP,IZZ)
C0(IPP,IZZ)= C(IPP,IZZ)
V0(IPP,IZZ)= V(IPP,IZZ)
CONTINUE
CONTINUE
```

```
UG = Q_KMOLS/RHOG_LAB/XA
DO 51 IZ = 1,NZ
QRXN(IZ) = 0.
THETA = DT/VOL_IZ/RHOG(IZ)
THETA_C = DT/VOL_P /RHOG(IZ)
V_ADS = 0.
DO 76 IPX = 1,NP
76 V_ADS = V_ADS + V0(IPX,IZ)
C IF(V_ADS.GT.VT) V_ADS = VT*0.9999
DO 77 IPV = 1,NP
RXN_AD = RKA(IPV)*(C0(IPV,IZ)*RHOG(IZ))**A1*(VT - V_ADS)
RXN_DE = RKD(IPV)*V0(IPV,IZ)
RXN(IPV,IZ) =-(RXN_AD - RXN_DE)*W_IZ
QRXN(IZ) = QRXN(IZ) + RXN(IPV,IZ)
77 CONTINUE
C WRITE(21,*)IT,IZ,RKA(4),C(4,IZ),RHOG(IZ),V(4,IZ),VT

DO 52 IP = 1,NP
CROSS = QR(IP)*(Y0(IP,IZ) - C0(IP,IZ))*RHOG(IZ)
IF(QRXN(IZ).LE.0.) THEN
QPORE = Y0(IP,IZ)*QRXN(IZ)
ELSE
QPORE = C0(IP,IZ)*QRXN(IZ)
ENDIF

IF(IZ.EQ.1) THEN
Q_G(1) = Q_KMOLS + QRXN(1)
CONV_IN = Q_G(1)*Y0(IP,1) - Q_KMOLS*Y_IN(IP,IT)
DIFF_C = Q_V*(C0(IP,2)*RHOG(2) - C0(IP,1)*RHOG(1))
DIFF_V = CIRC*(V0(IP,2) - V0(IP,1))
ELSE IF (IZ.EQ.NZ) THEN
Q_G(NZ) = Q_G(NZ-1) + QRXN(NZ)
CONV_IN = Q_G(NZ)*Y0(IP,NZ) - Q_G(NZ-1)*Y0(IP,NZ-1)
DIFF_C = Q_V*(C0(IP,NZ-1)*RHOG(NZ-1)- C0(IP,NZ)*RHOG(NZ))
DIFF_V = CIRC*(V0(IP,NZ-1) - V0(IP,NZ))
ELSE
```

```
Q_G(IZ) = Q_G(IZ-1) + QRXN(IZ)
CONV_IN = Q_G(IZ)*Y0(IP,IZ) - Q_G(IZ-1)*Y0(IP,IZ-1)
DIFF_CM = Q_V*(C0(IP,IZ-1)*RHOG(IZ-1) - C0(IP,IZ)*RHOG(IZ))
DIFF_CP = Q_V*(C0(IP,IZ+1)*RHOG(IZ+1) - C0(IP,IZ)*RHOG(IZ))
DIFF_C = DIFF_CP - DIFF_CM
DIFF_VM = CIRC*(V0(IP,IZ-1) - V0(IP,IZ))
DIFF_VP = CIRC*(V0(IP,IZ+1) - V0(IP,IZ))
DIFF_V = DIFF_VP - DIFF_VM
ENDIF
Y(IP,IZ) = Y0(IP,IZ) -(CONV_IN + CROSS - QPORE) *THETA
C(IP,IZ) = C0(IP,IZ) +(DIFF_C + CROSS - QPORE) *THETA_C
C(IP,IZ) = C(IP,IZ) + RXN(IP,IZ) *THETA_C
V(IP,IZ) = V0(IP,IZ) +(DIFF_V -RXN(IP,IZ))*THETA_V
WRITE(22,246)IP,IZ,TIME,RXN_AD,RXN_DE,Y(IP,IZ),C(IP,IZ),V(IZ)
CONTINUE
CONTINUE

WRITE(6,*)Q_G(IZ)/XA*1000./RHOG(NZ),UG (mms^-1)

IF(IT_REF.EQ.NT_INC) THEN
IT_REF = 0
ITT = ITT + 1
DO 53 IP = 1,NP
YFIT(IP,ITT)= Y(IP,NZ)
YFIT(IP+NP,ITT)= C(IP,NZ)
CONTINUE
YFIT(9,ITT)= V_ADS/VT
DO 81 IR = 1,NZ
YFIT(IR+9,ITT)= Q_G(IR)/RHOG(1)/XA*1000.
YFIT(IR+9,ITT)= Y(4,IR)
continue
WRITE(22,246)TIME,RXN_F,C0(4,NZ),RHOG(NZ),V0(NZ),V(NZ),UG
C FORMAT(1X,I3,1X,I3,1X,12(G12.5,2X)) ENDIF
CONTINUE
RETURN
END
```

PHYSICAL CONSTANTS

```
SUBROUTINE DATA
COMMON/BK1/ Y_IN(4,90000),Y_I(4,600),Y_E(4,600),YFIT(99,600)
COMMON/BK2/ DT,DZ,DIA,PI,NT,NZ,NP,NT_INC,NT_DATA
COMMON/BK3/ VAR(20),QR(4),RKA(4),RKD(4),CIRC,A1,VT
COMMON/BK4/ NPARM,NDATA,JEXP,IRLNCNT,IPARM(20)
COMMON/BK5/ RHO_B,RHO_P,RHO_SC,EPSILON,VOL_SK,EPS_T,EPS_SK
COMMON/BK6/ Q_MLMIN,W_CAT,VOL,VOL_CAT,VOL_P,XA
COMMON/BK7/ T_LAB,P_LAB,RHOG_LAB,DELTA_P,HEIGHT
COMMON/EQUT/ EPGB,IGB,IERR,IFRST,N,M
READ(10,*)TIME,DT,NT_INC
READ(10,*)DIA,HEIGHT,NZ,NP
READ(10,*)Q_MLMIN,W_CAT,CIRC
WRITE(6,*)Q_MLMIN,W_CAT,CIRC
READ(10,*)RHO_B,RHO_P,RHO_SK
READ(10,*)NPARM,(IPARM(I),I=1,NPARM)
READ(10,*)T_LAB,P_LAB
READ(10,*)(QR(IP),IP=1,NP)
READ(10,*)(RKA(IP),IP=1,NP)
WRITE(6,*)(RKA(IP),IP=1,NP)
READ(10,*)(RKD(IP),IP=1,NP)
WRITE(6,*)(RKD(IP),IP=1,NP)
READ(10,*)VT,A1
AA = 1.0
PI = 4.0*ATAN(AA)
XA = PI/4.*DIA*DIA
VOL_T = HEIGHT*XA
EPS_SK = 1. - RHO_P/RHO_SK
VOL_CAT = W_CAT/RHO_P
VOL = VOL_T - VOL_CAT
EPSILON = 1. - VOL_CAT/VOL_T
EPS_T = (VOL - VOL_CAT)/VOL
T_K = 273. (K)
T_LAB = 23.+ T_K (K)
```

P_LAB = 1. (bar)
RHOG_LAB = P_LAB/0.08314/T_LAB (kmol m^{-3})
DELTA_P = W_CAT*9.81/XA/100000. (bar)
VAR(1) = Q_MLMIN
VAR(2) = EPSILON
VAR(3) = VOL_SK
VAR(4) = EPS_T
VAR(5) = QR(1)
VAR(6) = QR(2)
VAR(7) = QR(3)
VAR(8) = QR(4)
VAR(9) = RKA(1)
VAR(10) = RKA(2)
VAR(11) = RKA(3)
VAR(12) = RKA(4)
VAR(13) = RKD(1)
VAR(14) = RKD(2)
VAR(15) = RKD(3)
VAR(16) = RKD(4)
VAR(17) = A1
VAR(18) = CIRC
VAR(19) = VT

INLET CONDITIONS
NT_DATA = INT(TIME/DT)
DT = DT/NT_INC
WRITE(6,*)'DT',DT,NT_DATA
NT = INT(TIME/DT)
IT_C = 0
DO 76 IT = 1,NT_DATA
READ(11,*)DUM1,(Y_I(I,IT),I=1,NP),(Y_E(I,IT),I=1,NP)
DO 75 ITT = 1,NT_INC
IT_C = IT_C + 1
DO 74 IP = 1,NP
Y_IN(IP,IT_C)= Y_I(IP,IT)
CONTINUE

```
CONTINUE
RETURN
END
```

OUTPUT DATA

```
SUBROUTINE OUTDATA
COMMON/BK1/ Y_IN(4,90000),Y_I(4,600),Y_E(4,600),YFIT(99,600)
COMMON/BK2/ DT,DZ,DIA,PI,NT,NZ,NP,NT_INC,NT_DATA
COMMON/BK3/ VAR(20),QR(4),RKA(4),RKD(4),CIRC,A1,VT
COMMON/BK4/ NPARM,NDATA,JEXP,IRLNCNT,IPARM(20)
TM = DT*FLOAT(NT_INC)/2.
WRITE(6,*)'HERE OUTDATA',TM,NT_DATA
DO 60 IT = 1,NT_DATA
WRITE(20,200)TM,(YFIT(IP,IT),IP=1,8),YFIT(9,IT),YFIT(10,IT)
WRITE(21,200)TM,(YFIT(9+I,IT),I=1,10)
WRITE(22,200)TM,(YFIT(9+I,IT),I=11,NZ)
TM = TM + DT*FLOAT(NT_INC)
CONTINUE
FORMAT(1X,F6.2,1X,10(G12.5,1X))
RETURN
END
```

MULTIPLE R^2 CALCULATION

```
SUBROUTINE MULTR2
REAL YMEAN(9),TOT1(9),TOT2(9),DEL1(9),DEL2(9)
COMMON/BK1/ Y_IN(4,90000),Y_I(4,600),Y_E(4,600),YFIT(99,600)
COMMON/BK2/ DT,DZ,DIA,PI,NT,NZ,NP,NT_INC,NT_DATA
COMMON/BK3/ VAR(20),QR(4),RKA(4),RKD(4),CIRC,A1,VT
COMMON/BK4/ NPARM,NDATA,JEXP,IRLNCNT,IPARM(20)
COMMON/BK8/ R2(6)
NS = NT_DATA - NT_DATA/3
DO 50 IP = 1,NP
YMEAN(IP) = 0.0
TOT1(IP) = 0.0
TOT2(IP) = 0.0
```

```
DO 52 IP = 1,NP
DO 51 IT = 1,NS
YMEAN(IP)= YMEAN(IP) + YFIT(IP,IT)
YMEAN(IP) = YMEAN(IP)/FLOAT(NT_DATA)
CONTINUE

DO 54 IP = 1,NP
DO 53 IT = 1,NS
DEL1(IP) = Y_E(IP,IT) - YFIT(IP,IT)
DEL2(IP) = YFIT(IP,IT) - YMEAN(IP)
TOT1(IP) = TOT1(IP) + DEL1(IP)*DEL1(IP)
TOT2(IP) = TOT2(IP) + DEL2(IP)*DEL2(IP)
CONTINUE
R2(IP) = 1.0 - TOT1(IP)/TOT2(IP)
CONTINUE
RETURN
END

SIMPLEX METHOD (NELDER-MEAD)
SUBROUTINE AMOEBA(P,Y,MP,NP,NDIM,FTOL,FUNK,ITER)
REF. P.404, NUMERICAL RECIPES IN FORTRAN, PRESS, TEUKOLSKY,
VETTERLING AND FLANNERY, 2ND EDITION 1996
INTEGER ITER,MP,NDIM,NP,NMAX,ITMAX
PARAMETER (NMAX=20,ITMAX=1000)
REAL FTOL,P(101,100),Y(101)
EXTERNAL FUNK
INTEGER I,IHI,ILO,INHI,J,M,N
REAL RTOL,SUM,SWAP,YSAVE,YTRY,PSUM(NMAX),AMOTRY
ITER=0
DO 12 N=1,NDIM
SUM=0.
DO 11 M=1,NDIM+1
SUM=SUM+P(M,N)
END DO
PSUM(N)=SUM
```

```
END DO


ILO=1
IF (Y(1).GT.Y(2)) THEN
IHI=1
INHI=2
ELSE
IHI=2
INHI=1
ENDIF
DO 13 I=1,NDIM+1
IF (Y(I).LE.Y(ILO)) ILO=I
IF (Y(I).GT.Y(IHI)) THEN
INHI=IHI
IHI=I
ELSE IF (Y(I).GT.Y(INHI)) THEN
IF (I.NE.IHI) INHI=I
ENDIF
END DO
RTOL=2.*ABS(Y(IHI)-Y(ILO))/(ABS(Y(IHI))+ABS(Y(ILO)))
IF (RTOL.LT.FTOL) THEN
SWAP=Y(1)
Y(1)=Y(ILO)
Y(ILO)=SWAP
DO 14 N=1,NDIM
SWAP=P(1,N)
P(1,N)=P(ILO,N)
P(ILO,N)=SWAP
END DO
RETURN
ENDIF
IF (ITER.GE.ITMAX) PAUSE 'ITMAX EXCEEDED IN AMOEBA'
ITER=ITER+2
YTRY=AMOTRY(P,Y,PSUM,MP,NP,NDIM,FUNK,IHI,-1.0)
IF (YTRY.LE.Y(ILO)) THEN
YTRY=AMOTRY(P,Y,PSUM,MP,NP,NDIM,FUNK,IHI,2.0)
```

```
ELSE IF (YTRY.GE.Y(INHI)) THEN
YSAVE=Y(IHI)
YTRY=AMOTRY(P,Y,PSUM,MP,NP,NDIM,FUNK,IHI,0.5)
IF (YTRY.GE.YSAVE) THEN
DO 16 I=1,NDIM+1
IF (I.NE.ILO) THEN
DO 15 J=1,NDIM
PSUM(J)=0.5*(P(I,J)+P(ILO,J))
P(I,J)=PSUM(J)
END DO
Y(I)=FUNK(PSUM)
ENDIF
END DO
ITER=ITER+NDIM
GOTO 1
ENDIF
ELSE
ITER=ITER-1
ENDIF
GOTO 2
END

FUNCTION AMOTRY(P,Y,PSUM,MP,NP,NDIM,FUNK,IHI,FAC)
INTEGER IHI,NDIM,NP,NMAX
PARAMETER (NMAX=20)
REAL AMOTRY,FAC,P(101,100),PSUM(NP),Y(101),FUNK
EXTERNAL FUNK
INTEGER J
REAL FAC1,FAC2,YTRY,PTRY(NMAX)
DUMP= MP
FAC1=(1.-FAC)/NDIM
FAC2=FAC1-FAC
DO 11 J=1,NDIM
PTRY(J)=PSUM(J)*FAC1-P(IHI,J)*FAC2
END DO
YTRY=FUNK(PTRY)
```

```
IF (YTRY.LT.Y(IHI)) THEN
Y(IHI)=YTRY
DO 12 J=1,NDIM
PSUM(J)=PSUM(J)-P(IHI,J)+PTRY(J)
P(IHI,J)=PTRY(J)
END DO
ENDIF
AMOTRY=YTRY
RETURN
END
```

RANDOM NUMBER GENERATOR

```
FUNCTION RAN0(IDUM)
INTEGER IDUM,IA,IM,IQ,IR,MASK
REAL RAN0,AM
PARAMETER (IA=16807,IM=2147483647,AM=1./2147483647.,
+IQ=127773,IR=2836,MASK=123459876)
INTEGER K
IDUM = IEOR(IDUM,MASK)
K = IDUM/IQ
IDUM = IA*(IDUM-K*IQ)-IR*K
IF (IDUM.LT.0) IDUM=IDUM+IM
RAN0 = AM*IDUM
IDUM = IEOR(IDUM,MASK)
RETURN
END
```

INITIALIZE RNLIN FITTING VARIABLES

```
SUBROUTINE RNITIAL
COMMON/BK2/ DT,DZ,DIA,PI,NT,NZ,NP,NT_INC,NT_DATA
COMMON/BK3/ V(20),QR(4),RKA(4),RKD(4),CIRC,A1,VT
COMMON/BK5/ RHO_B,RHO_P,RHO_SC,EPSILON,VOL_SK,EPS_T,EPS_SK
COMMON/BK6/ Q_MLMIN,W_CAT,VOL,VOL_CAT,VOL_P,XA
Q_MLMIN= V(1)
EPSILON= V(2)
VOL_SK = V(3)
```

```
EPS_T = V(4)
QR(1) = V(5)
QR(2) = V(6)
QR(3) = V(7)
QR(4) = V(8)
RKA(1) = V(9)
RKA(2) = V(10)
RKA(3) = V(11)
RKA(4) = V(12)
RKD(1) = V(13)
RKD(2) = V(14)
RKD(3) = V(15)
RKD(4) = V(16)
A1 = V(17)
CIRC = V(18)
VT = V(19)
RETURN
END
```